QUASIPARTICLE AND PHONON TRANSPORT IN SUPERCONDUCTING PARTICLE DETECTORS

Gavin Burnell

King's College, Cambridge

A Dissertation Submitted for the degree of Doctor of Philosophy
in the University of Cambridge

August 1998

Summary

For over a decade now there has been much research into the use of superconductors in X-ray, gamma ray and other particle detectors. Detectors based on superconductor-insulator-superconductor(SIS) and superconductor-insulator-normal metal(SIN) tunnel junctions have been widely developed. To date, the predicted excellent energy resolving ability of such detectors has not been realised. Various energy loss processes have been suggested as possible causes for the failure to obtain energy resolutions close to the thermodynamic and quantum limits predicted.

In my experiments, I have used both SIS and SIN tunnel junctions to investigate the transport of quasiparticles and phonons in structures similar to the proposed detector designs. I have used multiple distributed junction geometries to perform injection-detection type experiments. One junction is used to inject quasiparticles and/or phonons into the device structure, whilst the current-voltage characteristic of a second junction is monitored for a response to the injected quasiparticles/phonons.

Using this type of experimental set-up, I have measured the transport of non-thermal equilibrium quasiparticles in an epitaxial niobium film. Using a simple random walk model, I have calculated an effective lifetime for quasiparticles. I have not observed the process of quasiparticle multiplication that has been observed by other researchers - I attribute this to differences in the microstructure of my devices and comment on the implications of this to possible quasiparticle loss mechanisms.

I have investigated the energy transport in a device with a number of SIN tunnel junctions connected to a common normal metal electrode. Phonon transport via the substrate is found to be the dominant coupling process between the tunnel junctions, although the device design can result in some junctions being effectively shielded from the substrate phonons by the common electrode.

Finally, the possibilities of using a superconducting heterostructure to control the rate at which quasiparticles recombine and emit phonons have been explored. Excessive recombination is believed to limit the effectiveness of large areas SIN tunnel junctions as thermometers for particle detecting bolometers.

Preface

This dissertation, which is submitted for the degree of Doctor of Philosophy in the University of Cambridge, describes work carried out from October 1994 to August 1998 in the Department of Materials Science and Metallurgy, University of Cambridge. Except where specific reference is made, this work is entirely the result of my own work and includes nothing that is the outcome of work done in collaboration. No part of this work has been or is being submitted for any other qualification at this or any other university.

Gavin Burnell
Device Materials Group, Dept. Materials Sci., University of Cambridge
August 1998.

It would not have been possible for me to carry out this work without the help and support of many people. Firstly, I must thank my supervisor, Dr. Mark Blamire, who has shown extreme forbearance, despite having a student seemingly bent on doing everything that had absolutely nothing to do with the his research project. I would also like to thank the head of the Device Materials Group, Dr. (now Prof.) Jan Evetts, and the heads of the Materials Science and Metallurgy Department, Profs. Humphreys and Windle, for providing laboratory facilities. I have been supported financially by the Engineering and Physical Sciences Research Council, and the US Naval Research Laboratory. In addition, I thank King's College Cambridge for help with travelling expenses.

Important on a day to day basis to my research have been the other members of Device Materials Group. In particular I would like to thank (now Dr.) Wilfred Booij who has provided invaluable advice, measurement hardware, and rather more meals than I gave in return ! Dr. Zoe Barber has shown much patience with my intemperate and normally unfounded accusations against the clean-room equipment. Richard Moseley and Dr. Ikuo Kanno have helped enormously as we have

collectively struggled over far too many months with our device processing failures. Dr. Ed Tarte has always been ready to attempt to increase my knowledge of theory. Others who made my time very enjoyable include, (hopefully soon to be Drs.) Dolores Vazquez Navarro and Steve Isaac, Yogesh Soman, Daniel Jardine, Dr. Robert Herzog, Dr. Jessica Owens and Dr. Martin Goodchild.

Outside of the laboratory, I must firstly thank my housemates: Rebecca and Percy Preston, who have had to put up with me doing far less than my fair share of the housework. I would also like to thank all of the Cambridge Young Friends, in particular Ruth Sanders who helpfully contributed the word 'monkey' for this thesis. Thanks are also due to my relations, in particular my parents, Martin and Jocelyn. Finally, and in no means least, I would like to thank Rachel Muers who has endured my stressed state over the last 18 months.

This thesis was proof-read by Dr. Wilfred Booij, Richard Mosely and Rachel Muers, to whom I am very grateful.

Preface to the 2nd Edition

In this the second edition of this thesis, I should like to thank my examiners, Dr. Ed Tarte and Prof. Gordon Donaldson, firstly for recommending me for the degree of PhD on the basis of this work, and seondly for bringing to my attention some loosely worded, wild, or just plain wrong statements. In addition to these corrections, a new section of the conclusions has been added, various software induced typesetting glitches removed, and a quote corrected. I am also happy to record that since the first edition, those listed above as soon to be Drs. are now also actual Drs.

G.B. Cambridge, December 1998

Contents

CHAPTER 1

Introduction

In the beginning the Universe was created.
This made a lot of people very unhappy and has been widely regarded as a bad move.

(Douglas Adams, "The Restaurant at the End of the Universe")

1.1 Cryogenic Particle Detectors

For approximately the last decade, the field of low temperature detectors has blossomed from its origins in the search for solar neutrinos and dark matter into a fast growing field covering many areas of science and industry(Pretzl 1996). The driving forces have been the searches for the ever better energy resolution and lower thresholds that are required to perform 'state-of-the-art' experiments.

The first particle and high energy electro-magnetic radiation detectors, such as Geiger counters, proportional counters and scintillators, utilised ionisation and excitation processes with energy quanta of around 20 eV. Such coarse resolution permitted little spectroscopic investigation, the obtainable energy resolution being about equal to the energy being measured. A major advance came with the introduction of semi-conductor detectors that were able to sense energy in quanta of order 1 eV, allowing true spectroscopic studies. However, many of the applications require an energy resolution that is two orders of magnitude better than that offered by semiconductor detectors. It is to fulfil that need that many cryogenic detector concepts have been suggested and developed. Such detectors offer the ability to sense energy in much smaller quanta than previous types of detectors, for example, the binding energies of Cooper pairs in a superconductor (~meV) or phonon energies at low temperature (~μeV for mK temperatures). Thus, these new detectors potentially can deliver better than one part in a thousand energy resolution.

To date, however, the promised two orders of magnitude improvement in resolution has not been realised. The problems that have arisen are many-fold and complex. There are issues of materials science - the selection of optimum materials that are compatible with the fabrication routes chosen and development of those fabrication techniques. Then there are issues of electrical engineering - development of low-noise read-out electronics and signal processing. Still there remain problems in the fundamental physics of these detector concepts, unexplained or poorly understood phenomena that limit the possible resolution.

This work is aimed at addressing some of these problems for the types of cryogenic detector that we have been developing for the last ten years in the Device Materials Group at the Department of Materials Science, Cambridge University. Our detectors are based on thin film, metal-insulator-metal systems, in which at least one of the metal films is a low critical temperature superconductor. In such detectors, the role of the electronic excitations from the superconducting groundstate, the quasiparticles, and thermal and athermal phonons in sensing the energy of an incident particle are paramount. The particular concern has been to improve our understanding of how energy deposited in a detector is transported from the location of the detection event, to and within the sensing region, and then how that energy is dissipated in such a way as to allow the detector to sense another event. The work which I report in this thesis has been in support of a continuing programme of X-ray detector development and testing work, carried out in collaboration with the US Naval Research Laboratory, Washington D.C., and latterly the Astrophysics Group at the Department of Physics, Imperial College, London.

Our own facilities do not allow the use of X-rays directly for testing in our devices. The experiments that have been carried out and reported here have utilised current injection from a metal-insulator-metal tunnel junction to create a population of quasiparticles and/or phonons at one specific location in a device. We have measured the result of this injection using other metal-insulator-metal junctions in our devices. This steady-state approach allows us to control both the location of the energy deposition, by fabricating devices with a number of current-injection junctions, and indirectly of the energy distributions of the populations of quasiparticles and phonons produced, by varying the current and bias applied to the injecting junction. In terms of developing a viable particle detector, we have to remember that steady state injection is different from particle absorption and that transient, time dependent, effects are not reproduced. Nevertheless, the technique does allow us to probe aspects of the energy transport in such devices.

1.2 Form of this Thesis

In chapter 2 we introduce the basic theory of superconductors, and tunnel junctions. We include discussions of both the proximity effect - i.e. heterogeneous superconductors, and non thermal-equilibrium superconductivity -i.e. cases where the population of quasiparticles and phonons in a superconductor is significantly different from that of a superconductor in thermal equilibrium with its surroundings. A discussion of the applications and designs of cryogenic detectors based on superconductors starts in Chapter 3. This is followed by a detailed examination of some of the processes that can be expected to occur in a superconducting particle detector, and how these may influence performance. Chapter 4 describes the experimental methods that have been used to carry out the experimental work that is presented in chapters 5 to 7.

Chapter 5 discusses measurements of the quasiparticle lifetime and dynamics in epitaxial Nb films. We have examined the effect of niobium oxides, a result of the fabrication route used, on both the quasiparticle lifetime and the relaxation of the quasiparticles from their injected non-equilibrium distribution. Of particular interest was to determine whether the niobium oxide resulted in a faster loss of quasiparticles and hence a degradation in the signal that would result from a detection event(Gijsbertsen 1996b). In addition, we found that in our devices the existing theories for quasiparticle multiplication did not describe our results. We have examined this in the context of the microstructure of our devices, and interpret it in terms of the scattering of quasiparticles in the presence of significant amounts of niobium oxide.

Chapter 6 describes our work on the development of bolometers with readouts using a superconductor-insulator-normal metal tunnel junction. In particular we have examined how our devices respond to energy deposition in a normal metal absorber, and the importance of phonon transport through the substrate relative to heat transport through the electrons in the metal. This work has implications not only for the design of bolometers, where the energy is deposited in a normal metal film, but also for those in which the energy is deposited in a dielectric crystal.

We continue our study of the physics of superconductor-insulator-normal metal junctions in chapter 7. We explore the use of a controlled superconducting heterostructure to minimise self-heating effects resulting from absorption of excess quasiparticles and phonons from the superconductor back into the normal metal. Such processes have been suggested to be a major limiting factor in the use of superconductor-insulator-normal metal tunnel junctions as temperature sensors(Drury 1997; Jochum 1998). We find that we can influence the self-heating by the use of the heterostructure, although any gain to be had in controlling the lifetime of the quasiparticles to reduce the localised heating is easily swamped by phonon transmission through the substrate.

Finally, chapter 8 presents the conclusions resulting from this work. Two appendices are also included. The first is a paper written by the author for ASC 1996, containing calculations of the cooling effect that can be achieved by the appropriate use of superconductor-insulator-normal metal junctions to remove energetic electrons from a normal metal. This cooling effect is part of the attraction of using superconductor-insulator-normal metal tunnel junctions as temperature sensors, and is discussed in detail in chapter 3. The second appendix contains a paper presented by the author at the Low Temperature Detectors Workshop 7, held in Munich, in July 1997, and describes work which is also presented in chapter 6.

CHAPTER 2

Theory of Superconductivity

In this chapter, the aspects of the theory of superconductors that are required to understand the experimental work presented in the following chapters are outlined. We begin, after a brief historical introduction, with the microscopic theory of Bardeen, Cooper and Schrieffer(Bardeen 1957), upon which most of this work depends. This is followed with a discussion of the properties of various classes of tunnel junctions. Next, the lifetimes of quasiparticles, phonons and electrons in the superconductors, normal metals and substrates used are examined. In this work, results based on heterogeneous superconducting thin films are presented, so next some theories of the proximity effect must be introduced. Finally, some widely used approaches to studying superconductors driven far from thermal equilibrium will be mentioned. It is not possible in the space available to present as full a description of the basic theory and its historical development as one might wish, indeed there are many text books which do a more than adequate job of this and the reader is directed towards these. In particular, the author has found the work of Tinkham(Tinkham 1996) to be very clear and helpful.

2.1 Historical Introduction

The discovery of superconductors was heralded in 1911 by the first measurement of their best-known property, that of vanishing electrical resistance below a critical temperature, by Kamerlingh Onnes in Leiden(Onnes 1911). Three years previously, he had successfully liquefied Helium, thus making the necessary low temperatures of a few degrees Kelvin available for the first time. In 1933 Meissner and Ochsenfeld discovered that a superconductor exhibited perfect diamagnetism, so that it would expel any magnetic field less than a certain critical magnetic field when cooled below its critical temperature T_c(Meissner 1933). This, the so-called Meissner effect, is what distinguishes a superconductor from merely a perfect conductor which will also show zero resistance. A phenomenological model of the electrodynamical properties of superconductors was introduced by the brothers F. and H. London(London 1935) in 1935.

The importance of the interaction of phonons with the superconducting charge carriers was indicated by the discovery in 1950 of the isotope effect, in which T_c was

found to scale with the inverse square root of the atomic mass. Also in 1950 Ginzburg and Landau applied Landau's general theory of second order phase transitions to superconductors. In 1957 a successful microscopic model for superconductivity (BCS Theory) was introduced by Bardeen, Cooper and Schrieffer(Bardeen 1957).

2.2 Phenomenological Models of Superconductivity

Before introducing the BCS microscopic theory of superconductivity, we mention three phenomenological approaches to understanding superconductivity, those of the London brothers, Pippard, and Ginzburg and Landau.

2.2.1 London Theory

The theory of F. and H. London is based on a two fluid concept, in which there are superconducting electrons and conventional conduction electrons(London 1935). The number density of the superconducting electrons was expected to be 0 for T=0, rising rapidly to a density of the same order as the conduction electron number density for $T \ll T_c$. The London brothers proposed two equations to describe the microscopic electric and magnetic fields:

$$\mathbf{E} = \frac{\partial}{\partial t}\left(\Lambda \mathbf{J}_s\right) \tag{2.1}$$

$$\mathbf{h} = -c.curl\left(\Lambda \mathbf{J}_s\right) \tag{2.2}$$

$$\Lambda = \frac{4\pi\lambda^2}{c^2} = \frac{m}{n_s e^2} \tag{2.3}$$

Here n_s is the number density of superconducting electrons, E and h are the microscopic electric and magnetic fields respectively, m and e the mass and charge of an electron and c the speed of light. J_s is the current flux of superconducting electrons. The first equation (2.1) expresses perfect conductivity, since the electric field continuously accelerates the superconducting electrons. The second equation leads to an understanding of λ when taken with the Maxwell equation $curl\,\mathbf{h} = 4\pi\mathbf{J}/c$ to give:

$$\nabla^2 \mathbf{h} = \frac{\mathbf{h}}{\lambda^2} \tag{2.4}$$

This implies that the magnetic field inside a superconductor decays exponentially with a characteristic length λ - the Meissner Effect. Hence, λ is the penetration depth of the magnetic field into the superconductor. The London penetration depth is given by:

$$\lambda_L(0) = \left(\frac{mc^2}{4\pi ne^2} \right)^{\frac{1}{2}} \tag{2.5}$$

2.2.2 Pippard Non-Local Electrodynamics

Experimentally it was found that the measured penetration depth always exceeds the London penetration depth. Pippard was able to account for this discrepancy by considering a non-local generalisation of the London Equation(Pippard 1953). The basic concept rests on the supposition that the current at any point **r** depends on the electric field **E(r')** within a region of characteristic radius ξ_0. ξ_0 is the Pippard coherence length which can be found from the uncertainty principle. If one assumes that only electrons within $k_B T_c$ of the Fermi surface play a part in the superconducting state, then the uncertainty in the momentum is $\Delta p = k_B T_c / v_F$. Hence $\Delta x > \hbar v_F / k_B T_c$, and a coherence length can be defined as:

$$\xi_{Pippard} = a \frac{\hbar v_F}{k_B T_C} \tag{2.6}$$

where a is numerical parameter that was found experimentally to be 0.15 and 0.18 in BCS theory. Using this coherence length, Pippard was able to fit experimental data for both aluminium and tin.

2.2.3 Ginzburg-Landau Theory

Ginzburg-Landau theory(Ginzberg 1950) postulates that a superconductor can be described with a spatially varying complex order parameter Ψ(r). $\Psi^2(r)$ is identified with the superfluid density of the London model of superconductivity (essentially the density of superconducting charge carriers). Gor'kov(Gor'kov 1960) extended this to identify Ψ(r) with the pair potential Δ(r). The basic postulate is that the free energy of the superconductor can be expanded in a series of the form:

$$G_S = G_N + \alpha|\Psi|^2 + \frac{\beta}{2}|\Psi|^4 + \gamma\left|\nabla\Psi + \frac{2e}{\hbar}A\Psi\right|^2 + \frac{1}{2\mu_0}\left(B - B_E\right)^2 \tag{2.7}$$

where **A** is the vector potential, G_N is the free energy of the normal state at the same temperature, **B** and $\mathbf{B_E}$ are the net and external magnetic fields. The first three terms give the free energy for a homogenous superconductor in the absence of an applied field, the fourth term is the kinetic energy associated with changes in pair potential and magnetic field and the final term is the magnetic self energy of the supercurrents. After minimising the free energy, and selecting suitable signs for α,β and fixing γ to normalise Ψ^2, we find:

$$\frac{\hbar^2}{4m}\frac{\partial^2\Psi}{\partial x^2} = \left(\alpha + \beta|\Psi|^2\right)\Psi \tag{2.8}$$

for a one dimensional normal metal-superconductor interface with no applied field. If $\alpha >> \beta|\Psi|^2$ this can be solved to give an exponential decay of the order parameter on a length scale of $\xi_{GL}/\sqrt{2}$ within the superconductor and with a length scale of ξ_{GL} within the normal metal where ξ_{GL} is given by:

$$\xi_{GL} = \frac{\hbar}{\sqrt{4m_e|\alpha|}} \tag{2.9}$$

ξ_{GL} is the Ginzburg-Landau coherence length. For $T << T_c$ and pure superconductors this is quite close to the Pippard coherence length. In the dirty limit, where the mean free path $l << \xi_{GL/Pippard}$, ξ_{GL} varies as $\sqrt{\xi_{GL} l}$ and $\xi_{Pippard}$ as the reciprocal sum of $\xi_{Pippard}$ and l.

2.3 Aspects of BCS Theory

2.3.1 BCS Theory for 0 K

2.3.1.1 Introduction

The basis for understanding the behaviour of the superconducting thin films and tunnel junctions that we discuss in this work is the microscopic theory of superconductivity of Bardeen, Cooper and Schrieffer(Bardeen 1957).

In 1956 Cooper showed(Cooper 1956) that if two electrons which interacted by a weak attractive potential were placed in the presence of a Fermi sphere of electrons, then they would exist in a bound state, even if the potential was too weak to hold them had they been isolated. The Fermi sea of unbound electrons in this case serves to prohibit the two bound electrons from occupying states with wavenumber k less than the Fermi wavenumber, k_f, thus stabilising the bound state irrespective of how weakly attractive the interaction is.

The linkage between the phonons and the superconducting state had been established by the measurement of the isotope effect in 1950. The implication of this is that the attractive force responsible for the bound electron pair state is phonon mediated. Since the phonon spectrum has a cut-off at the Debye energy ($\hbar\omega_D$), the cut off for the interaction ($\hbar\omega_c$) should be of the same order of magnitude. An approximation for the interaction potential, $V_{kk'}$, can be made so that:

$$V_{kk'} = \begin{cases} -V & \varepsilon_f < \varepsilon_k \varepsilon_{k'} < \varepsilon_f + \hbar\omega_c \\ 0 & otherwise \end{cases} \tag{2.10}$$

where ε_k,$\varepsilon_{k'}$ are the energies of the two electron states with wave vectors **k** and **k'** and ε_f the Fermi energy. If the interaction potential V is extremely weak, so that $N(0)V \ll 1$, where N(0) is the single spin density of states at the Fermi surface, then the energy of the bound state can be found by solving the Schrödinger Equation for the system to find:

$$E = 2\left(\varepsilon_f - \hbar\omega_c e^{-\frac{2}{N(0)V}}\right) \tag{2.11}$$

Therefore, there is a bound state with an energy that is less than the Fermi energy (the factor two in (2.11) arises from that fact that bound state contains two electrons), but for which the kinetic energy is greater. The attractive potential energy of forming the bound state outweighs the excess kinetic energy.

2.3.2 BCS Ground-State

Given that the Fermi sea is unstable against the formation of a bound pair state if there is an attractive potential between electrons, we might expect that further electrons would form bound pair states until some equilibrium is established. BCS

theory extends the work of Cooper to consider this process, allowing all the electrons within $\hbar\omega_c$ of the Fermi surface to form bound pairs.

To describe the ground state for the BCS model we use the language of second quantization in which the occupied states are specified by the use of "creation operators" such as $c^+_{k\uparrow}$ and $c_{k\uparrow}$ which respectively create and annihilate an electron of momentum **k** and spin up. In this notation the wavefunction for one pair state is written:

$$\left|\psi_0\right\rangle = \sum_{k>k_F} g_k c^+_{k\uparrow} c^+_{-k\downarrow} \left|F\right\rangle \tag{2.12}$$

Where $|F\rangle$ represents the Fermi sea with all states filled out to k_F. A general N-electron wavefunction can be written as:

$$\left|\Psi_N\right\rangle = \sum g(k_i,\ldots,k_l) c^+_{k_i\uparrow} c^+_{-k_i\downarrow} \cdots c^+_{k_l\uparrow} c^+_{-k_l\downarrow} \left|\phi_0\right\rangle \tag{2.13}$$

with $|\phi_0\rangle$ the vacuum state with no particles in it, $\mathbf{k_i}\ldots\mathbf{k_l}$ the set of M **k** values in the band which are occupied for any single term in the sum and g a weighting term with which each set of N/2 pairs of creation operators appears. This wavefunction needs considerable simplification to be useable, since there will be:

$$\frac{M!}{\left[M-(N/2)\right]!(N/2)!} \approx 10^{10^{20}} \tag{2.14}$$

combinations in which N/2 pair states can be chosen. BCS theory assumes that the occupancy of each state **k**, depends only on the average occupancy of all the other states. Interestingly, this approximation relaxes the constraint of particle conservation so that only the mean number of particles $\overline{N}$ is conserved. We then have the BCS ground state:

$$\left|\psi_\varphi\right\rangle = \prod_k (u_k + v_k c^+_{k\uparrow} c^+_{-k\downarrow}) \left|\phi_0\right\rangle \tag{2.15}$$

where u_k^2 is the probability that a pair state $(k\uparrow,-k\downarrow)$ is empty and v_k^2 the probability that it is occupied. The problem then becomes one of minimising the ground state energy to fix the coefficients u_k and v_k. This is equivalent to solving:

$$\left\langle \Psi_\varphi \left| H - \mu\widehat{N} \right| \Psi_\varphi \right\rangle = 0 \tag{2.16}$$

with the H the Hamiltonian for the system, μ the chemical potential and $\hat{N}$ the particle number operator (so that $\langle \hat{N} \rangle = \overline{N}$). BCS theory further neglects all interactions between the electrons other than the weak pairing interaction $V_{kk'}$, so that we may write:

$$H = \sum_{k,\sigma=\uparrow,\downarrow} \varepsilon_k c_{k\sigma}^{+} c_{k\sigma} + \sum_{k,k'} V_{kk'} c_{k\uparrow}^{+} c_{-k\downarrow}^{+} c_{k'\uparrow} c_{-k'\downarrow} \tag{2.17}$$

The first term is the kinetic energy of the electrons, and the second the pairing interaction. This problem can be solved either by a variational method or by canonical transformation, and with the introduction of two parameters:

$$\Delta_k = -\sum_{l} V_{kk'} \langle c_{k'\uparrow} c_{-k'\downarrow} \rangle = -\sum_{l} V_{kk'} u_{k'} v_{k'} \tag{2.18}$$

$$E_k = \sqrt{\Delta_k^2 - \xi_k^2} \tag{2.19}$$

where ξ_k is the energy of a state **k** relative to the Fermi energy ε_F. Following this process results in expressions for the pair occupation probability, v_k^2:

$$v_k^2 = \frac{1}{2}\left(1 - \frac{\xi_k}{E_k}\right) \tag{2.20}$$

and since a pair state is either occupied or not, so that

$$u_k^2 + v_k^2 = 1 \tag{2.21}$$

$$u_k^2 = \frac{1}{2}\left(1 + \frac{\xi_k}{E_k}\right) \tag{2.22}$$

The approximation for the interaction potential $V_{kk'}$ in (2.10) implies that Δ_k is in fact independent of **k**, so that we have one value of Δ which we identify as the *order parameter*. This order parameter Δ can be related to the critical temperature for the weak coupling limit (i.e. where $N(0)V \ll 1$) by:

$$\Delta(T = 0K) = 1.764 k_B T_C \tag{2.23}$$

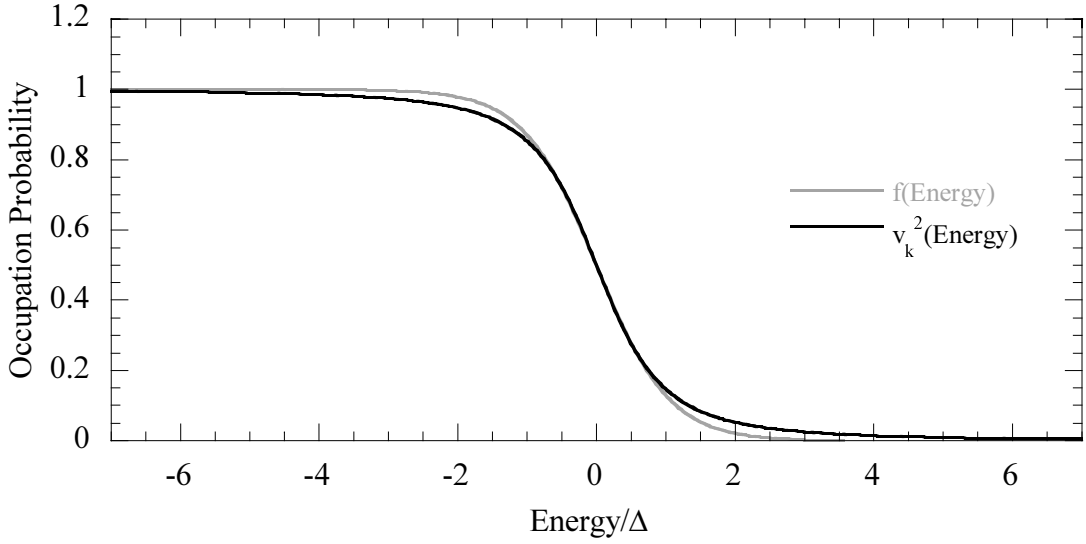

Figure 2.1 Pair state occupation probability and fermi function at T_c.

where k_B is Boltzmann's constant. Figure 2.1 shows a plot of v_k^2 and the Fermi function at T_c. for a weakly coupled superconductor. We see that the actual occupation fractions of the electrons is little changed between the normal and superconducting states, rather the electrons condense into Cooper pairs ordered in momentum space and reduce their overall energy.

2.3.2.1 Excitations from the Ground-State

Having considered the ground state of a superconductor under BCS theory, we are now ready to examine the excitations from the ground state. As we shall see in the following chapters, it is the excitations from the ground state which are the key to the applications of the work presented here.

Given that the ground state involves the condensation of single electrons into pair states, it follows that the excitations involve the reverse of this process. Bogoliubov and Valatin(Bogoliubov 1958; Valatin 1958) independently introduced the following operators to create such excitations:

$$\begin{aligned}\gamma_{k0}^{+} &= u_k^{+} c_{k\uparrow}^{+} - v_k^{+} c_{-k\downarrow} \\ \gamma_{k1}^{+} &= u_k^{+} c_{-k\downarrow}^{+} + v_k^{+} c_{k\uparrow}\end{aligned} \tag{2.24}$$

γ_{k0}^{+} places an electron into a state with momentum $\hbar\boldsymbol{k}$ and spin up (which we can label $|k\uparrow\rangle$) from a pair state $|k\uparrow,-k\downarrow\rangle$; the first term definitely occupies $|k\uparrow\rangle$ if

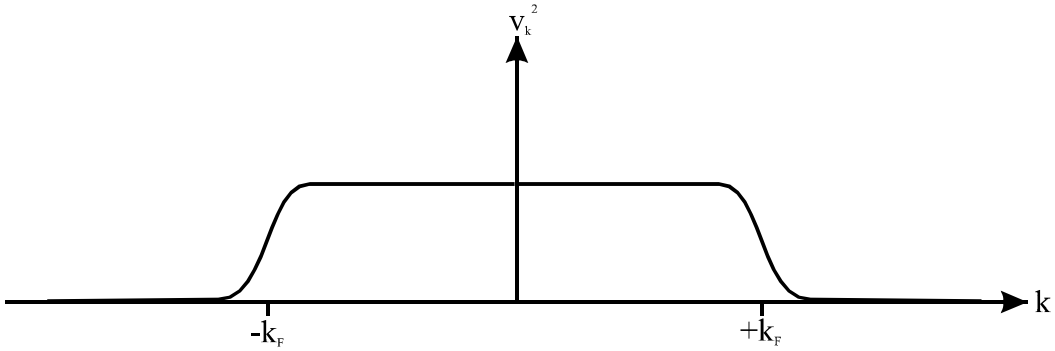

Figure 2.2 Ground state occupation probability vs. wave number.

$\left|k\uparrow,-k\downarrow\right\rangle$ was empty, whilst the second definitely empties $\left|-k\downarrow\right\rangle$ if $\left|k\uparrow,-k\downarrow\right\rangle$ was occupied. The second operator, γ_{k1}^{+} performs the exactly analogous operation, creating an electron in the state $\left|-k\downarrow\right\rangle$, whilst ensuring that $\left|k\uparrow\right\rangle$ is empty.

We can consider how these operators effect the occupation probabilities as a function of k. Figure 2.2 shows the probability of occupation in the ground state, we see that for states with $|k|<<k_F$ (k_F being the Fermi wave number), the occupation probability $v_k^2\approx1$. For states with $|k|>>k_F$, $v_k^2\approx0$ and for states with $|k|\approx k_F$, v_k^2 is continuous and varies as in figure 2.1.

The difference between the effect of the two operators in (2.24) when plotted on diagrams such as figure 2.2 is only whether the state at +k or –k is filled since we do not consider the spin of the electrons. There is, however, an important difference in the nature of the excitations depending on whether k is greater than, less than or close to the Fermi wavenumber k_F.

If an excitation fills a state with $|k_h|<< k_F$, and consequently empties the state

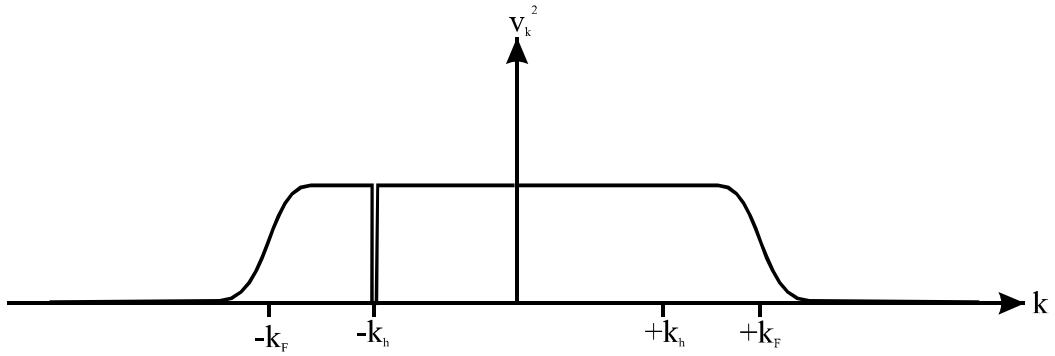

Figure 2.3 Occupation probability for a quasihole.

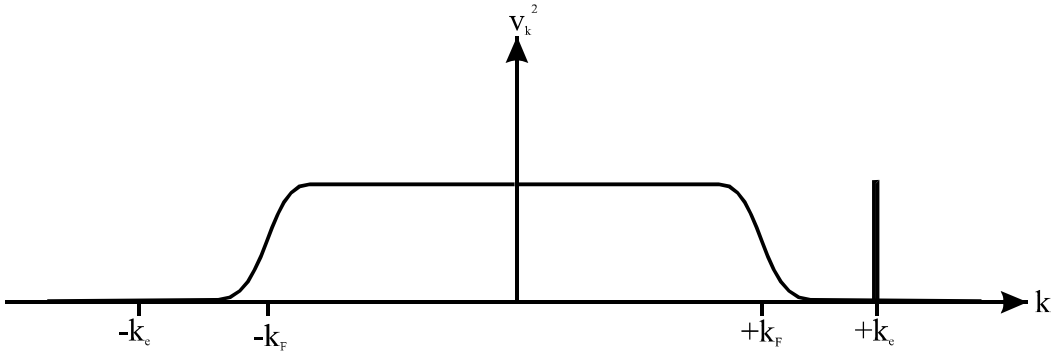

Figure 2.4 Occupation probability for a quasielectron.

at $-k_h$ (figure 2.3), then the probability of occupation of the state at k_h changes from very slightly less than 1 to exactly 1, which is a negligible effect. On the other hand, the state at $-k_h$ now has an occupation probability of zero, a significant change from its previous value of approximately one. The excitation can therefore be said to have a *hole-like* behaviour.

If, however, the excitation operates on states with $|k_e| >> k_F$ (figure 2.4), then it is the state at k_e, in changing occupancy from approximately zero to 1, which undergoes the most significant change. The state at $-k_e$ changes occupancy from slightly greater than zero to exactly zero. In this case the excitation has an *electron-like* behaviour.

We have been careful in the above description to use the terms *hole-like* and *electron-like* since as the wavenumber k approaches k_F, the situation in figure 2.5 occurs. We have shown the occupation probability of pair states at the Fermi wavenumber is continuous, thus for an appreciable range of wavenumbers around k_F the changes in the occupation probabilities at both k and –k due to an excitation are

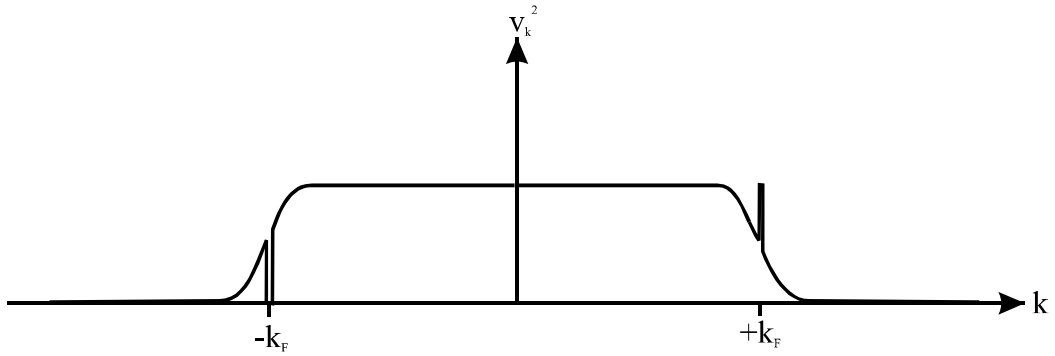

Figure 2.5 Occupation probability for a quasiparticle.

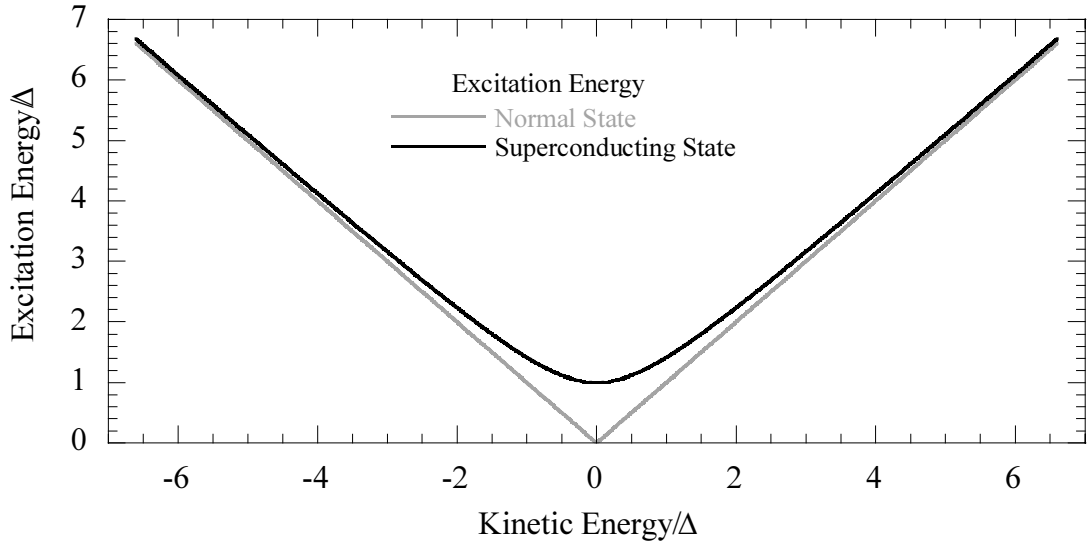

Figure 2.6 Excitation energy vs. kinetic energy.

significant. This results in excitations that are neither (or both !) *electron-like* and *hole-like*. It is due to this possibility of this mixed character that the excitations are known as *quaisholes* ($k<<k_F$), quasielectrons ($k>>k_F$) and collectively as *quasiparticles*.

2.3.2.2 Density of States

It can be shown in the derivation of (2.20) and (2.22), that the energy to create a quasiparticle with a kinetic energy ξ_k is the parameter E_k given by (2.19). The equivalent for an electron in the normal state is therefore just ξ_k. Figure 2.6 shows the excitation energy as a function of the kinetic energy, from which it is immediately apparent that there is a minimum excitation energy, Δ.

We are now able to find the density of states for the quasiparticles. We note that quasiparticles are fermions and there is a one to one correspondence between the electron states in a normal metal and the quasiparticle states in the superconductor so that:

$$\begin{aligned} & N_s(E_k)dE_k = N_n(\xi_k)d\xi_k \\ \Rightarrow \quad & \frac{N_s(E_k)}{N_n(\xi_k)} = \frac{d\xi_k}{dE_k} \end{aligned} \tag{2.25}$$

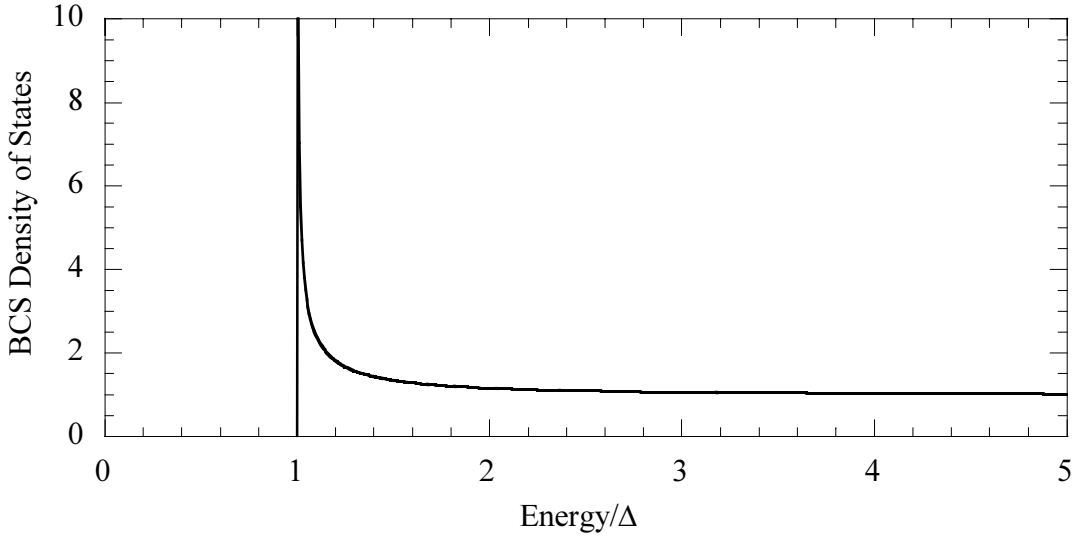

Figure 2.7 BCS density of states

where N_s and N_n are the number of quasiparticles in the superconductor and number of electrons in the normal metal respectively. For energies close to the Fermi surface (of order meV), we can assume that $N_n(\xi_k)$ is a constant N(0). (2.25) is easily solved by using (2.19) to give the BCS density of states:

$$N_s(E_k) = N(0)\begin{cases} \dfrac{E_k}{\sqrt{E_k^2 - \Delta^2}} & E_k > \Delta \\ 0 & E_k < \Delta \end{cases} \tag{2.26}$$

This is plotted in figure 2.7.

2.3.2.3 Semiconductor Model

A convenient model when considering the behaviour of quasiparticles in a superconductor is the so-called semiconductor representation. This uses the relatively obvious analogies between quaisholes and quasielectrons and the holes and electrons in a semiconductor. The superconductor is represented as an ordinary intrinsic semiconductor with a band-gap equal to twice the energy gap Δ. The density of states for both the holes and electrons is given by (2.26) (the density of states for the holes is that same as that for the electrons after being reflected through the Fermi energy). The result is illustrated in figure 2.8. Conventionally the quasiholes are shown in the bottom half of the diagram, though they have positive excitation energy like the quasielectrons and increasing excitation energy scales as the distance from the Fermi

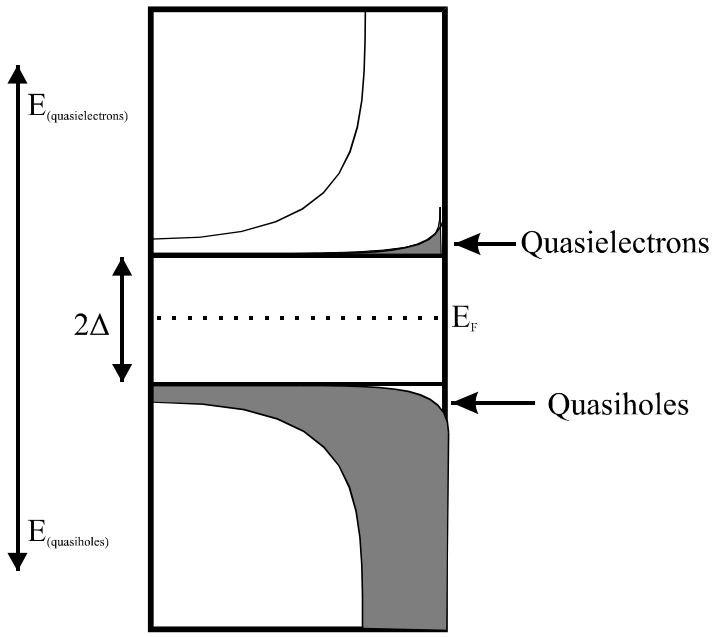

Figure 2.8 Semiconductor representation.

energy in the diagram. Strictly speaking, the semiconductor representation is a model of the tunnelling of quasiparticles, and is only valid when the electron distributions in the superconductor are not significantly perturbed. Thus, a large degree of caution must be applied before using the semiconductor model in situations far from equilibrium.

2.3.3 Finite Temperatures

Thus far, our discussion has only been for the zero temperature case. Obviously, in practice our devices do not operate at zero temperature, but at some finite temperature (albeit normally low relative to the critical temperature).

As we have stated above, quasiparticles are fermions, and thus obey Fermi-Dirac statistics, so that the probability that a particle in thermal equilibrium is excited is given by the Fermi function:

$$f(E,T) = \frac{1}{1+e^{E/k_BT}} \tag{2.27}$$

where E is the excitation energy and T the temperature. This modifies our definition of Δ in (2.18) to give:

$$\Delta_k = -\sum_{k'} V_{kk'} u_{k'}^{+} v_{k'} \left[1 - 2f(E_{k'},T)\right] \tag{2.28}$$

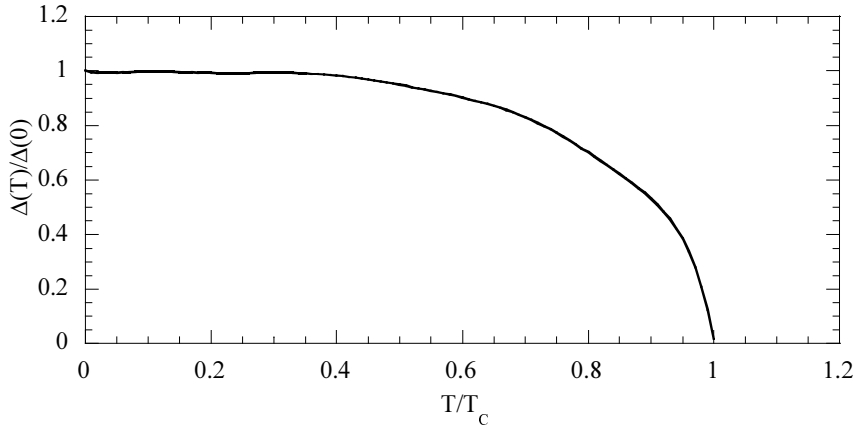

Figure 2.9 Temperature dependence of BCS energy gap

Using the BCS approximation that $V_{kk'}=V$, and that $\Delta_{k'}=\Delta$ we have:

$$\frac{1}{V}=\frac{1}{2}\sum_{k}\frac{\tanh\left(E_k/2k_BT\right)}{E_k} \tag{2.29}$$

2.3.3.1 Critical Temperature

The critical temperature, T_c, is defined as the temperature at which the order parameter, Δ, tends to zero. At this point the excitation energies of quasiparticles, E_k, tend to the kinetic energy, ξ_k, and the excitation spectrum becomes that of a normal metal. We can then use (2.29), replacing the excitation energy E_k with ξ_k, replacing the summation with an integral and solving to find (2.23). In practice it is found that the experimental values of Δ for different materials and directions in k-space fall in the region of $1.5k_BT_c$ to $2.25k_BT_c$(Tinkham 1996).

2.3.3.2 Temperature Dependence of the Energy Gap

From (2.29) it is possible to numerically calculate $\Delta(T)$. For weak coupling superconductors this gives a universal curve $\Delta(T)/\Delta(0)$ as a function of T/T_c which decreases monotonically from 1 at T=0 to zero at $T=T_c$. Figure 2.9 shows a plot of the BCS energy gap (from data tabulated in (Mühlschlegel 1959)). Close to T_c the energy gap falls to zero with a vertical tangent, which can be approximated by:

$$\frac{\Delta(T)}{\Delta(0)}\approx 1.74\sqrt{\left(\frac{T_C-T}{T_C}\right)} \tag{2.30}$$

however, in this work we generally consider $T<<T_c$, in which case, as shown in figure 2.9, $\Delta(T)\approx\Delta(0)\approx1.76k_BT_c$. Physically, this approximation follows from the fact that the energy gap is not significantly reduced until there is an appreciable population of thermally excited quasiparticles. As we shall see below, a significant population of non-equilibrium quasiparticles can have the same effect.

2.4 Tunnel Junctions

The common feature in all the devices discussed in this work is their use of tunnel junctions. It is therefore appropriate to consider the properties of the various classes of tunnel junctions, in particular to examine their current-voltage characteristics.

Quantum mechanics predicts that it is possible for a particle to exist on both sides of a barrier with a potential energy greater than the kinetic energy of the particle. A generic tunnel junction is a sandwich structure of two conductors separated by a thin insulating region, that forms such a barrier.

The probability of a particle tunnelling through the barrier in this way can be found from the solution of the Schrödinger equation and can easily be shown (see any good solid state physics text book such as (Ashcroft 1976)) to depend exponentially on the potential energy height of the barrier and its thickness and inversely on the volume from which tunnelling occurs. The tunnelling current from one side of the barrier to the other is given by:

$$I_{1\to2} \propto \int_{-\infty}^{\infty} |T(E)|^2 N_1(E) f(E) N_2(E+eV)\left[1-f(E+eV)\right]dE \tag{2.31}$$

where T(E) is the tunnelling matrix element – i.e. the probability that an electron at an energy E will tunnel. $N_{1/2}$ are the density of states in region 1/2, f(E) is the Fermi function, so that N_1f and $N_2(1-f)$ are the number of occupied initial states and empty final states respectively. If we assume that the barrier energy is much higher than any state we consider, then T(E) is a constant, and so the net current flow is found by subtracting the reverse current from (2.31). The net current is then given by:

$$I \propto \int_{-\infty}^{\infty} N_1(E) N_2(E+eV)\left[f(E)-f(E+eV)\right]dE \tag{2.32}$$

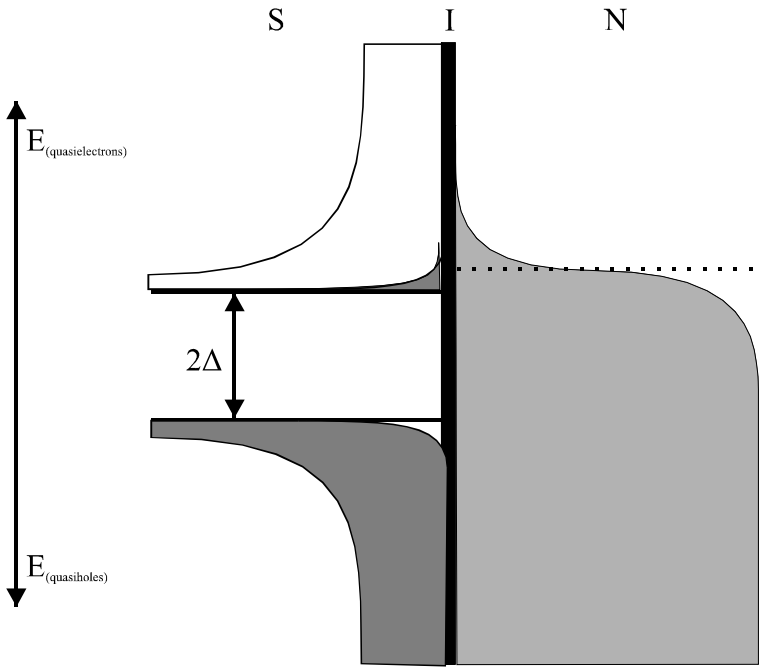

Figure 2.10 Semiconductor representation of a SIN Tunnel Junction

2.4.1 Normal Metal-Insulator-Normal Junctions

The simplest of the tunnel junction structures that we examine here is the Normal-Insulator-Normal (NIN) junction. In this case, we can represent the density of states on either side of the junction as being a constant. This assumption is similar to that made in the BCS density of states (2.26), where the density of states is constant for states far from the Fermi energy. (2.32) gives us:

$$\begin{aligned} I_{NIN} &\propto N_1(0)N_2(0)\int_{-\infty}^{\infty}\left[f(E)-f(E+eV)\right]dE \\ &\propto N_1(0)N_2(0)eV \\ &= \frac{V}{R_N} \end{aligned} \tag{2.33}$$

so that the junction has a well defined resistance that is independent of bias V, and is thus *ohmic*, and is in addition independent of temperature.

2.4.2 Superconductor-Insulator-Normal Metal Junctions

The superconductor insulator normal metal (SIN) junction is the first of the two classes of tunnel junctions used in this work. Its schematic cross section, and density of states (in the semiconductor representation) is shown in figure 2.10.

Only the quasiparticles will tunnel through the barrier to the normal metal since they are effectively single electron particles. The pair states cannot tunnel since by definition there are no pair states to tunnel to. It is possible for the pair states to undergo Andreev reflection at the interface with the barrier (see 2.6.4). However this is of very low probability for realistic thicknesses of tunnel barriers(Jug 1997).

Using the BCS density of states, (2.26), in (2.32) we find the general expression for the current in an SIN junction:

$$\begin{aligned} I_{SIN} &\propto N_1(0)\int_{-\infty}^{\infty} N_2(E)\left[f(E)-f(E+eV)\right]dE \\ &= \frac{1}{eR_N}\int_{-\infty}^{\infty} \frac{E}{\sqrt{\left(E^2-\Delta^2\right)}}\left[f(E)-f(E+eV)\right]dE \end{aligned} \tag{2.34}$$

where R_N is the same junction resistance as found above for the NIN junction. Trivially this follows since for $T>T_c$, $\Delta=0$, so (2.34) becomes equal to (2.33).

2.4.2.1 Low Bias ($eV<\Delta$)

In general, (2.34) needs to be calculated numerically in order to compare experimental data with theory due to the singularities in the BCS density of states. Figure 2.11 shows the result of such an evaluation for biases in the range $\pm 4\Delta$ at T=0 K. As can be seen, in this idealised case, there is no current flow until $e|V| \gtrsim \Delta$, whereupon there is a rapid increase in the current as the chemical potential difference provides enough energy to create a quasiparticle in the superconductor. In terms of the semiconductor this can be visualised as the normal metal states being raised by eV, so that electrons at the Fermi surface in the metal can tunnel through the barrier to the empty states above the energy gap in the semiconductor (figure 2.10).

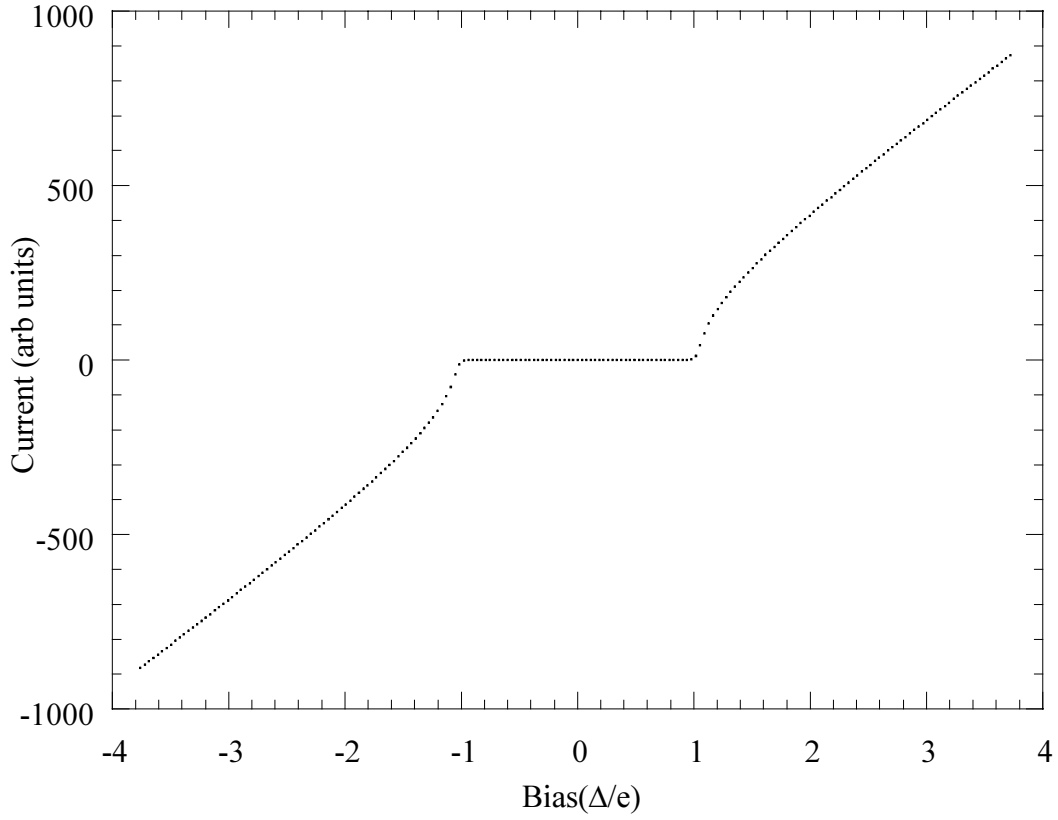

Figure 2.11 Current-voltage characteristic of a SIN tunnel junction

If we examine the differential conductance of the SIN junction then from (2.34) we have:

$$G_{SIN}(V) = \frac{dI_{SIN}}{dV} = \frac{1}{R_N}\int_{-\infty}^{\infty} \frac{N_S(E)}{N(0)}\left[-\frac{\partial f(E+eV)}{\partial(eV)}\right]dE \tag{2.35}$$

the term $-\dfrac{\partial F(E+eV)}{\partial(eV)}$ is a bell shaped weighting function with unit area and a width of approximately $4k_BT$, which for T=0 becomes a δ function, so that:

$$G_{SIN}\Big|_{T=0} = \frac{1}{R_N}\frac{N_S(e|V|)}{N(0)} \tag{2.36}$$

In the limit of low temperatures, therefore, the differential conductance directly measures the density of states in the superconductor.

2.4.2.2 High Bias (eV>Δ)

For sufficiently high bias, the BCS density of states (2.26) tends towards that of the normal state, so that we approach the situation of NIN tunnelling. In this case $N_{2(s)}(E)/N_{2(N)}(0) \approx N_{1(N)}(E)/N_{1(N)}(0)$, so that:

$$I_{SIN}(eV >> \Delta) = \frac{V}{R_N} \tag{2.37}$$

thus we can refer to the *normal-state resistance* to mean the resistance of the junction at high bias ($=R_N$).

2.4.2.3 Temperature Dependence

Using (2.34) it is possible to examine the temperature dependence of the current-voltage characteristic. As we have noted above, for high bias conditions the current-voltage characteristic tends towards that of the equivalent NIN junction, and so does not show any temperature dependence. However, for low biases where eV<Δ it is necessary to evaluate (2.34) with the appropriate temperature. We can go one stage further, and use separate temperatures in the S and N electrodes, to simulate an artificially increased electron temperature in one or other of the electrodes. In the next chapter we shall see that this is indeed the case for some applications. Figure 2.12 shows the sub-gap current (i.e. eV<Δ) for the case of increased S and N electrode electron temperature, as can clearly be seen, the sub-gap current (at eV=Δ/2) is strongly dependent on the N electrode temperature, but not on the S electrode temperature. This was shown analytically to be the case by Donaldson (Donaldson, 1967). For a bias $V<\Delta$, the number of electrons able to tunnel from the normal electrode scales as $e^{-(\Delta - eV/k_BT)}$, whilst the quasiparticle population in the S electrode scales as $e^{-\Delta/k_BT}$.

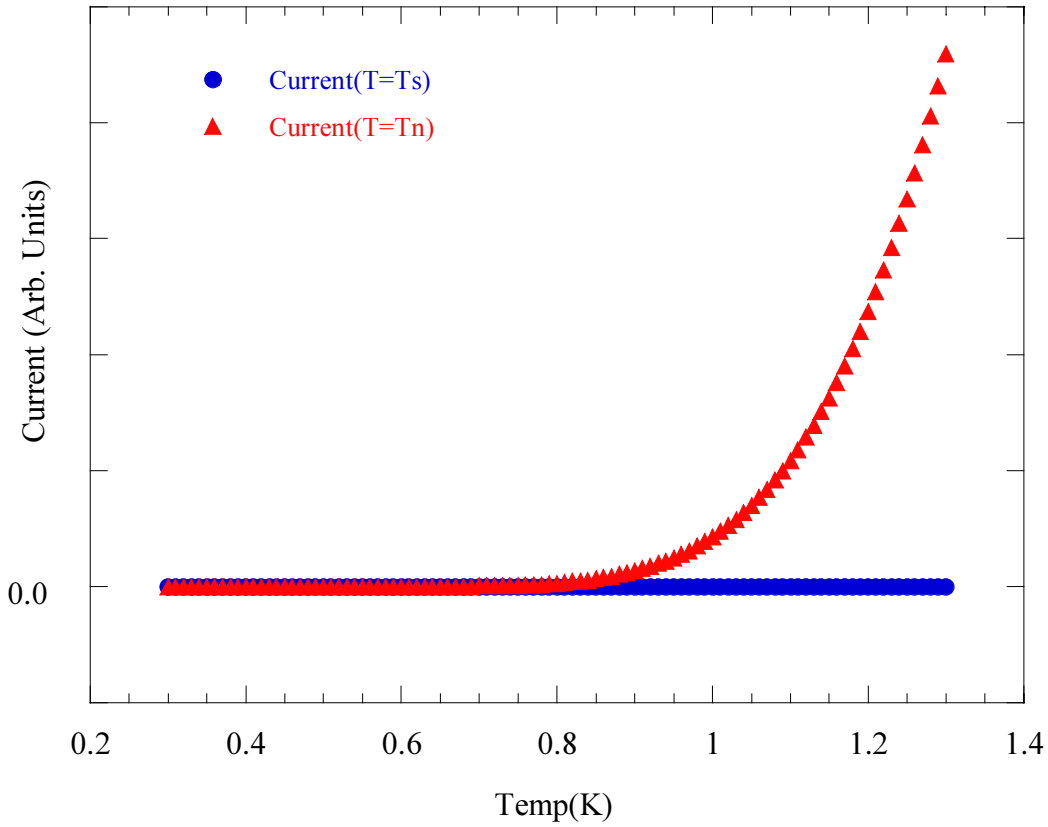

Figure 2.12 Temperature dependence of current in a SIN tunnel junction

From (2.35) we can find the conductance at any given temperature and bias, however for V=0 and low temperatures, we can find that the conductance is related to the energy gap Δ via:

$$\left.\frac{G_{SIN}}{G_N}\right|_{V=0,k_BT<<\Delta} = \left(\frac{2\pi\Delta}{k_BT}\right)^{\frac{1}{2}} e^{-\left(\frac{\Delta}{k_BT}\right)} \tag{2.38}$$

where G_N is the normal state conductance (i.e. $1/R_N$).

2.4.3 Superconductor-Insulator-Superconductor Junctions

The schematic semiconductor model representation of a superconductor-insulator-superconductor tunnel junction (SIS junction also known as an STJ) is shown in figure 2.13. Both electrodes are now superconductors with a BCS density of states, and so from (2.32) and inserting the BCS density of states expression (2.26) we find:

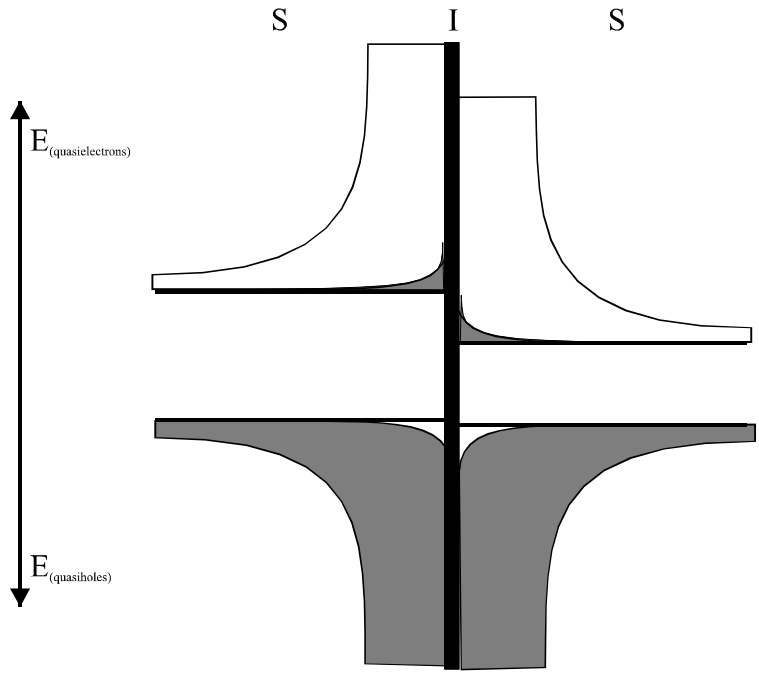

Figure 2.13 Semiconductor representation of a SIS tunnel junction at low bias.

$$I_{SIS} = \frac{1}{eR_N}\int_{-\infty}^{\infty} \mathrm{Re}\left\{\frac{|E|}{\sqrt{E^2-\Delta_1^2}}\right\}\mathrm{Re}\left\{\frac{|E+eV|}{\sqrt{(E+eV)^2+\Delta_2^2}}\right\}\left[f(E)-f(E+eV)\right]dE \quad (2.39)$$

where Δ_1 and Δ_2 are the energy gaps for the two superconducting electrodes. Taking the real part of the BCS density of states functions ensures that the density of quasiparticles states is treated as being zero within the energy gap region. (2.39) represents only the tunnelling of quasiparticles, and not the pair states. The tunnelling of the pairs needs to be considered separately.

2.4.3.1 Zero Bias

In the ground state at T=0, the only possibility of tunnelling across the junction will be that of the pairs, which we will return to in 2.4.3.4. At non-zero temperatures there will be thermally excited quasiparticles, however, even if the two energy gaps are not equal there will be no net current flow since there will be equal numbers of quasielectrons and quasiholes tunnelling.

2.4.3.2 Low Bias ($eV<\Delta_1+\Delta_2$)

For biases below the sum of the energy-gap voltages, the semiconductor representation gives the situation illustrated in figure 2.13. For T=0, (2.39) would predict zero quasiparticle current, however for finite temperatures the thermally excited quasiparticles may tunnel. There are two process through which an electron is transferred from one electrode (S_1) to the other (S_2):

1. Annihilation of a quasielectron in S_1 and creation of one in S_2. If the energy is conserved (i.e. the two quasiparticle states are at the same vertical position in the semiconductor representation), then this process will reach a maximum rate when the peaks in the density of states on either side of the junction are aligned, i.e. $eV=\Delta_2-\Delta_1$.
2. Annihilation of a quasihole in S_2 and creation of one in S_1. Like the first process, this will peak when the peaks in the density of states on either side of the junction are aligned. Since we are considering a process involving quasiholes, the bias condition is $eV=\Delta_1-\Delta_2$.

Together, these two processes produce an increase in current for biases in the range $0<V<(\Delta_1-\Delta_2)/e$, and then a reduction in the current for biases between $(\Delta_1-\Delta_2)/e<V<<(\Delta_1+\Delta_2)/e$. Acting in competition with these processes are the reverse ones, transferring electrons for S_2 to S_1 which will also peak at $V=\pm(\Delta_1-\Delta_2)/e$. This is the so-called *gap difference peak* in the sub-gap current (see figure 2.14). Obviously, if we have a symmetric SIS junction then the gap-difference peak does not exist as processes 1 and 2 cancel for all biases.

For biases within this regime, the current maybe found from the evaluation of (2.39), but for a symmetric junction (i.e. where $\Delta_1=\Delta_2$) can be approximated by(van Duzer 1981):

$$I_{SS} = \frac{2}{eR_N} e^{-\Delta/k_B T} \sqrt{\frac{2\Delta}{eV+2\Delta}} (eV+\Delta) \sinh\left(\frac{eV}{2k_B T}\right) K_0\left(\frac{eV}{2k_B T}\right) \tag{2.40}$$

where K_0 is the zero order modified Bessel function.

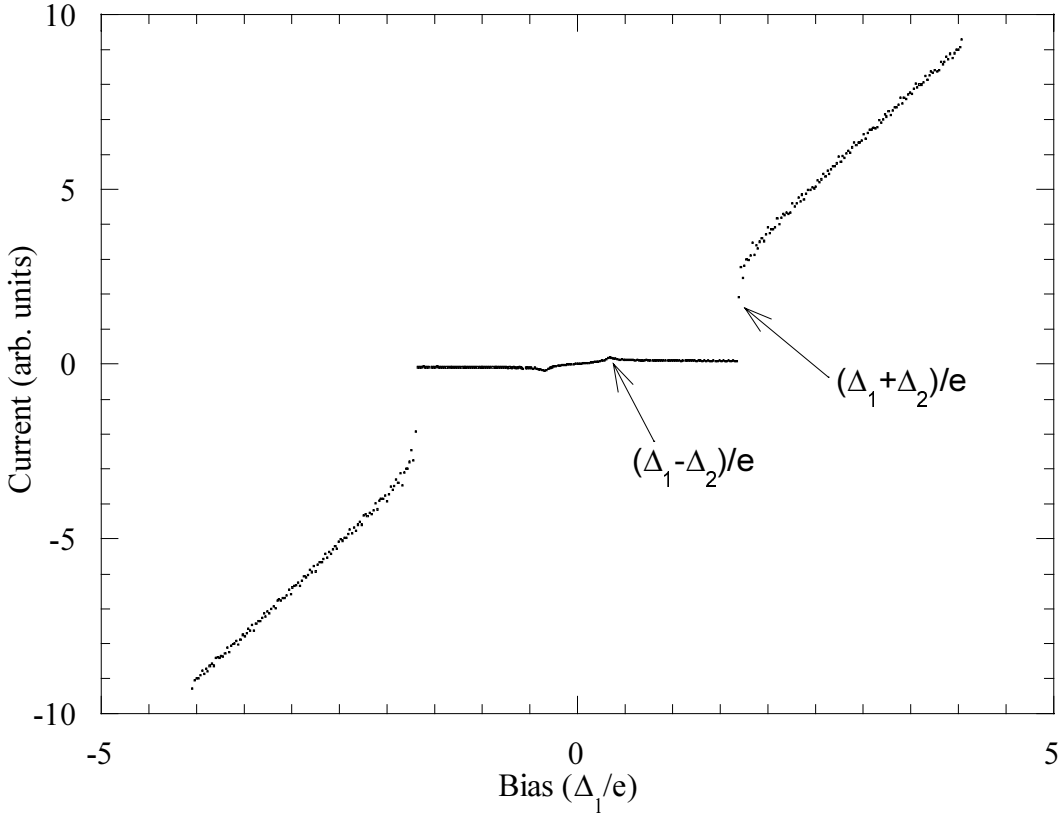

Figure 2.14 Current-voltage characteristic of a SIS tunnel junction.

2.4.3.3 High Bias ($eV>\Delta_1+\Delta_2$)

When the bias across the junction is increased to $\Delta_1+\Delta_2$ then there are two further processes which result in the transfer of electrons from S_1 to S_2:

3 The annihilation of a quasielectron in S_1 and of a quasihole in S_2. Again, the requirement for the conservation of energy gives us a limit on the biases at which this process can operate. Specifically, we are limited to bias $V>(\Delta_1+\Delta_2)/e$.

4 The fourth and final process is the creation of a quasihole in S_1 and the creation of a quasielectron in S_2. The bias condition for this process is that $V<-(\Delta_1+\Delta_2)/e$.

Like the first two processes there are the reverse processes that transfer electrons from S_2 to S_1. Although all the processes operate in parallel, and within the model of

independent electrons, separately of each other, in practice there will be one dominant process depending on the bias conditions.

When the bias approaches the sum of the energy-gaps then either process 3 or process 4 becomes dominant, and a very rapid increase in current is observed. The current as a function of bias is illustrated in figure 2.14, which was found by numerically evaluating (2.39). Both the gap-difference peak and the sum-gap step are clearly visible. The presence of these two features allows the accurate measurement of D1 and D2.

As the temperature is increased, the number of thermal excitations is increased, so the tunnel current due to processes 1 and 2 increase (scaling as f(E,T)), which is measured by an increase in the sub-gap current. Processes 3 and 4 are weakly dependent on the temperature, since they scale as 1-f(E,T), so the current-voltage characteristic for biases eV□D1+D2 is not markedly affected (beyond the fact the fact that D will be reduced if the temperature becomes a significant fraction of Tc).

Finally, we should note that for very high biases ($eV>>(\Delta_1+\Delta_2)/e$), the tunnelling is mainly dominated by the transfer of electrons from states well below the Fermi surface to states well above the Fermi surface, and the current-voltage characteristic is linear with a resistance R_N which is the same as in the case of NIN tunnelling (section 2.4.1).

2.4.3.4 DC and AC Josephson Effects

We stated in our discussion above that we were neglecting the effects of pair tunnelling, which we now consider here. In a situation of zero bias we experimentally measure a current, known as the Josephson Current after the Nobel Prize winning work of Josephson(Josephson 1962). As we shall see in the next chapter, in the applications that we are concerned with here we normally suppress this zero bias current. However, no description of SIS junctions would be complete without at least mentioning this phenomenon and there are effects arising from this that do directly impinge upon our applications. When two superconductors are placed on either side of a tunnel barrier, the pair state wave functions penetrate the barrier. Assuming a sufficiently thin barrier, the two wavefunctions will reduce the overall energy if they

couple and their phases become locked with respect to one another. In this situation, pairs may pass freely from one superconductor to the other and transport a superconducting current. The pair tunnelling current density is related to the voltage across the junction, *V*, and the phase difference φ by the Josephson equations(Josephson 1962):

$$J = J_c \sin\varphi \tag{2.41}$$

$$\frac{d\varphi}{dt} = \frac{2e}{\hbar} V \tag{2.42}$$

where J_c is the maximum current density (which gives the maximum or critical current I_c). A magnetic field in the junction **B** causes a modulation in the junction given by:

$$\nabla_{xy}\varphi = \frac{2ed}{\hbar}\mathbf{B}\times\mathbf{n}_z \tag{2.43}$$

where $\mathbf{n}_z$ is a unit vector perpendicular to the barrier, d is the magnetic thickness (= $2\lambda_L$+t), with λ_L the London penetration distance and t the barrier thickness.

For junctions that are small compared to the Josephson penetration depth,

$$\lambda_J = \sqrt{\frac{\Phi_0}{2\pi\mu_0 d J_c}} \tag{2.44}$$

with Φ_0 the elementary flux-quantum=hc/2e, self field effects can be neglected. For larger junctions these need to be included, see for example (Isaac 1998). In the case of small symmetric junctions, the critical current is found from:

$$I_c(B) = 2J_c\int_{-L/2}^{L/2} f(x)\cos\left(\frac{2\pi B_y d}{\Phi_0}x\right)dx \tag{2.45}$$

where f(x) is a positive and even function that describes the junction shape in the region ±L/2. In general, this gives an oscillatory function in which the maxima fall off as reciprocal power of the field **B**. For a rectangular junction the resulting pattern is the well known Frauenhofer pattern.

If a junction is held a constant bias *V*, it follows from (2.42) that there is a constant rate of phase slippage between the pair state wavefunctions on either side of the junction. This then gives an oscillatory current from (2.41) with a frequency (the Josephson frequency):

$$\omega = \frac{2eV}{\hbar} \tag{2.46}$$

the constant between frequency and bias being 483.6 MHz/μV. Whilst this is not directly measurable, it can induce an electromagnetic field which for certain voltages will have a wavelength that will excite standing wave resonances of the junction cavity. For current biased junctions they are observed as steps in the junction's current-voltage characteristic, known as the Fiske resonances. In the general case, the Fiske resonances can be calculated by finding the local phase difference φ(x,y,t) and integrating (2.41). The procedure to find φ(x,y,t) involves solving a two-dimensional perturbed Sine-Gordon Equation which is the result of combining the Maxwell Equations and the Josephson Equations. A comprehensive study of this has been performed by Gijsbertsen(Gijsbertsen 1994).

2.5 Quasiparticle and Phonon Lifetimes

We shall be concerned with the lifetimes of quasiparticles and phonons in our devices. A thorough theoretical analysis of the lifetimes of quasiparticles and phonons in near thermal equilibrium has been undertaken by Kaplan *et al.* (Kaplan 1976). For larger departures from thermal equilibrium the coupled kinetic equations of Chang and Scalapino(Chang 1977) as discussed in section 2.7.3 are required.

2.5.1 Quasiparticle Lifetimes

A quasiparticle at some energy E that is above the energy gap (i.e. E>Δ), may undergo a number of different processes. It may recombine with another quasiparticle to form a bound pair; it may scatter inelastically either from another quasiparticle or from a phonon; or it may undergo elastic scattering.

2.5.1.1 Elastic Scattering

The rate of elastic scattering of quasiparticles is highly dependent on the microstructure of the superconductor. In the case of thin sputtered films as studied here, the greatest factor in the microstructure is the degree of epitaxy of the film with respect to the substrate. For fully epitaxial films the mean free path of electrons, and

hence of quasiparticles, is limited by surface scattering. In this case the mean free path will be of the order of the film thickness. At the other extreme the mean free path is limited by the grain size of polycrystalline films, which typically can be as low as 10 nm. The mean free path can be quantified by means of the residual resistance ratio(RRR) of the film to calculate the mean free path of electrons (it is assumed that quasiparticles will have the same elastic mean-free path).

The residual resistance ratio is defined as:

$$RRR = \frac{\rho_{thermal}(300K) + \rho_{residual}}{\rho_{residual}} \tag{2.47}$$

where $\rho_{thermal}$ is the resistivity due to phonon scattering and $\rho_{residual}$ is the resistivity due to impurity, defect and interface scattering. In practice it is not necessary to measure the resistance at vanishing temperatures; for a normal metal, liquid Helium temperature (4.2 K) is sufficient for the non-thermal resistance mechanisms to dominate. For a superconductor, obviously, we need to use a temperature above T_c. The residual resistivity can be found from catalogued values of bulk resistivity ρ_b from:

$$\rho_0 = \frac{\rho_b(300K) - RRR\rho_b(T \to 0)}{RRR - 1} \tag{2.48}$$

the residual resistivity – mean-free-path product is a material constant which is given by:

$$\rho_0 L = \frac{m^* v_F}{ne^2} \tag{2.49}$$

with mean free path L, Fermi velocity v_F, number density of electrons n. For electrons the lifetime against scattering $\tau_{els}=L/v_F$. For quasiparticles, strictly one should take account of the dispersion relation implied by (2.19) to calculate the velocity of a quasiparticle at energy E:

$$v_{qp} = v_F\sqrt{\left(1 - \frac{\Delta}{E}\right)} \tag{2.50}$$

in which case the elastic scattering time becomes $\tau_{els}=L/v_{qp}$.

2.5.1.2 Inelastic Scattering

Although quasiparticles may scatter from both phonons and other quasiparticles, the latter process can be neglected. The rate of scattering by phonon emission varies as E^3/ω_D^2, where ω_D is the Debye frequency and E the electron energy. The electron scattering rate varies as E^2/μ, where μ is the chemical potential. Kaplan *et al.* have tabulated $\hbar\omega_D^2 / \mu k_B T_C$ and show that it is much less than 1 for most superconductors. Therefore, for quasiparticles in the range $k_B T_c < E < \hbar\omega_D$, electron-phonon scattering dominates.

Kaplan *et al.* showed that a quasiparticle at energy E, and with a thermal distribution of phonons and quasiparticles, may scatter inelastically by the emission or absorption of a phonon with lifetimes given by:

$$\tau_{absorption}^{-1}(E) = \frac{2\pi}{\hbar Z_1(0)\left[1-f(E)\right]} \int_0^{\infty} d\Omega \alpha^2(\Omega) F(\Omega) \rho(E+\Omega) \left(1 - \frac{\Delta^2}{E(E+\Omega)}\right) n(\Omega)\left[1-f(E+\Omega)\right] \quad (2.51)$$

$$\tau_{emission}^{-1}(E) = \frac{2\pi}{\hbar Z_1(0)\left[1-f(E)\right]} \int_0^{E-\Delta} d\Omega \alpha^2(\Omega) F(\Omega) \rho(E-\Omega) \left(1 - \frac{\Delta^2}{E(E-\Omega)}\right) \left[n(\Omega)+1\right]\left[1-f(E+\Omega)\right] \quad (2.52)$$

where f(E) is the Fermi function, n(E) the Bose function, α^2 is the electron-phonon coupling constant, F the phonon density of states, $\rho(E)$ the BCS density of states, and $Z_1(0)$ a material dependent renormalisation constant (actually given by $1+N(0)V$), which typically is between 1 and 3. All the terms in these equations are well catalogued apart from the Eliashberg function $\alpha^2(\Omega)F(\Omega)$, which may be approximated from tunnelling measurements. For $E << \hbar\omega_D$ conventionally $\alpha^2(\Omega)$ is taken to be independent of Ω, and $F(\Omega)$ is taken as quadratic in Ω), so that $\alpha^2(\Omega)F(\Omega)$ is approximated by $b\Omega^2$. Values of b for various superconductors are given by Kaplan *et al.* In their work(Kaplan 1976), they showed that when normalised by a characteristic time τ_0 given by:

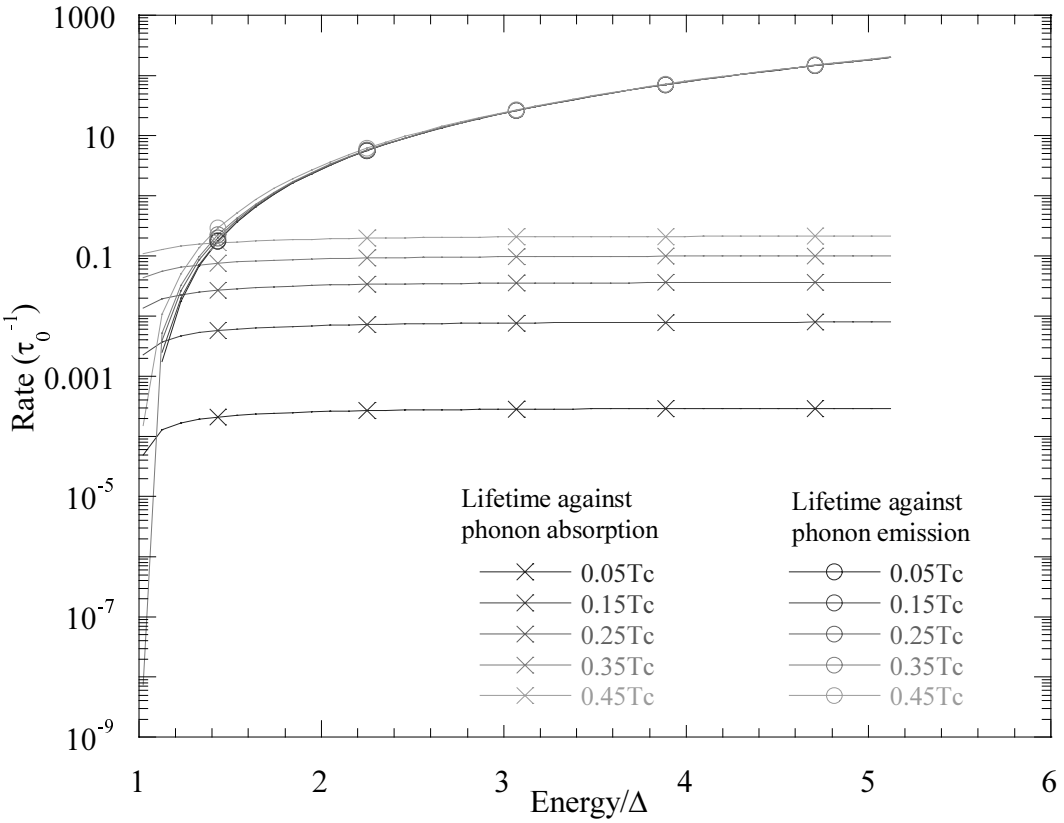

Figure 2.15 Quasiparticle lifetime against phonon emission and absorption.

$$\tau_0 = \frac{Z_1(0)\hbar}{2\pi b(k_B T_C)^3} \tag{2.53}$$

the times for inelastic scattering and recombination could be fitted by universal curves.

Values of τ_0 for various superconductors, as tabulated by Kaplan *et al.*, are listed in table 2.1 and plots of the quasiparticle lifetime against phonon emission and absorption for a range of energies and temperatures are shown in figure 2.15.

Superconductor	τ_0(ns)	τ_0^{ph}(ps)
Nb	0.149	4.17
Al	438[a]	242

Table 2.1 Calculated values of the quasiparticle (τ_0) and phonon (τ_0^{ph}) characteristic times (from (Kaplan 1976)) [a] Experimental measurements (e.g. (Chi 1979))suggest this figure is rather too high, indicating a value of around 100ns, more recently (Friedrich 1997) has reported a good fit to data for 440ns.

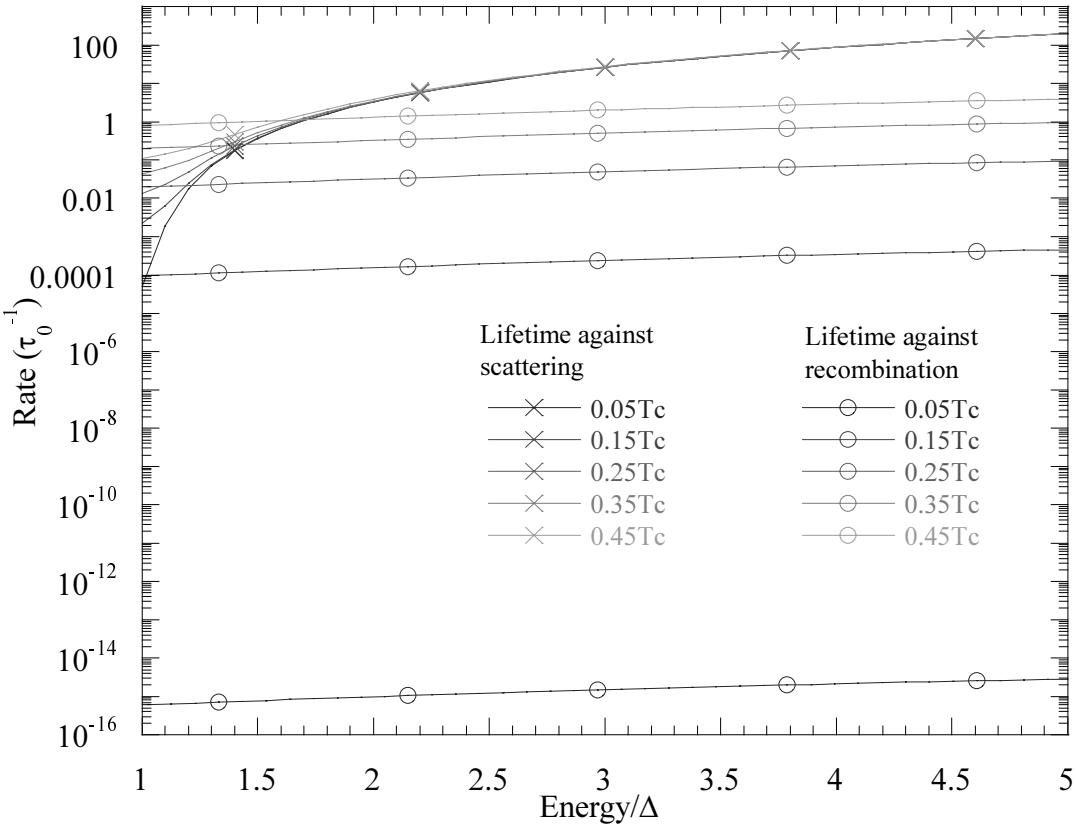

Figure 2.16 Quasiparticle lifetimes against scattering and recombination.

2.5.1.3 Quasiparticle Recombination

A quasiparticle at an energy E may recombine with another quasiparticle at an energy E' to release a phonon of energy Ω=E+E'. These recombination phonons thus have energies greater than 2Δ. The rate of this process is given by:

$$\tau_{recomb}^{-1}(E) = \frac{2\pi}{\hbar Z_1(0)} \int_{E+\Delta}^{\infty} d\Omega \alpha^2(\Omega) F(\Omega) \rho(\Omega - E) \left(1 + \frac{\Delta^2}{E(\Omega - E)}\right) \left[n(\Omega)+1\right] f(\Omega - E) \tag{2.54}$$

Figure 2.16 shows the recombination rate for the same range of quasiparticle energies and temperatures as in figure 2.15. In order more clearly to show the relative importance of these quasiparticle processes, in figure 2.16 we plot the inelastic scattering rate $\tau^{-1}_{\text{inelastic}}$ ($\tau_{inelastic}^{-1} = \tau_{emission}^{-1} + \tau_{abosrption}^{-1}$), recombination rate and elastic scattering rate for quasiparticle energies between Δ and 5Δ for a range of temperatures.

Here we should point out that the lifetime against recombination calculated above is only the time for the recombination of a specific pair of quasiparticles. As we shall see in the following sections, it is likely that the recombination phonon emitted in the process will cause a pair-breaking event and regenerate a pair of quasiparticles. Thus the quasiparticle population does not decay at the rate implied by the recombination rate.

2.5.2 Phonon Lifetimes

2.5.2.1 Phonon Lifetimes in Superconductors

We consider four competing processes that phonons in a superconductor may undergo. Pair breaking: to create two quasiparticles. Quasiparticle scattering: absorption by an existing quasiparticle to scatter it to a high-energy state. Anharmonic decay: scattering of phonons to lower energy phonons. Finally, loss from the film: typically to the substrate or another film within the device.

The rate of pair breaking by phonons was found by Kaplan *et al.* to be:

$$\tau_{pair-breaking}^{-1}(\Omega)=\frac{4\pi N(0)\alpha^2(\Omega)}{\hbar N_{ion}}\int_{\Delta}^{\Omega-\Delta}dE\rho(E)\rho(E-\Omega)\left(1+\frac{\Delta^2}{E(\Omega-E)}\right)\left[1-f(E)-F(\Omega-E)\right] \tag{2.55}$$

where N_{ion} is the number density of ion cores. The phonon-electron coupling constant, α^2, is found from α^2F which is determined from tunnelling experiments(Gray 1971) and dividing by the phonon density of states, F from neutron scattering experiments.

The phonon-quasiparticle scattering rate is given by Kaplan *et al.* as:

$$\tau_{ph-qp-scatter}^{-1}(\Omega)=\frac{8\pi N(0)\alpha^2(\Omega)}{\hbar N_{ion}}\int_{\Delta}^{\infty}dE\rho(E)\rho(E+\Omega)\left(1-\frac{\Delta^2}{E(E+\Omega)}\right)\left[f(E)-f(E+\Omega)\right] \tag{2.56}$$

The phonon lifetime against pair breaking and quasiparticle scattering can be expressed in terms of a material dependent characteristic lifetime τ_0^{ph}:

$$\left(\tau_0^{ph}\right)^{-1}=\frac{4\pi^2N_0\left\langle\alpha^2\right\rangle}{\hbar N_{ion}}\Delta(0) \tag{2.57}$$

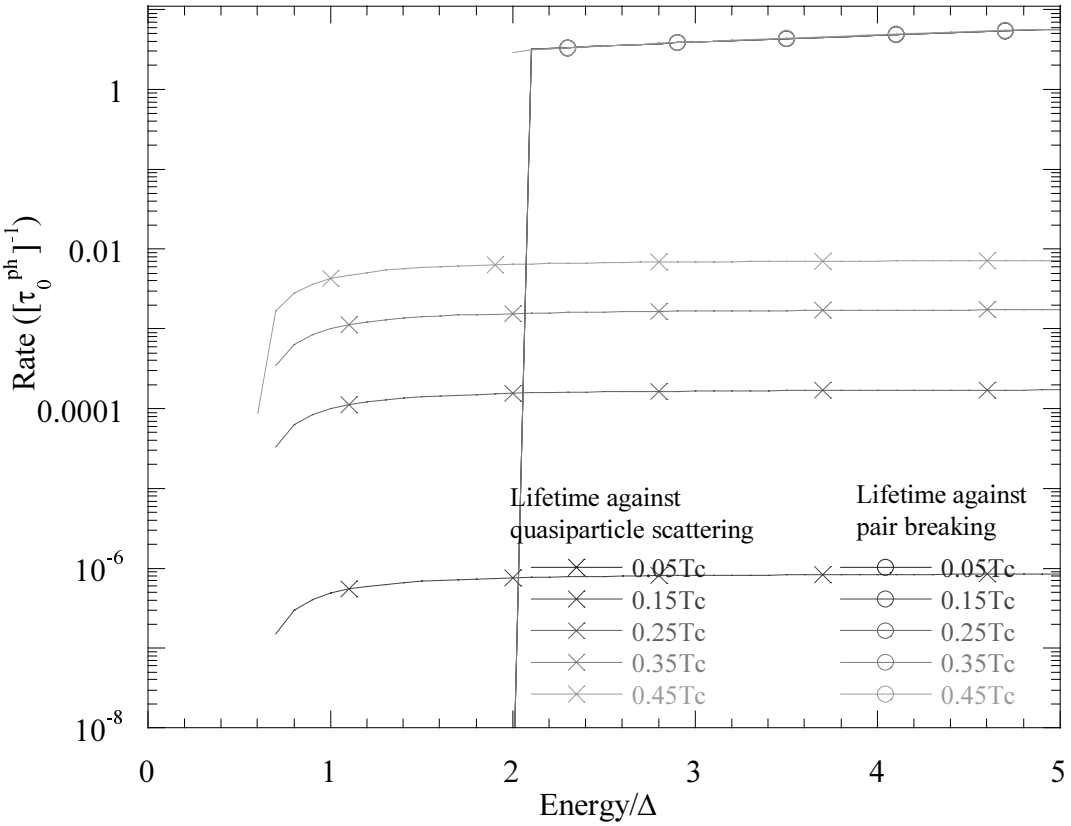

Figure 2.17 Phonon lifetimes against quasiparticle scattering and pair breaking

where $<\alpha^2>$, the average value of α^2 is given by:

$$\left\langle \alpha^2 \right\rangle = \frac{1}{3}\int_0^\infty d\Omega \alpha^2(\Omega) F(\Omega) \tag{2.58}$$

τ_0^{ph} is tabulated for Nb and Al in table 2.1.

In figure 2.17 we plot $\tau^{-1}_{\text{pair-breaking}}$ and $\tau^{-1}_{\text{ph-qp-scatter}}$ normalised against τ_0^{ph} for a range of temperatures between 0.25 K and 5 K and energies between 0 and 10Δ for Nb. For sufficiently low temperatures $(T/T_c)<0.3$ and energies $\Omega>2\Delta$ we can approximate the pair breaking rate as τ_0^{ph}. The phonon-quasiparticle scattering rate is orders of magnitude slower than pair breaking and normally can be neglected. For phonons of energy $\Omega<2\Delta$, however, the phonon-quasiparticle scattering is significant as these phonons do not have sufficient energy to break pairs.

In their studies of the anharmonic decay of phonons Orbach and Vredevoe(Orbach 1964) showed that the dominant decay processes were the three phonon processes, transverse phonon + transverse phonon ↔ longitudinal phonon and

transverse phonon + longitudinal phonon ↔ longitudinal phonon. In addition the transverse phonon lifetimes were orders of magnitude longer than those of the longitudinal phonons. Since the density of phonon states scales with $1/c^3$ where c is the speed of sound and generally the velocity of longitudinal phonons is twice that of the transverse phonons(Kaplan 1979), we expect the transverse phonons to dominate. The lifetime of longitudinal phonons can be calculated from: (Klemens 1967):

$$\tau_{L-anharmonic}^{-1}(\Omega) = \frac{3\pi}{4\sqrt{2}}\gamma^2 \frac{\Omega^5}{c_L c_T \hbar \Omega_D^3 M} \tag{2.59}$$

γ is the Grüneisen constant, $c_{L/T}$ are the speed of the longitudinal and transverse phonons, Ω_D the Debye Energy and M the atomic mass. For the materials we are interested in this gives anharmonic decay times for transverse phonons which are many orders of magnitude longer than the other phonon processes.

The final process that may occur for a phonon in a superconductor is loss from the film by escape to either the substrate or another layer in the device. The loss time for phonons from a film of thickness is d is given by:

$$\tau_{phonon-escape} = \frac{4}{c}\frac{V_{film}}{A_{interface}(1-R_{reflection})} = \frac{4d}{c\varsigma} \tag{2.60}$$

where c is the speed of sound, and ς the transmission co-efficient. This expression holds in the limit that the film thickness $d \gtrsim \Lambda$, where Λ is the pair breaking length. For thicker films, the bulk phonon losses become dominant and the phonon escape time is independent of film thickness and transmission co-efficient.

2.5.2.2 Phonon-Electron Processes in Normal Metals

Electron-phonon scattering in metals is a substantial field of study in itself. The reader is directed towards the available reviews in the literature, such as (Gantmakher 1974) for a more complete overview of the field. Of particular interest in this work will be the processes and associated length-scales that a athermal phonon (i.e. $\Omega >> k_B T$) undergoes in a normal metal. Typically this situation arises when a phonon resulting from a quasiparticle recombination or scattering process in a superconductor enters a normal metal.

The end point following the absorption of an athermal phonon will be for the electron and phonon systems to re-establish an equilibrium with a slightly higher temperature T^{final} with respect to the original temperature T. In the low temperature regimes which we consider in this work, the vast majority of the specific heat capacity of a normal metal is due to the specific heat capacity of the electron system(Nahum 1993). Furthermore the power transfer between the electron and phonon system is sufficiently low that the two systems are only weakly coupled and can have significantly different temperatures(Wellstood 1994). The coupling between the two systems is given by:

$$P_{electron-phonon} = V\Sigma(T_{electron}^5 - T_{phonon}^5) \tag{2.61}$$

where V is the volume of the sample, Σ is a material constant, and $T_{electron/phonon}$ are the electron and phonon temperatures. For Au (which is the normal metal used here) $\Sigma \approx 2\times10^9$ $Wm^{-3}K^{-5}$(Wellstood 1994). The stages between the initial phonon absorption and the final equilibrium are as follows:

- Athermal phonon undergoes rapid phonon-electron scattering to give a single hot electron. This is the independent hot-electron regime.
- The electron system re-establishes a thermal-like distribution with an effective temperature T*>T. This is the interacting hot-electron regime, in which there is electron-electron scattering, but not significant electron-phonon scattering.
- The electron and phonon systems re-establish an equilibrium. Although the system regains a uniform temperature, most of the energy is held in the electron system due to the relative heat capacities of electrons and phonons. This regime is important for the performance of certain classes of X-ray detector which we will discuss in the next chapter.

The length scales associated with these stages have been studied by workers performing noise measurements in micro- and mesoscopic wires, for example(Steinbach 1996). In general these length scales are bias dependent, but within an order of magnitude, the three stages above occur within 1 μm, 10 μm and 10 mm if $eV >> k_BT$ (V is bias along the wire).

2.5.2.3 Phonon Lifetimes in Substrate Materials

For a phonon in the substrate we consider two possible decay or loss processes, phonon loss to the film or chip holder and anharmonic decay. These processes have been discussed above for phonons in a superconducting film. From (2.60) we can find the time for loss back to a Nb film, which we would expect to be of order of μs for a typical substrate thickness of 0.5 mm (the actual magnitude will be dependent on the coverage of the device on the substrate).

Phonons in the substrate will scatter off impurities in the substrate's crystal structure, the surfaces of the substrate and anharmonicities in the ionic interaction energy. Given that the substrates are high quality, ultra-pure single crystals, impurity scattering can be neglected. Surface scattering is rather more problematic; some workers have assumed that the surface scattering is an elastic process(Warburton 1993a), other workers imply that this is not the case (for example (Schnagl 1997)). The scattering time from anharmonicities in the ionic energy can be estimated from (2.59), which for sapphire (using data from(Kaplan 1979)) gives a decay time of 3.4 μs.

2.6 Proximity Effect

In our discussion thus far, it has been assumed that our superconducting films are homogeneous. As we shall see in the next chapter, this is not the case for reasons of both materials selection, and optimum device design. Instead, we will employ superconducting films consisting of bilayers of superconductors with different properties. We therefore require information about the changes in properties of the superconducting film across the various layers, for which we require an understanding of the proximity effect. When a superconductor S_1 is placed in good contact with another superconductor S_2 which has a different pair interaction energy, and hence a different value of energy gap Δ, such that $\Delta_1 > \Delta_2$, then across the interface there will be some variation in the magnitude of Δ. Likewise, there will be some form of variation in the density of quasiparticle states, and in the critical temperature. These factors are important when considering the quasiparticle dynamics in such

superconducting heterostructures since the spatially varying parameters will potentially affect the lifetimes of quasiparticles and phonons in the system.

Three out of the many available approaches to the proximity effect are considered in addition to Ginzburg-Landau theory, which was discussed in section 2.2.3.

Ginzburg-Landau theory has been very successful when applied to the macroscopic properties of inhomogeneous bulk superconductors near T_c, but is not very useful for our case of thin film heterostructures at very low temperatures. It gives us information on the macroscopic properties of a superconductor in the vicinity of an interface with a normal metal, and thus allows us to predict, for example, the existence of the mixed state in type II superconductors and the critical current density in an SNS junction. What it fails to do is to give any information as to the expected density of quasiparticle states.

The theory of de Gennes, is mentioned for completeness; whilst it continues to be used with success in high T_c superconducting devices(Tarte 1992; Booij 1997), in the low T_c thin film devices community the dominant theories are those of M^{c}Millan and Golubov.

2.6.1 de Gennes Theory

The de Gennes theory of the proximity effect uses an approach based on the self-consistent field equations of Bogoliubov(Bogoliubov 1959) to find the density of states in a superconductor-normal metal bilayer(de Gennes 1963) or a superconductor-superconductor bilayer S_1S_2 ($\Delta_1>\Delta_2$) (Saint-James 1964).

The Bogoliubov-de Genneswh equations describe the quasiparticle wavefunction $\psi(u,v)$, where u and v are the electron and hole amplitudes which are coupled via the pair potential Δ:

$$\begin{aligned}\left(-\frac{\hbar^2}{2m}\nabla^2 - E_F + U(\mathbf{r})\right)u(\mathbf{r}) + \Delta(\mathbf{r})v(\mathbf{r}) &= Eu(\mathbf{r}) \\ \left(\frac{\hbar^2}{2m}\nabla^2 + E_F - U(\mathbf{r})\right)v(\mathbf{r}) + \Delta(\mathbf{r})u(\mathbf{r}) &= Ev(\mathbf{r})\end{aligned} \tag{2.62}$$

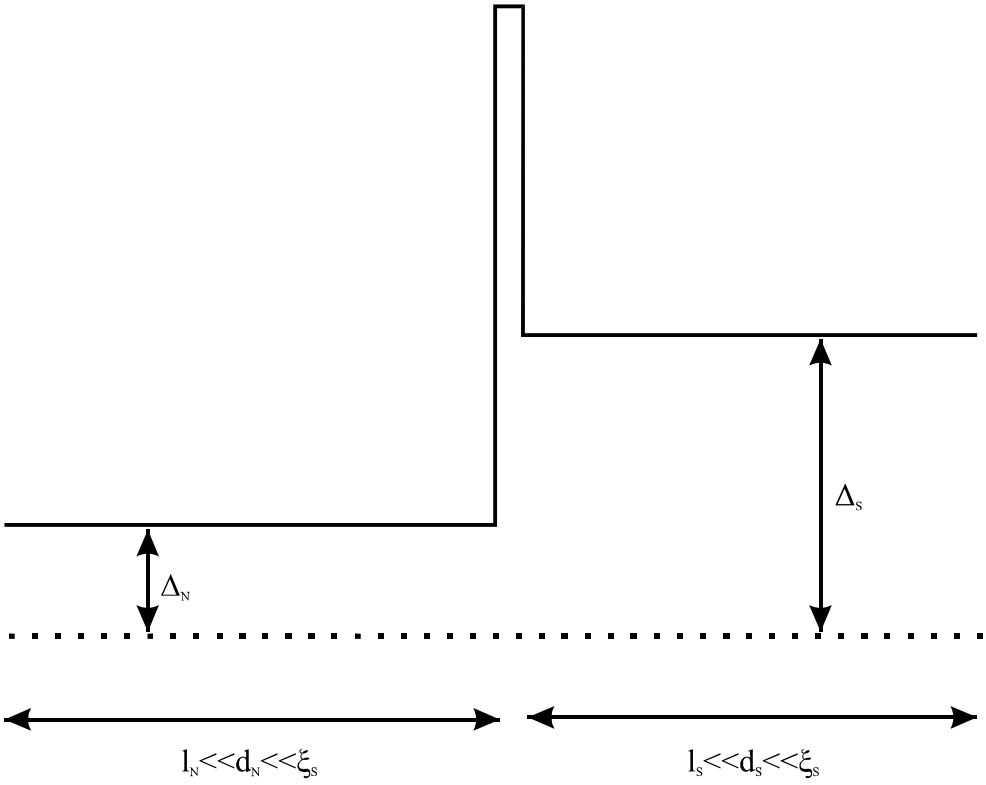

Figure 2.18 Energy gap in the McMillan model of the proximity effect.

where U(**r**) is the ordinary potential and E is the excitation energy. Equations (2.62) describe the pair potential Δ(**r**) which can be expressed as a product of the BCS electron-electron interaction potential V_{kk}(**r**) and a condensation amplitude F(**r**)=<ψ(u,↑) ψ(u,↓)>. The form of the density of states is found by matching the value and first derivative of ψ(u,v) at the interface. The results suggests that there is no gap, but there is always at least one peak at $E<\Delta_1$ due to a bound quasiparticle state in the N/S_2 layer. De Gennes theory is applicable to cases where the N (or S_2) layer is thick, or the situation is symmetrical (i.e. SNS structures) and for temperatures close to T_C. This is unlikely to be the case for our experimental situation.

2.6.2 McMillan Theory

The basis of the M^{c}Millan model of the proximity effect is to consider a potential barrier between the layers of a SN bilayer. The proximity effect can then be described in terms of tunnelling of electrons through the barrier. The BCS potential is then solved using a self consistency approach. The excitation spectrum, transition temperature, energy gap and electronic density of states can then be found.

To enable the calculation to be carried out a number of approximations need to be made. The thickness of the two layers is assumed to be thin compared to the superconducting coherence length, so that the properties are uniform across the thickness of both films. Practically, this is unlikely to be the case for most of the devices discussed in this work which have appreciably thick S electrodes. It is possible to work around this limitation by fixing the parameters in the spatially varying layer to suitable (albeit arbitrary) values. As mentioned above, it is also assumed that there exists a potential barrier between the S and N layers. Whilst this may have been the case for layers deposited in low quality vacuum systems, in the case of Nb/Al devices sputtered in modern systems this assumption is questionable(Le Grand 1994a)The final assumption is that tunnelling is a specular process so that momentum is not conserved, thus enabling one to take all the elements of the tunnelling matrix to be equal. This assumption implies that the mean free path in both the S and N layers is short – i.e. that they are both in the dirty limit - which is not necessarily true. Figure 2.18 shows a sketch of the BCS pair potential that results from these assumptions.

Using these assumptions M^{c}Millan found:

$$\Delta_{S\backslash N}(E)=\frac{\left(\Delta_{S\backslash N}^{ph}+\frac{\Gamma_{S\backslash N}\Delta_{N\backslash S}(E)}{\sqrt{\Delta_{N\backslash S}^{2}(E)-E^{2}}}\right)}{\left(1+\frac{\Gamma_{S\backslash N}}{\sqrt{\Delta_{N\backslash S}^{2}(E)-E^{2}}}\right)} \tag{2.63}$$

where $\Gamma_{S\backslash N}=\frac{\hbar v_{F}^{S\backslash N}\sigma}{2B_{S\backslash N}d_{S\backslash N}}$, B_x is a function of the ratio of mean free path to the layer thickness d_x in layer x, σ is the barrier penetration, Δ^{ph}_x is the BCS pair potential in layer x, which is assumed to be constant and can be found from the BCS self-consistency equation (2.18), which can be rewritten in integral form:

$$\Delta_{x}^{ph}=N(0)V\int_{0}^{\hbar\omega_{c}^{x}}\mathrm{Re}\left\{\frac{\Delta_{x}(E)}{\sqrt{E^{2}-\Delta_{x}^{2}}}\right\}dE \tag{2.64}$$

Equations (2.63) need to be solved numerically to find a solution for $\Delta_x(E)$. The density of states can then be computed from:

$$N_{S/N}(E) = \mathrm{Re}\left\{\frac{E}{\sqrt{E^2 - \Delta_{S/N}^2(E)}}\right\} \tag{2.65}$$

Although the McMillan Theory succeeds in modelling a lot of experimental data(Romagnon 1974; Gilabert 1979; Goldie 1990), it suffers from the major disadvantage that the gap parameter is constant in both layers, which is unlikely for thick electrodes. Furthermore, it is expected that in most cases that we are interested in the interfacial barrier between the S and N layers is minimal.

2.6.3 Golubov Microscopic Model

A microscopic model specifically formulated to consider the proximity effect in inhomogeneous thin film superconductors has been developed by Golubov and Kupriyanov(Golubov 1988). This model originally considered S-N bilayers, but has been extended to cover superconducting heterostructures.

The model applies only to superconductors in the dirty limit (i.e. mean free path, l<<coherence length, ξ) for which the normal and anomalous Green's functions (G, F) will obey the Usadel Equations(Usadel 1970):

$$\phi(\omega_n, x) = \Delta(\omega_n, x) + \xi_S^2 \frac{\pi T_C}{\omega_n G(\omega_n, x)} \nabla\left[G^2(\omega_n, x)\nabla\phi(\omega_n, x)\right] \tag{2.66}$$

$$\Delta(\omega_n, x)\ln\frac{T}{T_C} + 2\pi T\sum_{\omega_n}\frac{\Delta(\omega_n, x)}{\omega_n} - F(\omega_n, x) = 0 \tag{2.67}$$

$$\begin{aligned} &\phi = \omega_n F / G \\ &F = \frac{\phi}{\sqrt{\omega_n^2 + \phi^2}} \\ &G = \frac{\omega_n}{\sqrt{\omega_n^2 + \phi^2}} \\ &\omega_n = \pi T(2n+1) \qquad n = 0,1,2,... \end{aligned} \tag{2.68}$$

(2.66) is a type of diffusion equation which describes the proximity effect. (2.67) is a self consistency relationship to determine the order parameter $\Delta(\omega_n,x)$. $\phi(\omega_n,x)$ does not have a simple physical meaning, but rather is a convenient parameter. ω_n is the Matsubara frequency.

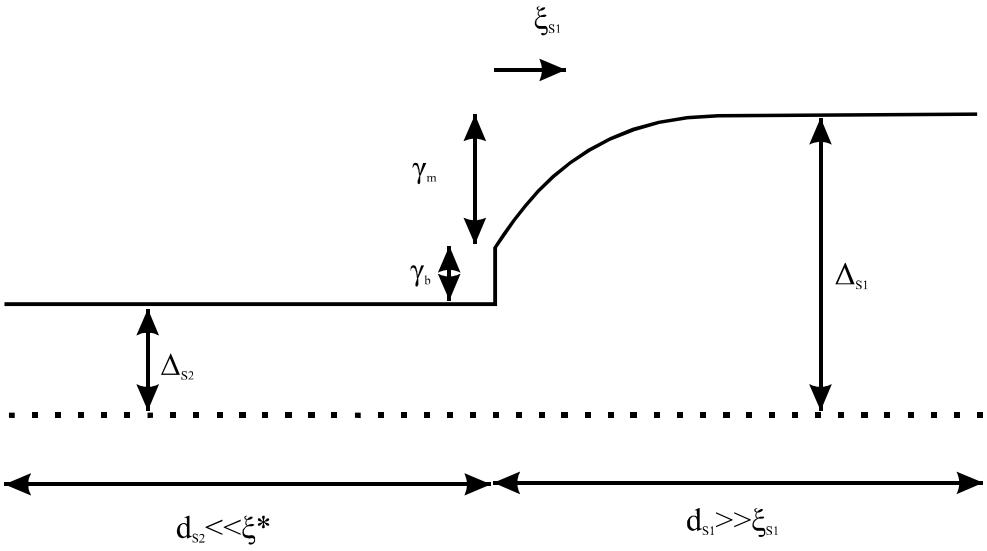

Figure 2.19 Energy gap in the Golubov model of the proximity effect.

As stated above, the model requires the superconductor to be in the dirty limit and in addition it imposes the following approximations:

$$\begin{aligned} & d_{S_1} >> \xi_{S_1} >> l_{S_1} \\ & l_{S_2} \le d_{S_2} << \xi^* \\ & \xi_{S_2} = \xi^* \sqrt{\left(\frac{T_{c,S_2}}{T_c^*} \right)} \\ & T_{c,S_1} > T_{c,S_2} \end{aligned} \tag{2.69}$$

where S_1 is a thick superconducting electrode and S_2 is a thin layer with a lower T_c (and energy gap Δ) d_x is the thickness of layer x, ξ is the coherence length (ξ^* is the effective coherence length in the thin S_2 electrode) and T^*_c is the effective critical temperature of the combined structure. The implication that S_2 is thin is that its parameters are constant across its thickness, whereas there will be a variation in the parameters in S_1.

The proximity effect can be characterised by two parameters (in addition to the ratio of critical temperatures) which are given by:

$$\gamma_m = \frac{\rho_{S_1} \xi_{S_1}}{\rho_{S_2} \xi^*} \frac{d_{S_1}}{\xi^*} \tag{2.70}$$

$$\gamma_b = \frac{R_b}{\rho_{S_2} \xi^*} \frac{d_{S_2}}{\xi^*} \tag{2.71}$$

where ρ_x is the normal state resistivity of layer x, R_b is the resistivity of the S_1S_2 boundary. γ_m is a measure of the difference in quasiparticle densities between the two layers – a large γ_m implies a high density of quasiparticles in S_2 relative to S_1 or a strong proximity effect. γ_b is a measure of the transparency of the interface, so that for $\gamma_b >> 1 >> \gamma_m$ we would have the case as described by the McMillan model. The relationship of γ_m and γ_b to the order parameter in such a bilayer is sketched in figure 2.19.

The set of equations (2.66),(2.67) and (2.68) need to be solved simultaneously for both layers, and in the general case numerically, to obtain $F(\omega_n,x)$ and $G(\omega_n,x)$ from which the density of states (given by $N(\varepsilon)=N(0)Re\{G(\varepsilon=-i\hbar\omega_n)\}$ can be found. In the limiting case of $\gamma_b=0$ the normalised density of states in S_1 and S_2 are equal, and the calculation is considerably simplified.

Having calculated F and G it is then possible to find quasiparticle lifetimes in the inhomogeneous superconductor by using these functions in the same fashion as Kaplan(Kaplan 1976) has for the homogenous case.

2.6.4 Proximity Effect and Andreev Reflection

Andreev(Andreev 1964) showed that if an electron at an energy E above the Fermi surface in a normal metal is incident upon a superconductor-normal metal interface with $E<\Delta$ then, whilst it may not enter the superconductor, it may undergo one of two reflection processes:

i) specular or diffuse scattering where the electron is reflected as an electron;

ii) Andreev reflection, in which case a cooper pair is transmitted in to the superconductor, and a hole reflected in the normal metal.

In order to conserve charge it is necessary that the reflected particle in the N layer is a hole, while in order to conserve energy it will be occupy a state at E below the Fermi surface and finally, to conserve momentum it is reflected back along the track of the incident particle – i.e. the reflection is time-reversed.

Andreev reflection of quasiparticles will give rise to resonance effects in tunnelling structures, for example the quasiparticle bound state that de Gennes and St-James(de Gennes 1963) demonstrated for an SINS structure can be considered in terms of resonant Andreev reflection.

Recently there has been much interest in examining the proximity effect in context of Andreev reflection in Superconductor-2D Electron Gas-Normal metal(Golubov 1996; Chrestin 1997; Hartog 1998). The Andreev reflected electrons and holes are correlated with the superconducting pairs, and retain this within the coherence-length. The result is to produce an energy gap in the 2DEG, which begins resemble the proximity effect. Experimentally this is observed by measuring the differential resistance of the system as a function of magnetic field, bias and temperature.

2.7 Non-Equilibrium Superconductivity

In our devices we shall frequently be driving the superconducting films out of thermal equilibrium (where the population of phonons and quasiparticles is determined entirely by the sample temperature T). For experimental reasons we will always be considering the formation of a dynamic equilibrium where the perturbations are balanced by relaxation and diffusion to establish a steady state. We will not, however, completely ignore the time-dependent cases, since as we shall see in the next chapter, many of our applications will require an understanding of precisely these cases.

As we have seen above, the populations of quasiparticles are linked to the population of 2Δ phonons via recombination and pair breaking effects. Furthermore, in (2.28) we saw that the energy gap Δ was dependent on the distribution of quasiparticles. We will first examine the ways of representing non-equilibrium quasiparticle populations, and then discuss two approaches to finding the non-equilibrium quasiparticle and phonon populations in the types of devices that we have used.

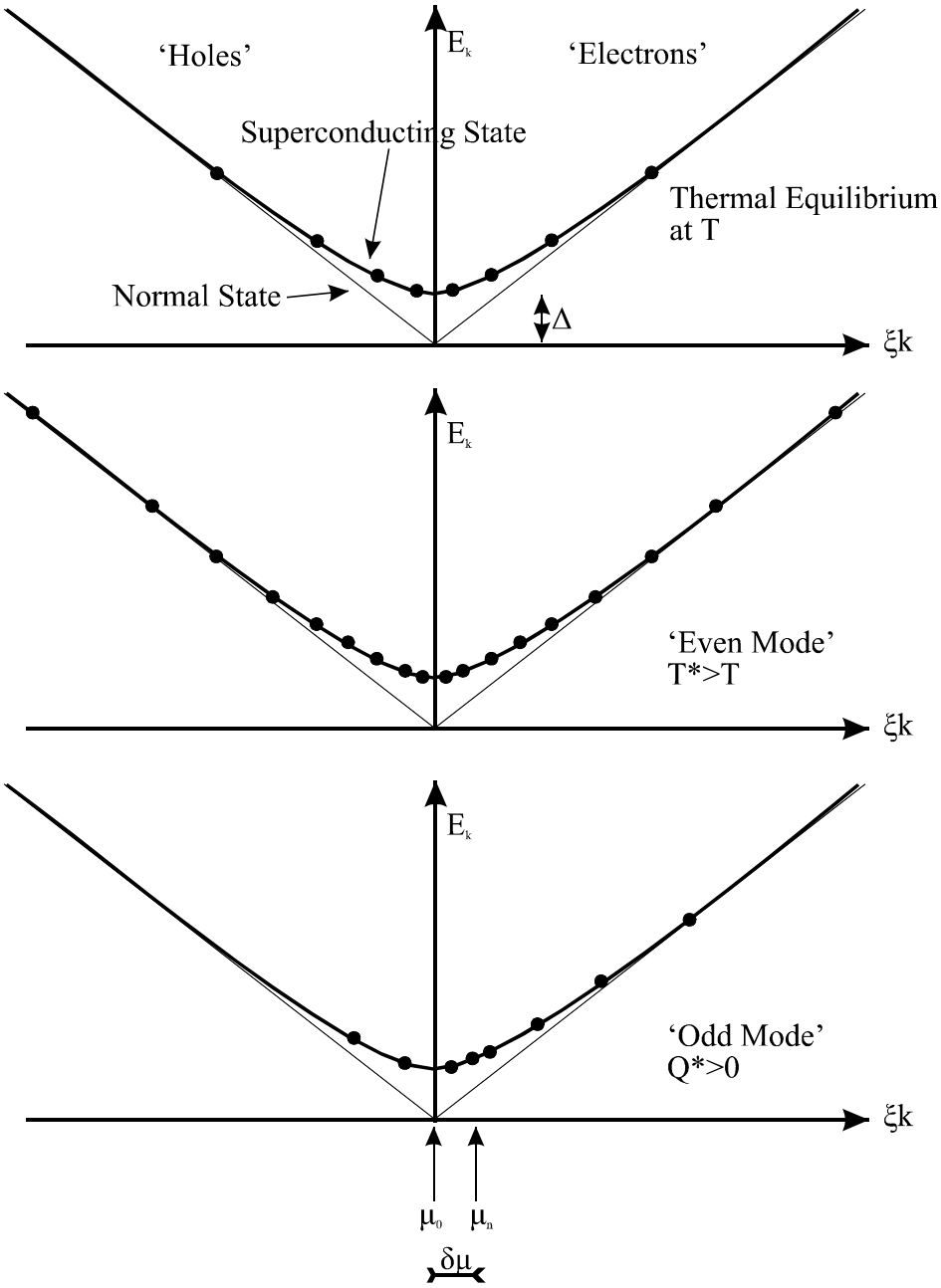

Figure 2.20 Charge and energy modes of non-equilibrium distributions.

2.7.1 Energy and Charge Mode Disequilibrium

To avoid having to handle the population probabilities f_k for all of k-space individually, it is conventional to consider only the deviation from thermal equilibrium:

$$\delta f_k = f_k - f_0(E_k / k_B T) \tag{2.72}$$

where f_0 is the Fermi function. We can then decompose δf_k into two functions that are even and odd with respect to inversion through the Fermi surface k_F. In figure 2.20 we illustrate the effect of these two types of distribution (after Tinkham(Tinkham 1996)). The even mode produces equal numbers of quasiholes and quasielectrons, and so has a similar distribution to that resulting from increasing the temperature. We can the approximate this by defining an effective temperature T* to characterise the quasiparticle distribution.

It should noted that we are not constrained to have the effective temperature, T*>T, the base temperature; it is possible to produce a non-equilibrium state where the population of quasiparticles is lower than the thermal population – in which case we can enhance the superconductivity. This can be achieved, for example, with microwave irradiation(Klapwijk 1976; Kommers 1977), or by extraction of quasiparticles through a tunnel junction(Blamire 1991; Nahum 1994; Leivo 1996).

The odd mode of the quasiparticle distribution function results in a charge imbalance, in which there is a net quasiparticle charge density, Q*, due to the non-thermal-equilibrium situation. Q* is given by:

$$Q^* = e\sum_k q_k \delta f_k = e\sum_k \frac{\xi_k}{E_k}\delta f_k \tag{2.73}$$

To maintain the total charge neutrality there must be a compensating change in the number of electrons involved in the pair state. This implies that electrochemical potentials of the pair and quasiparticles will shift relative to their common equilibrium value. This results in a potential difference within the superconductor.

Charge imbalance can be produced by injecting quasiparticles of only one character, for example from an SIS tunnel junction at high bias (or a SIN junction at any bias). For this case, the bias due to charge imbalance can be measured using a normal probe coupled to the superconductor far from the injector and was found to be: (Tinkham 1972)

$$V = R_{NS}\frac{\dot{Q}^*_{inj}\tau_{Q^*}}{2eN(0)} \tag{2.74}$$

where R_{NS} is the measured resistance of the probe junction, $\dot{Q}^{*}_{inj}$ is the rate charge imbalance injection and τ_{Q^*} is the charge imbalance relaxation rate. Kaplan(Kaplan 1976), gives:

$$\tau_{Q^*}^{-1} = 2\tau_{\delta f_{k(Q^*)}}^{-1} \leq \left(\tau_{emission}^{-1} + \tau_{absorption}^{-1} + \tau_{recombination}^{-1}\right) \tag{2.75}$$

where $\tau_{\delta fk(Q^*)}$ is the time for the quasiparticle population due to branch imbalance to relax.

2.7.2 Rothwarf-Taylor Equations

The Rothwarf-Taylor Equations are a set of coupled equations that describe a system of quasiparticles at energy Δ coupled to a population of phonons of energy 2Δ. They have been widely used to analyse the populations and lifetimes in superconducting films and devices when driven into non-equilibrium(Rothwarf 1967; Twerenbold 1986; Le Grand 1994a; Ohkubo 1996; Cristiano 1997; Krishna 1997; Rando 1998). The quasiparticle density N is split into the thermal population N_T and excess δN parts, likewise the phonon population P is composed of P_T and δP. The basic Rothwarf-Taylor equations are then:

$$\frac{dN}{dt} = I_N - RN^2 + 2\tau_{pair-breaking}^{-1}P \tag{2.76}$$

$$\frac{dP}{dt} = I_{Ph} + \frac{RN^2}{2} - P\tau_{pair-breaking}^{-1} - \delta P\tau_{phonon-loss}^{-1} \tag{2.77}$$

where I_x is the rate of quasiparticle and 2Δ phonon injection, R is the co-efficient of quasiparticle recombination. $\tau_{phonon\text{-}loss}$ is the time against phonon escape from the system – due either to phonon escape to the substrate or decay to sub 2Δ phonons. For thin film superconductors the former process will dominate. (2.76) needs to be modified to include tunnelling processes for devices such as we consider here, by adding a term $-N\tau_{tunneling}^{-1}$.

Rothwarf and Taylor used these equations to show that the effective lifetime of quasiparticles is increased from the lifetime against recombination due to the trapping of 2Δ phonons in the system. Qualitatively, a 2Δ phonon is released following a recombination event. This phonon will in turn break a pair so long as it

does not escape from the film, regenerating the quasiparticle population. It was shown that the effective quasiparticle lifetime was given by:

$$\tau_{recomb}^{eff} = \tau_{recomb}\left(1 + \frac{\tau_{phonon-loss}}{\tau_{pair-break}}\right) \tag{2.78}$$

In practice it has been found that this results in a substantial over-estimate of the quasiparticle lifetime for many devices(Warburton 1993a; Le Grand 1994a; Le Grand 1995; Gijsbertsen 1996a), indicating that there is an additional loss process that has not been considered. Some of these loss process may be due to materials problems, for example of the various Nb oxides, Nb_2O_5, Nb_2O_3 and NbO, NbO is metallic and below 0.5 K a superconductor. Other loss processes that have been suggested have involved Abrikosov vortices, non-equilibrium gap suppression, and quasiparticle diffusion away from the region being studied, e.g. down connecting leads.

2.7.3 Coupled Non-Equilibrium Rate Equations

The weakness of the Rothwarf-Taylor equations are that they assume that the population of quasiparticles has entirely relaxed to the energy gap and that the sub-gap phonons play no part in the dynamics of the system. Furthermore, the Rothwarf-Taylor equations do not take account of any spatial dependence, which for large area devices, dimensions $L > \sqrt{D_{qp}\tau_{recomb}^{eff}}$, will become important.

The latter problem can be worked around by adopting a diffusion equation based approach, however it has been found for a number of systems that quasiparticle diffusion is poorly predicted from available models(Zehnder 1995; Martin 1996; Friedrich 1997), and that the quasiparticle lifetimes have to be empirically derived.

Chang and Scalapnio(Chang 1977) considered a system of coupled integral equations which included the quasiparticle and phonon distributions based on Eliashberg's(Eliashberg 1960) work. They found that:

$$\begin{aligned}\frac{df(E)}{dt} = I_{qp}(E) &- \frac{2\pi}{\hbar}\int_0^{\infty} d\Omega F(\Omega)\alpha^2(\Omega)\rho(E+\Omega)\left(1-\frac{\Delta^2}{E(E+\Omega)}\right)\\ &\left\{f(E)\left[1-f(E+\Omega)\right]n(\Omega) - f(E+\Omega)\left[1-f(E)\right]\left[n(\Omega)+1\right]\right\}\\ &- \frac{2\pi}{\hbar}\int_0^{E-\Delta} d\Omega F(\Omega)\alpha^2(\Omega)\rho(E-\Omega)\left(1-\frac{\Delta^2}{E(E-\Omega)}\right)\\ &\left\{f(E)\left[1-f(E-\Omega)\right]\left[n(\Omega)+1\right] - \left[1-f(E)\right]f(E-\Omega)n(\Omega)\right\}\\ &- \frac{2\pi}{\hbar}\int_{E+\Delta}^{\infty} d\Omega F(\Omega)\alpha^2(\Omega)\rho(\Omega-E)\left(1+\frac{\Delta^2}{E(\Omega-E)}\right)\\ &\left\{f(E)f(\Omega-E)\left[n(\Omega)+1\right] - \left[1-f(E)\right]\left[1-f(\Omega-E)\right]n(\Omega)\right\}\end{aligned} \tag{2.79}$$

$$\begin{aligned}\frac{dn(\Omega)}{dt} = I_{ph}(\Omega) &- \frac{8\pi N(0)}{\hbar N}\int_{\Delta}^{\infty} dE\int_{\Delta}^{\infty} dE'\,\alpha^2(\Omega)\rho(E)\rho(E')\left(1-\frac{\Delta^2}{EE'}\right)\\ &\left\{f(E)\left[1-f(E')\right]n(\Omega) - f(E')\left[1-f(E)\right]\left[n(\Omega)+1\right]\right\}\delta(E+\Omega-E')\\ &- \frac{4\pi N(0)}{\hbar N}\int_{\Delta}^{\infty} dE\int_{\Delta}^{\infty} dE'\,\alpha^2(\Omega)\rho(E)\rho(E')\left(1+\frac{\Delta^2}{EE'}\right)\\ &\left\{\left[1-f(E)\right]\left[1-f(E')\right]n(\Omega) - f(E)f(E')\left[n(\Omega)+1\right]\right\}\delta(E+E'-\Omega)\end{aligned} \tag{2.80}$$

where n(Ω) is the density of phonons, f(E) the density of quasiparticles, and the other symbols have meanings as for (2.51),(2.52), (2.54), (2.55) and (2.56). Indeed it is possible to see the similarity between (2.79) and (2.51), (2.52) and (2.54), so that we may identify the three terms of (2.79) with quasiparticle scattering by absorption of a phonon, scattering by emission of a phonon, and quasiparticle loss by recombination. Likewise (2.80) is similar to (2.55) and (2.56), so that we may identify the two terms as being due to phonon-quasiparticle-scattering and pair-breaking. I_{qp} and I_{ph} are the quasiparticle and phonon injection rates that are the non-equilibrium driving terms.

These equations need to be solved numerically in order to find the quasiparticle and phonon distributions, from which it is possible to also calculate the energy gap. Chang and Scalapino did this for a number of experimental situations, including thermal phonon injection (e.g. by an adjacent heater), and electron injection from a SIN tunnel junction. In the linearisation procedure that they used, they introduced a free parameter corresponding to phonon escape from the system. The results were very dependent on this escape time, but particularly for short phonon

trapping times, the phonon and quasiparticle distributions were significantly different from the assumed distributions for the Rothwarf-Taylor equations.

CHAPTER 3

Superconducting Particle Detectors

In this chapter, the use of superconductors in a variety of particle detector designs is discussed. The first section outlines the applications for which the various detector concepts discussed in the second section are being developed. The final section examines some of the processes that must be understood in order to achieve the maximum performance from these types of detector. It is towards obtaining this understanding that the experimental work reported in this thesis has been aimed and in the discussion of the various processes the relationship with the experimental work will be highlighted.

3.1 Applications

The common feature of the applications that we consider here is the need to detect the energy of a particle, be it a photon, nuclear particle or molecular fragment, to a high accuracy. In addition, for some applications a position or angular resolution is desired to provide a full imaging capability.

The selection of applications discussed here is not exhaustive; it is, however, orientated towards those that have been the driving force in the low temperature detector field: X-ray astronomy and dark matter searches. In addition, two applications for which operating detectors have recently been demonstrated are described. The reader is also directed towards the available review articles, for example (Sadoulet 1996).

3.1.1 Astronomy

3.1.1.1 The X-ray Universe

The first measurement of extraterrestrial X-rays was made in 1949 by a group at the Naval Research Laboratory (NRL), Washington DC(Group 1994). Using Geiger counters aboard a modified V2 rocket, solar X-rays were recorded, thus confirming the emissions which had been postulated a decade earlier to explain the interference of radio transmissions during solar flares. The first extra-solar source was identified in 1962 with the discovery of Scorpius X-1(Giacconi 1962), the brightest accretion powered X-ray binary in the sky. In the following year another source was

discovered by a group at NRL in the remnants of the super-nova of 1054 – the Crab Nebula. By 1970 approximately 40 X-ray sources had been identified, a figure which had risen by the mid 1980s to 2000. The first satellite based X-ray imaging telescope, NASA's HEAO-2 (Einstein) mission, confirmed X-ray emission from virtually every known class of astronomical object from the interstellar medium to active galacti nuclei.

Within the astronomy community, there is a wish for high energy and spatial resolution studies of every stage of stellar evolution, the interstellar medium and galaxies. Of particular interest are measurements of Doppler shifts, ionic emission and absorption lines in many sources ranging from young T-Tauri type stars, through main sequence stars to stellar remnants such as X-ray binary systems. In interstellar gas studies there is potential for studying the X-ray absorption spectra, particularly the K shell features from Oxygen. Such studies require a good large area coverage of the sky, for example the Diffuse X-ray Spectrometer flown aboard the Space Shuttle in 1993 covered 5% of the sky for 0.15-0.28 keV. In studying active galactic nuclei (AGN) the main spectral emission line observed is the 6.4 keV iron line, which acts as a tracer of cold material close to the central source. This emission line is easily simulated in the laboratory using a ^{55}Fe source which emits 88% 5.89 keV Mn K_α and 12% 6.49 keV Mn K_β radiation. For this reason, unless otherwise stated the energy resolution is quoted as eV for a 6 keV photon.

3.1.1.2 Desired Specifications

In order to provide the desired resolution the required specifications are exceptionally demanding. The current generation of X-ray detectors is based on semi-conductor charge coupled device (CCD) technology. An incident photon creates electron-hole pairs and the charge is then read out to get a direct measure of the energy of the photon. The CCD technology allows the development of two dimensional detector arrays that permit imaging of the source. Although the quantum efficiency is close to 100% and the spatial resolution is good, the energy resolution at 100 eV is insufficient.

In order to meet the demands of the astronomy community, there has been substantial development work on a variety of cryogenic detector designs. However to date none of these has achieved the predicated energy and spatial resolutions. Nevertheless, the development work has achieved progress and continues to be an area of active study, for example the recently announced UK X-ray Cryogenic Spectrometer Programme (XCSP) (Blamire 1997) has set the following target detector performance specifications:

- Energy resolution: <5 eV for a 6 keV photon
- Quantum efficiency: >90%
- Imaging capability: >100-10000 detector elements in a 2D array
- Position resolution: ~0.1×0.1 mm (2 arc seconds for a 12m focal length)
- Throughput: ~5000 counts s^{-1} (including ~1000 counts s^{-1} $pixel^{-1}$)
- Operating temperature: 10-300 mK

The target date for laboratory development of such a detector is summer 2000, with it space qualified and ready to fly a mission (XEUS) by 2004. Fortunately, detector speed is not of primary concern in this application – background X-ray photon fluxes are of the order of 1 photon cm^{-2} s^{-1}, with maximum count rates likely to be less than 1000 counts s^{-1}.

3.1.2 Dark Matter Searches

Although the work reported in this thesis has been aimed towards the development of X-ray detectors, the nuclear physics community has been a consistent source of applications for cryogenic detectors.

The search for particles that may form the 'missing' dark matter of the universe is one of the most pressing problems in modern cosmology. A number of arguments suggest that it may be composed of something other than ordinary baryons. If this is the case then it might be due to some type of particle that formed in the hot primitive universe which subsequently only interacts weakly with the baryonic matter. Conversely, a number of particle physics theories, such as super symmetry, give rise

to non-baryonic dark matter at densities compatible with that which might be expected of just such a weakly interacting particle. For these reasons, there has been considerable international effort in the search for such weakly interacting massive particles (WIMPs).

The difficulties in the search for WIMPs are formidable, principally the number of interactions is very low of order 10^{-3} counts $kg^{-1}day^{-1}$, which is smaller than radioactive counts in even the purest of detectors. The detectors need to have low thresholds to detect efficiently low mass WIMPs - typically 0.5 keV is required. WIMP detectors, therefore, require both sensitivity and mass; for example the CRESST collaboration utilises 250 g Sapphire crystals with superconducting detectors that achieve the threshold of 0.5 keV. The requirement of background rejection and discrimination for WIMP detectors in turn makes the same detector concepts good candidates as detectors for these background events.

3.1.3 Materials Analysis

An important tool in materials microanalysis is the use of a scanning electron microscope equipped with an X-ray sensor to identify local composition of a sample from the emitted X-ray spectra. Conventional X-ray analysis has been confined either to semi-conductor energy dispersive X-ray detectors, with concomitant energy resolution limits of approximately 100 eV, or to wavelength dispersive X-ray detectors with associated poor collection and detector efficiencies. Cryogenic detectors offer a combination of excellent energy resolution, high spatial collection angles and good detector efficiency. Unlike the detectors for X-ray astronomy, detectors used on electron microscopes require count rates of many thousands of counts per second, which impose different constraints on the design to reduce recovery time between events.

Within the last few years a group based at the US National Institute of Standards and Technology has developed a superconducting transition edge sensor based detector (see section 3.2.4.2) mounted in an adiabatic demagnetisation refrigerator (ADR) (Wollman 1997). The ADR is in turn mounted adjacent to an SEM column, with the detector aligned to a port offering line of sight access to the sample.

The detector has been demonstrated, having a resolution of 7.2 eV for 5.89 keV. Using this detector, the NIST group has demonstrated its use in resolving closely spaced peaks in technologically useful applications, for example, the Si K_α and W M_α/M_β peaks (1.74, 1.774, 1.834 keV) and the Ba $L_{\alpha 1/2}$ and Ti $K_{\alpha 1/2}$ (4.46 and 4.51 keV) peaks.

3.1.4 Mass Spectrometry

Our final example of the use of a superconducting detector is the use of a SIN tunnel junction detector (see section 3.2.3.1) in a time-of-flight mass spectrometer. Matrix-assisted laser-desorption-ionisation time-of-flight spectroscopy is an important technique in the study of proteins and other large mass bio-molecules(Siuzdak 1994), but have limited mass resolution for larger mass molecules due to limitations in the microchannel plate detectors.

Cryogenic microcalorimeters can extend the usefulness of time-of-flight detectors by providing information not only about the time of flight of a molecular fraction, but also, the kinetic energy, hence charge and mass of the fractions. In addition, cryogenic detectors are potentially many orders of magnitude faster than existing state-of-the-art sequencers. It has been calculated that a cryogenic detector based system could sequence the entire human genome in a mere 25 hours compared to the 800 years currently required by a single sequencer(Twerenbold 1996).

The use of cryogenic detectors in this capacity was first suggested by Twerenbold at the Low Temperature Detectors 6 Workshop (Twerenbold 1996) and has recently been implemented by NIST(Hilton 1998). They have demonstrated a detector using a SIN readout bolometer mounted on a Si_3N_4 membrane that was able to read a mass spectrum for bovine serum albumin, in which the detector responded to energy depositions in the range 0-40 keV.

3.2 Designs

In this section we review the most commonly proposed designs for superconductor based energy resolving detectors. In particular we focus on the classes of detector to which the work reported here is most relevant.

3.2.1 Superheated Superconducting Granules

The basis of the superheated superconducting granule (SSG) detector is the detection of the superconducting transition in one or more small grains of a superconductor. The readout is by detection of the changes in an applied magnetic field as individual granules switch between normal and superconducting states and so via the Meissner effect the field is excluded (or not) from the granule. Calculating the length of time a grain was in the normal state gives the energy deposited(Turrell 1997).

In practice the performance of this type of detector is sensitive to the uniformity of the grains in both size and shape and to the uniformity in the distribution of the grains in the detector. Currently an SSG detector is in use in the ORPHEUS dark matter search at CERN(van den Brandt 1997) and SSG neutron detectors have been demonstrated(Meagher 1996).

3.2.2 STJ Detectors

The concept of the STJ as a particle detector was first demonstrated by Wood and White in 1969(Wood 1969) using tin/tin-oxide devices to detect α particles. During the ‘60s and ‘70’s STJs were widely used for phonon detection(Eisenmenger 1976), but it was not until 1982 that Kurakado suggested STJs for use as X-ray detectors(Kurakado 1982).

The principle of operation is analogous to the operation of a semiconductor device. An incident X-ray is absorbed in one electrode of a STJ, creating a number of energetic photoelectrons. The primary photoelectrons undergo electron-electron scattering, generating secondary photoelectrons. Within a few nanoseconds the electrons have scattered down in energy to create a population of quasiparticles close

to the gap edge(Schafroth 1996). The quasiparticles then diffuse through the absorber to the vicinity of the tunnel barrier where they are counted as a tunnelling charge. The resolution is theoretically limited only by the statistics of counting the quasiparticles. Monte Carlo simulations of the excitation processes give a mean energy to create a quasiparticle of:

$$\varepsilon = f\Delta \tag{3.1}$$

where f≈1.7(Kurakado 1982; Rando 1992). The resolution is then given by the statistics of coupled processes – Fano statistics - to give:

$$\frac{\delta E}{E} = \sqrt{\frac{F}{N}} \approx \sqrt{\frac{0.22(1.7\Delta)}{E_{photon}}} \tag{3.2}$$

where F≈0.22(Kurakado 1982; Rando 1992) is the Fano factor, N the number of excitations and E_{photon} the energy of the incident photon. For Nb (3.2) predicts an energy resolution of only 2.4 eV for a 6.4 keV photon. In practice the best resolution obtained has been an order of magnitude worse than this at 29 eV(Mears 1996).

3.2.2.1 Materials

In order to achieve high quantum efficiency, one requires a material that will absorb as many X-ray photons as possible. The absorption length is determined largely by the electron density in the material, but in general will be longer than a thin film can be reasonably grown. In addition, the tunnelling rate from the absorber is inversely proportional to the thickness of the region from which the quasiparticles tunnel. For this reason, one would expect, for example, Al to be a poor choice for the absorber and Ta to be a better one.

Of primary concern in the selection of materials is the availability of compatible superconductors and insulating barriers. The first materials to be used for STJ detectors were tin and tin oxide, which are not stable to repeated thermal cycling and so are not suitable for repeated experiments at low temperature. During the 1980s niobium/aluminium oxide devices were developed and have become the predominant technology(Goldie 1990; Stricker 1991; de Korte 1992; Kurakado 1993; Mears 1993). A number of groups have developed Ta based devices(Gaidis 1993; Le Grand 1994b; Blamire 1995; Friedrich 1996; Gutsche 1996; Nussbaumer 1996; Porter 1996; Bruijn

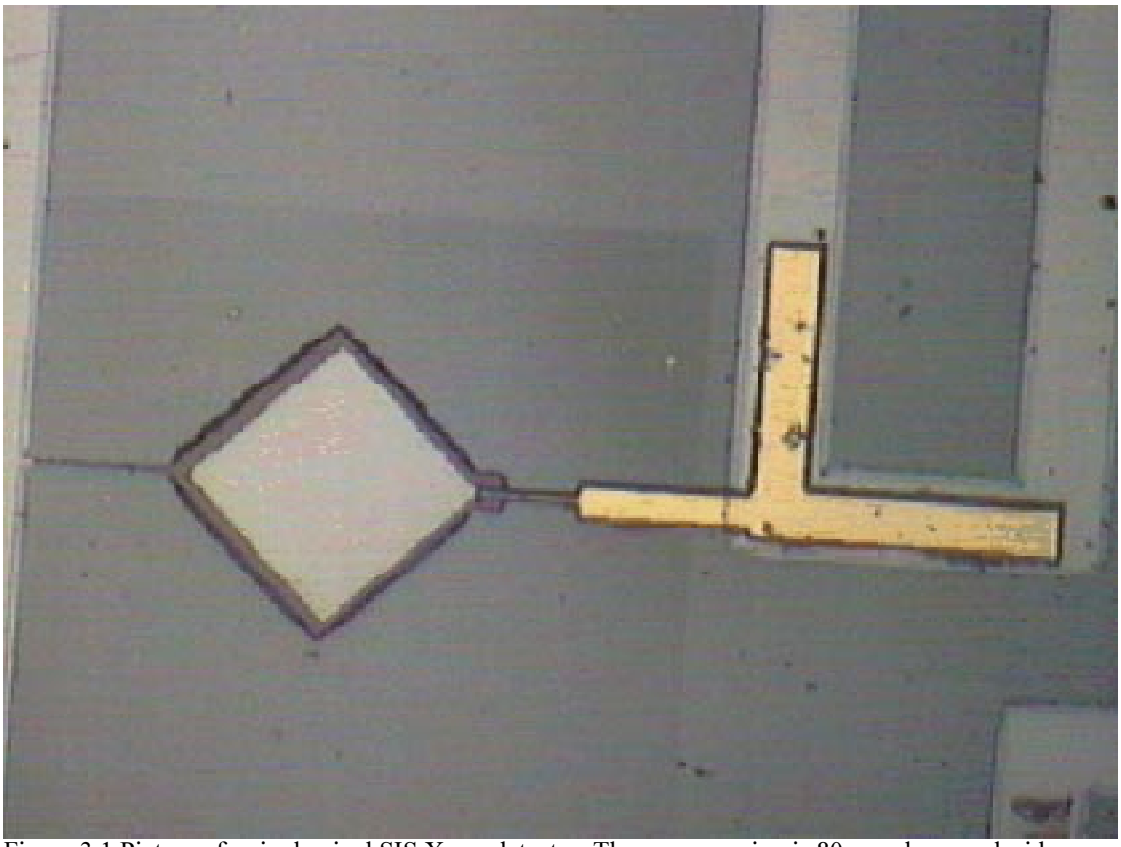

Figure 3.1 Picture of a single pixel SIS X-ray detector. The square region is 80 μm along each side.

1997; Peacock 1998), although in general it has been found that aluminium oxide barriers are more successful than native tantalum oxide barriers(Bruijn 1996).

One of the concerns in the development of STJ devices has been to maximise the quasiparticle diffusion from the absorption site to the tunnel barriers. To achieve this, epitaxial Nb and Ta layers have been tried (Porter 1994; Porter 1996; Verhoeve 1996), although these are more difficult to deposit successfully and may lead to increased loss of energy via phonons to the substrate. In an extreme case, it has been proposed to use bulk single crystals of superconductor as both absorber and substrate(Hamster 1996; Patel 1996; Bruijn 1997; Netel 1997), although it has been found difficult to grow high quality STJs on the crystal.

3.2.2.2 Single Pixel Devices

Many groups have produced single pixel STJ based detectors, using a variety of approaches to develop high resolution and large area detectors. A picture of a

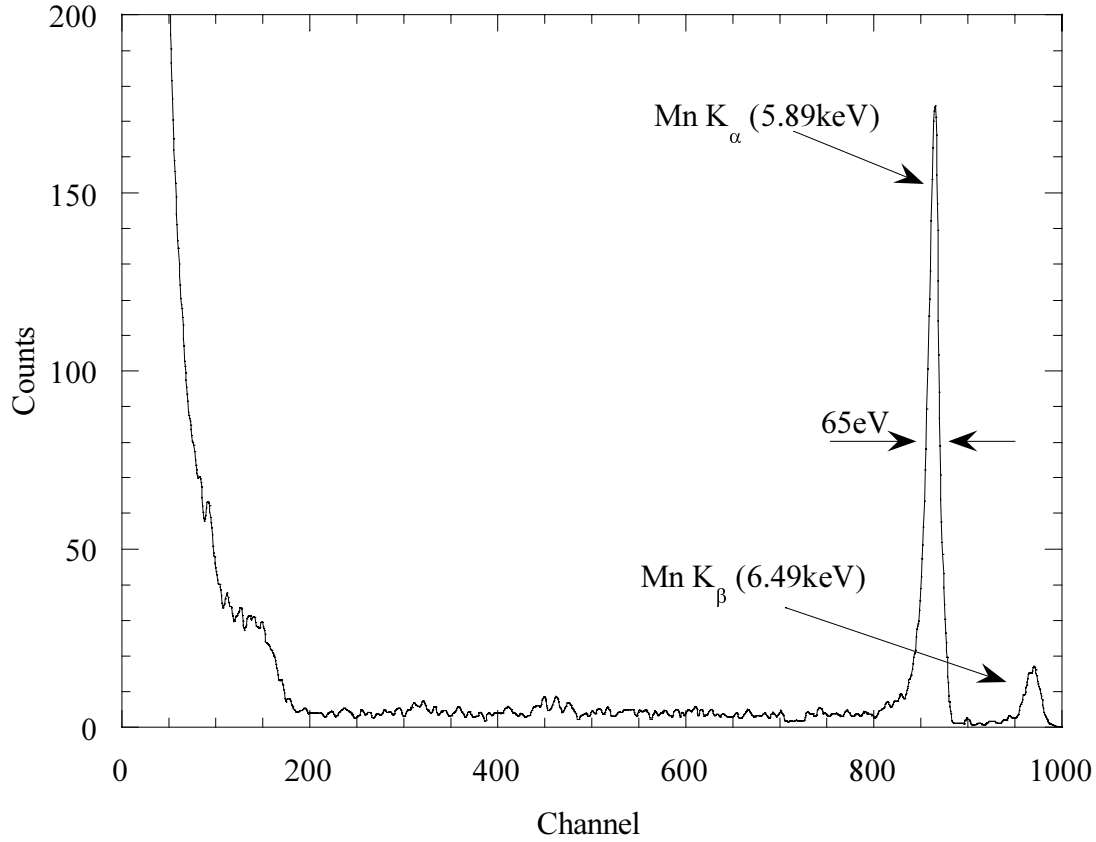

Figure 3.2 X-ray spectra for ^{89}Fe source showing Mn K_α and K_β lines for a device similar to that in figure 3.1. Results courtesy of Dr. F. Scott Porter, formerly of US Naval Research Laboratory.

typical single pixel detector produced by the author as part of a collaboration with NRL, Washington DC is shown in figure 3.1.

The detector consists of a square epitaxial Nb/Ta base layer of edge length 85 µm and thickness 400 nm. An AlO_x junction and Nb counter-electrode of edge length 80 µm is placed on the base layer. Finally, a Nb/Pd/Au contact wire makes a connection to the edge of the counter-electrode. During operation, the device was cooled to 300 mK, and a magnetic field applied to suppress the Josephson tunnel current. As outlined in section 2.4.3.4, the shape of the junction cavity will affect the magnetic field required to suppress the DC and AC Josephson effects. In this case the field is applied along the diagonals of the detector, so that the detector has a diamond shape. Other groups have experimented with different shapes of junction(Gijsbertsen 1994).

Our device is unusual in that the thin counter-electrode and the Pd/Au in the wiring layer suppresses signals from absorption events in the counter-electrode. For

the majority of STJ devices, pulse discrimination is required to separate base and counter-electrode events. Like many STJ detectors, this one utilised proximitised Al layers immediately adjacent to the barrier to trap quasiparticles close to the barrier. The process of quasiparticle trapping and associated effects are considered in greater detail in section 3.3. A sample X-ray spectra for a similar device is shown in figure 3.2, for which the author thanks Dr. F. Scott Porter, formerly of NRL, Washington DC. The full-width half-maximum value for the strong peak at 6 keV was 65 eV, a factor of 2.2 greater than the current world best of 29 eV(Mears 1996).

Single pixel devices have also been demonstrated as optical and UV photon counting detectors(Peacock 1997), typically achieving a resolution of 0.2 eV for a 5 eV photon, and counting incident photons with a quantum efficiency of approximately 60%.

3.2.2.3 Position Resolving Devices

In addition to an energy resolving capability, an important requirement is the ability to form an image. To do this, one requires a position resolving capability as well. There are two routes through which this can be achieved: either by making a multiple pixel device, or by using a signal division scheme. In the latter case, the signal from one event is split between two or more distributed detectors, the sum of the detector outputs giving the magnitude of the signal and the relative time lags of the detectors giving the position. This method was first demonstrated by Kraus (Kraus 1989), using a linear array of tin/tin-oxide devices with which he obtained a position resolution of 5 μm over 450 μm. A similar scheme using a Ta absorber and Al junctions has shown 1 μm resolution over 40 μm and a 54 eV resolution at 6 keV (Friedrich 1997). This method is however hampered by the, as yet, poorly understood quasiparticle loss processes combined with the slower than expected quasiparticle diffusion. These problems are addressed in part in chapter 5.

The alternative scheme involves forming arrays of STJ detectors to obtain a multi-pixel imaging ability. Small 3×3 arrays have been demonstrated(Hartog 1997), although there are many technical questions that remain to be resolved before large scale arrays can be fabricated. Most significant amongst these questions are the

problems of making connections to n^2 devices as n, the number of pixels along one edge, increases. Closely related to this is the problem of readout electronics; it has been found that best results are obtained with cooled electronics, often SQUID based. However this imposes problems of the heat-load on the cryostat, signal cross-talk and cost as the number of detector channels is increased.

3.2.3 SIN Based Devices

3.2.3.1 Bolometers

It was shown in section 2.4.2.3 that the dynamic resistance of a SIN tunnel junction was exponentially dependent on the temperature of the normal metal electrode. This feature has been exploited to utilise SIN tunnel junctions as readouts for bolometers. The principal of operation is simple; an incident X-ray photon is absorbed in a normal metal layer, depositing its energy into the electron and phonon systems of the metal. At low temperatures, the electronic specific heat capacity of a normal metal far exceeds the contribution to the specific heat capacity due to the phonons, thus the majority of the energy is held in the electron system. The increased electron temperature is then directly sensed as an increase in the tunnelling current in a SIN tunnel junction.

In the ideal case, if an energy ΔE was deposited in the normal metal electron system then the current in the SIN tunnel junction would increase by:

$$\Delta I = \frac{\Delta E}{C}\frac{\partial I}{\partial T}\Big)_V \tag{3.3}$$

where C is the combined specific heat capacity of the thermometer and absorber. By evaluating the numerical integral (2.35), one can show that the sensitivity of the SIN tunnel junction will increase exponentially as the temperature is lowered and the bias increased closer to (but less than) the energy gap Δ. In practice, this simple scaling is not achieved due to defect limited junctions, back tunnelling of quasiparticles (see 3.3.3) and heating from recombination of quasiparticles in the superconducting electrode (see 3.3.4). Although most of the energy is stored in the electron system, if the phonon system is at a significantly different temperature, by being well coupled to

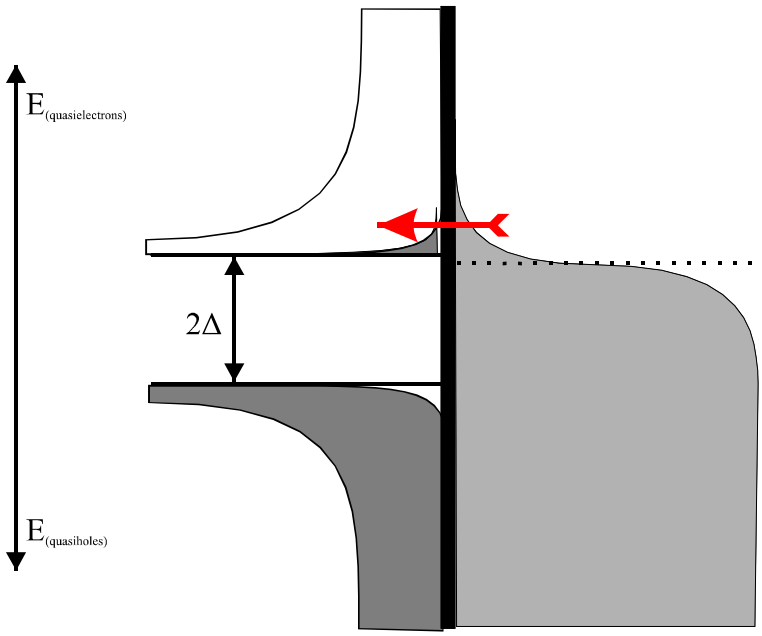

Figure 3.3 Semiconductor representation schematic of a SIN tunnel junction acting as a refrigerator. The tunnelling of electrons above the fermi energy in the metal to the superconductor is the dominant process of the four possible electron tunnelling processes.

the substrate phonon system for example, then there will be a heat flow out of the electron system that will degrade the energy resolution. To minimise this, one wishes to reduce the thermal conductivity from the absorber to the substrate. This can be achieved by placing the absorber on a membrane, commonly of Si_3N_4.

A bolometer of this design has been demonstrated both as an X-ray detector, exhibiting an energy resolution of 22 eV at 6 keV(Nahum 1995) and as an energy resolving detector in a mass spectrometer (see section 3.1.4).

3.2.3.2 Electron Refrigerators

Closely related to the use of SIN tunnel junctions to measure the electron temperature of the normal electrode was the observation that for a suitable bias they actively cool the electron system of the normal metal. The process is easily illustrated using the semiconductor representation, as shown in figure 3.3. By biasing the tunnel junction just below the energy gap Δ, so that eV≲Δ, electrons in the normal metal at an energy $\varepsilon > \varepsilon_F + \Delta - eV$ are able to tunnel into the superconductor where they may be removed from the junction region before recombining. The result is that the energetic electrons in the normal metal are selectively removed. If the device is a

symmetric SINIS structure then the energetic holes in the normal metal are removed as well. Such cooling has been demonstrated both for SINS structures(Nahum 1994; Fisher 1995; Fisher 1997; Manninen 1997), and for SINIS structures(Blamire 1991; Leivo 1996). To date, the largest cooled volume has been a relatively small 1660 μm^3 by a mere 2.5 mK from 125 mK(Fisher 1997). It is believed that performance of the device is limited by heating due to non-ideal junction characteristics and self-heating due to recombination phonons.

3.2.4 Superconducting Transition Sensors

Our final class of superconducting energy detector designs is based on the use of a superconductor with a tuned transition temperature as a thermometer. By depositing a superconductor-normal bilayer, a proximitised structure with a designed transition temperature is formed. By careful control of the relative thickness of the superconductor and normal metal layers such as Al and Ag, the transition temperature can be tailored to within 5 mK over a range of 500 mK(Irwin 1996). The transitions have a width of less than 5 mK, so by measuring the dynamic resistance an extremely sensitive thermometer is obtained.

3.2.4.1 Superconducting Phase Transition Sensors

The superconducting phase transition (SPT) sensor utilises a transition edge thermometer to detect athermal, ballistic phonons absorbed in a bulk substrate such as sapphire. These athermal phonons propagate through the crystal until they are absorbed in the thermometer, resulting in an increase in the resistance as the temperature of the thermometer is increased.

A detector of this type has been demonstrated as part of the CRESST dark matter search(Sisti 1997) using 32 g (40×20×10 mm) sapphire absorbers. It has recently been proposed as the basis of an X-ray detector using 10×20×1 mm sapphire absorbers(Cooper 1997).

Although this class of detector has not been a direct motivation for the work reported in this thesis, the work reported in chapter 6 on the detection of athermal substrate phonons is relevant to the design of such detectors.

3.2.4.2 Electro-Thermal Feedback Transition Edge Sensors

The electro-thermal-feedback transition-edge-sensor (ETF-TES) is the design that, at the time of writing, holds the world record for energy resolution at 6 keV. As mentioned in section 3.1.3, an impressive resolution of 7.2 eV has been demonstrated. The principle of operation is that the incident photon is absorbed in a normal metal region, resulting in a thermalised population of electrons and phonons that in turn heat the well coupled transition layer thermometer. The electro-thermal feedback component of the design was suggested by K. Irwin(Irwin 1995), as a means of overcoming the inherently slow recovery time of a bolometer – a consequence of the weak coupling of the sensor to the environment to maximise the fraction of the absorbed energy which is measured. Briefly, the TES is cooled below its transition temperature and then voltage biased, which results in the sensor being Joule heated. For a given bias point there will be a current that results in a Joule heating that exactly balances the cooling. The TES is then maintained at a constant temperature above the bath temperature. When the sensor is heated by an absorbed photon the resistance rises, so the bias current falls, so the Joule heating is reduced, so the sensor is cooled again. This not only reduces the recovery time but also provides the readout of the sensor by using a SQUID (or even a series array of SQUIDs) to bias the sensor and hence directly read the Joule heating current.

3.3 Detector Processes

In this section, we examine various quasiparticle and phonon processes that are relevant to the performance of the superconducting detectors discussed above. Of particular relevance are the processes which are expected to occur in the two classes of X-ray detectors that have been produced during the course of this work: STJ detectors and SIN bolometers.

3.3.1 Quasiparticle Trapping

In section 3.2.2 we mentioned the use of a superconducting heterostructure to confine quasiparticles created by an X-ray absorption event in an STJ detector close

to the tunnel barrier, thus increasing the probability of the quasiparticles tunnelling within their lifetime. This process of quasiparticle trapping will increase the signal associated with the X-ray event and hence should improve the signal to noise ratio. This use of a superconducting heterostructure was first proposed by N. Booth (Booth 1987), for application in dark matter detectors, where the large bulk necessitated some means of collecting the quasiparticles at the detectors.

The principle behind trapping is simple; quasiparticles in a superconductor with energy gap Δ will scatter to the gap edge and thus have an energy Δ. If they then enter a region with an energy gap $\Delta_{trap}<\Delta$ they will scatter to an energy Δ_{trap} emitting a phonon. The rate of inelastic scattering of quasiparticles can be estimated using the results of Kaplan(Kaplan 1976). However, for a 6 keV X-ray photon the total number of quasiparticles in Nb is approximately $2.4\ 10^6$, which, in a typical 100×100 μm detector volume results in a population of quasiparticles that is 10^6 greater than the thermal population at 0.3 K. Therefore, the calculations of Kaplan, which are based upon thermal populations, are not strictly valid. In order to escape from the trap, a quasiparticle will have to absorb a phonon of energy $\Omega\geq\Delta-\Delta_{trap}$. Kaplan(Kaplan 1976) predicts that the rate of phonon emission will exceed the rate of phonon absorption, so that there is a net quasiparticle trapping rate.

If these traps are adjacent to the tunnel barrier then the quasiparticle tunnel rate will be increased since the tunnelling time is inversely proportional to the volume of the region from which tunnelling occurs (assuming that $\tau_{tunnel}>>\tau_{trap}$, where $\tau_{tunnel\backslash trap}$ are the tunnelling and trapping times respectively). On the other hand, it has been suggested that regions of depressed gap away from the barrier could be a common source of quasiparticle loss and slow diffusion. Possible sources of depressed gap regions that have been suggested include Abriskov vortices(Van Vechten 1992; Golubov 1993; Le Grand 1996), metallic oxides(Gijsbertsen 1996a) and grain boundaries and gap anisotropy(Friedrich 1997). In chapter 5 we measure the quasiparticle lifetime in an epitaxial Nb device and compare it with the lifetimes in devices with different Nb microstructures reported in the literature.

In his initial work (Booth 1987; Booth 1993), Booth used a simple model of abrupt change in the gap parameter at the trap. Using this approximation, which

implies a potential barrier between the trap and bulk – i.e. the M^{c}Millan model of the proximity effect - he found that the trapping rate is:

$$\tau_{trap} = \frac{V_{trap}}{V_{bulk}} \tau_{phonon-emission}(\Delta) \tag{3.4}$$

where $V_{trap/bulk}$ are the volumes of the trap and absorber respectively. Booth has shown that the optimum trap size is given by:

$$\left(\frac{V_{trap}}{V_{bulk}}\right)^2 = \frac{\tau_{phonon-emission}(\Delta)}{2e^2 N(0) V R_N} \tag{3.5}$$

Quasiparticle trapping has been widely demonstrated to be effective in reducing the quasiparticle tunnelling time and increasing the charge collected for photon detection experiments. The linear variation of trapping rate with trap volume has been demonstrated using Cu traps, in which superconductivity was induced by the proximity effect(Goldie 1990) and a peak in phonon emission at Δ-Δ_{trap} was found(Goldie 1991),. In both cases, however, the variation in the gap parameter in the trap due to the proximity effect was neglected.

Golubov(Golubov 1993) has developed a model of quasiparticle trapping based on his model of the proximity effect. In his model, Golubov treats the reduced gap region as having a zero gap and an effective size that is dependent on the proximity effect. He finds that the trapping rate is then given by:

$$\tau_{trap}^{-1} = \frac{1.82}{d_S}\left(\frac{L_{eff}}{\tau_0} + \frac{L_{eff}^{trap}}{\tau_0^{trap}}\right)\frac{A_{trap}}{A} \tag{3.6}$$

where d_S is the thickness of the absorber layer, A and A_{trap} are the areas of the absorber and trap layers, τ_0 and τ_0^{trap} are the characteristic lifetimes for quasiparticles in the absorber and trap, and the effective length, L_{eff} is the length over which a normal material would have the same scattering rate as the reduced gap region in that layer, i.e.:

$$\int_0^\infty \frac{1}{\tau_{scatter}(x)}\,dx = L_{eff}\,\frac{1}{\tau_{scatter}(\Delta = 0)} \tag{3.7}$$

The significance of (3.6) is that in a system such as Nb/Al where the characteristic quasiparticle lifetimes are very different (by approximately 10^3), the trapping rate is

completely dominated by the layer with the shorter τ_0; in this case the Nb layer. Hence the majority of the quasiparticles are not trapped in the Al trap layer, but in the Nb layer.

Quasiparticle trapping has been the subject of many studies, including, within the Cambridge research group, the work of P.A. Warburton(Warburton 1993a). Much of the work reported here, in particular that in chapter 5, builds upon this earlier work and explores the influence of device microstructure upon the effects associated with quasiparticle trapping such as quasiparticle lifetime and multiplication effects.

3.3.2 Quasiparticle Multiplication

Quasiparticle multiplication is the process whereby quasiparticles undergoing inelastic scattering, release a phonon of sufficient energy to break a Cooper pair, and create two new quasiparticles, thereby increasing the total number of quasiparticles. Although this process will naturally occur during the cascade of quasiparticle creation during an X-ray absorption event, it is conventionally used to describe the gain resulting from quasiparticle trapping or injection via a tunnel barrier.

In order to produce a phonon capable of creating new quasiparticles by pair breaking, the original quasiparticle must scatter by at least 2Δ in energy. In a simple model, for the case of quasiparticle trapping this will occur if the energy gap in the trap, Δ_{trap} is:

$$\Delta_{trap} \leq \frac{\Delta}{3} \tag{3.8}$$

so that a quasiparticle at an energy Δ will be able to scatter to an energy Δ_{trap} and release a phonon of energy $2\Delta_{trap}$, to give three quasiparticles in the trap. The use of quasiparticle multiplication in trapping could potentially give a larger signal in an STJ X-ray detector, although in practise this will be negated by the extra noise introduced due to the additional statistical processes. Nevertheless, multiplication is a process that will occur with traps that satisfy (3.8), and in experiments utilising quasiparticle injection via a tunnel junction into states at a sufficient energy from the energy gap(Warburton 1995; Gijsbertsen 1996a).

The work presented in the remainder of this section (3.3.2) is based on work by the author and published elsewhere(Warburton 1993a; Burnell 1994).

In the simplest possible model of quasiparticle multiplication, one would assume that quasiparticles would always scatter directly to the energy gap, releasing a single phonon, which would then always break pairs if it were sufficiently energetic. Thus, a single quasiparticle starting at an energy between Δ and 3Δ, would result in just one quasiparticle. One quasiparticle starting between 3Δ and 5Δ would give three quasiparticles and one starting between 5Δ and 7Δ would give three quasiparticles one of which was at energy between 3Δ and 5Δ which would then scatter to give a total of 5 quasiparticles. One can define a quasiparticle multiplication factor m(ω), where ω is the energy of the initial quasiparticle and a mean multiplication factor that relates the multiplication to the current measured at a tunnel junction at a point at which all multiplication has ceased:

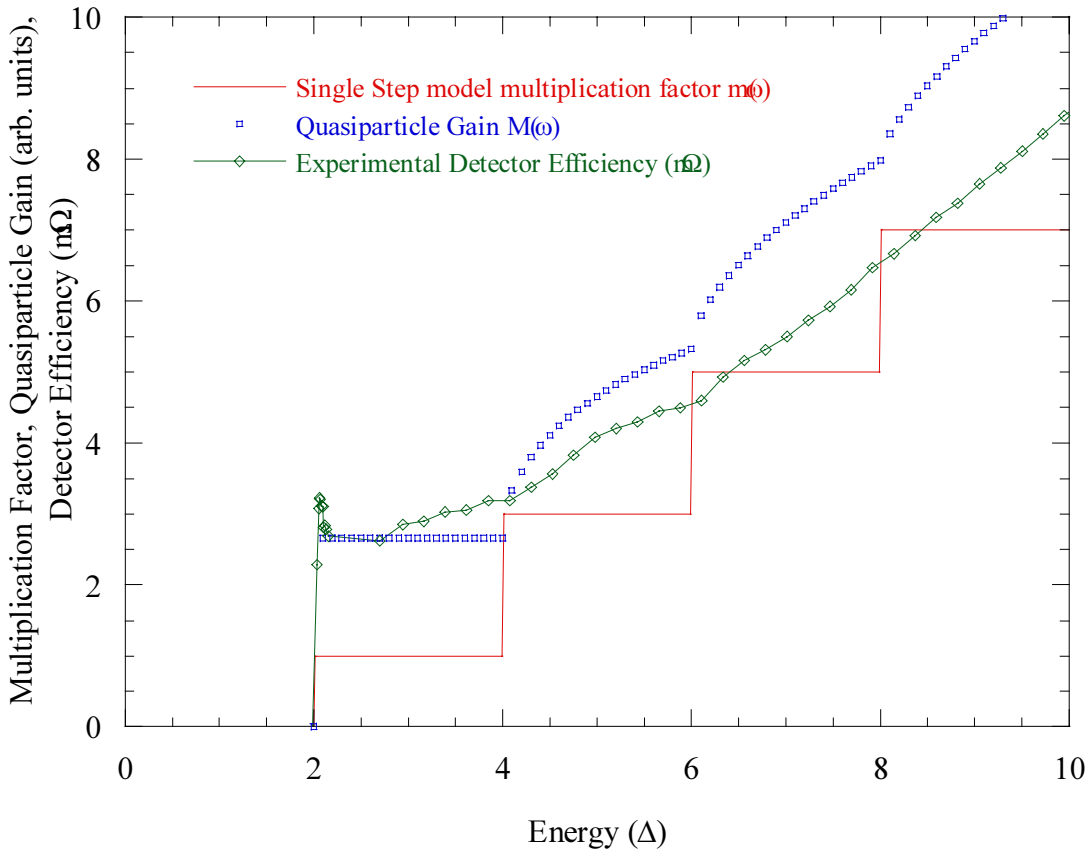

Figure 3.4 Quasiparticle multiplication factor, calculated quasiparticle gain and experimental data for a single step model of quasiparticle scattering. Data from (Burnell 1994).

$$M(V) = \frac{\int_{-\infty}^{\infty} m(E+V)J(E)dE}{\int_{-\infty}^{\infty} J(E)dE} \tag{3.9}$$

where J(E) is the integrand in (2.39). Figure 3.4 shows a plot m(E=eV) and M(V) for this simple model.

In practise however, quasiparticles will not necessarily always scatter to the gap edge in a single step. In the limit of near thermal populations of quasiparticles the theory of Kaplan may be used(Kaplan 1976). Equation (2.52) calculates the lifetime of a single quasiparticle against emission of a phonon, the integrand of which may be used to find the probability that a phonon of energy Ω is emitted. Thus:

$$p(\Omega) = \beta\left(\Omega^2\rho(E-\Omega)\left(1-\frac{\Delta^2}{E(E-\Omega)}\right)\left[n(\Omega)+1\right]\left[1-f(E-\Omega)\right]\right) \tag{3.10}$$

where β is chosen to normalise the integral of p(Ω) to 1. Although (3.10) is strongly

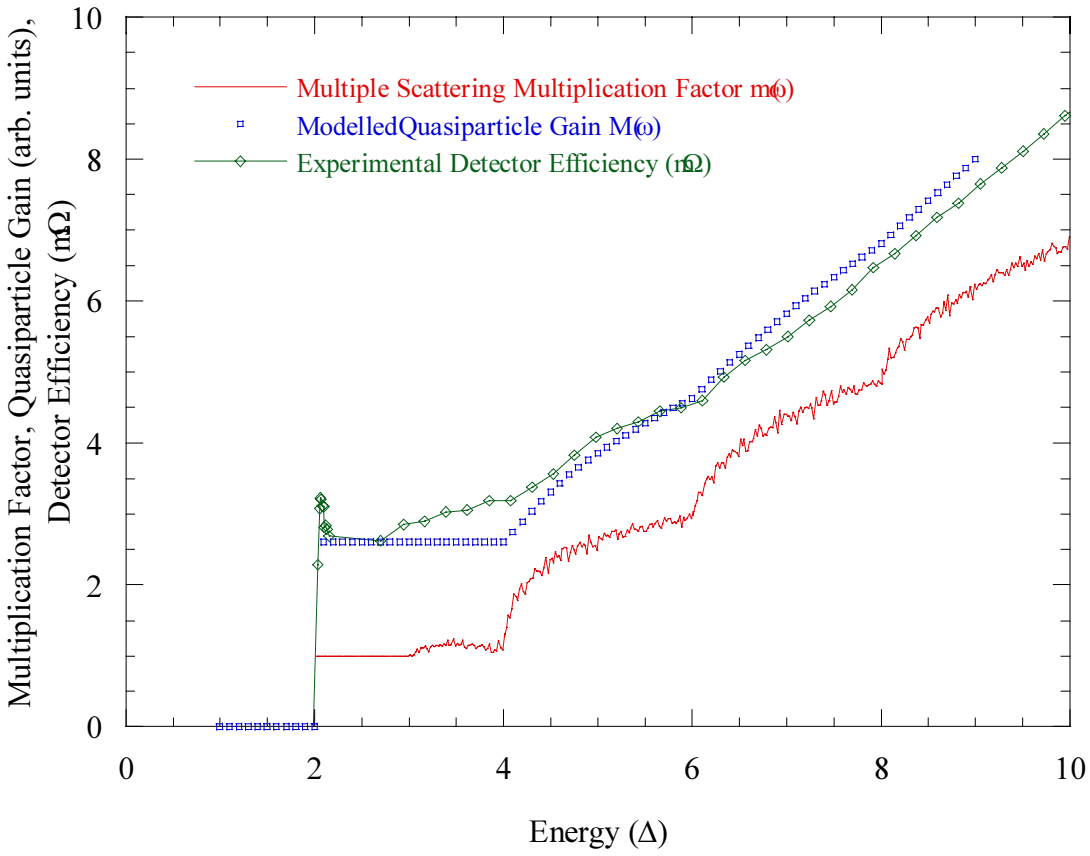

Figure 3.5 Quasiparticle multiplication factor, calculated quasiparticle gain and experimental results for a thermal equilibrium scattering model. Data from (Burnell 1994).

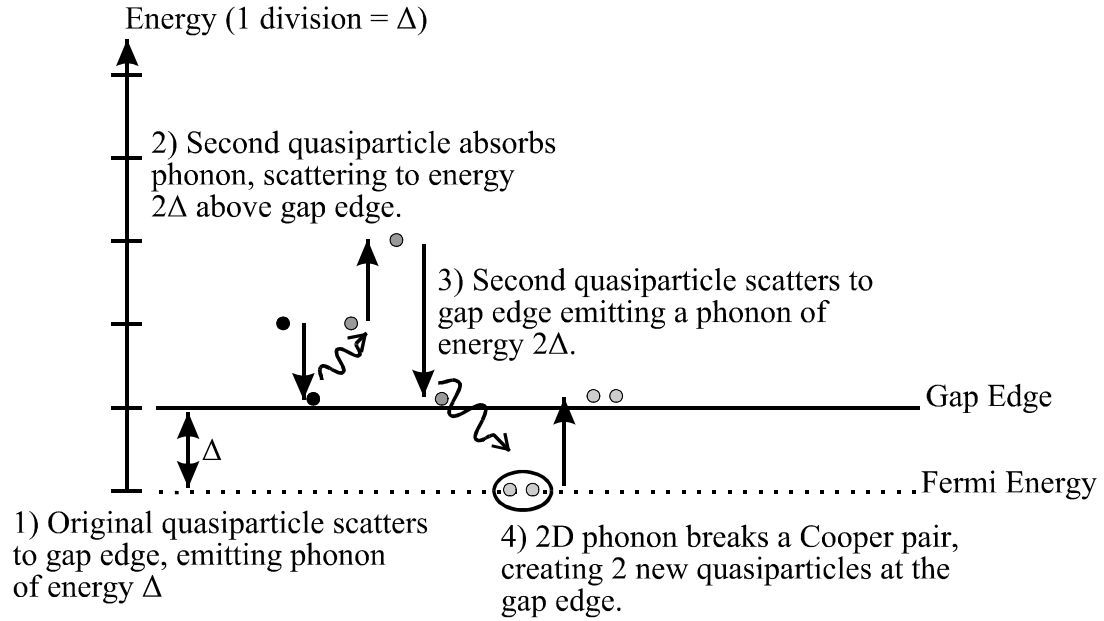

Figure 3.6 Non-Equilibrium scattering process.

peaked for Ω=E-Δ, it does permit the possibility that the quasiparticle may not always scatter directly to the gap edge. By performing a Monte-Carlo simulation using (3.10), following several hundred quasiparticles for initial energies between Δ and 10Δ until they have scattered to an energy of less than 2Δ, an average multiplication factor m(E) and mean multiplication factor M(V) may be found (figure 3.5).

This model has been applied relatively successfully to experimental data(Warburton 1993a; Gijsbertsen 1996a), however, it suffers from the weakness that it only considers a thermal population of quasiparticles and phonons. As we shall see in chapters 5-7, it is relatively easy to produce a significantly non-equilibrium population. We must consider, therefore, how we might modify our model to account for this.

In work studying quasiparticle multiplication in Mo traps in a Nb based system, Warburton(Warburton 1994) noted evidence of quasiparticles being excited out of the Mo traps by absorption of phonons emitted as other quasiparticles scattered into the trap. The equivalent process in simple quasiparticle multiplication would be for a quasiparticle at an energy of 2Δ to scatter to the gap edge, emitting a phonon of energy Δ that could be absorbed by another 2Δ quasiparticle to scatter it to 3Δ (figure 3.6). This second quasiparticle could then undergo multiplication in the normal fashion. The net result would be two quasiparticles for each original quasiparticle.

The resultant m(E) and M(V) are illustrated in figure 3.7. Only the region for $2\Delta \leq E \leq 3\Delta$ is changed – for lower energies the phonons emitted would be insufficiently energetic to promote a quasiparticle to an energy where it could release pair breaking phonons, for greater energies the released phonon will break pairs since the pair breaking time is much shorter than the phonon absorption time (figure 2.17).

This additional modification has been found to model the experimental data

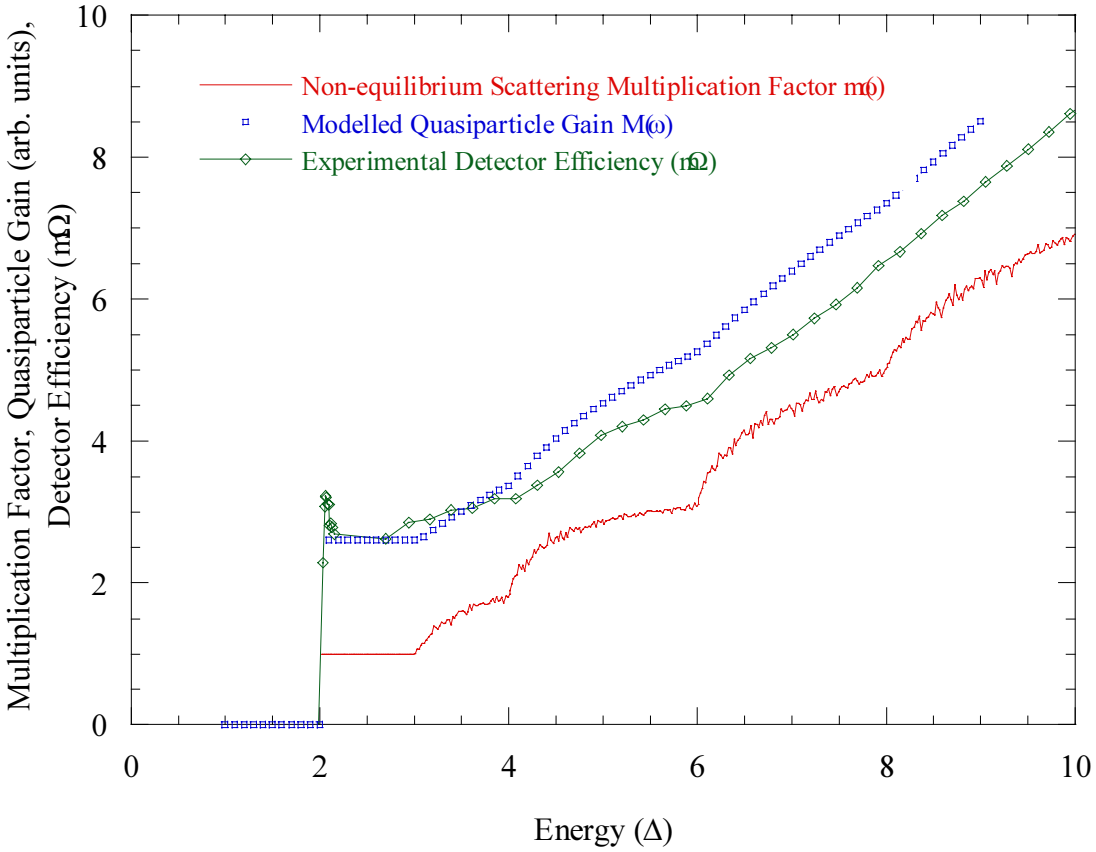

Figure 3.7 Quasiparticle multiplication factor, calculated quasiparticle gain and experimental data for the non-equilibrium process modified thermal equilibrium model. Data from (Burnell 1994).

more successfully(Burnell 1994). The model does, however, over-predict the degree of multiplication at higher biases – this could be attributed to the fact that the system is being driven so far from equilibrium that neither the scattering probability given by (3.10) nor the assumption that the recombination rate is constant are valid. Qualitatively, the recombination rate will be increased since it scales with the number of quasiparticles squared, thus reducing the quasiparticle lifetime. In extreme cases,

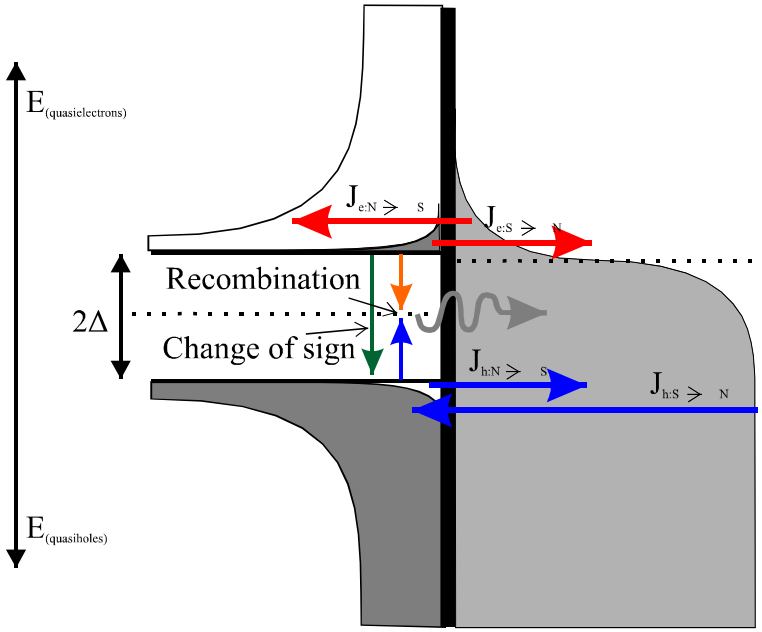

Figure 3.8 Back tunnelling in a SIN tunnel junction.

quasiparticles may not scatter all the way to the gap edge as (3.10) predicts for the thermal case.

3.3.3 Back Tunnelling and Multiple Tunnelling

In section 2.4.3 we discussed the processes whereby quasiparticle tunnelling leads to a current flow. One of the disadvantages of the semiconductor representation that we have used is that it obscures the fact that, while we consider quasielectrons and quasiholes at the energy gap to be distinct particles of negative and positive charge. In reality they are not distinct types of particles and do not have well defined charge. A possible process, therefore, is for a quasielectron at an energy E to become a quasihole at the same energy E. In the semiconductor representation this is equivalent to reflection through the Fermi energy (figure 3.8). The probability of this process occurring will increase the nearer the quasielectron is to the gap edge; at the gap edge the probability of this sign change process is exactly 50% - since these quasiparticle correspond to states with $|\mathbf{k}|=k_F$.

This process leads to two effects that are important to the performance of the devices discussed in this work. Firstly, we consider a SIN device with a bias of $eV \lesssim \Delta$,

such as would be used for both a detector or electron refrigerator (figure 3.8). Under these conditions, a thermally excited electron in the normal metal can tunnel into the superconductor to become a quasielectron close to the gap edge. This quasiparticle is, however, able to tunnel back into the normal metal as a hole at an energy of eV+Δ. The significance of this process has recently been considered by J. Jochum(Jochum 1998).

The number of electron charges being transferred by quasiparticle tunnelling in an SIN device is given by:

$$\begin{aligned} J_e &= \int \left(j_{e:N\to S} - j_{h:N\to S} - j_{e:S\to N} + j_{h:S\to N} \right) dE \\ &= \frac{1}{e^2 R_N} \int_0^\infty \rho(E) \left[f_N(E - eV) - f_N\left(E + eV\right) \right] dE \end{aligned} \tag{3.11}$$

where $f_{S/N}$ are the quasiparticle/electron distribution functions in the superconductor and normal metal and $j_{e/h:S/N\to N/S}$ are the particle fluxes as labelled in figure 3.8. The net particle flux is given by:

$$\begin{aligned} J_{particles} &= \int \left(j_{e:N\to S} + j_{h:N\to S} - j_{e:S\to N} - j_{h:S\to N} \right) dE \\ &= \frac{1}{e^2 R_N} \int_0^\infty \rho(E) \left[f_N\left(E - eV\right) + f_N\left(E + eV\right) - 2 f_S(E) \right] dE \end{aligned} \tag{3.12}$$

In the limit that the normal metal temperature $T_N << (\Delta+eV)/k_B$, then $f_N(E+eV) << f_N(E-eV)$ and hence:

$$J_{particle} = J_{charge} - \frac{N_S}{\tau_{back-tunnel}} \tag{3.13}$$

where N_S is the number of quasiparticles in the superconductor, which is given by the third term in (3.12). The energy removed from the normal metal can be found from the difference between the net currents of quasielectrons and quasiholes, taking into account that the quasielectrons each remove an energy (E-eV) and the quasiholes add an energy (E+eV). Thus, the cooling power is given by:

$$\begin{aligned} P_{cooling} &= \int\left[(E-eV)\left(j_{e:N\to S}-j_{e:S\to N}\right)-(E+eV)\left(j_{h:S\to N}-j_{h:N\to S}\right)\right]dE \\ &= \frac{1}{e^2R_N}\int_0^\infty \rho(E)E\left[j_{e:N\to S}+j_{h:S\to N}-j_{e:S\to N}-j_{h:N\to S}\right]- \\ &\qquad \rho(E)eV\left[j_{e:N\to S}-j_{h:S\to N}-j_{e:S\to N}+j_{h:N\to S}\right]dE \\ &\approx \overline{E}J_{particle}-eVJ_{charge} \\ &\approx \left(\overline{E}-eV\right)J_{charge}-\frac{\overline{E}}{\tau_{back-tunnel}}N_S \end{aligned} \tag{3.14}$$

$\overline{E}$ is the average energy transported by an electron tunnelling to the S electrode and is approximately equal to Δ. From (3.14), a condition for heating to be avoided can be found:

$$\frac{\Delta-eV}{\Delta}>\frac{N_S}{\tau_{back-tunnel}} \tag{3.15}$$

Evidently, if this condition is not met by an electron refrigerator device then it will not cool the normal metal's electron system. If the device is an X-ray detector with a SIN tunnel junction readout, then its resolution will be degraded, as there will be a minimum temperature below which the N electrode cannot be cooled. We can use (3.15) to determine appropriate strategies to minimise the base temperature of the normal metal electrode to maximise the detector's resolving ability.

Our second example of back tunnelling quasiparticles in a superconducting particle detector is its exploitation in a STJ detector as a gain mechanism. In the simplest case of a symmetric SIS junction there is the possibility of a multiple tunnelling process – the Gray Effect – as illustrated in figure 3.9. Briefly, we consider a quasielectron that tunnels from one superconductor (S_1) to another (S_2). After tunnelling the quasielectron will be at some energy E above the energy gap in S_s, Δ_2. It is then likely to scatter to close to Δ_2 – as we saw in section 2.5.1.2, quasiparticle scattering is more likely than recombination except close to the energy gap. Once it is close to Δ_2, it is unlikely to tunnel back into S_1 – if the junction is biased so that $eV<\Delta_1+\Delta_2$ then there are no states to tunnel in, otherwise the direct back-tunnelling current is negligible compared to the forward tunnelling current. The quasielectron may, however, tunnel back as a quasihole in S_1. This quasihole will then scatter back to close to Δ_1, where it may once again tunnel back to S_2 as a quasielectron. For each

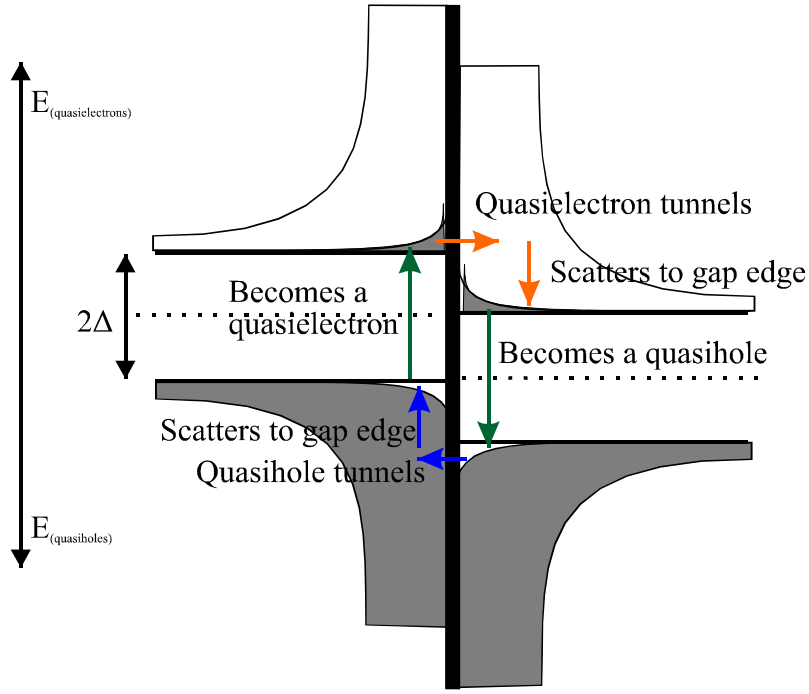

Figure 3.9 Gray Effect in a SIS device.

tunnelling event a charge of *e* is transferred from S_1 to S_2, but the charge transferred per quasiparticle created will be many times *e*.

This process will be enhanced if the quasiparticle recombination rate is low, due perhaps to a material with a long characteristic quasiparticle lifetime and also if the quasiparticles are confined close to the barrier. These conditions are both met in the case of deep Al traps in a Nb or Ta based STJ detector. The effect is to increase the responsivity of the detector to photons, which is to increase the charge collected per energy deposited. Recent measurements of Ta devices with Al traps(Verhoeve 1997) have recorded up to 190 tunnelling events per electron, which contributed to a responsivity of 16×10^4 e/eV. Without multiple tunnelling events the maximum responsivity is found from (3.1) to be 0.08×10^4 e/eV.

Unfortunately, the Gray Effect does have a drawback as a resolution improving mechanism. Like quasiparticle multiplication, multiple tunnelling is a statistical process, so that whilst it increases the signal strength it also contributes to the statistical noise. The noise has been predicted to be(Goldie 1994):

$$\Delta E = 2.355\sqrt{\varepsilon E\left(F+1+\frac{1}{\langle n\rangle}\right)} \tag{3.16}$$

where F is the Fano factor, and $\langle n \rangle$ is the mean number of tunnelling events. Using data for a typical Nb device with Al traps, Δ=1.25 meV, F=0.22 and a value of <n>=30, for a 6 keV photon we find ΔE=9.5 eV.

3.3.4 Self-Heating via Recombination Phonons

In our discussion in the previous section, we found a condition for a SIN device not to self-heat due to back tunnelling of quasiparticles, (3.15). In order to satisfy this we need either to make it unlikely for quasiparticles to back-tunnel, or to reduce the number of quasiparticles close to the tunnel barrier.

If the quasiparticles were rapidly recombining to form Cooper pairs then they would not be available to back tunnel. Unfortunately, the recombination would produce phonons with energy 2Δ, which will have a certain probability of being reabsorbed in the normal metal. The net heating effect is equivalent to the two quasiparticles having undergone back tunnelling. We need to modify (3.14) to account for this extra process:

$$\begin{aligned} P_{cooling} &= (1-\kappa)\overline{E}J_{particle} - eVJ_{charge} \\ &= \left((1-\kappa)\overline{E} - eV\right)J_{charge} - \frac{(1-\kappa)\overline{E}}{\tau_{back-tunnel}}N_S \end{aligned} \tag{3.17}$$

Our problem then, is to minimise the factor κ by reducing the fraction of tunnelled quasiparticles that recombine and whose recombination phonons are then absorbed in the normal metal.

Most reabsorbed recombination phonons will result from recombination events directly under the junction area, since the probability of re-absorption will scale with the solid angle at which there is normal metal within the phonon pair breaking length of the recombination event. We would then expect large junctions, though they are more favourable as coolers or temperature sensors, to suffer more from recombination phonon heating. This has indeed been found to be the case by P. Fisher working on SIN based cryo-coolers (Fisher 1997).

Rather than simply reducing the size of the junctions in use, one could change geometry to reduce the mean distance that a quasiparticle has to diffuse before it

leaves the junction region. This approach has been examined by the Berkley group(Drury 1997) who have found that junctions with long thin shapes showed less evidence of self-cooling than square ones of the same area.

The alternative strategy is to increase the distance quasiparticles will diffuse before recombining to allow quasiparticles to leave the junction area easily. There are two approaches to this. Increasing the quasiparticle mean free path will increase the diffusion coefficient, but is dependent on being able to control the microstructure of the superconducting film. In particular one would wish to use epitaxial films, but this is not possible for most substrates. The second approach is to increase the quasiparticle lifetime whilst retaining a reasonable energy gap to allow a higher base temperature. Generally, this is a material property, but by using a superconducting heterostructure of a material with a large energy gap and one with a longer characteristic quasiparticle lifetime, a combination of the desirable properties might be obtained. This is the motivation for the work that is reported in chapter 7.

3.3.5 Phonon Trapping

In section 2.7.2 the importance of phonon loss from a superconductor was mentioned in the context of non-equilibrium quasiparticles and phonons. In particular it was shown that the effective quasiparticles' lifetime was considerably extended if 2Δ phonons were retained in the superconducting thin film. This process has potential benefits in all devices in which a long quasiparticle lifetime is required. For Nb, which has a very short characteristic quasiparticle lifetime, it is essential for its use in STJ detectors.

For thin films, the phonon trapping is sensitive to the critical angle for total internal reflection, assuming a specular reflection of phonons at the interface with the substrate. For films where the thickness is around and slightly larger than the pair breaking length, the phonon trapping effect is governed by (2.60). For thicker films, the phonon trapping is independent of the thickness. For a given superconductor and thickness, phonon trapping is very sensitive to the acoustic mismatch between superconductor and substrate. The phonon trapping is closely related to the thermal boundary resistance , which so long as the film thickness is large enough to contain an

independent phonon system(Wellstood 1994), will be governed by Kapitza resistance(Kapitza 1941).

A direct measurement of the phonon trapping event in an Al film on a sapphire substrate(Schnagl 1997), has demonstrated an effective quasiparticle lifetime of 1.5 ms, which using (2.78), and a characteristic lifetime against recombination in Al of 438 ns, and a characteristic pair-breaking time of 242 ps, gives an estimated phonon trapping time constant of 845 ns. Using equation (2.60) and data from(Kaplan 1979), one would calculate the phonon loss time to be of order 3 ns.

Epitaxial Nb/Ta STJ detectors fabricated by the author and tested at NRL, Washington DC demonstrated that the loss of charge from the detector due to insufficient recombination phonon trapping resulted in a significant asymmetry in measured X-ray spectra. In an X-ray event at some distance from the junction, the quasiparticles created will have to diffuse some distance to the junction. The further the quasiparticles have to diffuse the more likely they are to be lost when a recombination phonon escapes the to the substrate. The result is a larger under-reading of the incident energy. When averaged over many X-ray events, it is found that for devices with a larger area of absorber not covered by the junction the X-ray spectra peaks show a large low energy shoulder(Porter 1996).

In bolometer detectors, such as SIN readout bolometers and TES-ETF detectors, that rely on the thermalisation of the energy of the incident particle, phonon trapping is essential to ensure the retention of most of the signal. For this reason these classes of detectors were fabricated on membranes in order to minimise the thermal conduction to the substrate. Phonon trapping in normal metal layers, or rather the lack of it, has been a predominant feature of our work on SIN based device (chapters 6 and 7).

CHAPTER 4

Experimental Methods

This chapter introduces and describes the range of experimental methods that have been used in carrying out the work discussed in the subsequent chapters. Broadly speaking, we follow the series of stages that are required in the production of a typical device. As a relatively wide variety of devices have been produced in pursuing this work we confine ourselves here to a description of the individual stages of device production. We leave the description of which processes have been used, and in what order, to the separate experimental chapters.

We commence with a short discussion of our choice of substrate material and the pre-deposition cleaning process that we developed. This is followed by a description of the ultra-high vacuum system used for sputtering the basic trilayers used in all our devices. The third section describes the fabrication processes that we can employ to define, isolate and connect the parts of our devices according to their design. The final section examines the device characterisation and measurement facilities that either were made available to, or have been developed by, the author.

4.1 Substrate Choice and Preparation

4.1.1 Substrate Choice

There are a number of factors that will influence one's choice of substrate material for any given experiment, for example: thermal conductivity, lattice matching to the film, acoustic matching(Kaplan 1979), robustness, cost, and availability. In this work we have almost exclusively used r-plane sapphire as our substrate material. For the majority of the work this has been due to its easy availability, our laboratory's familiarity with it as a substrate material and its robustness. Our work on epitaxial film devices (chapter 5), has introduced a further reason for this choice, as we shall see shortly. In one case in chapter 6, we have fabricated a device on a membrane, for which it is not possible to use a sapphire substrate, instead we have opted for a double sided Si_3N_4 coated Si wafer. The process of membrane fabrication is briefly described in section 6.5.2.

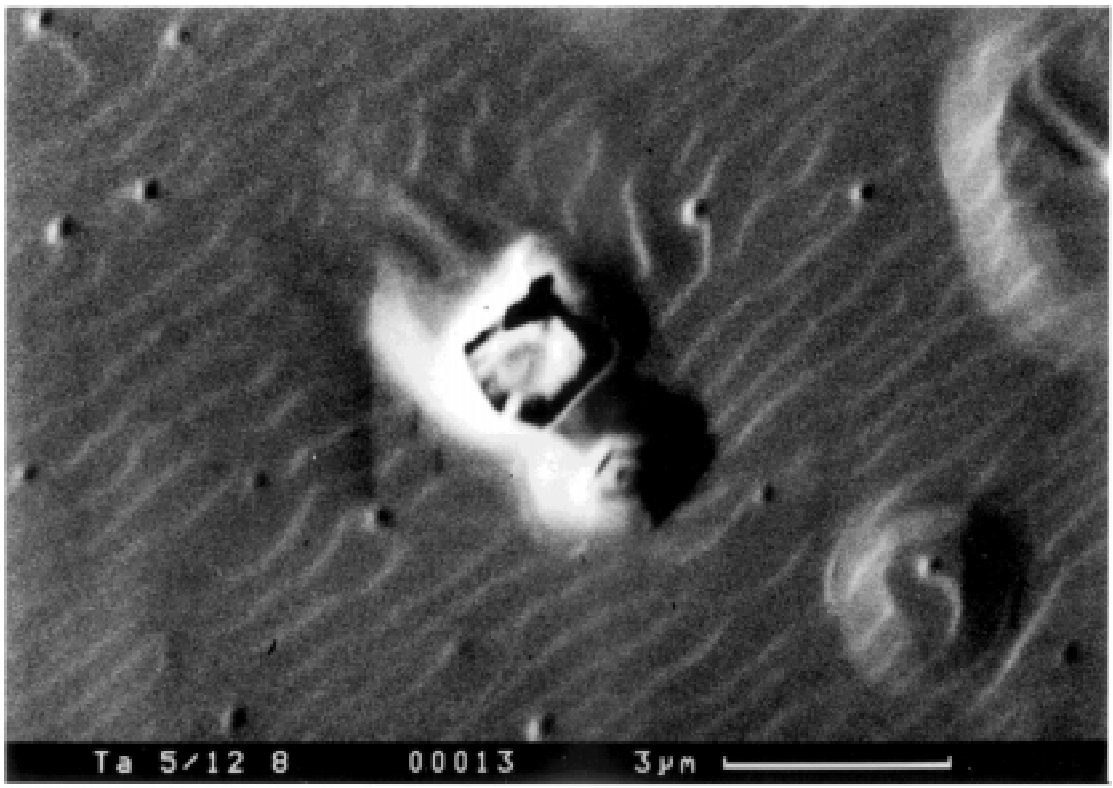

Figure 4.1 Characteristic defect on the surface of a film believed to result from insufficient substrate cleaning.

In order to achieve good epitaxial growth of the base electrode for the devices in which this was required, sapphire substrates were used, due to the excellent lattice matching with niobium(Huang 1991). In addition to this lattice matching, the substrates were heated to approximately 650°C during growth. This increases the surface diffusion of the sputtered niobium atoms which promotes growth in a single crystal lattice. During optimisation of the deposition procedure a-plane, r-plane, m-plan and c-plane substrates were used, however it was found that the optimal degree of epitaxy was achieved with r-plane substrates. Up to 15 substrates were placed on a foil heater of varying width with a constant current passed through it during the deposition. The substrates at the narrower end of the heater were thus at a higher temperature during the deposition than those at the wider. The optimum temperature was then identified by measuring the X-ray rocking curve width and residual resistance ratio (see section 4.4.1 and 4.4.2) for each substrate, and finding the relative position of the best film on the holder.

It was found that for epitaxial devices the substrate cleanliness was extremely important. The substrate-cleaning programme detailed in the next section was developed during this work to avoid persistent problems with gross defects in films, an example of which is shown in figure 4.1.

4.1.2 Substrate Preparation

The sapphire used for the substrates was obtained in 50 mm square × 0.5 mm thick wafers that were cut in-house down to ½" × ⅛" (12.5 mm × 3.5 mm) by 0.5 mm thick substrates before film deposition.

Prior to being loaded into the deposition system, the substrates were given a careful cleaning process to remove any wax and other contaminants remaining from the cutting process. The cleaning process consisted of ultrasonic baths in chloroform and weak HNO_3 (10 minutes each), gentle wiping with a cotton bud soaked in acetone and vigorous airbrushing with acetone and then isopropanol or absolute alcohol. Finally, they were dried carefully before being placed in a glass dish for transfer to the deposition system.

4.2 Film Deposition

All the devices discussed in this work were fabricated using whole-wafer techniques. The starting point in this process, therefore, is to form a complete device trilayer - i.e. a metal base electrode, an oxide barrier, and a metal counter-electrode. Here we describe the ultra-high vacuum system used to sputter the trilayers.

4.2.1 Sputtering System

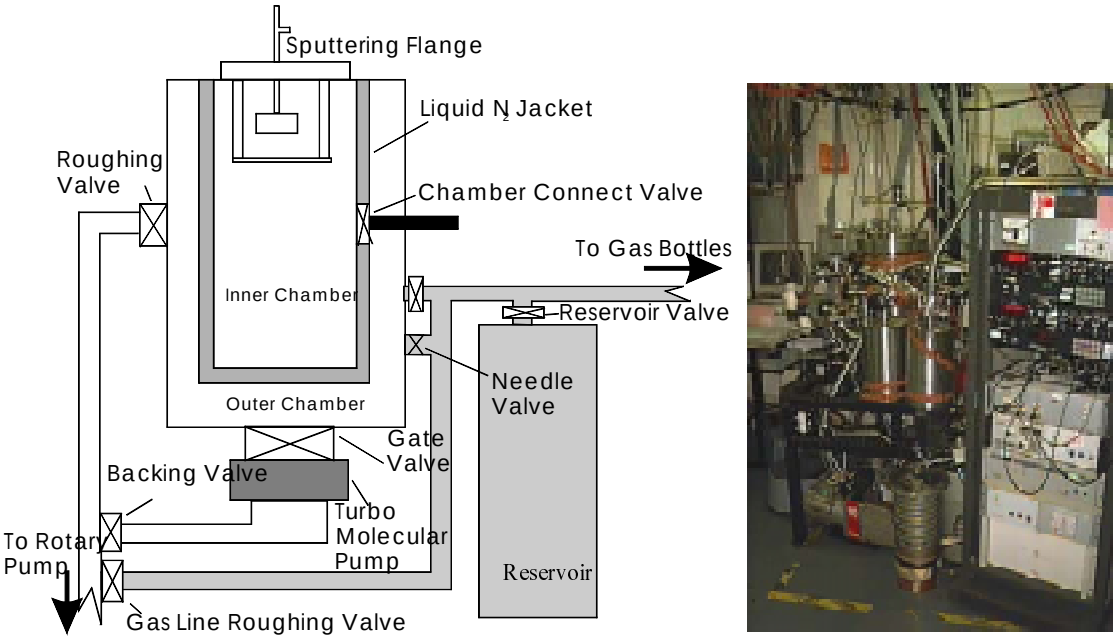

Figure 4.2 Schematic and picture (inset) of the Mk VII sputtering system. Picture courtesy of Dr. M.G. Blamire.

A schematic and picture (inset) of the sputtering system (the *Cambridge Device Materials Mark VII*) is shown in figure 4.2. The system consists of a single primary chamber with an inner secondary chamber, surrounded by a liquid N_2 jacket and pumped via a turbo-molecular pump. The system is roughed, and the turbo-molecular pump backed, by an Edwards 18 rotary pump. In order to control the admission of gas to the system during deposition, a gas reservoir and system of needle valves is attached to the main chamber. This system has been fully described in(Blamire 1988).

The magnetron and substrate stage and/or heater are all mounted on a single 200 mm flange that is then mounted on the top of the chamber. The system may therefore be used for a wide variety of materials and substrates by simply swapping one flange for another. In this work we have used two flanges which are shown schematically in figure 4.3.

The first has facilities for controlling the temperature of the substrates during deposition. The substrates are mounted on a Ta foil heater, as described above, through which a large DC current can be passed to raise the temperature to over 700°C. A cold-finger extends to one end of the substrate holder and is attached to a liquid N_2 line, through the use of which the substrates may be cooled. Three

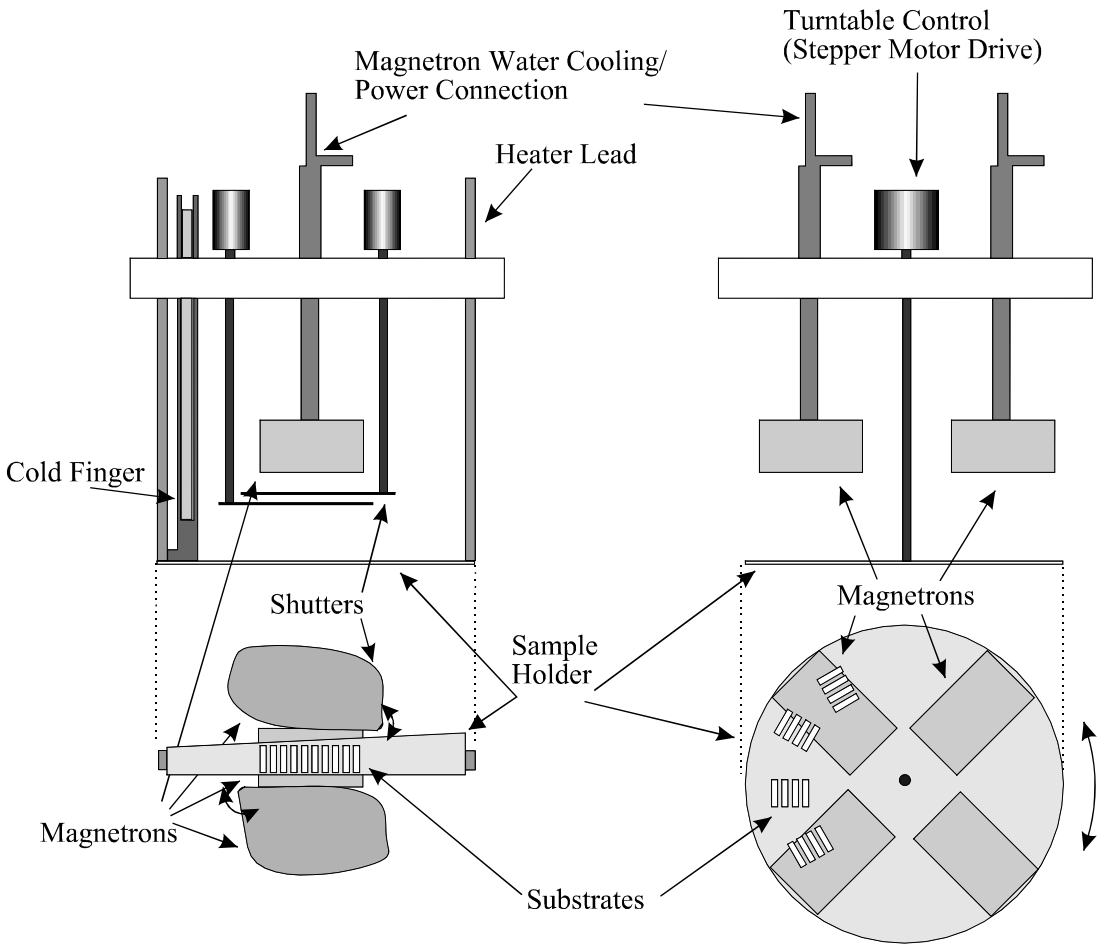

Figure 4.3 Schematics of the two flanges used in this work.

magnetrons are mounted directly above the substrate holder. Two shutters allow the substrates to be shielded from any of the magnetrons during a deposition.

The second flange used has four targets arranged about an axle on which the circular substrate holder is mounted. The holder has no facilities for heating or cooling, so this flange cannot be used for epitaxial film growth. Typically, the substrate holder is rotated during film deposition, the rate of film growth can be controlled by controlling the speed of rotation as the substrates pass under the active magnetron. A computer controlled stepper motor mounted to the axle allowed the necessary precise control of the rotation speed of the stage. Blanking of the substrates was achieved by simply rotating the stage away from the active magnetron.

4.2.2 Process

Before commencing the deposition, the system was generally allowed to pump overnight (i.e. at least 9 hours), during which it was heated to approximately 120°C for 4 hours during a bake out procedure. After this point, the base pressure of the system was of order 10^{-9} mbar. Sputtering was carried out in argon (better than 6 9s purity), at pressures between 0.5 and 2 Pa depending on the material being sputtered. For the base layer only a continuous flow of Ar was used, for other layers the system was closed off from the pumps and the pressure set by admitting a fixed amount of gas. For deposition of niobium and tungsten layers, the magnetron power supplies were computer controlled to ensure a constant sputtering power. The oxide barriers were formed by thermal oxidation, carried out at a constant pressure of 5 9s purity O_2 at ambient temperature. All the stages in the trilayer deposition were carried out without breaking vacuum, this has the advantage of forming clean interfaces between layers and minimising the chances of defects in the device.

Following deposition, the devices were taken to the Device Materials Group class 100 cleanroom for processing.

4.3 Device Processing

All the devices that we have made for this work have been fabricated using conventional optical photolithographic techniques and standard thin film processing routes. In this section we describe in detail these processes. In figure 4.4 we show how these processes can be combined to make a typical device such as those we have made.

4.3.1 Photolithography

4.3.1.1 Resist

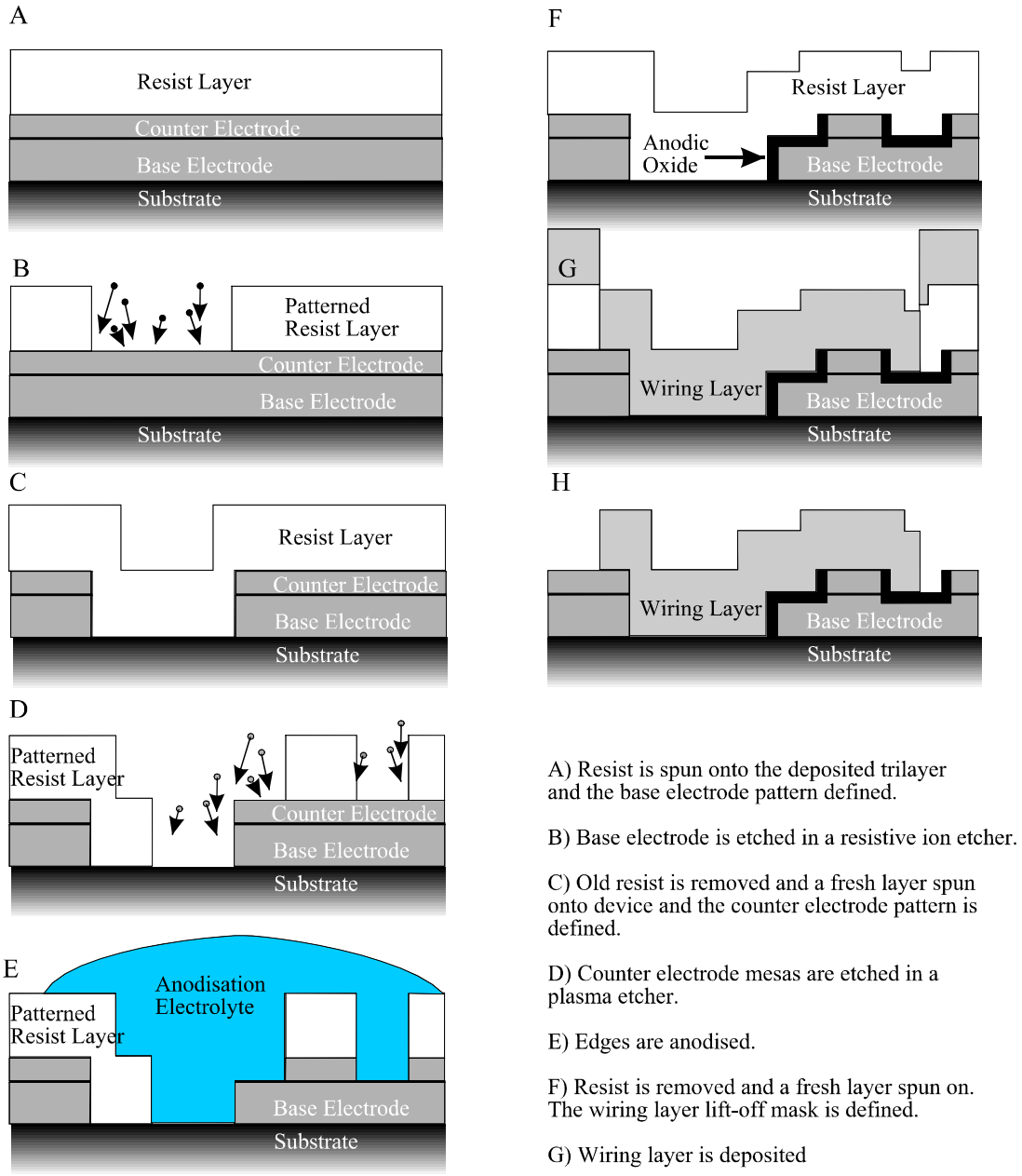

Figure 4.4 Processing steps for a typical device.

During the course of this work, two photoresists have been used, Shipley Microposit and latterly Hoechst AZ 1529. The thickness of the resist layer was determined by the speed and length at which the substrate and resist were spun. For both resists, we spun at 6000 rpm for 30 seconds. The subsequent baking procedure was different: for the Shipley Microposit we baked for 10 min at 78°C, for the AZ 1529 we baked for 1 min at 100°C.

For the resist for the wiring layer deposition stages (see 4.3.5), we used a soak in chloro-benzene (3 min for Microposit, 2 minutes for AZ 1529) followed by a post-bake (3 min for Microposit, 1 min for AZ1529). This process hardens the top layer of the resist and results in a overhang of around 1 μm at the edges of the resist. This overhang helps ensure that the lift off layer is removed successfully.

4.3.1.2 Photolithography

Most of the photolithography was performed using a Canon mask projection system, which has a resolution of approximately 2 μm. We used a standard exposure of 35 seconds, apart from the wiring layer lift-off stages where an exposure of 20 seconds was used. The exposed resist was then developed using the commercially available developers until all the exposed resist was removed from the device.

For some devices, we needed to modify the pattern produced from the mask. Either this was due to mistakes in the design of the mask, or to undertake experiments for which the mask set was not originally intended. We achieved this with combinations of multiple exposures with translations or rotations of the mask and by modifications with an optical microscope. In the latter case, we used a reflecting microscope as a simple X-Y scanning lithography system. With the microscope set for maximum magnification and the aperture stopped down to the minimum we were able to define line widths of around 15 μm.

4.3.1.3 Resist Removal

Following each process step, the resist layer was removed by placing the device in acetone in an ultrasonic bath for around 10 seconds. This was normally followed by a gentle airbrush using acetone. This process was found sufficient to remove most of the resist except in cases where the process temperature had been excessive. It was found that repeated resist layers tended to leave a residue that was not easily removed, this was a problem that particularly affected the Shipley Microposit resist.

4.3.2 Base Electrode Etch

The base electrode etch process was used whenever it was required to remove the complete trilayer from parts of the substrate. The etch was carried out in a reactive ion etching system using $SiCl_4$ and CF_4. Although etching times were dependent on the thickness of the layer to be etched, for our devices we typically used $SiCl_4$ for ten to twelve minutes at a forward RF power between 75 and 100 W, with 0-7 W reverse power. The $SiCl_4$ pressure was 36.5 Pa. This was followed by around a 2½ minute etch using CF_4 at a pressure of 39.5 Pa, forward power 75-100 W, reverse 0-5 W. The purpose of the CF_4 etch was to passivate any Cl radicals from the first stage; this was designed to help overcome a persistent problem previously found for this system(Warburton 1993a) in which niobium chloride grew in from the edge of the device and disrupted the trilayer structure. It has also been suggested that immersion in cold water immediately after the device was removed from the system helped avoid this problem. We were unable to confirm that this was always effective; we found that the maximum temperature of the device during the etch was more critical.

4.3.3 Counter-electrode/Mesa Etch

In a whole wafer route, it is often useful to remove selectively the top electrode from a region of the device. We achieved this by etching using CF_4, for which Al is an effective etch stop. Two similar systems were used for this work. One, a parallel plate etcher, although more effective, proved to be very unreliable. The second system, a plasma etcher, was therefore used for most of the devices. Prior to etching with the CF_4 plasma, a cleaning stage in O_2 (100 W forward, 15 W reverse, for one minute) was employed to remove any organic material from the region to be etched. This was then followed by the CF_4 etch (100 W forward, 10 W reverse, for between 2 and 4 minutes). The completeness of the etch could be verified easily as Al is significantly brighter when viewed under white light than the other metals used in these devices.

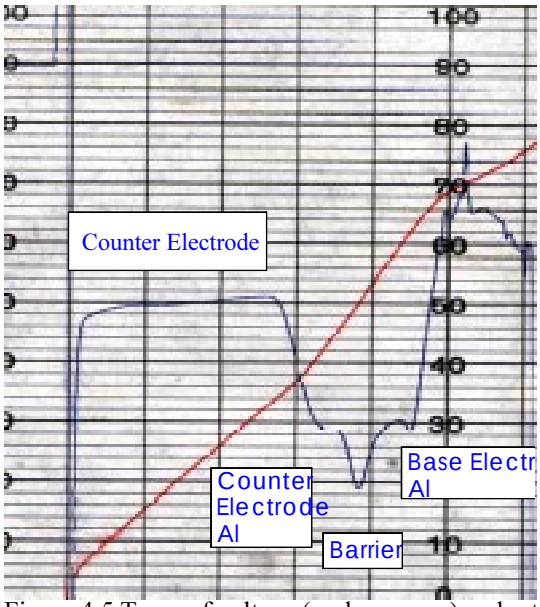

Figure 4.5 Trace of voltage (scale runs up) and rate of change of voltage (labelled, scale runs down) during anodisation. Scales are 1 $Vdiv^{-1}$ and 1 $Vs^{-1}div^{-1}$, horizontal scale 3 div min^{-1}.

4.3.4 Selective Anodisation

To provide isolation of the wiring layers from the base layers where contact was not required, we used a process of selective anodisation. Briefly, the area to be anodised was defined by a photoresist layer that covered the remainder of the device. A droplet of a buffered electrolyte solution (Kroger 1981) was placed over the window in the resist layer, and electrical contact made to the droplet and to a contact pad on the chip away from the droplet. A constant current of order 1 μA (dependent on the size of the region to be anodised) was passed. As the oxide formed, the voltage increased until a pre-set end-point was reached, whereupon the current was turned off.

During the anodisation, the voltage and rate of change of voltage were monitored. The rate of change of voltage gives information as to the material that is being anodised (see figure 4.5) and was used to verify the success of counter-electrode etches and to check the layer thickness and barrier integrity in the trilayers. In addition, anodised Nb shows distinctive colours according to the thickness of metal anodised (see figure 4.6) which gave a visible indication of the progress of the anodisation process. These techniques proved invaluable as many problems were encountered in successfully etching and anodising the material. Eventually the majority of these problems were resolved, and the cause was ascribed to out-of-date resist.

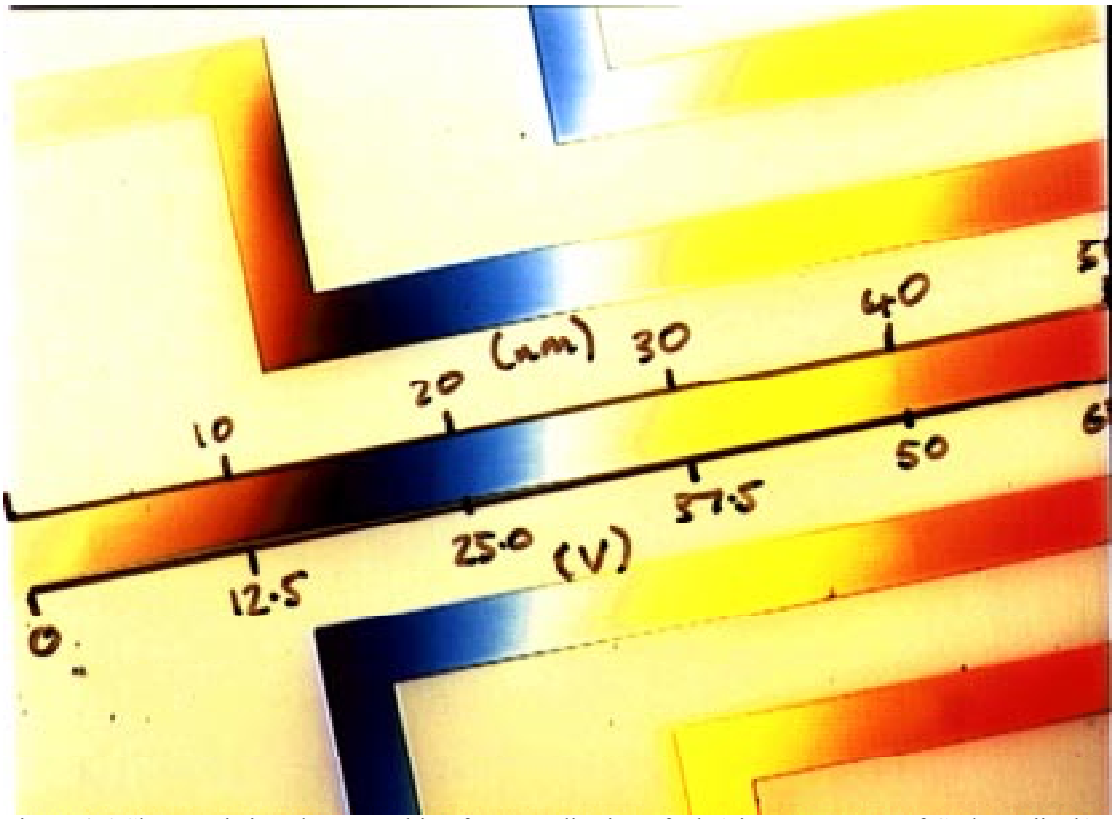

Figure 4.6 Characteristic colours resulting from anodisation of Nb (picture courtesy of G. de Muijnck). The labelled scales are estimates of the thickness of Nb oxidised and the required voltage, which were used to help verify correct anodisation.

For some of our devices, the mask design required the areas to be anodised to be temporarily connected together so that there was an electrical connection for the anodisation. In these cases, this link was removed using the same etching system and parameters as the base electrode etch (section 4.3.2).

4.3.5 Wiring Layer Deposition

The final processing step that we consider is the deposition of the wiring interconnects. Over the course of the work we have deposited a wide range of structures based around three metals: Nb, Pd and Au. The wiring layers have been deposited using a lift-off technique, whereby the film is deposited on top of a patterned resist film. After the deposition the resist is dissolved in acetone, and the film on the resist is floated off, leaving film only where the resist had been exposed and developed prior to deposition.

4.3.5.1 Nb/Pd Sputtering

The Nb and Pd layers (and latterly the Au as well) in the wiring interconnects were deposited by sputtering in a high vacuum deposition system within the Device Materials Group cleanroom. The system is fitted with a water-cooled sample holder that may be positioned for sputtering from a fixed water-cooled magnetron, from a stand-in un-cooled magnetron or positioned so that the sample can be milled by an Ar ion beam milling gun. The fixed magnetron was equipped with a Nb target; this permitted a very high Nb deposition rate that is required to produce superconducting Nb in what tends otherwise to be a relatively dirty system. The system is pumped via a conventional combination of an oil-based diffusion pump and rotary pump, and has a base pressure of approximately 5×10^{-7} mbar.

Prior to deposition, the device was subjected to a brief ion mill to remove any organic contaminants from the surface to be deposited on. The milling time, and beam voltage and current were radically different for the two resists used. Considerable time was spent re-optimising the milling conditions after the AZ1529 resist was introduced, as the AZ1529 seemed to leave much less residue from the developed area than the Microposit resist. Without milling, however, the devices experienced significant series resistance (of order of 10 Ω for a 8×8 μm junction, compared to a normal state resistance of order 1 Ω). These problems were resolved by decreasing the beam voltage (from 800 V to 500 V), the beam current (from 13.4 mA to 7.5 mA - for a beam with an diameter of about an inch) and milling time (from 13 sec. to 5 sec.).

4.3.5.2 Au Evaporation

For the devices reported in chapter 6, the gold layer in the wiring layer was deposited by evaporation, using an electron-beam, with a base pressure of approximately 2×10^{-5} mbar. Before depositing Au in the evaporator, a layer of Pd was sputtered as described above. The devices, mounted on metal holder, were then transferred from the sputtering system to the evaporator. This process required that the devices be exposed to atmosphere between layer depositions with associated risks of contamination. Furthermore, for the devices we discuss in chapter 6, we then needed to sputter a further Nb layer, which meant another change of system back to

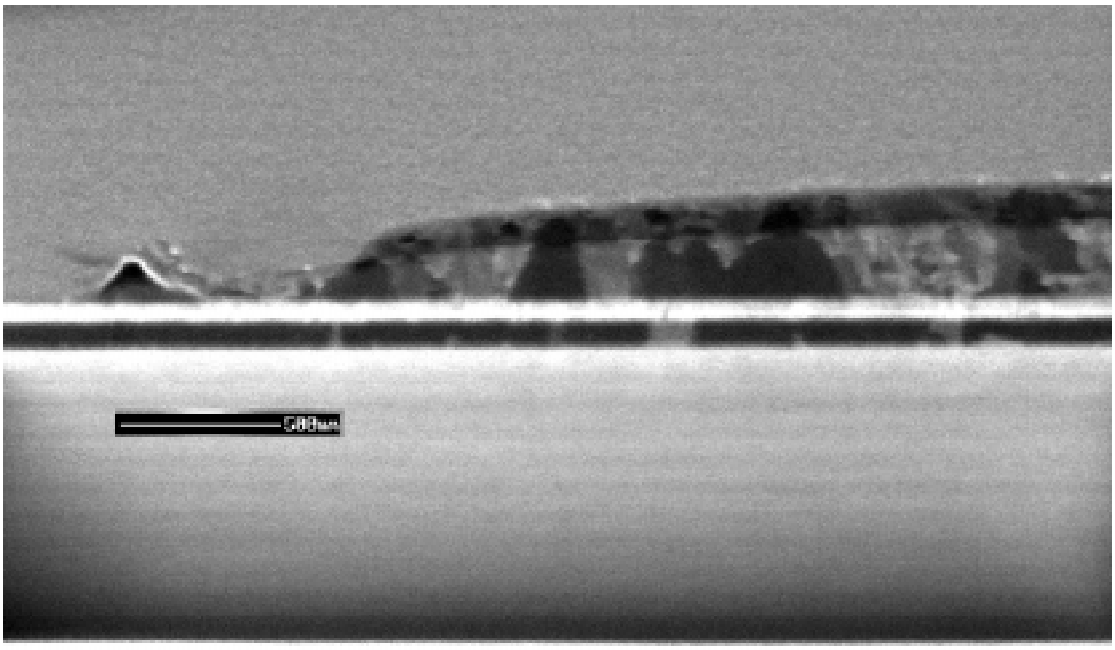

Figure 4.7 Focussed ion beam cross section of a completed device. (Picture courtesy of Dr. D. Foord)

our sputtering system. In addition to the two exposures to atmosphere between depositions, the resultant time demands on equipment were not always sustainable. To overcome this, we assembled a gold sputtering target in place of the stand-in Pd target and for later work did away with Pd cohesion layers and sputtered Au layers directly.

4.4 Device Characterisation and Measurement

In figure 4.7 we show a picture of a cross section of a completed device taken using the department's focussed ion beam system. The grain structure of the wiring layer is clearly shown, as is the grain structure in the Nb base. The anodised material shows up as a bright line due to charging effects. This technique provides a fascinating insight into device microstructure and an excellent diagnostic tool in device fabrication. Unfortunately, it was available only in the latter half of this work and so we were unable to make much use of it for diagnosing the many processing problems encountered.

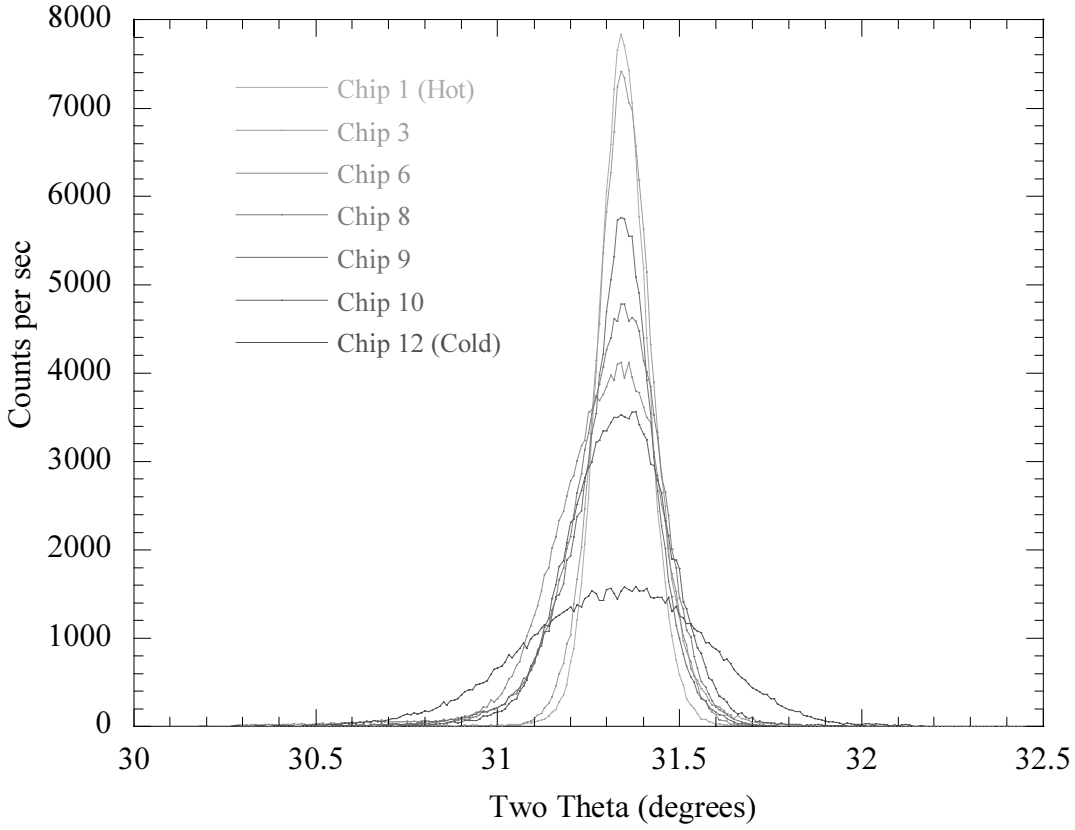

Figure 4.8 X-ray rocking curves for one run of films grown on the variable width sample holder.

4.4.1 Residual Resistance Ratio

We have discussed the use of resistance ratio measurements for determining the electron mean free path in thin films in section 2.5.1.1. We have measured the residual resistance ratio in our films using a simple pogo pin probe - i.e. where contact is made to the surface of the film via spring-loaded pins, using a constant current supply and standard digital voltmeters. For completed devices we simply used our standard measurement set-up and extracted the resistance from linear fits to the current-voltage characteristic.

4.4.2 X-ray Rocking Curve

Although the relationship between the width of peaks in an X-ray diffraction pattern of a film and the mean free path of electrons is also dependent on many other factors to do with the diffractometer set-up, it is the case that qualitative information can be obtained. While optimising our deposition process to grow epitaxial films we

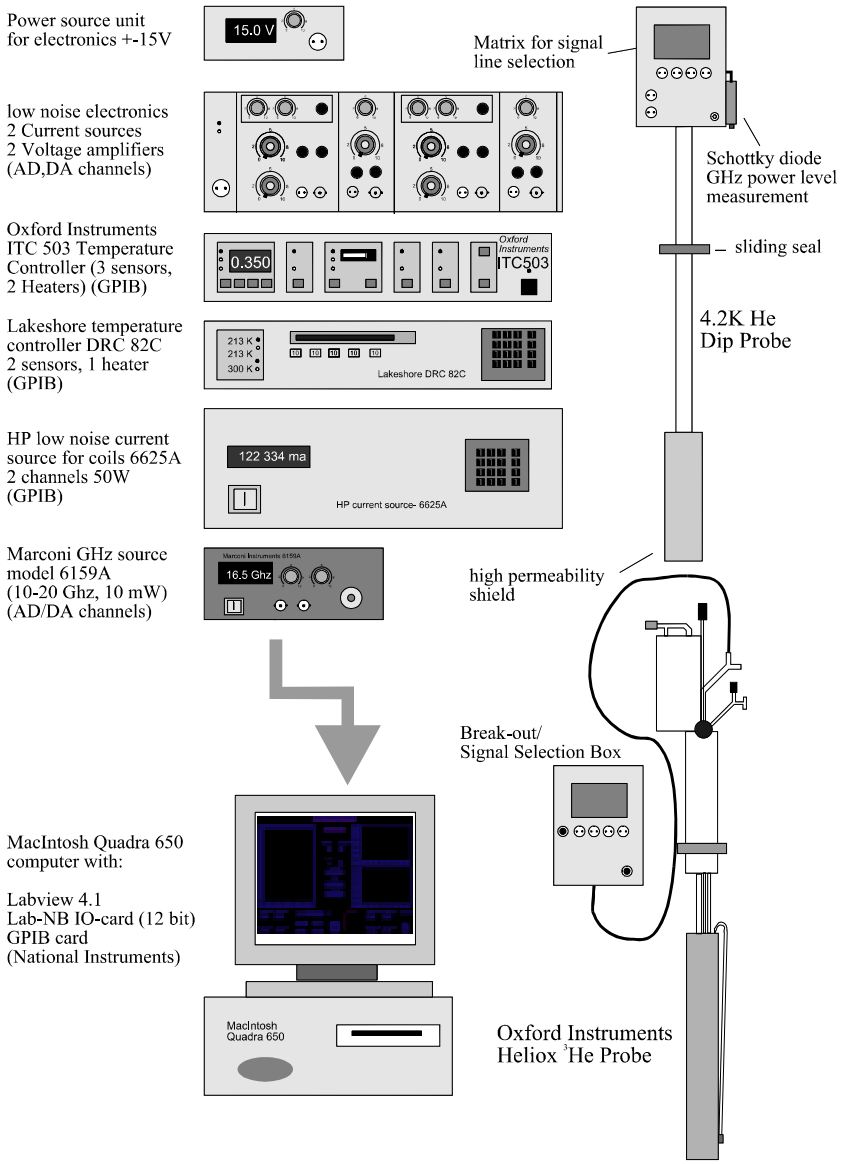

Figure 4.9 Schematic of our measurement set-up (original figure courtesy of Dr. W.E. Booij and updated by the author)

used the width of a diffracted peak (the 'rocking curve width') measured in a vertical X-ray diffractometer as an indication of the relative epitaxy within one run of films where each substrate was at a slightly different temperature. In figure 4.8 we show a plot of the rocking curve widths for samples from one particular run, showing the range of variation in width and height that we obtained.

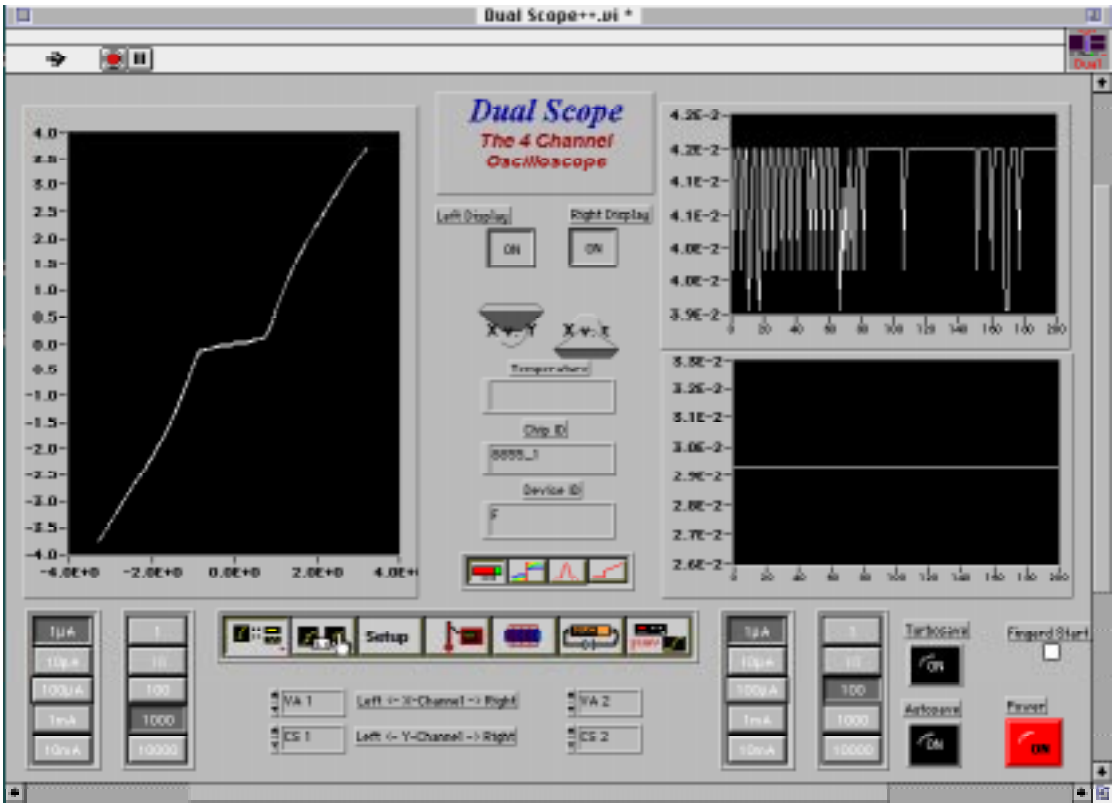

Figure 4.10 Screenshot of the LabVIEW™ measurement program in action.

4.4.3 Computer Software and Hardware

Although we have used many different cryogenic probes in this work, the room temperature electronics, data acquisition and processing set-up have been similar.

For some simple current-voltage characteristic measurements, we used separate constant current supplies and voltage amplifiers and acquired the data using a Nicolet™ 310 digitising oscilloscope. The data was then transferred via GPIB bus to an Apple Macintosh™ computer for processing using a National Instruments LabVIEW™ based program, written by the author, and saved to disc.

The bulk of the results reported in this work were obtained using an integrated dual current supply and low noise voltage amplifier set constructed by Dr. Wilfred Booij. The current monitor signal and amplified voltage response were then digitised using a National Instruments LabNB™ 12 bit digitising analogue to digital converter board and the data processed by a LabVIEW™ program written largely by the author and running on an Apple Macintosh™ Quadra 650. Our software program was

capable of recording up to four channels of data simultaneously whilst controlling a separate magnetic coil power supply, microwave power supply, or providing a controlled current to the device. Figure 4.9 shows a schematic of our measurement set-up and figure 4.10 a screen shot of the program whilst measuring one of the author's devices. The acquired data was saved to disc as a series of current-voltage characteristics and was then analysed offline using a second custom written LabVIEW™ program to extract and process the desired data.

4.4.4 4.2 K Measurements

We have used two different probes to measure devices at 4.2 K, both however being dipped into ^{4}He storage dewars. The first, constructed by Dr. Hilen Amin, was also used for our measurements at 2.2 K. This probe used two rows of eight pogo-pins to make contact to the pads on the device that was mounted on a small copper block with vacuum grease. The probe had no thermometry attached directly to it, so we relied either on the sample being at a known temperature (in the case of 4.2 K measurements), or thermometers mounted elsewhere on the system (in the case of the 2.2 K measurements). A magnetic field could be applied either by using strong hand magnets outside the storage dewar, or by the use of a small pair of coils which could be slid over the probe around the sample area. The principle advantage of this probe was that its narrow diameter permitted its use in the Oxford Instruments Lambda-Plate™ insert for measurements down to 2.2 K.

The second probe used was constructed by Dr. Wilfred Booij. The device is mounted on a small chip holder and contact is made by wirebonding. The holder is, in turn, plugged into a standard 'D' socket and up to nineteen signal lines are led to the room temperature part where they are filtered and connected to the electronics. This probe has built-in coils in two orientations (although for our devices only one orientation applies the field in the plane of the junctions), heater and thermometer. External stray magnetic fields are minimised by surrounding the sample area of the probe in a numetal shield. The probe also features a microwave wave-guide, however this was not used in this work.

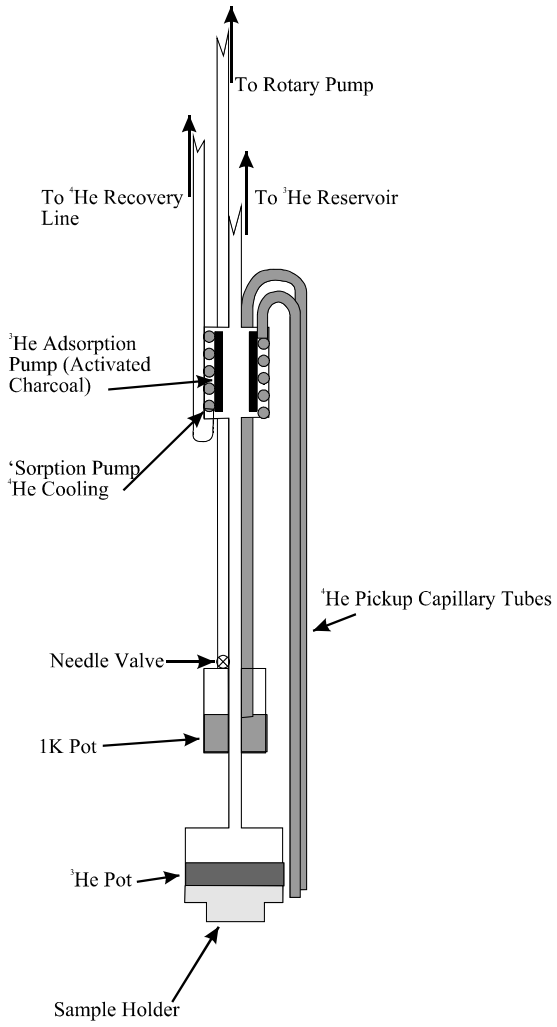

Figure 4.11 Schematic of the Heliox™ system.

4.4.5 2.2 K Measurements

For measurements at 2.2 K we used an Oxford Instruments Lambda-Plate™ insert. This is designed to fit in a standard 50 mm neck of a He storage dewar. The sample space is isolated from the main dewar space by a pre-pumped cavity. A probe containing the device to be measured is then lowered into the sample space of the insert. By pumping on a line attached to the bottom of the sample space, the He in the sample space can be cooled to the lambda point of He (2.2 K) in only a few minutes. The principle disadvantage with this system is that the sample space is relatively restricted, with an internal diameter of less than 1". This imposes quite tight constraints on the design of the sample probe, and in particular in our case precluded the use of any of our wirebonding designs.

4.4.6 0.35 K Measurements

The bulk of the measurements reported in this thesis have been carried out at a temperature of 0.3-0.35 K. This has been achieved using an Oxford Instruments Heliox™ ^{3}He system which is designed to be fit into a ^{4}He storage dewar and has a base temperature of 0.3 K. A schematic of the system is shown in figure 4.11. The first stage in its operation, following pumping the sample space, is to cool to 4.2 K in liquid He (with a pre-cool stage in liquid N_2). Once the probe is cooled, the ^{3}He sorption charcoal is heated whilst the 1 K pot is filled with ^{4}He via a capillary and needle valve whilst being pumped by a rotary pump. This results in the 1 K pot

Figure 4.12 Picture of the sample holder used in the Heliox™ system. The inset is a computer-generated detail of the sample holder without wiring and dual-in-line connectors.

temperature falling so that ^{3}He condenses and runs down to the ^{3}He pot on which the sample is mounted. The sample can now be cooled to base temperature by ceasing to heat the charcoal sorption pump, which will therefore start to pump on the ^{3}He. The base temperature is reached in as little as two hours after starting. Temperatures in the range 0.3-1.5 K are achieved by heating the charcoal sorption pump to reduce its efficacy. Above this temperature, however, there is no liquid ^{3}He left, so the sample is directly heated, with this heating being balanced by indirect cooling from the 1 K pot. With practice, the full range of temperatures between 0.3 and 10 K can be reached, although stability can be problem, with temperature swings of up to 5% over periods of minutes not being unknown.

The sample was mounted in a holder system designed by the author (see figure 4.12). The sample is mounted on circuit board and copper holder, with contact being made by wirebonding. The holder is then attached to a fixed lower stage which consists of a copper block and 0.9" dual-in-line socket. The whole assemblage is

bolted to the ^{3}He pot of the Heliox™. The thin copper signal wires are permanently soldered from the dual in line socket to the experimental wiring ports on the Heliox™. This deign of holder has now been adopted for a variety of probe designs within our group.

CHAPTER 5

Epitaxial Niobium SIS Devices

5.1 Introduction

In this chapter, we present work on double tunnel junction devices with epitaxial niobium base electrodes and polycrystalline niobium counter-electrodes. These devices, unlike the superconductor-insulator-normal metal junction based devices discussed in the chapters 6 and 7, are primarily sensitive to quasiparticle density in the common base electrode and have been used to examine the diffusion processes of quasiparticles in the Nb base electrode.

In discussing the results that we have obtained for these devices, we compare them with those from similar devices reported by Warburton(Warburton 1993a), in particular relating the differences in quasiparticle multiplication to different device fabrication routes used. By use of a simple two-dimensional random walk model we show that the lifetime of quasiparticles in our devices is comparable to that reported by other workers(Warburton 1993a; Gijsbertsen 1996b).

5.2 Device Production

5.2.1 Film Deposition

The films used to produce the devices discussed here were deposited by Dr. M.G. Blamire with the assistance of the author using the vacuum system described in chapter 4.

We have chosen to use epitaxial Nb films for these devices in order to maximise the distances over which quasiparticles are likely to travel over their lifetime. We have described the reasons for our substrate selection and the cleaning process adopted in section 4.1.2. The deposition sequence for the films used in these devices was as follows:

- 40 minutes at 40 W Nb, substrates exposed 15 sec. per minute
- 30 minutes at 20 W Nb
- 12 minutes at 40 W Nb

- 10 minutes at 12 W Al
- 1 hour oxidation at 1 kPa O_2
- 3 minutes at 12 W Al
- 12 minutes at 50 W Nb

During the initial stage, the substrates were shielded from the Nb target for 45 seconds in every minute by means of a rotating shutter that could be swung between the target and substrates. This allowed the sputtered Nb atoms to relax into single crystal lattice positions whilst maintaining a sufficient flux of Nb atoms to the substrate that the impurity level was kept low. During optimisation of the deposition for epitaxial growth, only the first three stages were carried out, the films then being characterised. The deposition rate for Nb was 0.1 $nmW^{-1}min^{-1}$, giving a base electrode thickness of approximately 150 nm. The Al layer thicknesses were around 3 nm(top) and 5 nm(bottom).

For the devices discussed here, the residual resistance ratio of the base electrode was 99±8. Taking the residual resistivity – mean-free-path product to be 460 nΩm.nm(Huang 1991) and the bulk resistivity of Nb to be 139.5 nΩm(Desai 1984□), we find mean-free paths of 323±30 nm. Given the base electrode thickness, it is clear that surface scattering was the dominant scattering process. The other measure of epitaxy used was the width of a diffracted peak in a vertical X-ray diffractometer (the 'rocking curve width'). For Nb films grown on r-plane sapphire, the peak around $2\theta=55.6°$ corresponds to the Nb {200} planes; full-width-half-maximum (FWHM) values for this peak were 0.15°, which, although a function of the diffractometer conditions, compares favourably with the 0.36° reported in previous studies(Warburton 1993a).

5.2.2 Device Fabrication

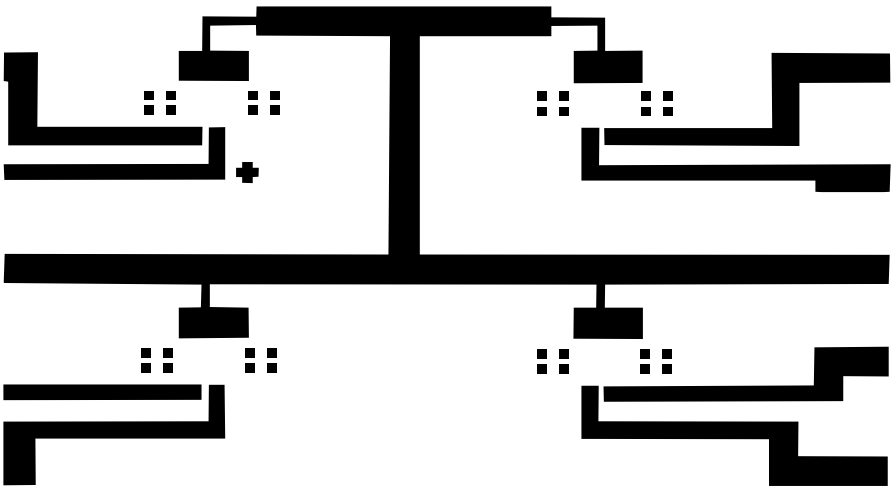

Figure 5.1 Schematic of the central region of the CAM 13 Mask set. The four rectangular pads are 32 μm×72 μm.

The general steps used in the production of all the devices produced for this work have been described in chapter 4, so we will confine ourselves here to a description of the order in which the separate stages were carried out and any specific differences. The mask set used for these devices was the CAM-13 set designed by Dr. P. Warburton (figure 5.1). Essentially it consists of four rectangular base areas (32×72 μm) which share a common connection for current return. To each base area, two contacts can be made to connect to the counter-electrode of the trilayer. Unwanted contact with the base electrode can be avoided by selective etching and anodisation of the base area. The result is a pair of junctions (8×8 μm) sharing one common electrode, which can be biased independently of each other. The mask set allows for devices with four different separations of the pairs of junctions (6, 8, 16 and 24 μm). This allows the quasiparticle density to be probed as a function of distance. The sequence of processing steps used was as follows:

- Base electrode definition and etch (see 4.3.2) using the CAM-13 mask set.,
- Resist removal,
- Counter-electrode definition and etch (see 4.3.3) using a mask designed by the author to compliment the CAM-13 mask set,
- Resist removal,
- Wiring layer definition using CAM-13 mask set.,

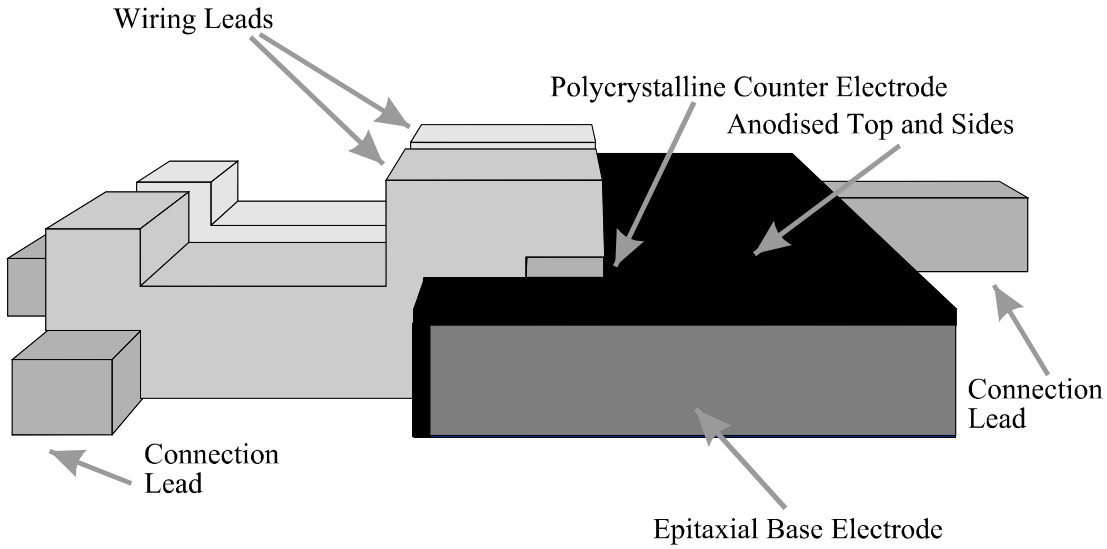

Figure 5.2 Schematic of one common base and pair of junctions on a completed CAM 13 device.

- Nb wiring layer deposition (see 4.3.5.1), at 175 W for 2×30 sec. with a 2 minute cooling period between the depositions,
- Wiring layer lift off and resist removal.

A schematic of a completed device is shown in figure 5.2.

5.3 Device Characterisation

After fabrication, the completed devices were mounted in a pogo-pin probe (see section 4.4.4) for initial testing at 4.2 K. The quality of a device was assessed from the current-voltage characteristic, an example of which is shown in figure 5.3, the quality parameter chosen being the ratio of the current at the top of the gap edge ($eV=2\Delta$) to the sub-gap current at 2 mV ($<2\Delta/e$). For our devices we found this ratio to be of order 35 to 40 at 4.2 K, rising to around 140 at 2.2 K as the thermal sub-gap current is reduced. For these devices, it was found that the sub-gap current was dominated by thermal currents down to 2.2 K. The sharp increase in current associated with the gap edge in the current-voltage characteristic occurred at around 2.5 mV, implying a proximitised Nb energy gap of $\Delta_{Nb}=1.25$ meV. At the top of the gap-edge step in the current voltage characteristic is a peak that occurs when the bound states on either side of the barrier have equal energy. For these devices this

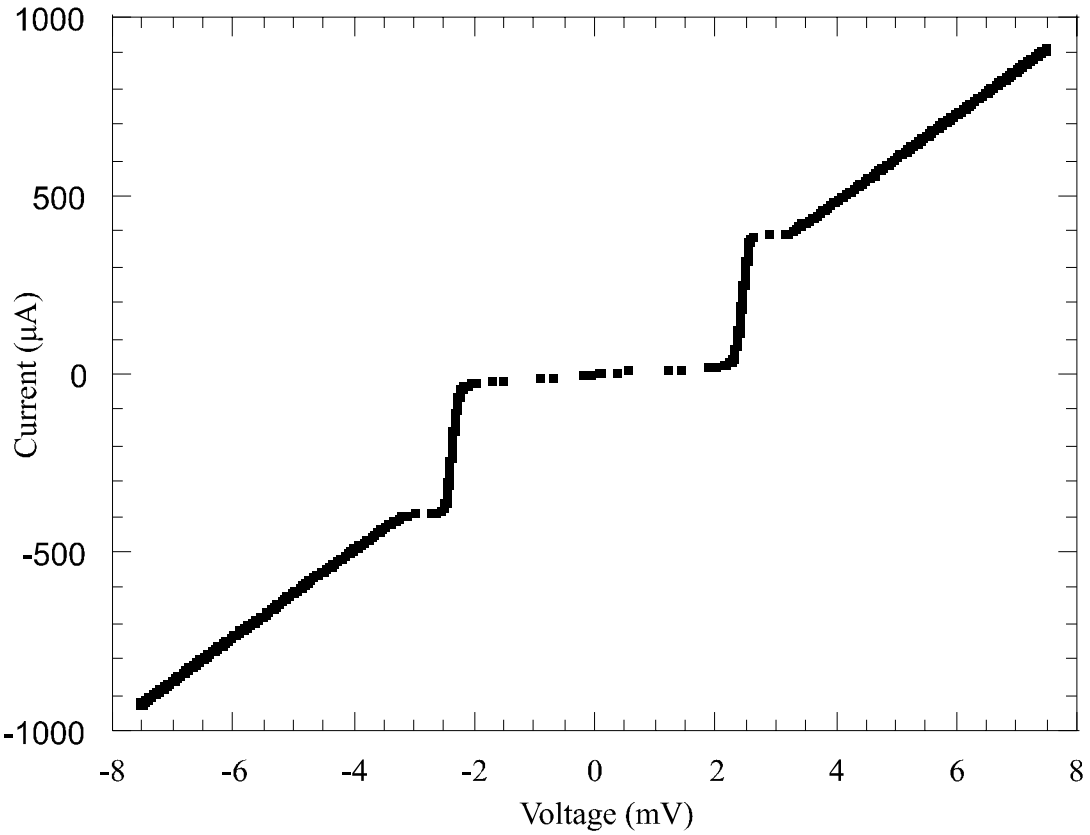

Figure 5.3 Current-voltage characteristic of a device (at 4.2 K).

occurred at 2.7 mV, which would give a bound state energy of E_0=1.35 meV, some 0.17 meV lower than the bulk energy gap of Nb (1.52 meV).

In order to measure the sub-gap current it was necessary to reduce the Josephson tunnelling current to less than the quasiparticle current by applying a small magnetic field (of order mT) parallel to the plane of the device. This was achieved by mounting a small pair of coils to the probe (see section4.4.4) and sweeping a current through them to identify the point at which the critical current was suppressed. In practice, the lowest possible coil current was used during the experiments to minimise the heat loading on the probe.

An oft-cited reason for the adoption of the Nb-Al system for device production is the excellent long-term stability of devices and the lack of thermal cycling effects(Kurakado 1993). Several of the devices reported here were re-tested over two years after they had been fabricated and were found to have undergone no significant variation in device characteristics.

5.4 Injection-Detection Experiments

5.4.1 Background

When one junction in a pair on a common electrode is biased at or above twice the gap energy, a large quasiparticle current is injected into the common base electrode. Quasiparticles thus injected may diffuse through the base electrode, undergoing a variety of scattering, recombination, regeneration and loss processes. If the quasiparticle density under the second junction is significantly altered, a change in the sub-gap current of the second device may be observed. Here we follow the approach of Warburton(Warburton 1993a) in the analysis of these experiments.

We are interested in the excess detector sub-gap current due to the excess population of quasiparticles above the thermal population. We define this as the difference between the measured current $I_{\mathrm{det}}(V,I_{\mathrm{inj}})$, and the current for zero injected current $I_{\mathrm{det}}(V,I_{\mathrm{inj}}=0)$. Thus:

$$I_x(V, I_{inj}) = I_{\mathrm{det}}(V, I_{inj}) - I_{\mathrm{det}}(V, I_{inj} = 0) \tag{5.1}$$

We can therefore find the fraction of the injected current, I_{inj}, which we measure at the detector. However, this needs to be scaled by the normal state resistance of the detector junction to compare results from different devices with slightly different normal state resistances. We take this is into account when defining a normalised detection efficiency η:

$$\eta(V, I_{inj}) = \frac{I_x(V, I_{inj})}{I_{inj}} R_N \tag{5.2}$$

This parameter is a measure of the coupling between the injector and detector junctions, however it makes no distinction between coupling processes. Warburton has examined the various possibilities of coupling between the injector and detector junctions(Warburton 1993a) and concluded that only two mechanisms gave significant coupling between the two junctions:

i) diffusion of quasiparticles, coupled to recombination phonons in the Nb, and

ii) diffusion of recombination phonons directly through the substrate.

Here, we have concentrated on process (i), and, where necessary, have removed the effect of (ii) by simple subtraction using data from (Warburton 1993a).

5.4.2 Experimental

Except where stated otherwise, all the experiments reported in this chapter have been carried out at a bath temperature of 2.2 K using an Oxford Instruments 'Lambda-Plate™' insert (see section 4.4.5). As described above, a small magnetic field was applied to suppress the Josephson current. The *I-V* characteristic of the detector junction was measured by sweeping a constant current source at approximately 2 Hz, and measuring the bias between detector counter-electrode leads and the common base electrode. The injection current was supplied by a second constant current supply which was incrementally increased, so as to bias the injector junction in the range ±20 mV (±16Δ/e). Each detector *I-V* characteristic was recorded to disc and processed off-line using a LabVIEW™ program written by the author.

To process the acquired data, the injector current was scaled to an injector voltage by using a separately recorded *I-V* characteristic of the injector junction. The detector *I-V* characteristics were each sorted into 101 equally spaced voltage bins, and averaged. The excess current I_x was then found by subtracting the detector *I-V* characteristic for zero injection current. The excess current was then divided by the injection current and multiplied by the normal state resistance of the detector junction to give the normalised detection efficiency η.

5.4.2.1 Variation of η with Detector Bias V_{det}

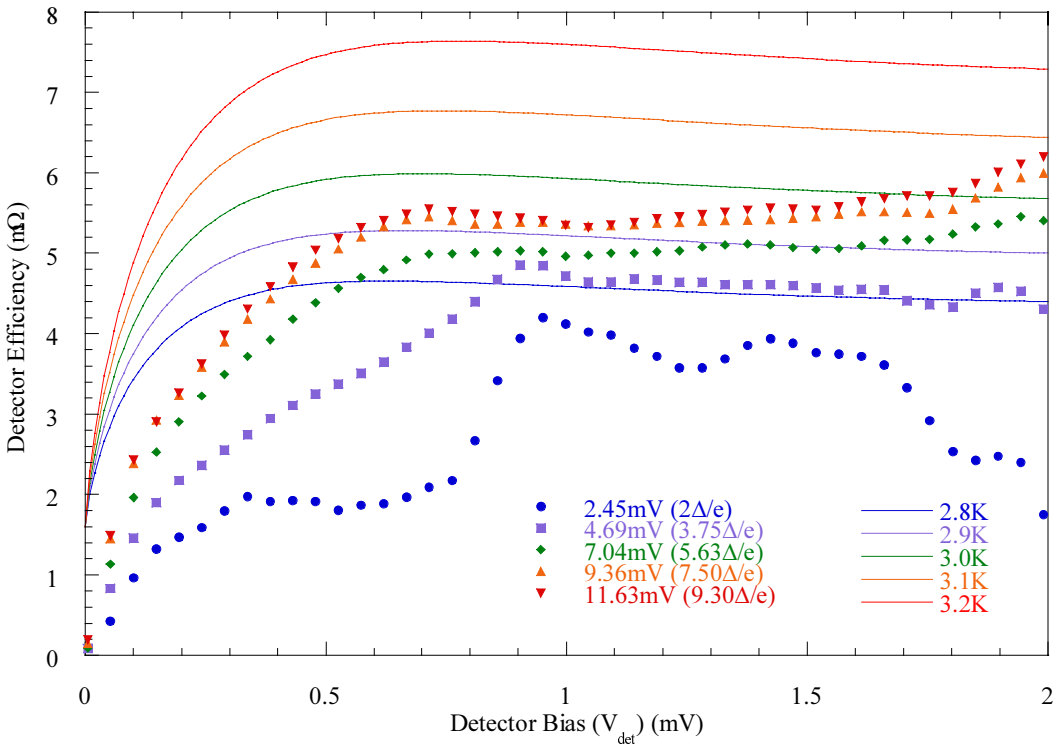

Figure 5.4 Variation of η with detector bias. Lines are a fit to (2.40)(in arbitrary units).

As our experimental procedure measures the changes across the whole sub-gap region of the detector *I-V* characteristic, it is easy to examine this to find the optimum bias point at which to measure η. Figure 5.4 shows the variation of η with detector bias for a variety of injector junction biases. Also shown is the expected thermal quasiparticle tunnel current (in arbitrary units) for temperatures between 2.8 K and 3.2 K as calculated from equation (2.40).

For injection biases of $V_{inj} \approx 2\Delta/e$, η initially increases and then reaches a plateau between 0.4 mV and 0.9 mV before increasing sharply to reach its maximum value at approximately 1 mV. The overall form of η is very dissimilar to a predicted thermal quasiparticle tunnel current, implying a athermal distribution of quasiparticles in the base electrode. As the injector bias is increased, the form of η resembles the modelled thermal data much more closely, at a bias of $V_{inj} = 3.75\Delta/e$ the low bias plateaux is lost, η rising nearly linearly until V_{det}=1 mV. For even higher biases η resembles the thermal quasiparticle data to a greater extent, even showing a slight peak at V_{det}=0.75 mV. A thermal quasiparticle tunnel current at a temperature of 3 K

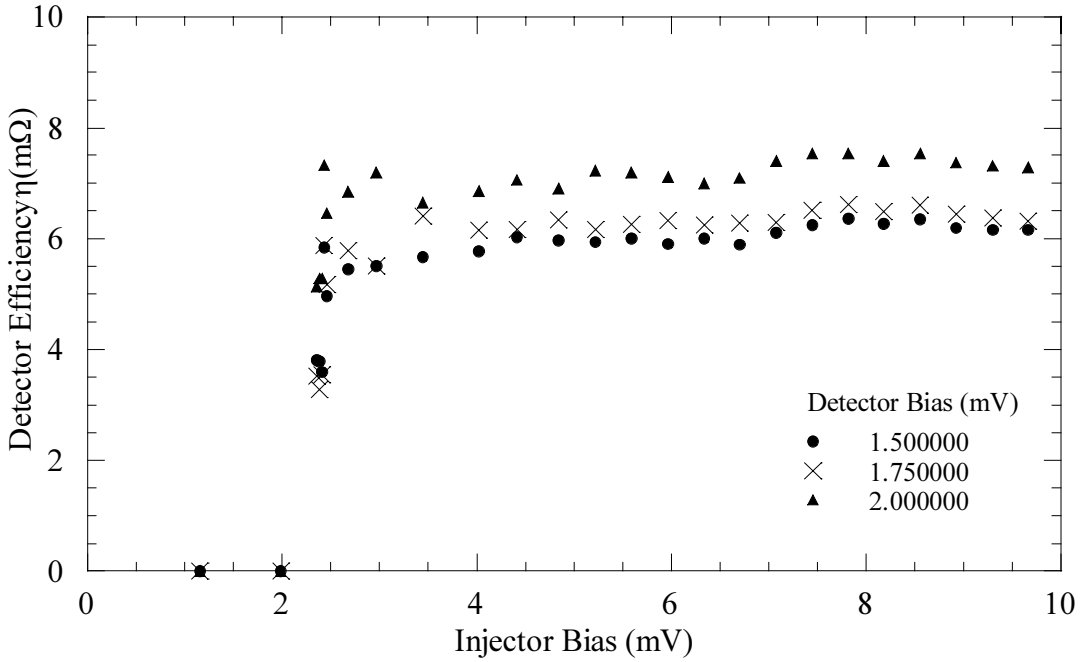

Figure 5.5 Variation of detection efficiency (η) with injector bias, for a device with 8 μm separation between injector and detector junctions.

would also show a peak at this bias, although the experimental η does not increase as rapidly as the modelled thermal quasiparticle data does in the very low detector bias range $0<V_{det}<0.7$ mV. From this we deduce that the quasiparticle distribution at the detector junction may be represented by a thermal distribution with an increased temperature T* above the bath temperature.

This result directly contradicts that reported by Warburton(Warburton 1993a) using devices with very nearly identical geometry and similar mean free paths in the base electrode. On the other hand, Gijsbertsen(Gijsbertsen 1995) reported equivalent results which were well described by a quasi-thermal distribution of quasiparticles in his one dimensional injection-detection experiments for which the mean-free path was calculated to be 6.5 nm. We shall discuss these differences in below.

5.4.2.2 Variation of η with Injector Bias V_{inj}

On the basis of the previous section, we concluded that in order to measure the maximum value of η we should measure at a detector bias $V_{det} \geq 1$ mV. Figure 5.5 shows the variation of η at $V_{det}=2$ mV as the injector bias is varied between $0 \leq V_{inj} \leq 10$ mV for a device with the injector and detector junctions separated by 8 μm.

For injector bias < 2Δ/e we observe no excess detector current – as we would expect since the only quasiparticles which are injected are the relatively few thermally excited quasiparticles. At an injector bias of $V_{inj}=2\Delta/e$ we observe a sharp increase in the detector efficiency η, again consistent with what would be expected, as a large number of quasiparticle are injected into the base electrode. As the injector bias is further increased, we see *no further increase* in η.

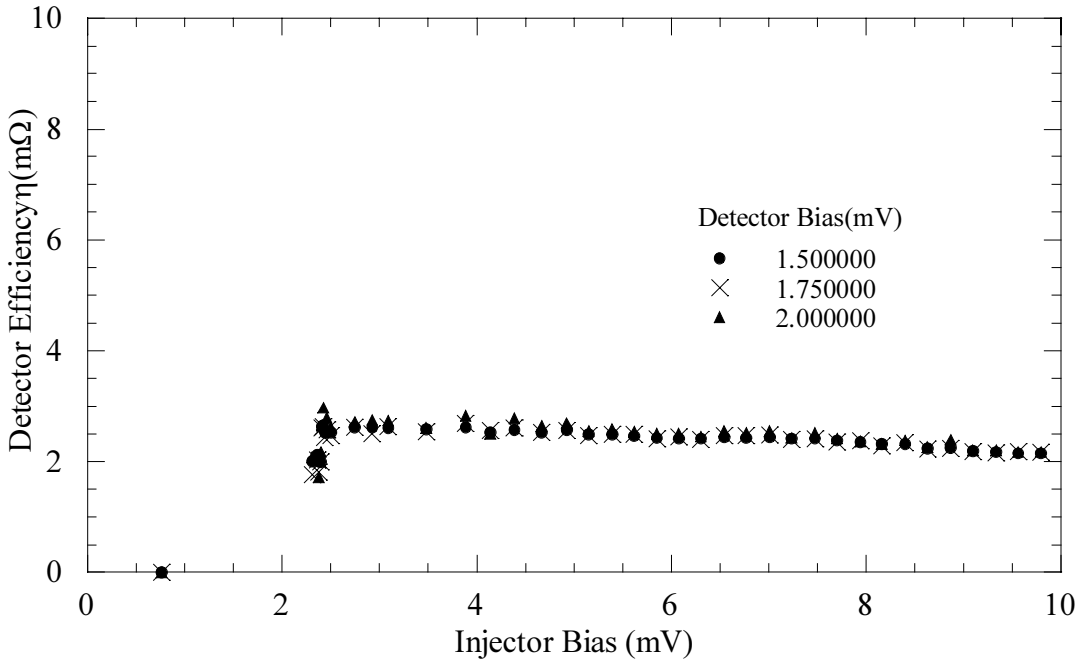

Figure 5.6 Variation of detection efficiency (η) with injector bias, for a device with 16 μm separation between injector and detector junctions.

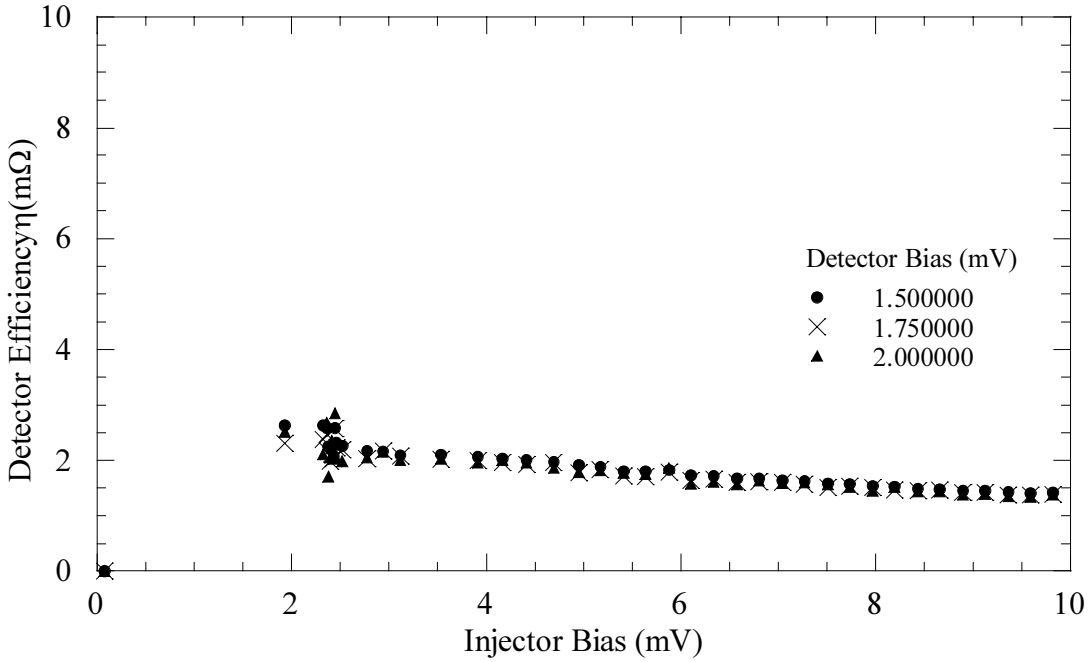

Figure 5.7 Variation of detection efficiency (η) with injector bias, for a device with 24 μm separation between injector and detector junctions.

This result is at odds with what has been reported previously, both by Warburton(Warburton 1993a) and Gijsbertsen(Gijsbertsen 1995) who reported that for injector biases above 3Δ/e the detector efficiency increased due to quasiparticle multiplication. In these devices, we see *no evidence* for quasiparticle multiplication, a result that we found to be quite surprising. Indeed when we examine devices with injector-detector separations of 16 μm (figure 5.6) and 24 μm (figure 5.7) we see a reduction in η for higher biases.

5.4.3 Analysis

In his measurements of η, and the effects of quasiparticle multiplication and trapping, Warburton(Warburton 1993a) assessed the contribution to η of phonon transmission through the substrate by measuring devices in which the direct diffusion of quasiparticles had been suppressed be etching a slot between the injector and detector. He found that in these devices η was reduced by a factor of 3.1 at V_{inj}=2Δ/e, however η did not increase with increasing injector bias, i.e. in the devices with the slot there was less quasiparticle multiplication. This, in itself, was a rather puzzling

observation since it implied that the presence of the slot was significantly modifying the quasiparticle dynamics.

Based on this, an obvious supposition would be that in our devices substrate phonons were the predominant coupling process, with a rapid quasiparticle recombination process resulting in very few quasiparticles diffusing directly between junctions. We are led to believe that this is not the case however, since if we compare η at $V_{inj} \approx 2\Delta/e$ in our results with those of Warburton and those of Gijsbertsen, we find that they are broadly consistent if one allows for the effect of different base layer thickness. To assist in understanding this we have used a random walk model as described in the next section.

5.4.4 Random Walk Model

Following the analysis of Warburton(Warburton 1993a),we have used a random walk model to estimate the quasiparticle lifetime in our Nb films. We consider the effect of releasing single quasiparticles into a two dimensional region with the same area as our base electrodes, allowing them to undergo a random walk with a step length related to the experimentally determined mean free path from residual resistance ratio measurements. We monitor the number of times a quasiparticle passes through a given elemental region after a predetermined time and use this to calculate a probability of the quasiparticle tunnelling through a junction at that region. From this, we can determine a quasiparticle detection efficiency, and then, by adjusting the simulated time of the random walk, can estimate quasiparticle lifetimes.

5.4.4.1 Description of Model

In the simulation, the effective lifetime of a quasiparticle, τ_{eff}, (which is the simulated time of the random walk) is given by:

$$\tau_{eff} = n\tau_{els} \tag{5.3}$$

where n is the number of steps the quasiparticle takes and τ_{els}^{-1} is the elastic scattering rate, which is in turn given by:

$$\tau_{els}^{-1} = \frac{v_{qp}}{l} \tag{5.4}$$

where l is the mean free path, from RRR data, and v_{qp} is the mean velocity of the quasiparticles. It has been common when considering the velocity of quasiparticles in the literature, to set it equal to the Fermi velocity, v_f(Warburton 1993a; Le Grand 1995; Schafroth 1996). Recently, however, a number of researchers (Gijsbertsen 1996a; Friedrich 1997; Ullom 1997) have pointed out that one should modify this to account for the dispersion relation for quasiparticles – this can be seen in figure 2.6, where for energies near the energy gap Δ, the kinetic energy of the quasiparticles is no longer proportional to the excitation energy. The quasiparticle velocity is thus as given in (2.50).

We assume here that the quasiparticles scatter rapidly to an energy where their probability of absorbing a thermal phonon equals the probability of emitting one. We justify this by noting that calculations based on the non-equilibrium kinetic equations of Chang and Scalapino(Chang 1977) for the case of the quasiparticle population following absorption of 5.89 keV X-rays indicate that the majority of quasiparticles have scattered to close to the energy gap within 5 ns(Schafroth 1996). If we consider a thermal equilibrium situation as considered by Kaplan(Kaplan 1976) then for Nb, the equilibrium energy would be at $E \approx 1.15\Delta$. Under these circumstances, assuming T=2.2 K, $v_{qp} \approx 0.5 v_f$. This gives τ_{els}=1.05 ps, taking v_f as 0.62×10^6 ms^{-1}(Soukoulis 1982), Δ=1.25 meV from our tunnelling measurement and the mean free path to be 326 nm, from our residual resistance ratio measurement. If we take reported quasiparticle lifetimes from the literature, of order 100 ns(Warburton 1993a; Gijsbertsen 1995; Martin 1996), then we find that each quasiparticle will have to scatter of the order of 100000 times. We therefore run our simulation for an order of magnitude longer than this, pausing periodically to record the number of times the quasiparticle has passed through each element of the base area – in effect this gives us the relative quasiparticle density in the element. We have chosen an element area of 100×100 nm, which given a base region of 72 μm×32 μm, gives a grid 720×320.

The step length in the simulation is given by:

$$L = \frac{l}{\pi} \tag{5.5}$$

where l is the three-dimensional mean free path from residual resistance ratio measurements which gives L=104 nm. This is small compared to the lateral dimensions of the device, and therefore the interactions with edges of the device are unimportant. For simplicity, we merely confine the scattering quasiparticle such that it never crosses a boundary. In the real device, the base electrode has a 6 μm wide lead connecting it to the current return opposite the injector and detector junctions down which quasiparticles could potentially escape. We have neglected this in the model, as a quasiparticle that the model recorded reaching the detector from the injector, but that actually might have been lost down the lead, would need to travel at least 64 μm, or an average of over 400000 scattering events. Having used the model to find a quasiparticle lifetime, we rechecked the validity of this assumption.

In order to calculate the probability of a quasiparticle tunnelling, we need to calculate the tunnelling time constant τ_{tun} for our device. The probability of tunnelling is then given by:

$$P = \frac{\tau_{junction-region}}{\tau_{tun}} \tag{5.6}$$

where $\tau_{junction\text{-}region}$ is the time spent by a quasiparticle directly under the detector junction. If n(r) is the number of times a quasiparticle passed through an element r, then:

$$P = \frac{\tau_{els}}{\tau_{tun}} \sum_{junction-area} n(\underline{r}) \tag{5.7}$$

The tunnelling time constant for is given by(Eisenmenger 1976):

$$\tau_{tun} = 4Z_1(0)N_0R_N Ad \frac{\sqrt{(eV + \Delta)^2 - \Delta^2}}{eV + \Delta} \tag{5.8}$$

Where $Z_1(0)N_0$ is the single spin density of states at the Fermi surface, ($Z_1(0)$ is the phonon renormalisation factor given by(Kaplan 1976) as 2.8, N_0 is the bare-band density of states which we take from (Soukoulis 1982) as 2.5×10^{47}). R_N is the normal state resistance of the device, which was 4.68 Ω, A is the junction area (64 μm^2), d the film thickness (150 nm) and V the bias (2 mV). This gives us τ_{tun}=2.98 μs.

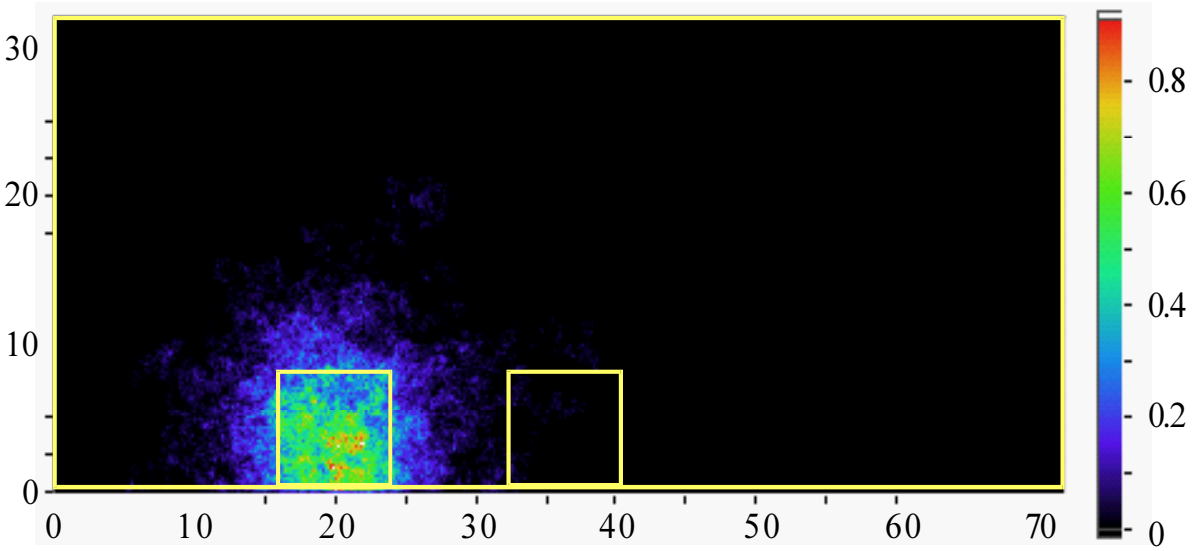

Figure 5.8 Random walk model after 5000 scatters. The X and Y scales are in µm, the z (colour) scale gives the number of quasiparticles per 100×100 nm region.

The probability of tunnelling gives us the fraction of the injected current that tunnels in the detector junction. To complete the comparison with experimental data we need to multiply this by the normal state resistance to produce a normalised detection efficiency.

5.4.4.2 Application of Model

A simulation as described in the previous section was written using

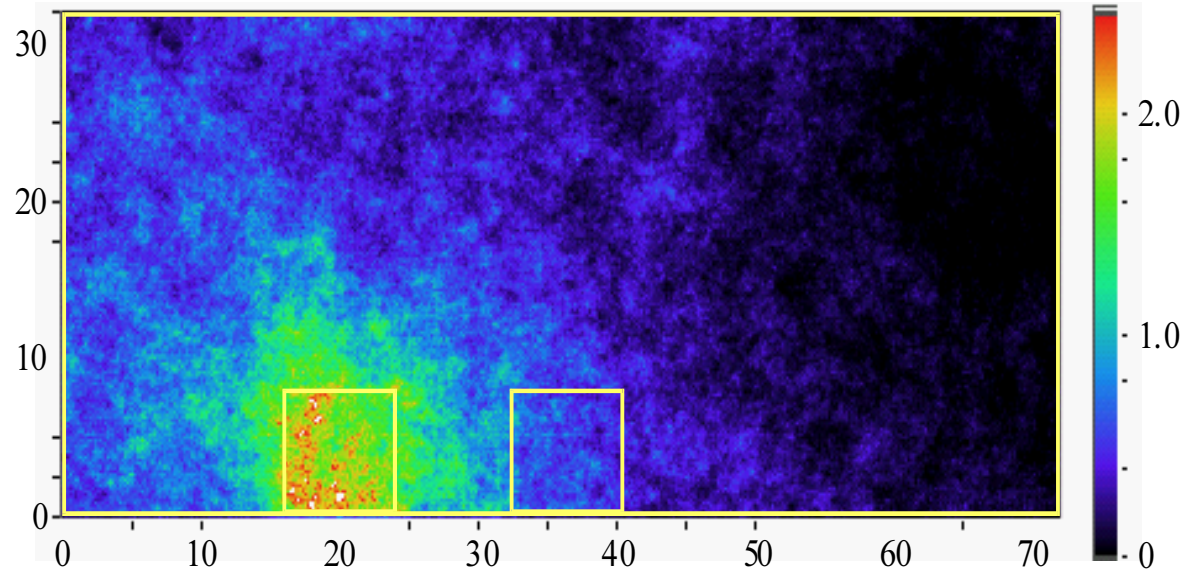

Figure 5.9 Random walk model after 100000 scatters. The X and Y scales are in µm, the z (colour) scale gives the number of quasiparticles per 100×100 nm region.

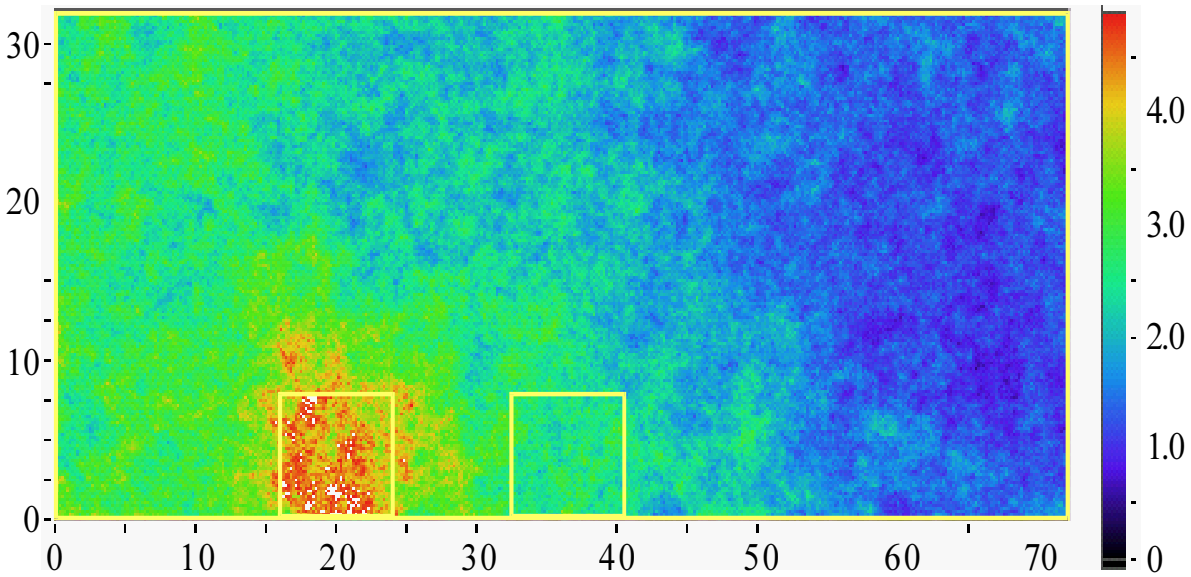

Figure 5.10 Random walk model after 500000 scatters. The X and Y scales are in µm, the z (colour) scale gives the number of quasiparticles per 100×100 nm region.

LabVIEW™. In the simulation quasiparticles were released at random positions within the injector junction region, and allowed to undergo a random walk. At each stage a new scattering direction was chosen using a uniform random number generator, the resultant vector applied to the position of the quasiparticle, and the new position checked to ensure that it lay inside the base electrode. The whole base electrode was represented by a two dimensional array of integers, each element of which corresponded to one 100×100 nm element of base electrode. The co-ordinates of the new position were used to determine which element the quasiparticle had entered and the count for that element incremented. The whole array was plotted as a false colour intensity plot and saved to disc every 5000 scatters. The process was repeated for a few hundred quasiparticles.

Figure 5.8 shows the quasiparticle density after 5000 scatters (τ_{eff}=5.2 ns). The warmest colours correspond to the highest quasiparticle density, and the coolest to the lowest. The peak quasiparticle density was 0.9 per 100×100 nm element. The outlines of the injector and detector junctions are overlaid over the plot. After 100000 scatters (τ_{eff}=104 ns) the quasiparticle density is raised over a significantly wider area, as shown in figure 5.9. Finally, after 500000 scatters (τ_{eff}=520 ns) the quasiparticles have diffused over the whole extent of the base electrode (figure 5.10).

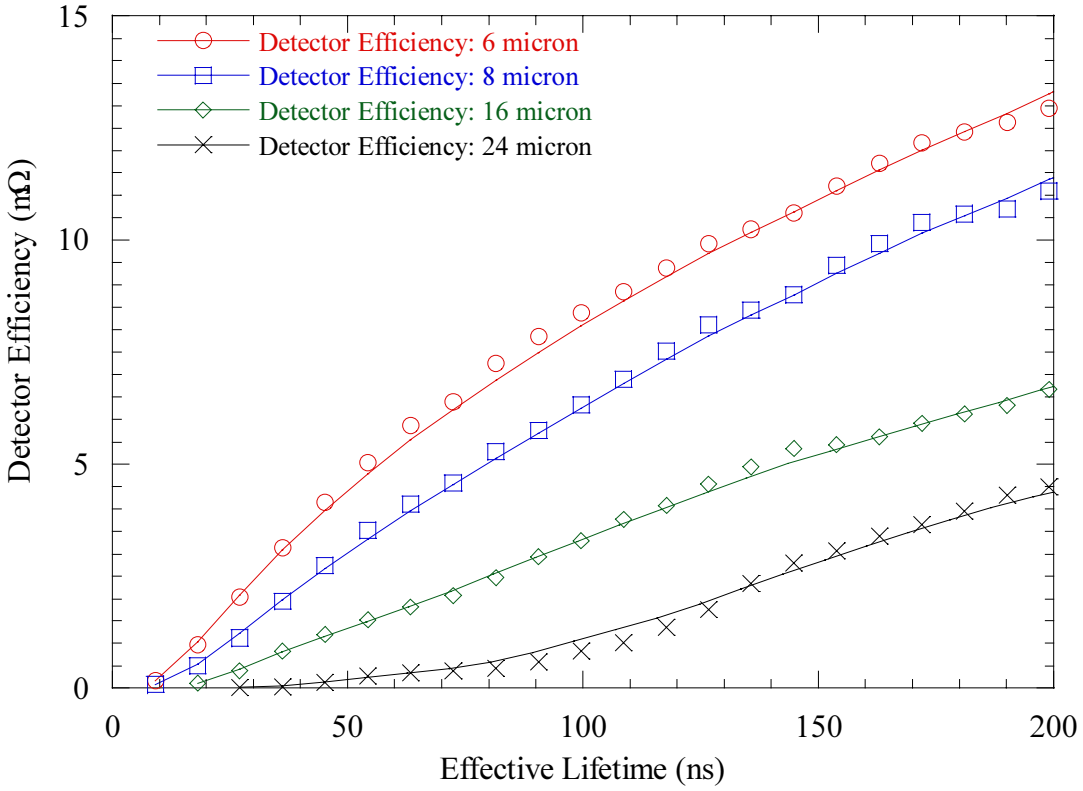

Figure 5.11 Modelled detector efficiency (η) versus modelled quasiparticle lifetime. The lines are to guides to the eye only.

5.4.4.3 *Effective Quasiparticle Lifetime*

We are now able to estimate the effective quasiparticle lifetime in our devices by comparing the measured experimental detector efficiency with that produced from our random walk simulation. It should be noted that as the simulation does not consider inelastic scattering events, it has no provision for modelling any quasiparticle multiplication processes. For this reason, the appropriate injector bias V_{inj} at which to measure the experimental value for η is in the range $2\Delta<V_{inj}<3\Delta$, in which there are no multiplication processes available.

In figure 5.11 we plot the modelled normalised detector efficiency η against the modelled effective lifetime of the quasiparticles, for an injector-detector junction spacing of 8 μm. One might expect that η would vary as the square root of the effective lifetime (number of scattering steps) from the random walk nature of the simulation. In practice this is not the case. This is partly as neither the injector, nor

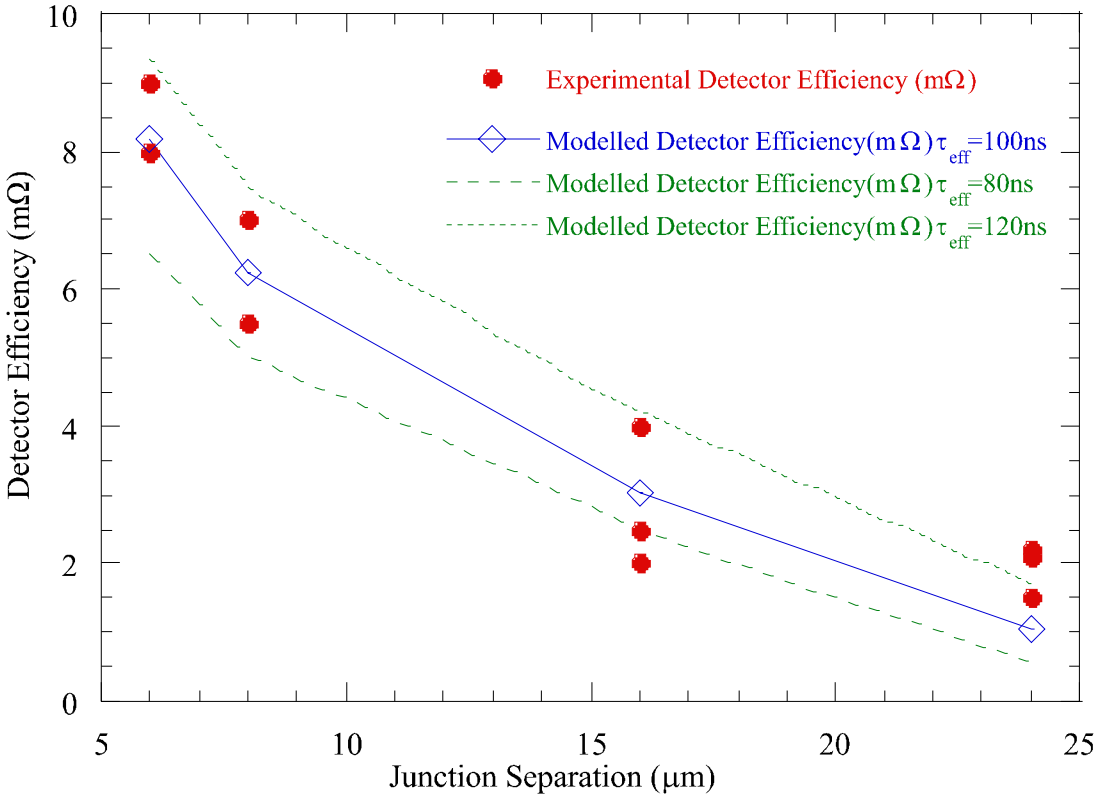

Figure 5.12 Modelled and experimental detector efficiency (η) for 6,8,16 and 24 μm separations. The lines are top guide the eye only.

detector are point sources in either the experiment or the simulation. In the simulation, this was modelled by starting each quasiparticle scatter at a random point within the injector junction, and by summing the quasiparticle density over the whole detector junction. In addition, the quasiparticles are confined to the base electrode area, and in the limit of long quasiparticle lifetimes the average quasiparticle density will be linear with the lifetime. For the longer quasiparticle lifetimes modelled we are approaching this limit, with the quasiparticle density becoming increasingly uniform – compare for example figures 5.9 (τ_{eff}=104 ns) and 5.10 (τ_{eff}=520 ns).

From figure 5.5 we see that the detector efficiency for an injector-detector junction separation of 8 μm is 6.25 mΩ±0.75 mΩ. From figure 5.11 this corresponds to an effective lifetime τ_{eff} of 99 ns(±15 ns), or approximately 100000 elastic scattering events.

We can test the validity of this estimated lifetime by finding the same effective quasiparticle lifetime using data for the other injector-detector separations (viz. 6, 16 and 24 μm). Figure 5.11 shows the simulated detector efficiency with effective

lifetime for these separations. From experimental data we have $\eta_{6\mu m}$=8.5 mΩ±0.5 mΩ, $\eta_{16\mu m}$=2.85±1 mΩ and $\eta_{24\mu m}$=2±0.3 mΩ. From figure 5.11, this gives us lifetimes $\tau_{eff(6\mu m)}$=107±7 ns, $\tau_{eff(16\mu m)}$=95±25 ns and $\tau_{eff(24\mu m)}$=130±10 ns. Figure 5.12 summarises these results by showing both experimental values η and from the model based on effective quasiparticle lifetimes of 80,100 and 120 ns for the four junction separations measured.

Up to this point we have neglected the fraction of the experimental values of η that is due to substrate phonon coupling, as a result of which the estimates of the quasiparticle lifetime τ_{eff} given above will be the upper-bound values. As discussed above, Warburton(Warburton 1993a) was able to place limits on the substrate phonon coupling for this geometry by means of post-processing a slot between the injector and detector junctions. He found that with the slot the substrate phonon coupling resulted in a value of η at V_{inj}=2Δ approximately 30% of that without the slot. This ratio was independent of the junction separation. We define the normalised quasiparticle detection efficiency ζ:

$$\xi(V_{inj}) = \eta_{no-slot}(V_{inj}) - \eta_{slot}(V_{inj}) \tag{5.9}$$

If we assume the same fraction of coupling in our devices to be substrate phonon mediated, and recalculate the quasiparticle lifetimes based on this then we find a mean τ_{eff}=80±20 ns. This assumes, however, that the rate of phonon loss to the substrate and the rate of phonon re-entry to the film are the same in these devices and those measured by Warburton. If we assume that phonons propagate uniformly and at some well defined average speed, then the rate of phonon loss to the substrate from a thin film is given by (2.60).

For a film thickness of 150 nm, we find that τ_{ϕ}≈0.5 ns (c.f. 1.5 ns for devices in (Warburton 1993a)). Thus, we would expect a higher rate of phonon loss to the substrate for these devices. Even so, this time is still around two orders of magnitude longer than the time against pair breaking, so in practice only those phonons emitted within the pair breaking length of the interface with the substrate will leave the film. Similarly, the time from phonon re-entry to the film can be found from (2.60) where d, c and ς refer to the substrate (0.5 mm thick sapphire). In this case we find that

$\tau_{\phi}^{\text{substrate}>\ \text{film}}$=3.4 μs. This is similar to the lifetime against anharmonic decay. It follows from this that phonons may well re-enter the film with the same energy as they left. In this case the mean free path of phonons in the substrate will be of order of millimetres. Substrate phonon coupling should therefore be only weakly dependent on distance, so one would expect the substrate phonons to give a constant background signal to the measured detector efficiency, independent of the distance between the injector and detector.

5.4.5 Quasiparticle Multiplication

As mentioned above, previous studies (Warburton 1993a; Gijsbertsen 1996a) have found that for injection biases $V_{\text{inj}} \geq 4\Delta$ quasiparticle multiplication occurs, whereby quasiparticles scattering to the energy gap edge release phonons with energy $\geq 2\Delta$ which may break pairs and thus generate more quasiparticles. This is reflected in the experimental data by an increase in the detection efficiency η with injector bias. In cases where the injected quasiparticle density is much greater than the thermal density, some non-equilibrium processes are found(Burnell 1994).

As can be seen for figures 5.5,5.6 and 5.7, however, there is no measured increase in η as the injector bias is increased in the devices reported here. This would imply that either the quasiparticles are not scattering from their injection energies producing phonons with energies greater than 2Δ, or that there is an injection bias related quasiparticle loss process.

5.4.5.1 Injection Bias Related Loss Processes

If we postulate the existence of an injection bias related loss process to account for the lack of observed quasiparticle multiplication in these devices then we can define its necessary characteristics. Firstly, it must scale approximately linearly with the injection bias (or current, since in the range on injection under consideration the current-voltage characteristic is linear). Secondly, it must occur close to the injector junction, since as we have seen above the variation in η with distance from the injector is well characterised by our random-walk model and is consistent with the results reported for devices which do show quasiparticle multiplication. Thirdly, any

loss process must not be a source of 2Δ phonons, or else quasiparticles could be generated outside of the trap region. Finally, the loss process must be specific to the microstructural detail of these devices relative to those of Warburton and Gijsbertsen.

The model of quasiparticle multiplication (described in section 3.3.2) used by Warburton(Warburton 1993a) and Gijsbertsen (Gijsbertsen 1995) is based on the calculations of Kaplan(Kaplan 1976) which assume a thermal distribution of quasiparticles and phonons, with a modification for one particular non-equilibrium scattering process. It is questionable to what extent a thermal distribution can be maintained. One could use the coupled kinetic equations of Chang(Chang 1977) to account for the non-equilibrium scattering and phonon emission and absorption events. However, at a simpler level we can demonstrate how far these devices are from thermal equilibrium by finding the quasiparticle density at the injector junction and calculating both the effective temperature that this would imply, and hence the degree of gap suppression.

The excess sub-gap tunnel current can be found from the quasiparticle density(Eisenmenger 1976) to be:

$$I_x = enAd\tau_{tun}^{-1} \tag{5.10}$$

where n is the quasiparticle density, d the film thickness, A the junction area and τ_{tun}^{-1} the tunnelling rate. For a tunnelling time of τ_{tun}=2.98 μs, junction area 64 μm^2, film thickness 150 nm, normal state resistance 4.68 Ω a detector efficiency η=6.25 mΩ(for an 8 μm injector-detector junction separation) and an injector bias of 5 mV, we find that I_x=1.4 μA and n=2.7×10^{24} m^{-3} at the detector. We now note that for an effective quasiparticle lifetime τ_{eff}=100 ns, our random walk model would predict that the density at the injector junction was a factor of 4.4 times greater than that at the detector junction. We would, therefore, find that the density of quasiparticles at the injector was 1.2×10^{25} m^{-3}. The number of thermally excited quasiparticles is given by(Eisenmenger 1976):

$$\begin{aligned} n_{thermal} &= 4Z_1(0)N_0\int_\Delta^\infty \left(\frac{E}{\sqrt{E^2-\Delta^2}}\right) f(E)dE \\ &= 2Z_1(0)N_0\sqrt{2\pi\Delta(T)k_BT}\,e^{-\Delta(T)/k_BT} \end{aligned} \tag{5.11}$$

Taking $Z1(0)N_0=2.8\times2.5\times10^{47}\,m^{-3}J^{-1}$(Soukoulis 1982), and assuming $\Delta(2.2\,K)=1.25$ meV, we find $n_{thermal}=3.75\times10^{23}\,m^{-3}$, or 32 times less than the density of non-equilibrium quasiparticles. We would expect, therefore, that non-equilibrium quasiparticle scattering processes will dominate in the region near to the injector.

5.4.5.1.1 Gap Suppression by Local Hot Spot Formation

An important possibility to consider would be the formation of a localised hot-spot leading to a localised depression in the energy gap. Quasiparticles which scattered to the gap edge would emit phonons with sufficient energy to cause pair-breaking, however the resultant quasiparticles would be in the region of reduced energy gap and would be trapped. Recombination of the trapped quasiparticles would result in phonons of energy $2\Delta_{trap}$, but since $\Delta_{trap}<\Delta_{base}$, they would have insufficient energy to break pairs in the rest of the base electrode.

We can calculate the effective temperature at the injector by assuming that the quasiparticles occupy states in a Boltzmann like distribution. Using (5.11) we can solve for T for a given density of quasiparticles. Therefore we can find an effective temperature T^* for the density of non-equilibrium quasiparticles(Adkins 1973). Using this we find that for $n=1.2\times10^{25}$, $T^*=4.11\,K\approx T_C/2$. Mühlschlegel(Mühlschlegel 1959) has tabulated the form of variation of the BCS energy gap as a function of reduced temperature (T/T_C), which Warburton has fitted with a polynomial approximation(Warburton 1993a). From this we find that at T=4.11 K, and assuming $T_C=9.2$ K, the energy gap will have been reduced from 1.25 meV to 1.22 meV, however this is only $0.15k_BT$ (T=2.2 K). We would therefore conclude that it is unlikely to be an effective trap of quasiparticles. This would rule out this mechanism as our quasiparticle loss mechanism.

5.4.5.1.2 Self Recombination of Quasiparticles

If the excess non-equilibrium quasiparticle density does not significantly reduce the gap, can a non-equilibrium scattering or recombination process account for the lack of multiplication?

Combining (2.54) and (5.11) we find that:

$$\tau_r^{-1} = Rn \tag{5.12}$$

where R is :

$$R = \left(\frac{2\Delta}{k_B T_C} \right)^3 \frac{1}{4 N_0 \Delta \tau_0} \tag{5.13}$$

which is a material constant and n is the density of quasiparticles. If the non-equilibrium quasiparticle distribution can be represented by an effective temperature T*, then Fermi function f(E) may be replaced with non-equilibrium distribution function, however equations (5.11) and (2.54) still hold. The recombination rate follows from the recombination time from (2.76):

$$\Gamma_r = \frac{\partial N(t)}{\partial t}\Bigg)_{I_N = 0} = N(t)\tau_{recomb}^{-1}(t) = RN^2(t) \tag{5.14}$$

In the non-equilibrium dc-injection case $n(t) \approx n_{non\text{-}equilibrium}$.

If we supposed that quasiparticle multiplication was occurring, then in the first approximation it would lead to a linear increase in η with injection bias V_{inj}. This would imply a quadratic increase in the excess current, and from (5.14), a quadratic increase in the quasiparticle density, which in turn would lead to a linear increase in the quasiparticle recombination rate with V_{inj}. If the time for quasiparticles to travel from injector to detector remained constant, this would result in a linear increase in the quasiparticle density at the detector. This would then give a constant η.

Unfortunately, this mechanism fails the test of being explicable in terms of microstructural differences between these devices and those of Gijsbertsen and Warburton. Self-recombination relies on the high quasiparticle density in the locality of the injector junction, but the mean free path in these devices is similar to those of Warburton, and far longer than those of Gijsbertsen. We would expect, therefore, that the quasiparticle density is similar or lower than devices in which quasiparticle multiplication was observed to occur.

5.4.5.2 Anomalous Quasiparticle Scattering

If the lack of quasiparticle multiplication were not due to excess quasiparticles being trapped or lost, then we would conclude that the excess quasiparticles were never created. In effect, we would require a mechanism whereby quasiparticles at energies greater than 2Δ above the energy gap could scatter to the energy gap

producing phonons with energy less than 2Δ. Furthermore, such a process would need to be faster than the 'conventional' inelastic scattering processes. Although, as outlined above, the base electrode is in a non-thermal equilibrium state, we can still derive useful information by considering the analysis of Kaplan(Kaplan 1976). We note that from equations (2.51) and (2.52) that the thermal equilibrium inelastic scattering time for a quasiparticle at energy of 3Δ (the minimum energy at which a quasiparticle could emit a pair-breaking phonon and hence cause quasiparticle multiplication) is approximately $\tau_0/15$ and that for Nb τ_0 is given by (Kaplan 1976) as 0.153 ns. Therefore, under conditions of *thermal equilibrium* we would expect the inelastic scattering event to occur within approximately $10\tau_{els}$. Any proposed scattering mechanism would seem to have to operate on a time scale faster than this.

We consider now how the devices used here differ from those of Warburton. As has been detailed above the films are broadly similar structures, the ones here being rather thinner, but having a slightly longer mean free path. The normal state resistances of the junctions are the same, as are the dimensions of the base electrode, the areas of the junctions and the separation of the junctions. The most significant difference is in the isolation of the wiring layer from the base electrode. In his devices Warburton used a self-aligned-whole-wafer process(Blamire 1989), where the junctions are formed at one edge of the base electrode, thus requiring insulation of the wiring layer and base electrode only along the vertical edge of the base electrode. In the devices made for this work a different route was followed. The counter-electrode was etched to form mesas some 8 μm from the edge, and the whole of the top surface of the base electrode was anodised to allow the wiring layer to cross it to contact the counter-electrode mesas. Thus in these devices we have a much larger area of anodic NbO_x which has been widely suggested to be a potential trapping and loss site for quasiparticles due to its variety of metallic and superconducting sub-oxides(Halbritter 1987; Matsumura 1993).

Having stated that the only significant difference between the devices here and those of Warburton lies not within the injector junction region but outside of it, we must consider how likely it is that quasiparticles could reach the anodised regions without releasing significant numbers of 2Δ phonons. For 8×8 μm junctions,

quasiparticles will have to travel, on average, a distance of approximately 4 μm before leaving the vicinity of the junction. This would represent a minimum of 12.25 elastic scattering steps, and more typically, this squared i.e. 150. For quasiparticles at energies significantly above the energy gap Δ, the quasiparticle velocity can be taken to be equal to the Fermi velocity, which results in each elastic scattering step taking approximately 0.5 ps. With this elastic scattering time, the quasiparticle would reach the edge of the junction in $0.5\tau_0$. This is, however, a factor of five slower than the thermal equilibrium inelastic scattering rate.

A full treatment of the inelastic scattering in the non-equilibrium case requires solution of the coupled kinetic equations of Chang(Chang 1977). If we were to assume a T^* model, where the quasiparticle distribution is assumed to resemble that at a temperature $T^*>T_{base}$, and recalculate the phonon scattering and recombination times, then we would find little change for the scattering time, whilst the recombination rate would be increased. This is because the scattering rate is dominated by the rate of phonon-emission, which is only weakly dependent on the quasiparticle distribution – for all reasonable quasiparticle temperatures (i.e. $T^*<<T_C$) the majority of states into which a quasiparticle would scatter will be empty. On the other hand, the recombination rate is strongly sensitive to the quasiparticle distribution, as we have seen in section 5.4.5.1.2. On this basis, we would find it difficult to explain the rather long lifetimes against quasiparticle scattering that we would require to allow quasiparticles to reach the edge of the junction. We should note, however, that all these calculations are based on thermal and thermal-like distributions of quasiparticles and phonons. Chang(Chang 1977) has shown that if there is any degree of phonon trapping (i.e. where the phonon system is not perfectly coupled to the substrate phonon system), then the resultant distributions are significantly athermal.

A further objection to our thesis that rapid scattering in or at the NbO_x results in no quasiparticle multiplication, follows from the results of Gijsbertsen(Gijsbertsen 1995), whose devices showed quasiparticle multiplication in a device with significant NbO_x present. Indeed, he studied the variation in the quasiparticle loss rate associated with differing relative fractions of anodic NbO_x surface in his devices. The first point

is answered when one considers the mean-free path in those devices, which was of the order of 10 nm. In this case a quasiparticle will need to take approximately 250000 steps in order to emerge from under his 10×10 μm junctions. This will take 4 ns at the very minimum, or $26\tau_{0(Nb)}$. In this case, even in an extreme non-equilibrium case, we would expect most quasiparticle multiplication to have occurred. The second point is more difficult to answer, apart from the observation that the experimentally determined quasiparticle lifetimes between Gijsbertsen's, Warburton's and this work are all remarkably consistent, and in devices with significantly differing amounts of anodic NbO_x present. One might speculate that the loss sites were, in fact, the grain boundaries in the anodic NbO_x rather than the oxide itself. Given the epitaxial nature of our films and the polycrystalline films of Gijsbertsen it is conceivable that our devices have less oxide grain boundary and thus our devices and Warburton's have a similar density of quasiparticle loss sites, and yet all three experimenters measure consistent quasiparticle lifetimes.

5.5 Experiments at 4.2 K

We suspect that the non-thermal equilibrium distribution of quasiparticles in our devices is responsible for the anomalously long quasiparticle lifetime that we require to explain the lack of quasiparticle multiplication. If this is the case, then repeating these experiments at a higher temperature at which we are closer to thermal equilibrium should result in the predicted behaviour and give quasiparticle multiplication.

We repeated our injection-detection experiments in a conventional ^{4}He dip probe (see section 4.4.4) for a description of this probe), measuring a device with 8 μm junction separations. In figure 5.13 we plot the detector efficiency, η, against the injector bias for this measurement. Firstly, we should observe that the detector efficiency is much smaller than for the same devices at a lower temperature. This is simply due to the fact that the recombination rate is much faster and so the quasiparticle lifetime is much lower. Using on our random walk model, we would find the quasiparticle lifetime to be approximately 5 ns or a factor 20 lower than at 2.2 K. The second point to observe is that we do obtain an increase in η with injection

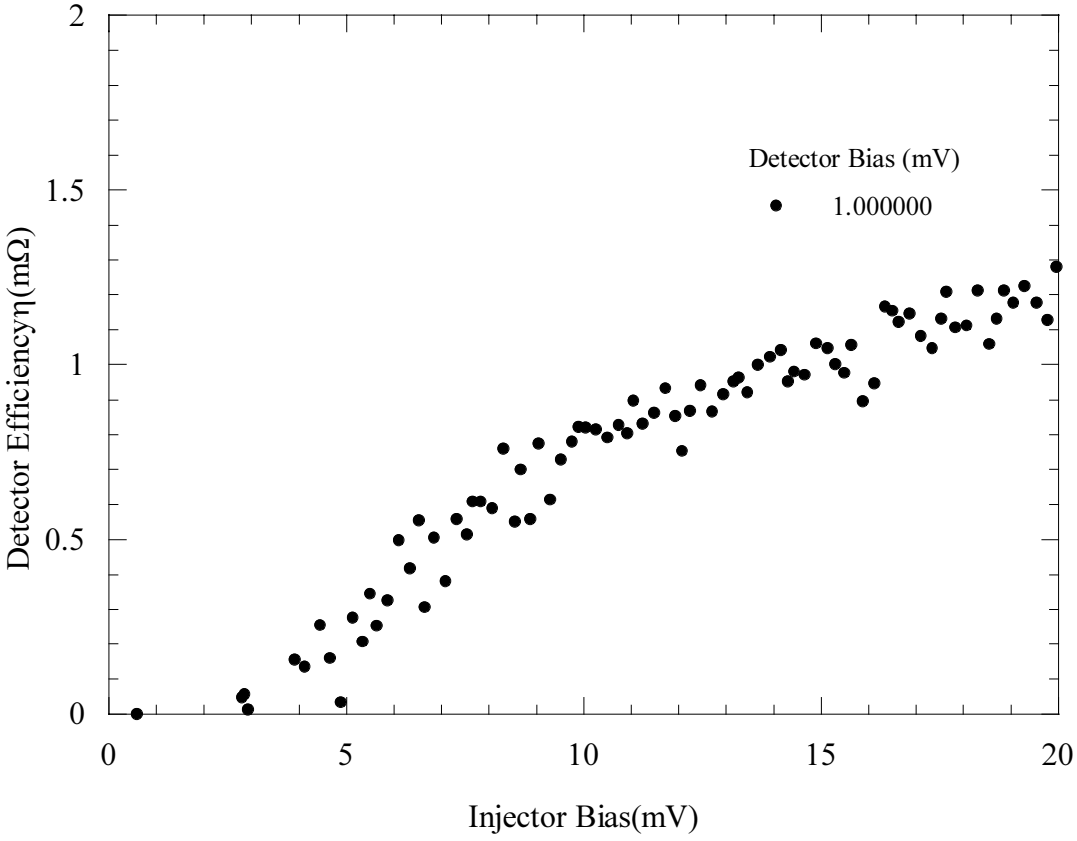

Figure 5.13 Detector efficiency (η) for an 8 μm injector-detector separation measured at 4.2 K.

junction bias. Although there is too much scatter in the data to observe the characteristic bumps in the detector efficiency that we would expect from a model of multiple quasiparticle scattering to the gap edge (see section 3.3.2 and figure 3.7), clearly there is quasiparticle multiplication occurring. We do not believe that this increase can be attributed to simple heating of the device. If anything, the cooling power available is significantly better than that in the 'Lambda-Plate™' insert as the device is well anchored to a relatively massive copper block on which the thermometers are mounted and whole assembly immersed in liquid ^{4}He.

This experiment would seem to confirm our hypothesis that the lack of multiplication is due to the non-thermal quasiparticle distribution giving a slower than expected inelastic scattering rate whilst the quasiparticles are under the junction area. Rapid inelastic scattering occurs at the interface between the Nb and anodic NbO_x producing sub-gap phonons so that quasiparticle multiplication does not occur, and a more thermal like distribution of quasiparticles is obtained at the detector.

5.6 Summary and Conclusions

In this chapter, we have measured the transport of quasiparticles over distances between 6 μm and 24 μm in our epitaxial Nb films. Using a simple random walk model, we have deduced the effective lifetime of the quasiparticles to be 100 ns±20 ns. This lifetime agrees well with those measured by Warburton and Gijsbertsen, both of whose experiments have much in common with these measurements. Unlike Warburton, we find that the distribution of quasiparticles in energy is well described by a thermal-like model with an effective temperature T^* greater than the bath temperature.

We have not been able to observe quasiparticle multiplication in our devices at our lower measurement temperature of 2.2 K, but have been able to observe it when measuring at 4.2 K. This is qualitatively different from the results of other injection-detection experiments. We have attributed this to a rapid quasiparticle inelastic scattering process related to the presence of anodic NbO_x in our devices. We believe that the long mean free path and extreme non-thermal-equilibrium in our devices results in quasiparticles leaving the injection junction area in our devices without having undergone significant inelastic scattering. Most of the inelastic scattering, therefore, occurs in close proximity to the anodic oxide regions. By increasing the base temperature of the device, we regain a quasiparticle population more nearly in thermal equilibrium, resulting in inelastic scattering occurring before the quasiparticles have left the injector junction region. Although the quasiparticle lifetime is reduced significantly, since the inelastic scattering occurs away from the anodic oxide, quasiparticle multiplication is possible.

CHAPTER 6

Normal Metal Base SIN Devices

6.1 Introduction

In this chapter, we shall present results from work on superconductor-insulator-normal metal junction based devices that have multiple junctions with a common normal metal electrode. This work has been carried out as part of a programme developing SIN tunnel junction readout based bolometers for astrophysical applications. In particular we have focussed on the response of the device to heating from current injection at various distances to simulate heating from X-ray photon absorption events.

We discuss the observed geometrical dependencies and non-linear response of the device in terms of the non-equilibrium phonon distribution and propagation within the devices.

The work presented here has been carried out with invaluable assistance of Dr. Ikuo Kanno, visiting from the Department of Nuclear Engineering at Kyoto University, Japan.

6.2 Device Production

6.2.1 Thin Film Deposition

The films used to manufacture the devices discussed here were deposited by Dr. M.G. Blamire, with the assistance of the author and Dr. Kanno, using the ultra-high vacuum system described previously in chapter 4.

Unlike the devices presented in the previous chapter, the superconducting films presented here were polycrystalline rather than epitaxial. This is for two reasons:

i) It was intended eventually to produce devices on membranes, for which the most common substrate is Si_3N_4. This substrate is amorphous, and so it is not possible to grow an epitaxial film.

ii) Irrespective of the substrate material, the electrode of interest is the N metal electrode, so quasiparticle mean free path in the superconductor leads was neglected for reasons of ease of film deposition. For realistic detector configurations it has been found that the re-heating of the junctions by quasiparticle recombination in the superconductor is important(Jochum 1998); this will be discussed in the next chapter.

For most of the devices reported here, the substrate used was r-plane sapphire, which was chosen purely on grounds that it was the substrate that was most familiar to the author and co-workers and easier to obtain than Si_3N_4 coated Si wafers. After cleaning using the process detailed in section 4.1.2, the substrates were loaded on a flange with a rotating stage (see section 4.2.1) for the deposition.

The typical sequence of depositions used to produce the trilayers for these devices was as follows:

- 2 minutes at 60 W Nb, pressure 0.7 Pa
- 13 minutes at 60 W Nb, pressure 1.2 Pa
- 6 minutes at 10 W Al, pressure 0.7 Pa
- 1 hour oxidation at 1 kPa pure O_2.
- 5 minutes at 10 W Al, pressure 0.7 Pa
- 1 minute at 50 W Nb, pressure 1.2 Pa

For most deposition stages the substrate stage was rotated at 1 rpm. For the final stage the rotational speed was increased to 2 rpm to ensure even coverage during the short deposition. The deposition rate of 0.1 $nmW^{-1}min^{-1}$ gave a lower Nb thickness of 90 nm. The Al layer thicknesses were approximately 3 nm, with a barrier thickness of order of 1 nm. The top Nb layer (thickness approximately 5 nm) was deposited to prevent extra oxidation of the upper Al layer during fabrication.

6.2.2 Device Fabrication

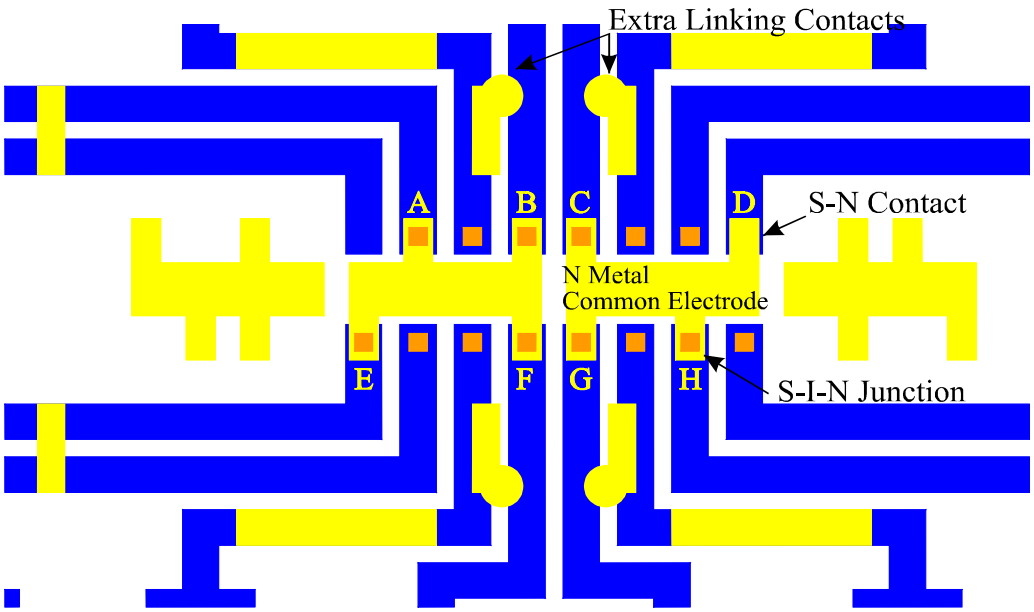

Figure 6.1 Schematic of the CAM 20 mask. For clarity the anodised region around the junctions is not shown; instead the junction positions have been shown and labelled A-H. The junction sizes are 10×10 μm.

We have described in detail the general steps used in the fabrication of the devices in chapter 4, so here we will only list the order in which the various stages were carried out. The mask set used for these devices (known as the CAM 20 mask) was designed by Dr. Kanno with the assistance of the author (figure 6.1). It consists of a base layer definition stage which brings sixteen tracks of width 20 μm into the central region as two rows of eight. A junction definition stage allows the creation of either 16 square junctions in four different sizes (16×16, 10×10, 8×8 and 6×6 μm in groups of four, or 14 square junctions of size 10×10 μm with two of the sixteen tracks without any junctions at all (illustrated in figure 6.1). The common N metal electrode was formed by depositing a wiring layer using a lift off process. Only half the available junctions were connected to the common electrode to ensure that there were two leads to each junction for four terminal measurements. There were a number of variations of the wiring layer mask available. The options were: one common electrode that would connect to eight of the junctions; or two common electrodes each connected to four junctions; or (not used) three common electrodes attached to three junctions each. Due to an error in the mask design, the two common electrode variant could not be used as originally intended. In an attempt to provide maximum redundancy of leads both electrodes were coupled in such a way as to provide an

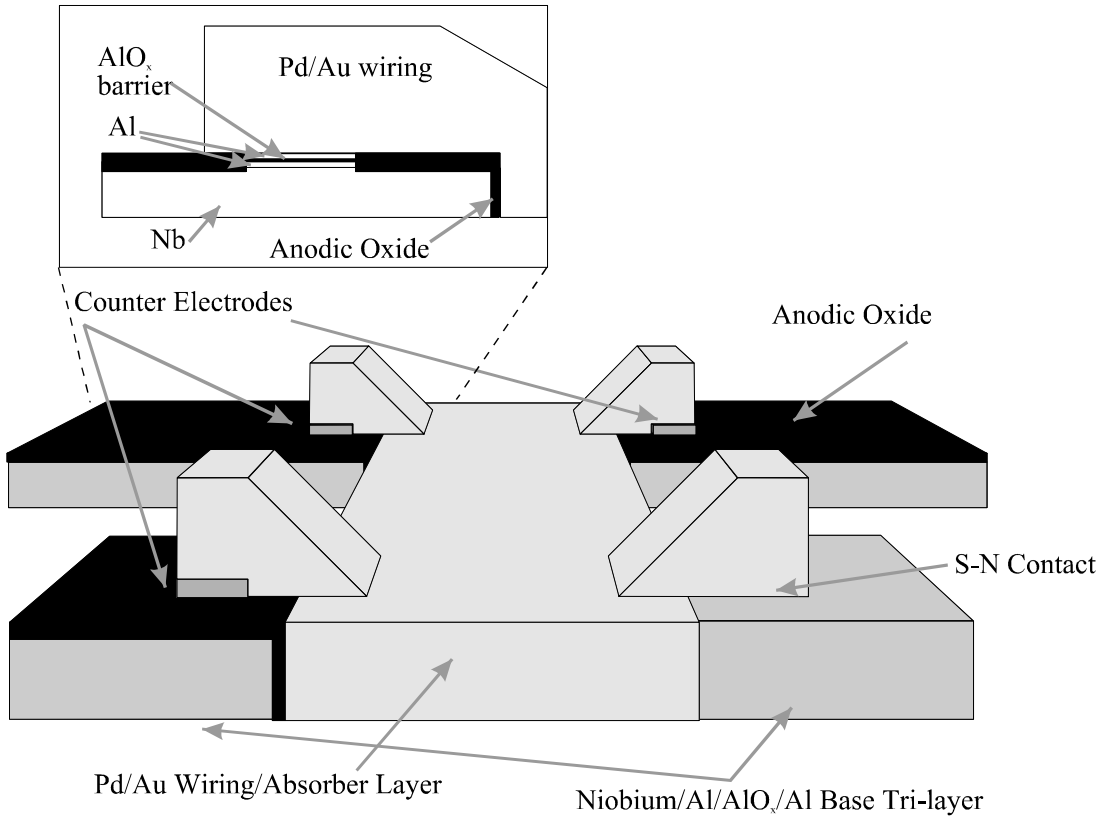

Figure 6.2 Schematic of completed CAM 20 device

indeterminate current path. This restriction was solved by performing a double exposure of the mask, with a 180° rotation between them. For this reason figure 6.1 shows 4 common electrodes, two of which lie outside the central region with the 16 base leads.

The sequence of processing steps was then as follows:

- Base electrode definition and etch (see 4.3.2),
- Resist removal,
- Counter-electrode definition and anodisation (see 4.3.4),
- Resist removal,
- Anodisation ring removal definition and etch (see 4.3.4),
- Resist removal,
- Wiring layer definition,

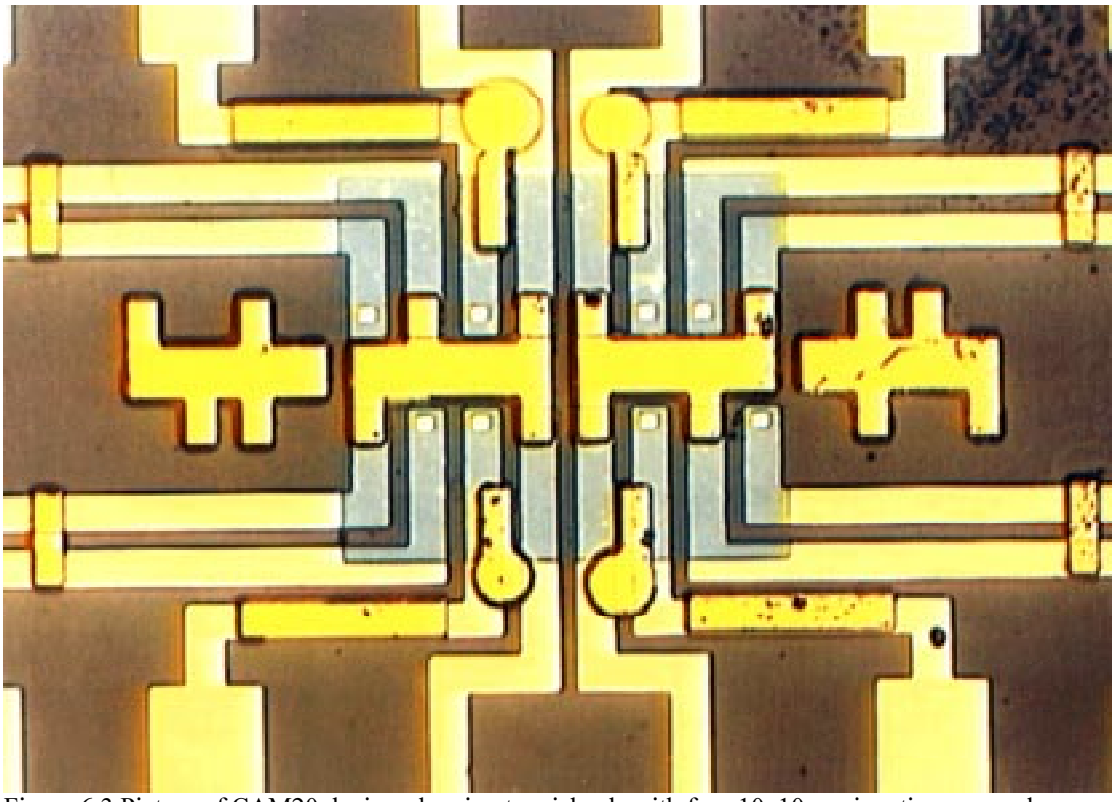

Figure 6.3 Picture of CAM20 device, showing two islands with four 10x10 μm junctions on each.

- Pd/Au wiring layer deposition (see 4.3.5), 5 minutes at 12 W Pd followed for most devices by transfer to an evaporator for 1 min Au deposition,
- Wiring layer lift off and resist removal.

A schematic and picture of a completed device is shown in figure 6.2 and figure 6.3.

6.2.3 Device Characterisation

Initial device characterisation was carried out at 4.2 K using a pogo pin probe(section 4.4.4). The current-voltage characteristics were recorded and used to assess the device quality. An example of one such characteristic is shown in figure 6.4 . Suitable devices had currents in the sub-gap region (i.e. bias < Δ) that were nearly entirely due to thermal excitations in the N electrode, and typically had a current near the gap edge of tens of μA for a 10×10 μm junction. The appropriate quality factor for an SIN based device is the ratio of the differential resistance at zero bias with that at high bias (the so-called normal state resistance). This is a strong function of temperature, and for our devices at 4.2 K was generally around 4 or 5 which is approximately in line with that predicted from (2.38). Quality factors of order 10^3 (at

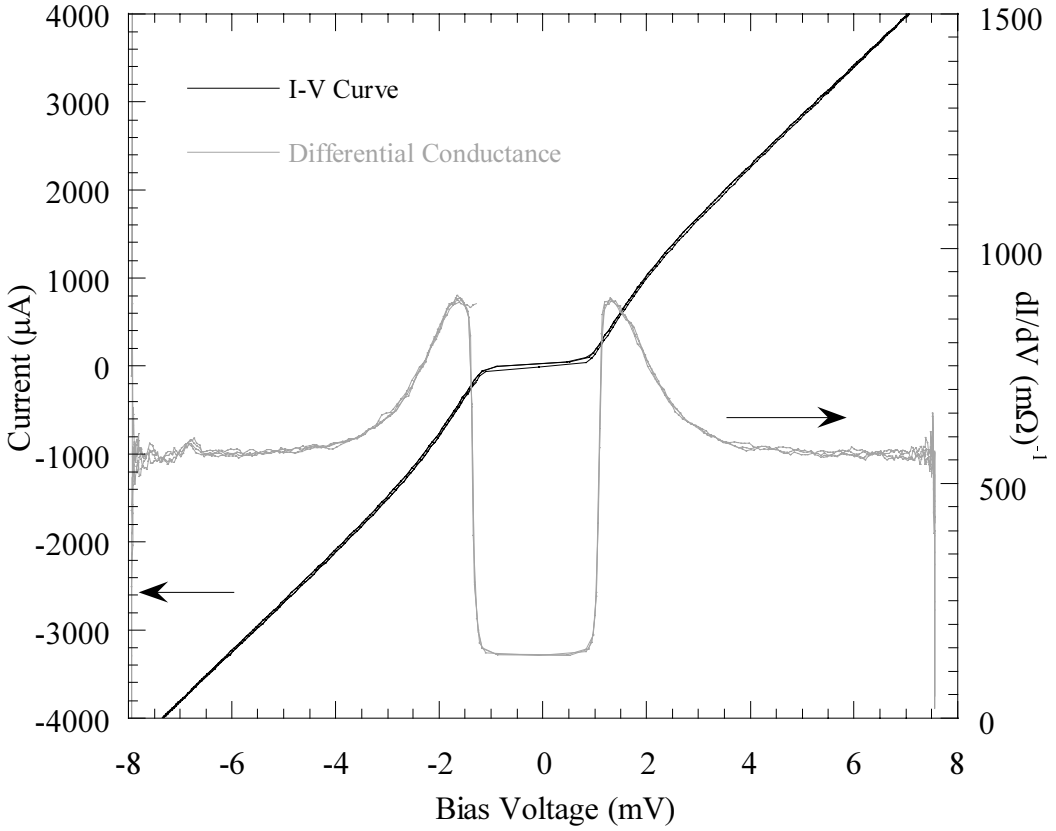

Figure 6.4 Current-voltage characteristic (left scale) and differential conductance (right scale) of a device.

80 mK) have been reported by some workers(Nahum 1993; Fisher 1997), however it was found that for the devices reported here the best achieved was at least an order of magnitude lower than this. Figure 6.4 shows the differential resistance for one device, found by numerically differentiating current-voltage data using a 2nd order, 9 point Savitsky-Golay smoothing filter(Savitzky 1964).

Subsequently it was discovered that the probe and electronics were extremely adversely affected by RF interference from contaminated mains. This manifested itself as a reduced sub-gap resistance, which could be minimised in most cases by changing the measurement configuration, for example by swapping the current and voltage contacts on the detector junction. Whilst this problem will have reduced the sensitivity of the junctions to very small injected currents, the magnitude of the changes observed were greater than the degradation due to the interference. Following upgrading of the filtering in the system, average quality factors were increased by an

order of magnitude. Results from the devices produced after the upgrade are reported in the next chapter.

6.3 Injection-Detection Experiments

6.3.1 Background

Like the SIS devices covered in the previous chapter, the basis of the injection detection experiments carried out here was to measure the response of one junction in a device to injection of current at another. In this case however, the common electrode is not a superconductor, but a normal metal. Therefore, we are measuring changes to the electron energy distribution in the normal metal. If the injector and detector junctions were close together, so that they were closer than the electron-electron interaction length (see section 2.5.2.2) then the injected electrons would propagate to the detector without relaxing from the original injection energy distribution. The measured detector current-voltage characteristic would then be influenced by these directly injected electrons. On the other hand if the separation was greater than the electron-electron interaction length, but less than the electron-phonon interaction length then the electron distribution would appear to be thermal, but corresponding to a temperature in excess of the phonon system. For these devices, however, the distances between the injector and detector system were many tens of microns, therefore the electron and phonon systems in the metals have re-established an equilibrium, albeit one at a higher temperature than the base temperature of the system.

Rather than measure an extra electron current, as we did for the SIS devices discussed previously, essentially we wish to measure the temperature change of the normal metal at the detector junction. For the work presented in this chapter we have used two methods to assess this temperature change.

Firstly, in a fashion analogous to the approach used in the last chapter, we define an excess current:

$$I_x(V, I_{inj}) = I_{\det}(V, I_{inj}) - I_{\det}(V, I_{inj} = 0) \tag{6.1}$$

where I_{det} is the measured detector current. Since the tunnelling current will scale with the normal state resistance of the junction, we need to multiply the excess current by the normal state resistance to form a parameter that is independent of the designed parameters of the detector junction.

$$\theta(V, I_{inj}) = I_x(V, I_{inj})R_N \tag{6.2}$$

What we have not considered, however, is the quality of the junction. Since there is a continuous density of states in the normal metal side, the sub-gap current is much greater for a SIN junction relative to a SIS junction, ideally we wish to measure the device at a significantly lower temperature than we used in our work with SIS devices. Too low a temperature, however, may take the junction below the point at which it is limited by leakage currents and therefore further cooling will not reduce the sub-gap current any further. Finally, there is an intrinsic self-heating of the junctions, which we study in detail in the following chapter.

A common measure used by other workers(Fisher 1997) that is closely related is to measure the changes in bias for a fixed detector current. This is commonly used in the X-ray detector field where sweeping of a current to measure a current-voltage characteristic is not practical (since one would not be able to synchronise detection events with the current sweep), and voltage biasing is difficult as the dynamic resistance of tunnel junctions is very high so that the bandwidth required for stable biasing is excessive.

For injection-detection experiments, however, the system is in a steady state and so it is possible to sweep a current source to measure a complete current-voltage characteristic. Ideally, we wish to minimise the influence of heating of the detector junction on the measurement, therefore we use the differential conductance of the detector junction at zero detector bias to measure the response of the device.

$$\vartheta = \frac{\left.\frac{\partial I_{det}}{\partial V_{det}}\right)_{V=0}}{\left.\frac{\partial I_{det}}{\partial V_{det}}\right)_{V>>\Delta/e}} = R_N \left.\frac{\partial I_{det}}{\partial V_{det}}\right)_{V=0} \tag{6.3}$$

We can normalise this for any junction by multiplying by the normal state resistance (6.3), in which case the temperature dependence (assuming a perfect BCS junction) is

given by equation (2.38). A non-perfect junction with a leakage current will give a minimum conductance, reducing the sensitivity of the device. For a number of devices we have used a slight variant of this as a measure; we first subtracted the baseline data (i.e. I_{inj}=0) and then differentiated and multiplied by R_N:

$$\begin{aligned} I\left(I_{inj}\right) &= f\left(V, I_{inj}\right) = f^{0}(V) + \delta f\left(V, I_{inj}\right) \\ \left.\frac{\partial I\left(I_{inj}\right)}{\partial V}\right|_{V=0} R_N &= const + \left.\frac{\partial \delta f\left(V, I_{inj}\right)}{\partial V}\right|_{V=0} R_N \end{aligned} \tag{6.4}$$

6.3.2 Experimental

6.3.2.1 Methodology

Unless stated otherwise, all the results presented in this chapter have been carried out between 0.30 K and 0.35 K using an Oxford Instruments Heliox™ ^{3}He insert (described in section 4.4.6). Following cooling to the base temperature (which was in the range given above, dependent upon the heat loading from the wiring and the holder), and initial measurements of current-voltage characteristics, 3 terminal current injection-detection experiments were performed. The *I-V* characteristic of one junction (the detector) was measured by sweeping a current-biased source at a frequency of around 2 Hz while a constant current was injected in via another junction from a second current source. Both current sources shared a common return path through either a third junction or an S-N contact. Finally, a fourth junction was used to make a voltage return to allow four terminal measurement of the detector junction. Since this requires 4 terminals to the common electrode, the variant of the mask with 3 islands with 3 junctions each could not be used, and the two island variant left no redundancy.

Each *I-V* characteristic was recorded using the computer based ADC with LabVIEW™ software as described in section 0, and saved to disc for processing offline.

6.3.2.2 Potential Distribution in Common Electrode

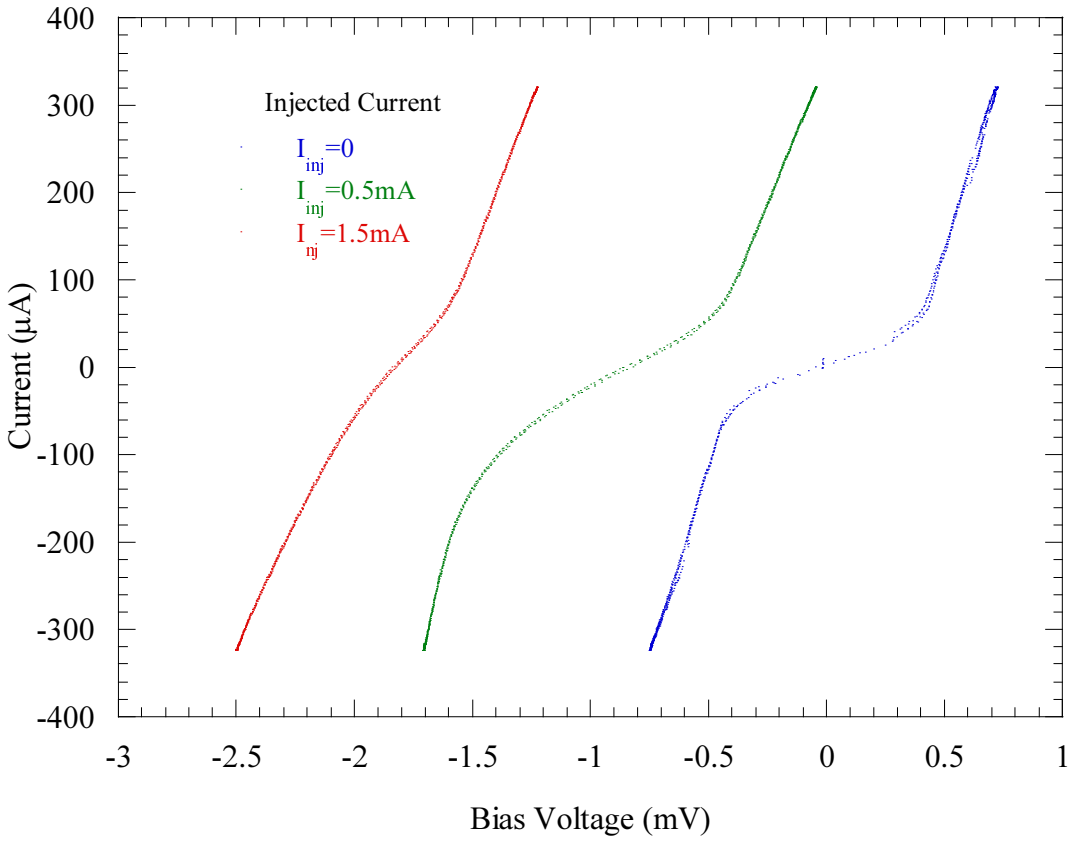

Figure 6.5 Offset current-voltage characteristics for one device with current injection at a second junction on the same normal metal electrode.

During initial measurements, the detector current-voltage characteristic was observed to undergo significant shifts in bias that varied with the injection current and the measurement configuration. For high injection currents the offset was sufficient to render it difficult to measure the detector current-voltage characteristic (figure 6.5). This was eventually realised to be a result of the common electrode being a normal metal. Thus the separation of the current and voltage paths for performing a four terminal measurement was not well defined, which in combination with the injection current giving a potential gradient throughout the common electrode resulted in the observed shifts.

To investigate whether we could compensate for the extra potential differences in the common electrode we calculated the potential difference within the central rectangular region of the common electrode. This involves solving Laplace's Equation for our geometry:

$$\underline{\nabla}^2 . \underline{V} = 0 \qquad (6.5)$$

As we have a thin film geometry, we solved only for a two-dimensional system and neglected the effect of the 'tabs' that connect the central rectangular region to the junctions. For boundary conditions, we can specify either the absolute potential at the boundary, or the normal derivative – i.e.:

$$\frac{\partial \underline{V}}{\partial \underline{r}_n} = \underline{E}_n \tag{6.6}$$

where $\mathbf{r_n}$ is a unit vector normal to the boundary and $\mathbf{E_n}$ is the value of the boundary condition, which is the electric field strength. For a normal metal, this will be proportional to the current entering the region at this point on the boundary, so that in order to conserve current, we require:

$$\oint_{boundary,L} \underline{E}_n . \underline{r}_n dl = 0 \tag{6.7}$$

where the region has a continuous boundary L. In general, this has to be solved numerically. Fortunately the well-known NAG FORTRAN library includes a routine for solving just this problem(NAG). Ideally we need to solve the problem for any combination of injection, detection and current return points for a range of injection currents. We are spared some of the computational effort by utilising the fact that we can take a linear combination of solutions to (6.5) to find further solutions. What we did, therefore, was to calculate the distribution of the potential *V* for a unit of current injected and extracted through every combination of pairs of junctions (see figure 6.1 for the layout of the device) which we could then combine to find the potential distribution for any required current distribution.

The simulation was written in two sections. A driver program written in Perl that ran on a Linux workstation fed boundary conditions and collated completed results. A calculation engine written in FORTAN that called the NAG library routine running on a Sun Microsystems Ultra-Sparc Unix system performed the actual calculations. The simulation was performed on a grid of 113 points × 15 points, corresponding to the device's 225 μm×30 μm central region.

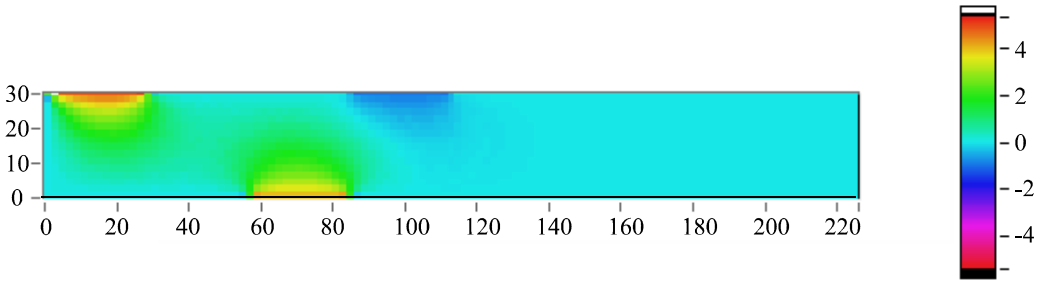

Figure 6.6 Contour plot of potential distribution in central region of a common electrode. 5 arb. units of current are being injected at junction A (top left), with a -1 arb. unit current at junction B (top middle) and current return at junction F (bottom middle-left). Current and potential (Z scale) are in arbitrary units, X and Y scales are in μm.

Figure 6.6 shows a representative result from calculating the potential distribution in the island for the case of injection of 5 arb. units of current into junction A (see figure 6.1), whilst using -1 arb. current unit at a detector junction B and F acting as the current return.

6.3.2.3 Superconducting Top Layer

Although we could calculate the extra contribution to the measured detector current-voltage characteristic due to the potential distribution resulting from the injected current, it did not solve the fundamental problem that it was difficult to measure the *I-V* characteristic if it was offset beyond the range of the voltage amplifier.

To solve this problem, it was necessary to find a way to remove the potential difference along the common electrode. The easiest way of doing this was to deposit an additional superconducting layer on top of the common electrode. The superconducting layer then carries most of the current travelling laterally across the common electrode, thus eliminating the troublesome potential differences. A further, related, advantage was that the measured normal state resistance was now independent of the measurement configuration. Without the superconducting layer the length of normal electrode that contributed to the measured series resistance of the device was not well defined since it depended on the relative positions of the four measurement contacts. With the superconducting top layer, virtually all of the current will traverse only the thickness of the Pd/Au layer directly above the junctions. The measured series resistance is therefore independent of the measurement configuration.

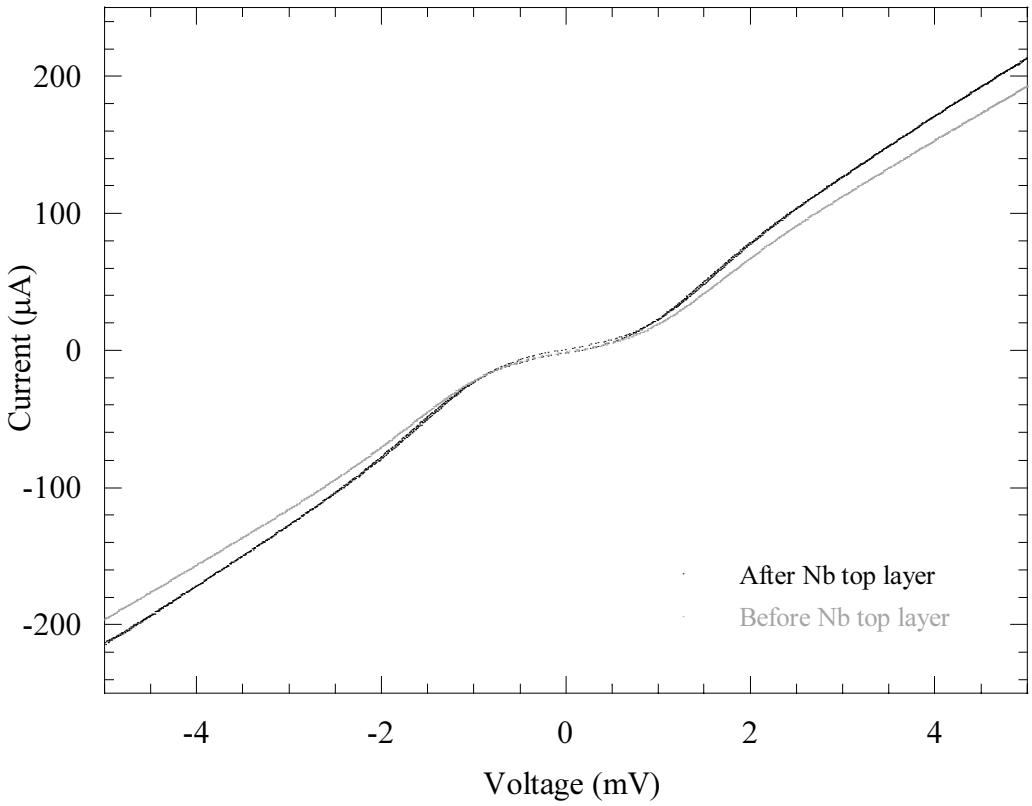

Figure 6.7 Current-voltage characteristics before and after the Nb shorting layer was deposited, showing the decrease in apparent R_N

This has a small but definite effect on the measured current-voltage characteristics (see figure 6.7).

The disadvantage of this extra layer is that it introduces a potential complication with interactions between the injected electrons, which may be 'hot' in the sense of not being in thermal equilibrium with the phonon system, and the superconducting layer. In particular it is possible that such electrons will undergo Andreev reflection at the interface, and since the reflected hole travels back along the time reversed track of the incident electron, this may serve to concentrate the hot electrons in the immediate vicinity of the injecting junction. In practice, the mean free path, given the measured RRR of 1.3, in the normal metal layer is sufficiently short, such that the mean free path is much shorter than the film thickness. Given this, electrons will undergo normal scattering throughout most of the film thickness, with only a layer of thickness l below the superconducting layer significantly affected by Andreev reflection.

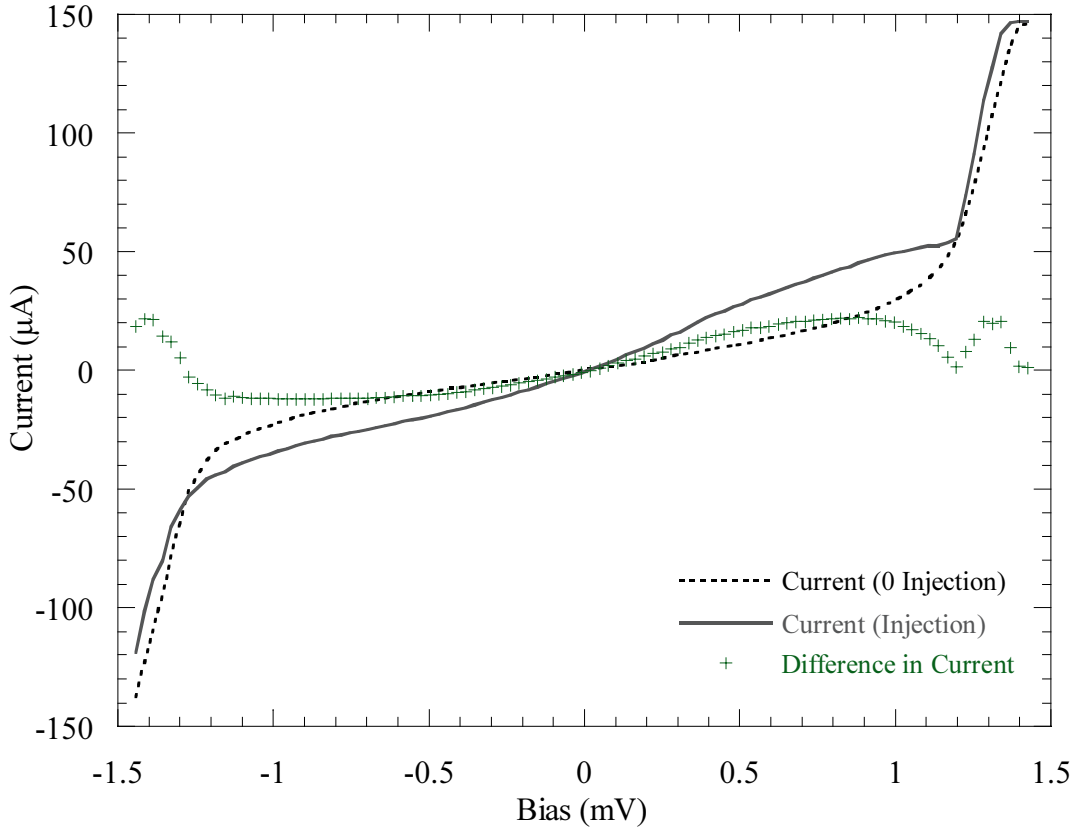

Figure 6.8 Current-voltage characteristics with and without injected current, also showing the difference, i.e. net excess current.

6.4 Results

Having developed a device design that allowed us to measure reliably the effect of the current injection on the current-voltage characteristic of the detector junction, we were able to proceed with measurements.

For some configurations of injector, detector, current return, and voltage contact, we were able to observe a change in the current-voltage characteristic, as illustrated in figure 6.8. This type of response was not, however, observed for all measurement configurations – for some configurations the response was notably asymmetric with respect to the detector junction bias, and for other configurations there was only a small response, if any at all. Furthermore, the magnitude of the response, when there was one, was very non-linear with the current, bias or power of the injector. These features of the results are discussed in greater depth in the following sections.

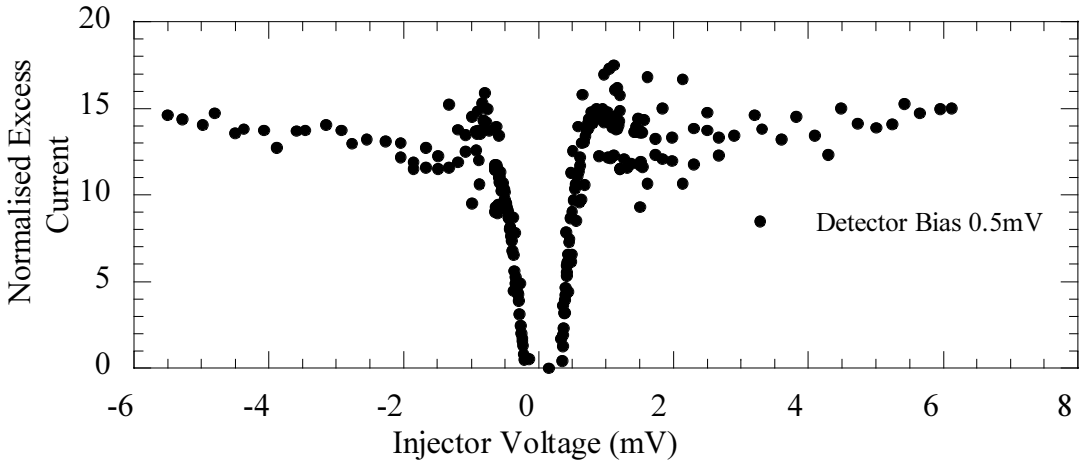

Figure 6.9 Class 1 response - large and symmetric about zero injector bias.

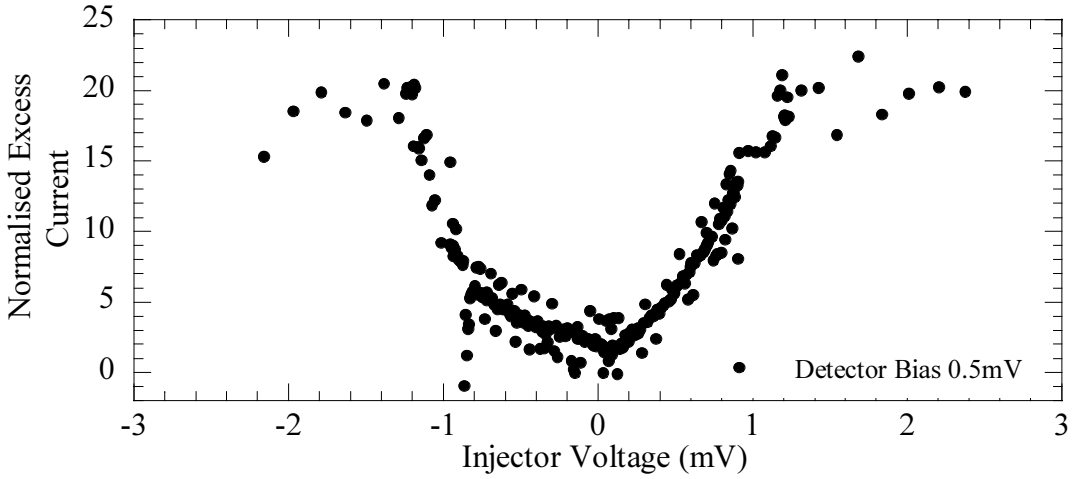

Figure 6.10 Class two response- large and asymmetric about zero injector bias.

6.4.1 Geometrical Dependency

6.4.1.1 Classification of Responses

As described above, we were able to identify essentially three classes of response when measuring the normalised excess current, θ (from(6.2)):

1) Large symmetric response of device (figure 6.9)

2) Large, but asymmetric response of device w.r.t detector bias (figure 6.10)

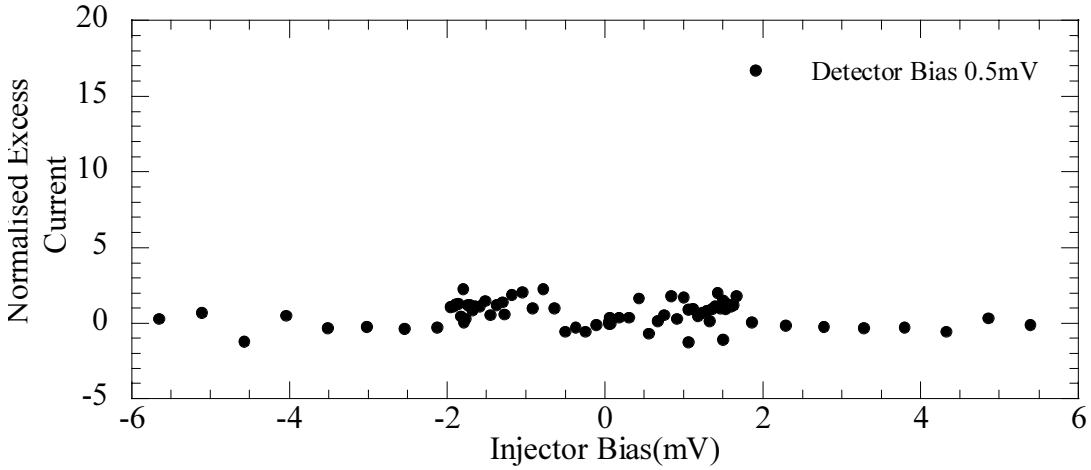

Figure 6.11 Class three response - small and indistinct response.

3) Small, indistinct response (figure 6.11)

It is important to stress that whilst the size of the response was dependent on the quality of both the injector and detector junction, it was possible to get all three classes of response using either the *same detector junction* or the *same injector junction*. Therefore, we conclude that the different classes of response were not solely due to junction quality issues.

6.4.1.2 Experimental Configuration and Class of Response

We found that we were able to predict which class of response would be obtained based on the geometry of the measurement configuration. We can refer to the side on which a junction is. By this, we mean to which of the long sides of the central rectangular region of the common electrode the junction is attached. We then find that which class of response we observe is determined by on which sides the detector, injector and current return junctions are. For the initial work we measured a device with a configuration using two common electrodes (see figure 6.1), so that we made connections to all four junctions on one common electrode, therefore we had three distinct arrangements of the injector, detector and current return junctions (figure 6.12).

We observed that a class 1 response (large, symmetric) was always associated with a configuration as in figure 6.12a, where the detector and injector were on the same side of the device, with the current return and voltage contact on the other. Class 2 responses (large, asymmetric) were associated with the configuration in figure 6.12 b, with the detector and current return on the same side and injector and voltage contact on the other. Finally the third class of response (small) were found for configurations like figure 6.12c, where the detector and voltage contact shared one side, with the injector and current return on the other. One could further subdivide the classifications of configuration according to which of the junctions on the far side of the detector was opposite it - for example, for the first configuration whether the voltage contact or current return was directly opposite the detector. In practice, it was found that there was no significant difference in the response of the detector to these two configurations.

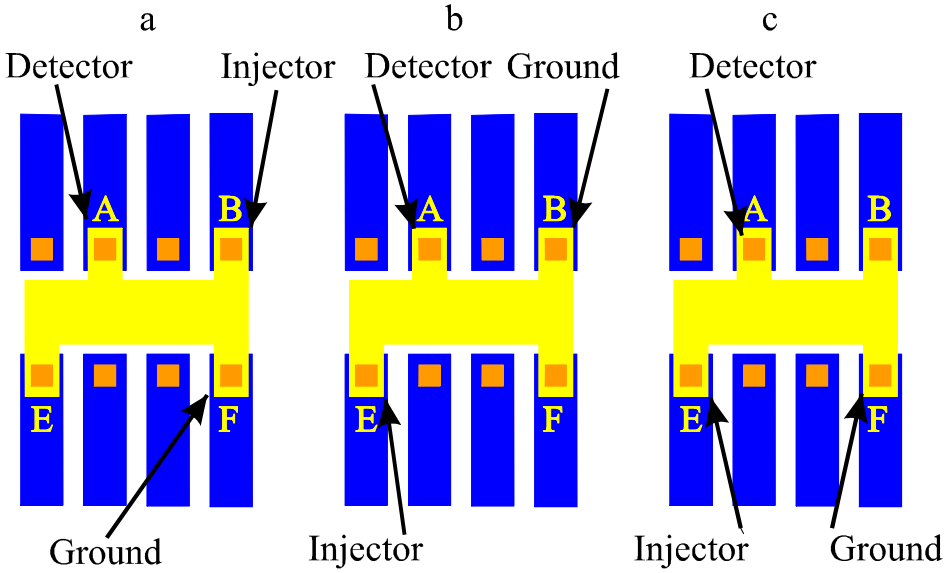

Figure 6.12 Three different measurement configurations. (a) Detector and injector on the same side and opposite the current return. (b) Detector and current return on the same side and opposite the injector. (c) Detector opposite the injector and current return.

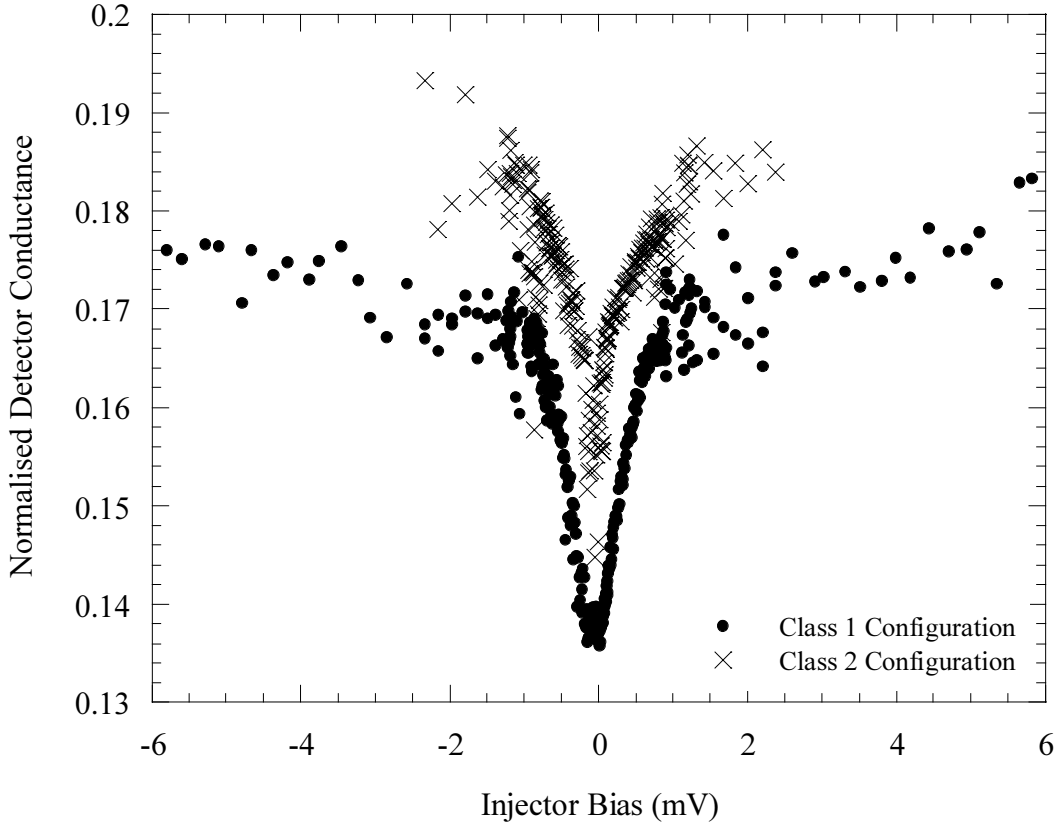

Figure 6.13 Differential conductance for class 1 and 2 responses

It was observed that the degree of asymmetry associated with the class 2 type of results were directly related to the detector bias current, the response having a minimum when the detector and injector currents were opposite and equal. At this point the current flowing through the current-return connection (which is adjacent to the detector junction for the relevant configurations) will be zero. The determining factor was therefore the current through the junction adjacent to the detector, in which case class 1 and 2 results are essentially the same. This was confirmed by using the change in differential conductance at zero detector bias as the measure of device response. Since the detector junction is at zero bias, the current through the current return is equal to that through the injector. We then obtain very similar results for both class 1 and class 2 configurations (figure 6.13).

6.4.1.3 Distance between Injector and Detector Junctions

The two island configuration only allows two different distances between the injector and detector junctions if we are limited to placing both on the same side of

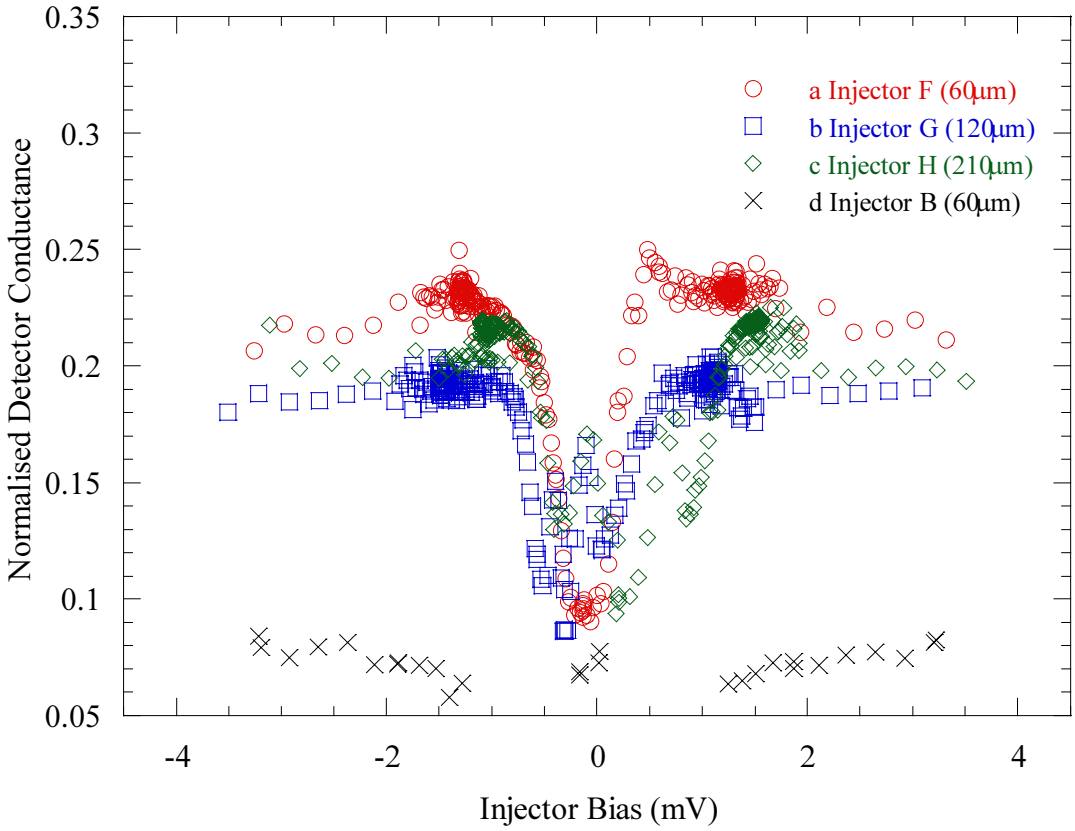

Figure 6.14 Differential conductance for different detector-injector distances (detector E). Figure 6.18 shows a plan of the single island configuration, showing junction labels.

the common electrode. Additionally, it was found that there were considerable variation in the quality factors between the junctions in any given device when measured at 0.35 K, so that to assess any effect of distance between the injector and detector it would be desirable to use the same detector junction. For these reasons, a single electrode configuration was used to measure any change in the response as a function of the distance between the injector and detector junctions. Given the dependence on geometry observed, one might expect that the common electrode was being non-uniformly heated. In that case, it would be likely that the magnitude of the response would be less the further the injector was from the detector.

In figure 6.14 we show plots of the response on junction E from current injection at junctions F (plot a, 60 μm from E), G (plot b, 120 μm) and H (plot c, 210 μm) and for comparison A (plot d, 60 μm across the common electrode). The distances quoted are from the centre of the detector junction to the centre of the

injector junction. As is readily observed, there is no systematic change in the response as a function of distance.

6.4.1.4 Source of Response

Implicit in our discussion hitherto has been the assumption that the source of the change in detector current can in fact be localised to specific junctions. To determine this we repeated the injection experiments for devices in which the injector junction was replaced by an S-N connection. Under these conditions, the injection current only passes through the Pd/Au layer before entering the superconducting top layer of the common electrode. For a configuration that gave a class 1 result with a junction, i.e. with the injector adjacent to the detector, we found that without a junction we observed no response, confirming that the junction was the source of the response. For the other possible configurations no change was observed, which would be expected if only the nature of the contact next to the detector is important.

Based on these results we conclude that the source of the response is associated with the junctions, but in addition, that there is a directional variation determining the magnitude of the observed response.

6.4.1.5 Injector-Detector Coupling Routes

We have not yet considered the possible coupling processes between the injector and detector beyond noting that direct hot electron transfer between the injector and detector is unlikely due to the relatively large scale of the device. Ultimately a SIN tunnel junction is sensitive to an enhanced electron temperature in the normal electrode, so we are measuring such an enhanced temperature at the detector. If we neglect the possibility of direct coupling by radiation, then the only methods that can heat the electrons close to the detector are either phonon transport through the substrate or coupled thermal electrons and phonons through the common electrode.

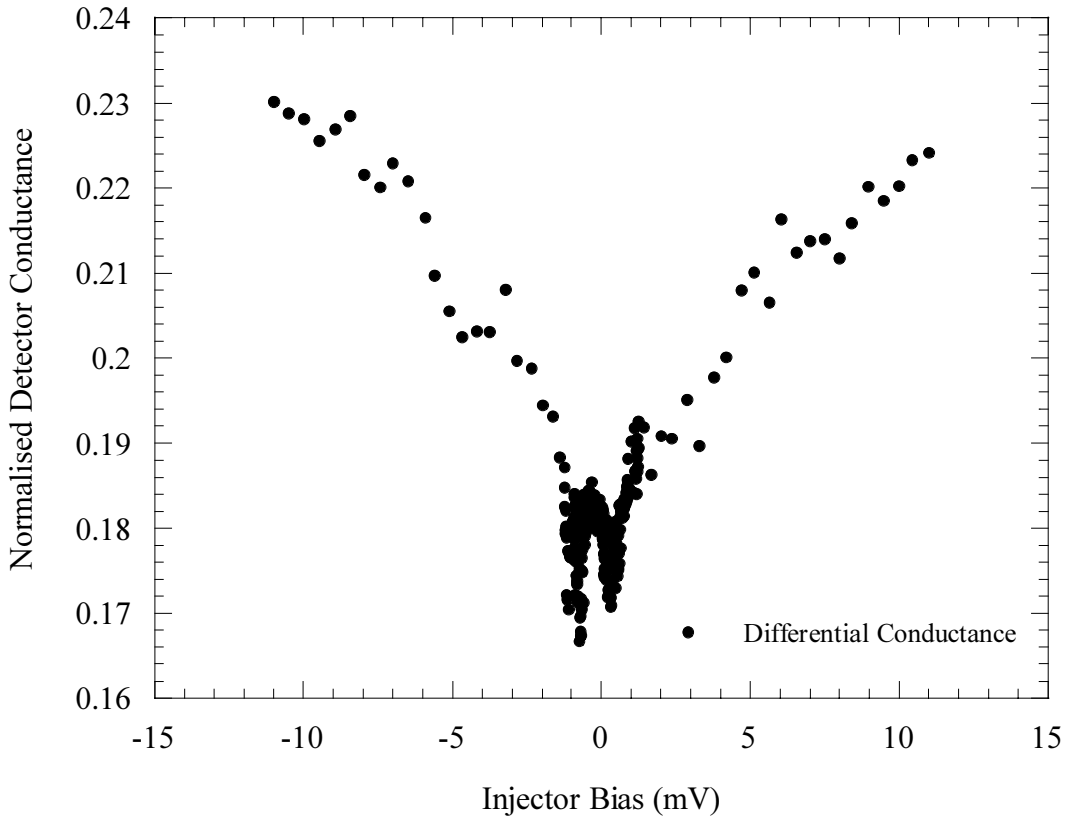

Figure 6.15 Normalised detector efficiency for the injector and detector on separate normal metal electrodes.

If the primary coupling mechanism was thermal electron and phonon transport through the common electrode, then we would have to assume that temperature in the common electrode was increased significantly throughout its volume. In that case, it would be difficult to explain the observed lack of response of the detector to a non-adjacent injector/current return. Therefore, it would appear that substrate phonon coupling is the most likely. We were able to test this relatively easily using the two common-electrode configuration, by using an injector on one electrode, and the detector on the second. The configuration most likely to give a response would be one with the injector/detector pair as close as possible whilst being on different electrodes i.e. junctions B & C or F & G. Figure 6.15 shows the response from one such experiment, confirming that there is indeed significant coupling via the substrate. A similar response was also observed for all configurations which gave a response for the single common electrode variant, e.g. detector A, injector C or D. In addition, a response for a configuration with the detector and injector junctions diagonally

opposite each other between the two electrodes (i.e. detector B and injector G) was measured.

We have demonstrated that coupling between the injector and detector via substrate phonons is the dominant coupling process. We have also shown that there is significant anisotropy in the coupling. We were unable to measure any response *across* the device even when the distance between the injector and detector was less than when a response was observed *along* the length of the device. One possible explanation to be eliminated would be anisotropy in the phonon propagation in the substrate. To do this devices were fabricated on a variety of different substrates, including a and c plane sapphire, silica, silicon and Si_3N_4 coated silicon substrates. No significant differences in the behaviour of the devices were observed compared to those fabricated on r-plane sapphire. The observed anisotropy in the results, therefore, must be due to the design of the device. The presence of the common electrode appeared to block the injector from the detector.

6.4.2 Injector Bias Dependence

In the previous section, we have been discussing the response of the detector in terms of a significant change in either the sub-gap conductance at zero bias or the sub-gap current as the injector was biased. We now consider the form of the response with respect to the processes occurring at the injector in more detail.

6.4.2.1 Summary of Results

In figure 6.13 we showed the form of the response as a function of the injector junction bias. It shows a rapid, approximately linear, increase in the sub-gap conductance as the injector bias is increased up to around Δ/e, after which the rate at which the sub-gap conductance increases rapidly decreases, to give a characteristic step shape. For very high injector biases ($V_{inj} \gtrsim 10$ mV) the sub-gap conductance increases, irrespective of the experimental configuration. We attribute this high bias change to simple sample heating. In order to achieve this bias currents of order mA were required (the normal state resistance of the device is of order 1 Ω). We are therefore depositing tens of μW into the device. In the limit of excess cooling power,

we can find the approximate temperature increase by calculating the solution of the appropriate heat diffusion equation for a semi-infinite slab of sapphire. The three dimensional heat diffusion equation is given by(Carslaw 1959):

$$\left(\kappa\nabla^2 - C\frac{\partial}{\partial t}\right)T(\underline{r},t) = P_{inj}\delta(\underline{r}) \tag{6.8}$$

where P_{inj} is the injected power, κ the thermal conductivity, C the specific heat capacity and δ the Dirac delta. This equation has been solved by Lemke(Lemke 1993), who gives:

$$T(\underline{r}) = \frac{P_{inj}}{4\pi|\underline{r}|\kappa} + T_0 \tag{6.9}$$

where T_0 is the base temperature. This gives a temperature rise of order of 10 mK for our geometry (taking κ=10 $Wm^{-1}K^{-1}$(White 1987)). Even at the base temperature of 350 mK this is a comparatively small temperature rise. Unfortunately, the cooling power available on the Heliox™ probe used was relatively small, and combined with the power deposited on the ^{3}He pot by the copper wires connecting to the sample the base temperature of the system was observed to rise rapidly for injection currents greater than approximately 1 mA. For injector biases around Δ/e the current required was of order of 100 μA, and so from (6.9) the expected temperature rise would be less than 1 mK. The sample temperature was not measured to increase, indicating that the heat-load was within the limits that the Heliox™ could sustain.

6.4.2.2 Low Bias Regime (V_{inj}<Δ/e)

If we consider the normalised change in conductance at zero detector bias as our measure of device response (6.3), then using equation (2.38) we should be able to assign a temperature dependence to the response. In practice this is complicated by two factors. Firstly, (2.38) assumes a BCS density of states in the superconductor. Our devices have a Nb-Al proximity structure, which according to the available models of the proximity effect will not have a BCS density of states. Secondly, the devices are somewhat leaky, so the minimum conductance is rather higher than would be expected.

If we do apply (2.38) to real data, using an assumed Δ/e of 1.15 meV, then we find that the temperature of the device is around 4-5 K. This is clearly not realistic – we would suspect that we have a significant density of states within the sub-gap region in the S electrode. If we suppose, however, that the form of the dependency of sub gap conductance on temperature in (2.38) is approximately correct, then we see that the temperature increase is linear with the injection current and bias.

6.4.2.3 Analysis

The increase in the detector sub-gap current was observed to occur up to an injector bias that corresponded with the energy gap Δ. It might be supposed that this is due to the sharp increase in both the current and injected power at the energy gap in the current-voltage characteristic of a SIN tunnel junction. However, if we plot the normalised sub-gap conductance against the injector bias, current and power (figures 6.16a, b, and c), then we observe that we retain the step feature. Therefore, the sub-gap conductance is not scaling with any simple measurement of the injector junction. Furthermore, by testing devices with a range of normal state resistances the step feature was always located at a bias of Δ/e, and not a consistent current or power. This indicates that the step feature is associated with a process occurring at the injector junction at this bias.

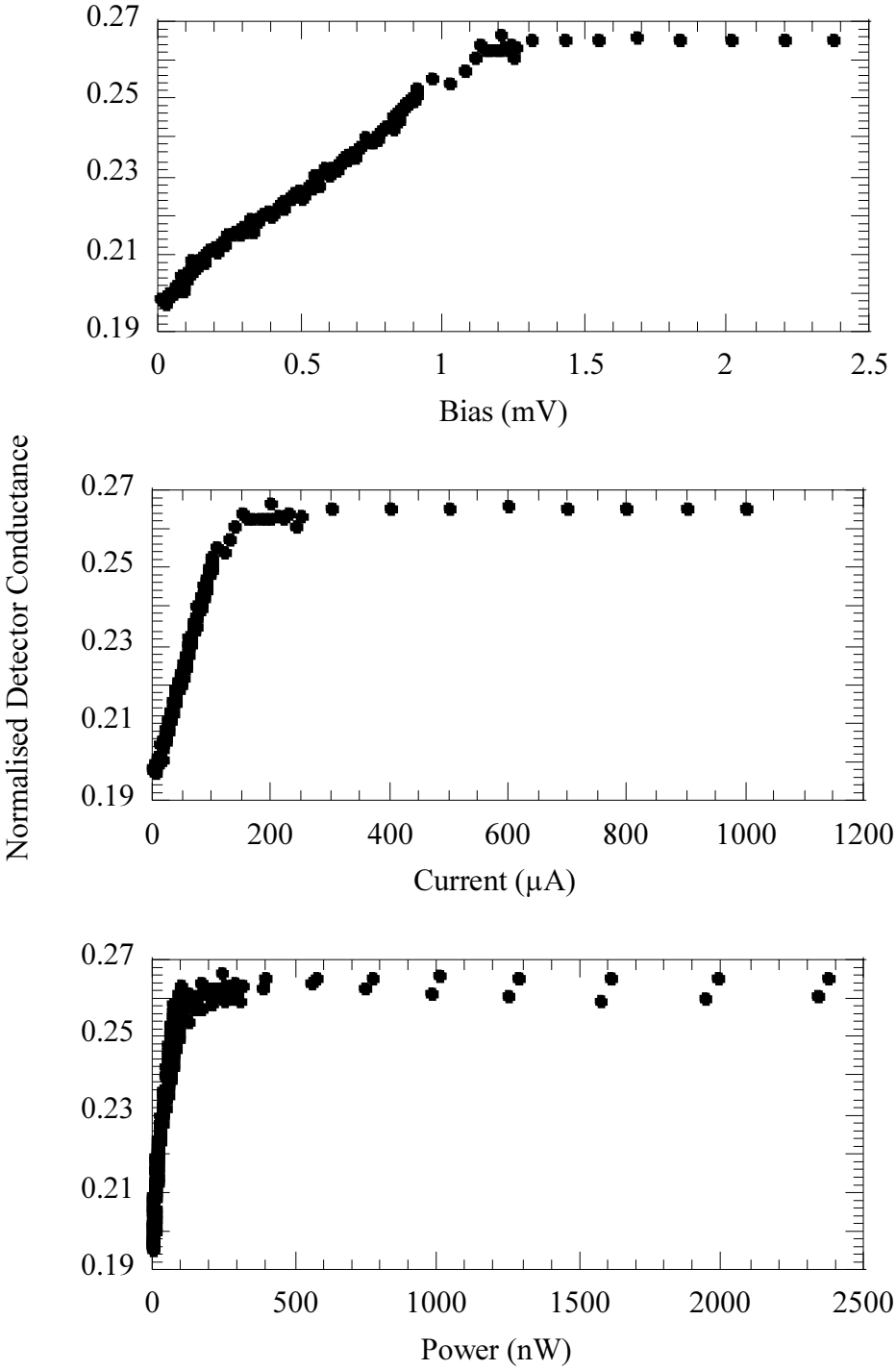

Figure 6.16 Differential conductance versus injector bias, current and power for the same device.

We consider the situation at the injector for biases close to Δ/e (figure 6.17). At this point, significant number of quasiparticles will tunnel from the superconductor to the normal electrode, resulting in an increase in 'hot' electrons (or holes) in the normal metal. These will relax to a thermal distribution of electrons by emitting phonons of energy $\Omega \approx k_B T$. They, however, cannot be directly responsible for the

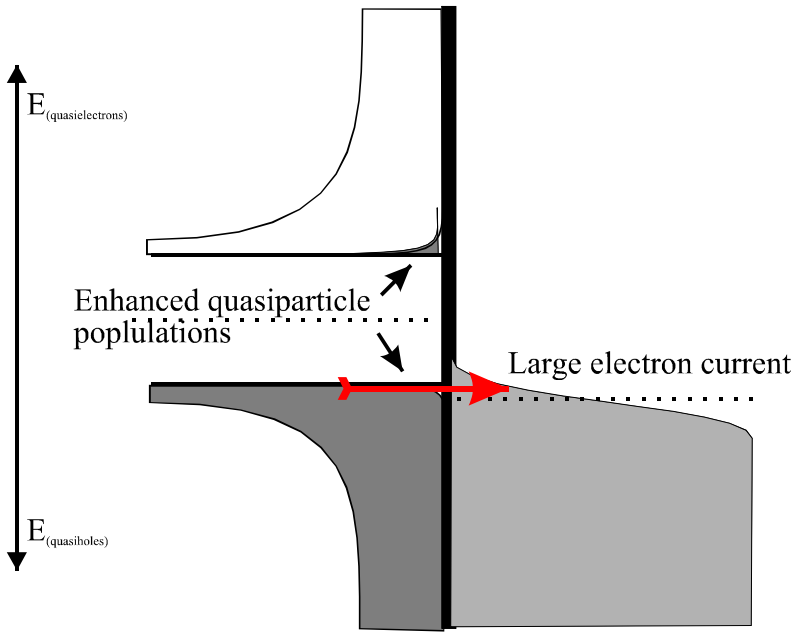

Figure 6.17 Semiconductor representation of a device biased near to Δ.

observed heating at the detector junction, otherwise a response would be observed for an S-N contact. Furthermore, the response would continue to scale with current. In the superconductor, the population of quasiparticles will be increased. These quasiparticles will be of predominately one character (either electron like or hole like depending on the bias of the junction), but this will be relaxed by branch mixing and recombination. The recombination rate will, however, rise steeply since even for a relatively small injection current, the density of quasiparticles will be many orders of magnitude greater than the thermal population at the base temperature of 0.35 K.

From equation (5.11) we find that the thermal density of quasiparticles is 6.4×10^{14} m^{-3}, and assuming a tunnelling time for quasiparticles which is similar to that for the SIS devices of chapter 5, would estimate the injected quasiparticle density for a typical injection current of 100 μA to be of order 10^{26} m^{-3}. The recombination rate is therefore in an extreme non-equilibrium condition.

6.4.2.4 Quasiparticle Recombination Rate and 2Δ Phonon Population

We can employ the Rothwarf-Taylor equations to estimate the population of 2Δ phonons for the injection currents that bias the injector close to Δ/e. If we consider (2.76) and (2.77)., since we operate in the steady state we can write:

$$\begin{aligned} 0 &= I_N - RN^2 + 2\tau_{pair-breaking}^{-1} P \\ 0 &= RN^2 - 2\tau_{pair-breaking}^{-1} P - 2\delta P \tau_{phonon-loss}^{-1} \end{aligned} \tag{6.10}$$

Here we assume that we have no 2Δ phonon injection (e.g. from the current-return junction via the substrate) and that the rate of quasiparticle tunnelling is slow compared to other processes. We can eliminate the quasiparticle recombination rate, and find:

$$I_N = 2\delta P \tau_{phonon-loss}^{-1} \tag{6.11}$$

Now, we can find I_N from the injection current using (3.13) and hence show that the rate of excess 2Δ phonon escape into the substrate should scale with the current.

The disadvantage of using the Rothwarf-Taylor equations is that they do not take account of the actual quasiparticle and phonon distributions. However, even if we employed the more sophisticated coupled kinetic equations of Chang and Scalapino(Chang 1977) we would inevitably find that the number of 2Δ phonons being emitted from the junction would increase with current. We are forced, therefore, to conclude that although large energy, athermal, phonons are required to observe the response, the step feature is not solely explicable in terms of the processes occurring at the injector junction.

6.5 Post-Measurement Fabrication Experiments

We return to considering the role of the device design in our measurements. In this section, we report a series of experiments involving modification of the fabricated devices following initial measurements. The alterations that we carried out were either the addition of various metal barriers and extensions to the common electrodes, or the

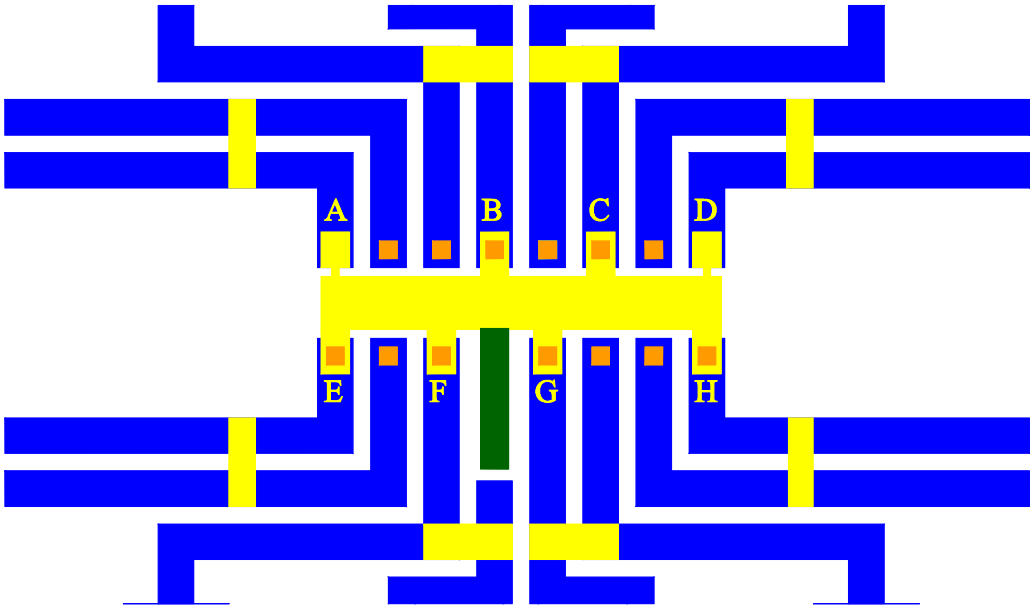

Figure 6.18 Plan of a single island device with a projecting barrier (dark shading)

removal of the bulk of the substrate in the region containing the common electrodes and junctions.

6.5.1 Normal Metal Barrier

It is apparent from the work on the geometrical dependencies in the results that the common normal metal electrode was serving to block the transmission of substrate phonons from the injector to the detector. An obvious experiment to attempt, therefore, was to construct an additional barrier between an injector-detector pair that previously showed a response.

Rather than have a new mask set made up to fabricate the barrier structures on the existing devices, we used an optical microscope as a make-shift scanning lithography machine as described in section 4.3.1.2. In order to fabricate the barriers we were required first to selectively remove areas of base electrode. This was done simply by defining an etch mask with the microscope and using the standard base electrode definition etch process. The barriers were deposited by using the standard lift-off process as used for the electrodes.

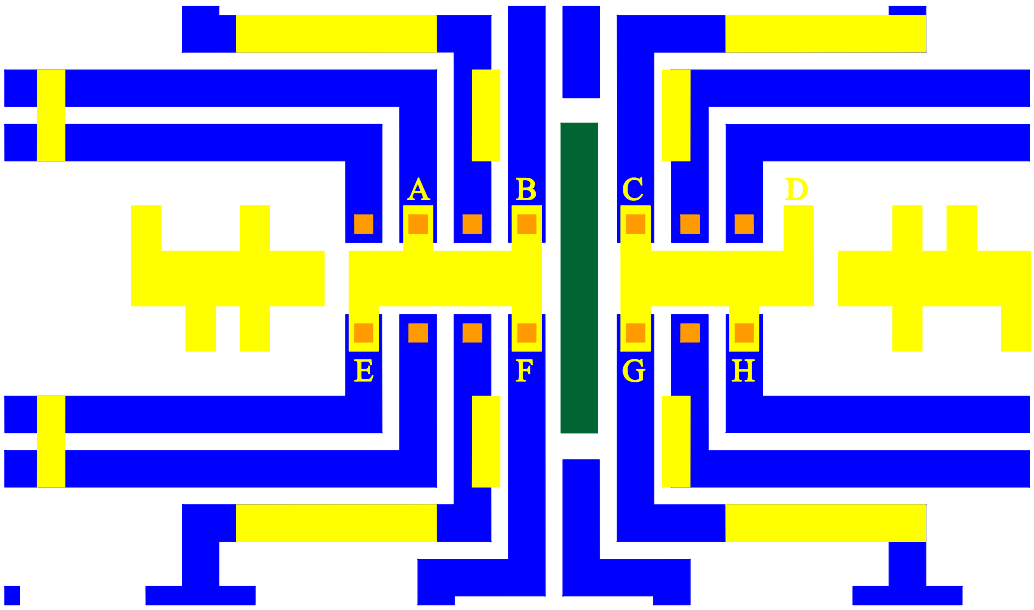

Figure 6.19 Plan of CAM20 two electrode device with barrier between them (shaded dark).

The devices were re-tested at a temperature of 0.35 K in the same injection/detection configurations as previously tested. Some deterioration of the junction quality parameters was observed; this seemed to affect junctions at random, so it became a matter of luck whether the particular junctions on a device that one was interested in survived. This seemed to be a common feature of the experiments in modifying devices and although not attributable to any particular stage of the processing, it was found that the deterioration scaled with the number of re-processing stages carried out.

To alleviate the problem posed by junction degradations we used two approaches. Firstly, we re-optimised the etching processing parameters to try to reduce the time and power of etching to the minimum required. Secondly, we sought a geometry of barrier that maximised the number of potential junction pairs that we could use.

Two different configurations of barrier were used: first we added a 20×40 μm barrier projecting from the side of a single common electrode device (figure 6.18). This design offered little redundancy if one junction characteristic was adversely affected by the extra processing. The solution was to modify the two common electrode design we had used previously. Due to the error in mask design, we were already required to perform two exposures to define the two common electrodes. It

was then a simple matter to increase the separation of the two electrodes by laterally displacing the mask by one set of base electrode leads, to leave a gap of 45 μm between the islands (see figure 6.19) into which we could deposit a 25-30×150 μm barrier structure.

Figures 6.20a and b show a typical response before and after the extra finger was added to the device. We were unable to measure a significantly different response that could not be solely due to the degraded junction characteristics, indeed, for some configurations the magnitude of the response even increased!

In the experiments with the normal metal barriers, the barrier cross-section was not the same as the electrode since it lacked the superconducting top layer. Both the top layer and base electrode were niobium, and therefore one would expect that majority of 2Δ phonons absorbed would be re-emitted as 2Δ phonons following a number of pair breaking and recombination events. The top layer, however, was deposited in a relatively dirty system, so might be expected to have degraded

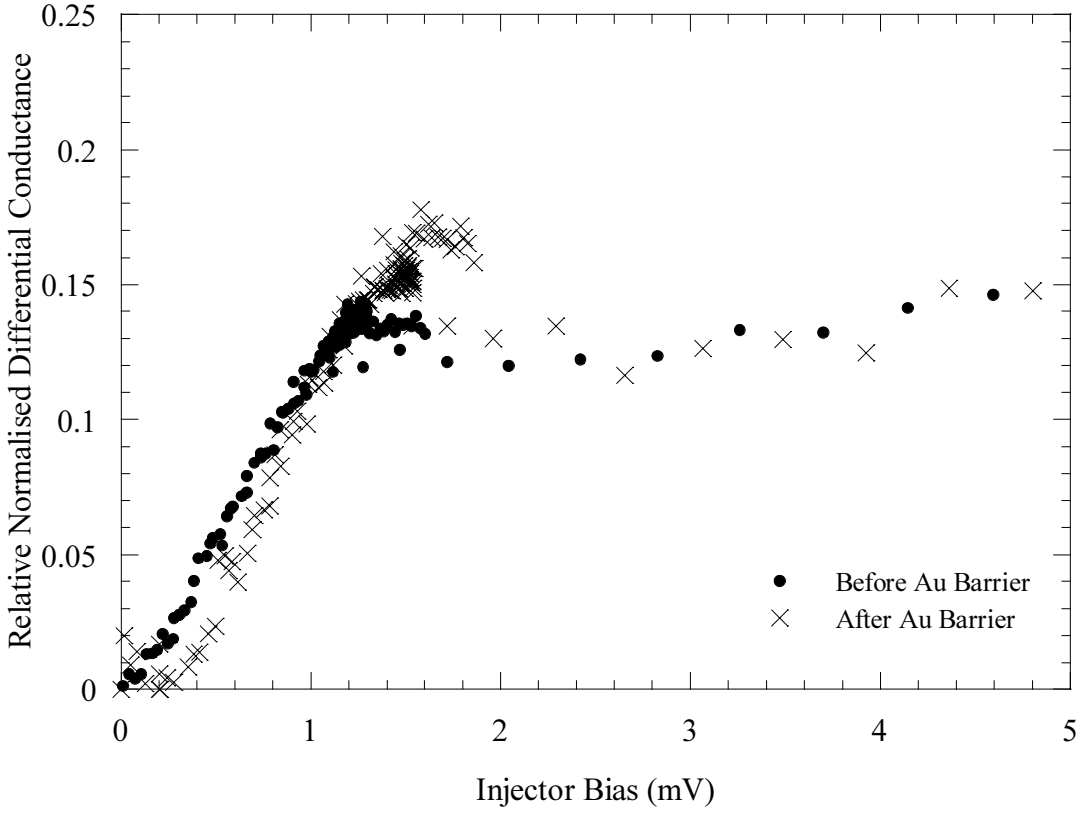

Figure 6.20 Response of a device before and after normal metal barrier deposition.

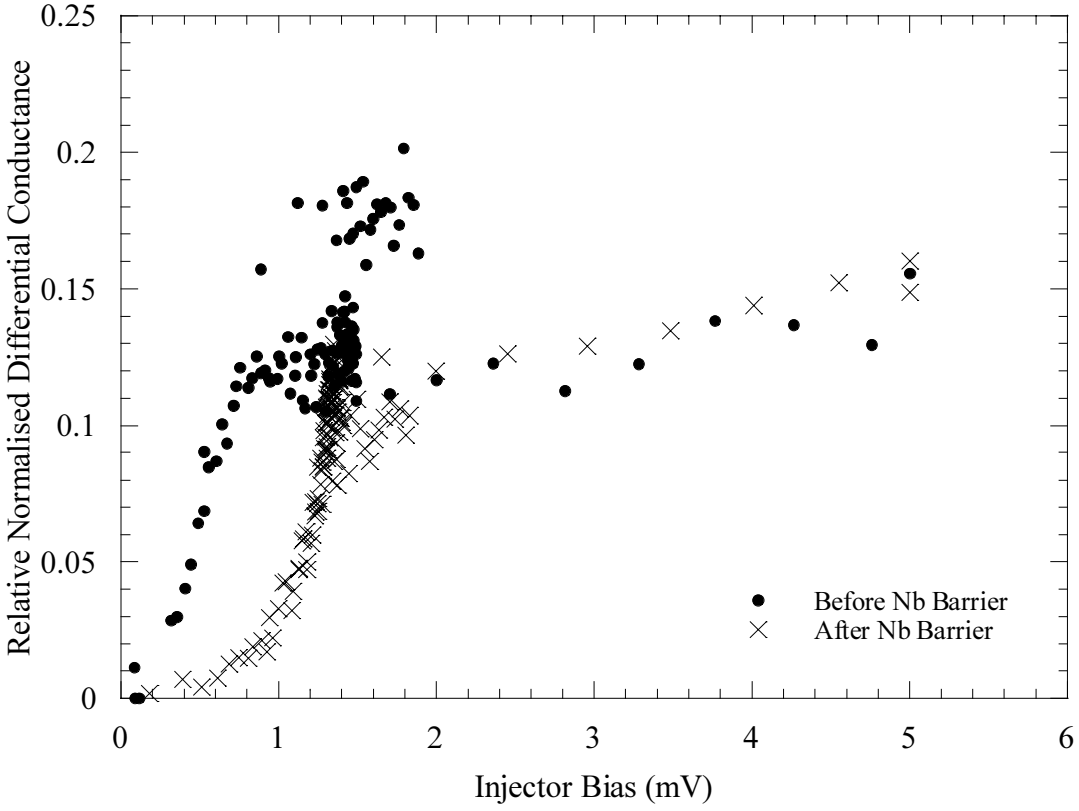

Figure 6.21 Response before and after a Nb barrier deposition.

superconducting properties (indeed the critical current of the top layer was at least an order of magnitude less than the base electrode). We expect then that the energy gap in the top electrode was significantly less than the bulk Nb value. It is then possible that the 2Δ phonons emitted from the injector could interact with the Nb top layer of the common electrode. However, it would still be expected that phonons of energy $2\Delta_{degraded}$ would be emitted eventually, and although unable to break pairs would be athermal (in that $\Omega >> k_B T$).

To investigate this we prepared a device with a niobium barrier between two common electrodes and performed injection-detection experiments with it. Typical results are shown in figure 6.21. As is readily seen, the magnitude and nature of the response is broadly similar – the presence of the Nb barrier seemingly having little effect on the phonon propagation from injector to detector.

In summary, we were unable to reproduce the substrate phonon blocking effect by introducing additional metal barriers between the injector and detector.

6.5.2 Membrane Fabrication

For almost all of the devices that we have reported here, we have used sapphire substrates. As we have demonstrated clearly, significant amounts of heat can escape from the device through the substrate. This will have a major degrading effect on any device that aims to absorb and measure accurately the heat deposited in the normal metal electrode. For particle detector applications, many workers have placed the absorber on a thin membrane in order to reduce the heat loss to the surroundings. Towards the end of the work presented in this chapter, co-workers in the research group developed techniques to produce membranes of Si_3N_4 of areas up to several mm^2. As a demonstration that the geometrical and injector bias dependencies of the measured response were strongly influenced by the substrate material, we fabricated one device on such a membrane.

Rather than attempt to deposit and fabricate the device on a wafer in which a membrane had already been made, we opted to fabricate the device first and then the membrane. The substrates used were Si_3N_4 double-sided coated Si wafers. The Si_3N_4 coating (deposited using low pressure CVD by the supplier) was 1 μm thick. The processing techniques described earlier were followed to fabricate the device with the exception of an additional CF_4 etch for 25 minutes at 100 W on the backside of the substrate. This etch was used to remove approximately 1 mm^2 of Si_3N_4 where the membrane would eventually be formed. The device was tested at 0.35 K prior to membrane fabrication to assess the quality of the junctions.

To make the membrane, a wet etching process using 33% KOH solution at a temperature of 94°C was employed. Under these conditions Si_3N_4 is not significantly etched whilst many other materials, silicon included, are. The Si is etched anisotropically, etching along <111> is 400 times slower than <100>(Zavracky 1994), which makes it particularly suitable for producing well defined rectangular membranes. By exposing the backside of the substrate to the etch, Si was removed from the area where the Si_3N_4 membrane had been removed during the initial fabrication.

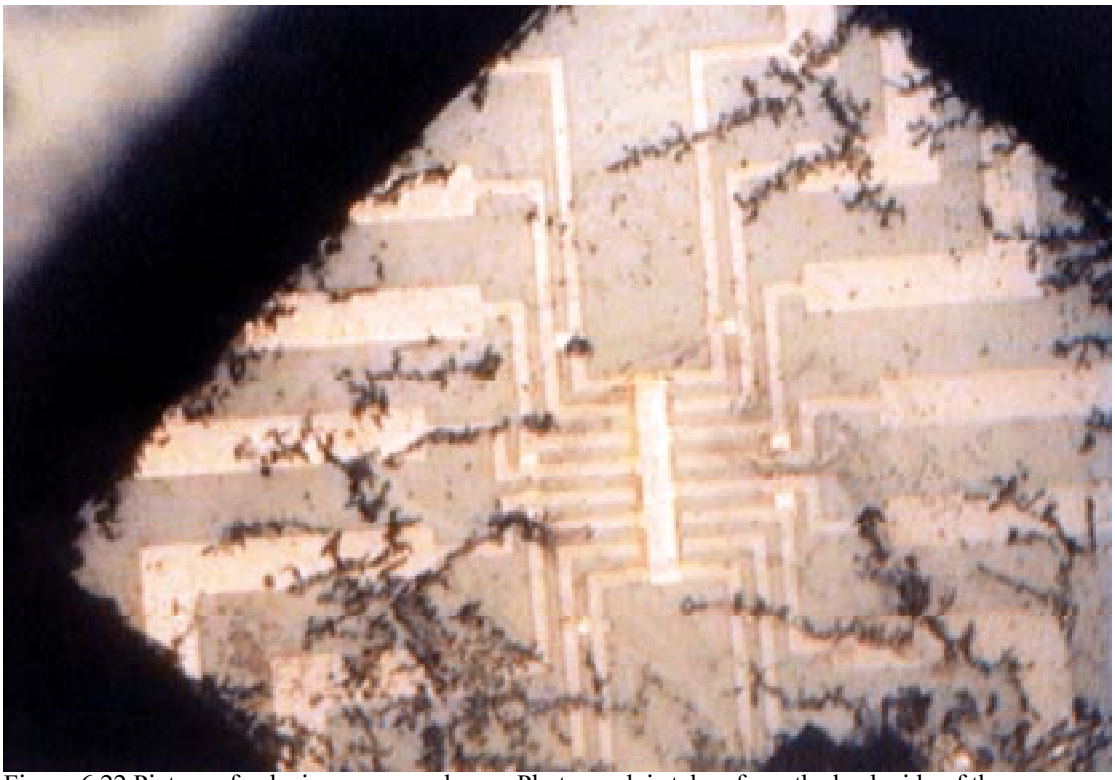

Figure 6.22 Picture of a device on a membrane. Photograph is taken from the back-side of the membrane, looking at the underside of the device. The dendrite-like dark material is Si which has not been fully removed during the etch. Picture courtesy of R.W. Moseley.

$$Si_{(s)} + 4OH^{-}_{(aq)} \xrightarrow{K^{+}_{(aq)}} SiO^{4-}_{(aq)} + 2H_{2(g)} \tag{6.12}$$

The end point of the reaction is reached after approximately 3½ hours; the etch having reached the Si_3N_4 of the front side of the substrate on which the device is fabricated. The result is a membrane of thickness 1 μm and size 0.8×0.8 mm. In figure 6.23 we show a picture of a similar device and membrane (the device photographed was produced by R.W. Moseley - the device reported here had a two electrode configuration).

During the membrane fabrication, care has to be taken to ensure that the KOH solution does not reach the topside of the chip lest the actual device is etched away. To prevent this the chip was placed in a PTFE holding clamp, designed by R.W. Moseley, and sealed using two O rings. Despite the precautions, some ingress of KOH occurred and the device outside the O ring was damaged. Fortunately this only destroyed contact pads and it was possible to wire bond directly to the 50 μm wide tracks.

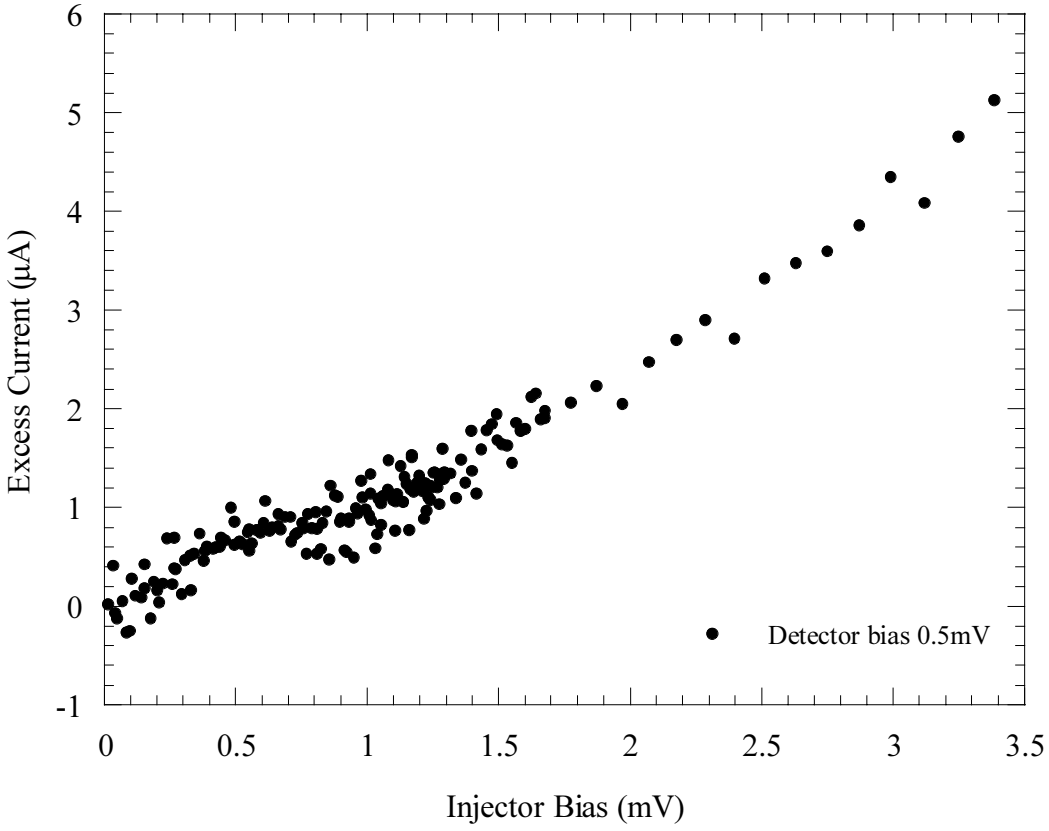

Figure 6.23 Response for a device on a membrane.

In figure 6.23, we show a typical result of the injector-detector experiments carried out after the membrane was made. The configuration chosen was one with the injector and ground junctions opposite the detector, so that with the substrate present only a weak response was observed. With the membrane present, however, the response is very pronounced. In addition, there is no evidence of the response saturating as we have reported for all the other devices. We found that a similar response was obtained for all configurations with the injector and detector on the same common electrode. Unfortunately, the quality of the junctions on the second electrode on the device was substantially degraded during the membrane fabrication so it was not possible to measure the coupling between the two common electrodes.

The implications of these results are clear; without the heat loss via the substrate, a much greater fraction of the energy deposited by the injector is retained in the electron system of the normal metal. In addition the electron system is more uniformly heated and so we lose the geometrical dependencies previously observed.

Since the response did not saturate for this device, we deduce that the saturation is a result of heat loss to the substrate and hence to the environment.

6.6 Summary and Conclusions

In this chapter, we have reported experiments to measure the change in the electron temperature during injection of heat in a thin normal metal film. Due to heat loss to the substrate, the temperature in the normal metal film is not uniform, and does not scale with either the injected current in the SIN junction used to heat the film or the injected power.

Our work on the detection of a response from a detector junction that is coupled only to the injector via the substrate indicates that the transport mechanism over distances of tens of microns is dominated by substrate phonons. This is confirmed by the measurements of detector response as a function of the injector-detector distance. We have shown that the response is independent of this distance, implying that either the propagation mechanism has a decay length substantially longer than tens of microns or the heating is uniform. Our results on the geometrical dependency would preclude the latter, and substrate phonons are the most likely candidate for the former.

For configurations where the injector and detector are separated laterally by the normal metal film, we do not see a significant increase in temperature. We attribute this to substrate phonons being absorbed by the normal metal, the energy locally heating the metal, before being lost once again to the substrate as phonons of energy k_BT.

We would conclude that our detectors are primarily sensitive to athermal substrate phonons; eventually virtually all the heat deposited by the injector must be lost to the substrate, yet our detectors only responded when there was a source of athermal 2Δ phonons in 'line of sight' –i.e. without a significant thickness of absorber between injector and detector. This type of behaviour is consistent with that reported (albeit for lower temperatures) in super conducting phase thermometers(Probst 1995), in which athermal phonons generated by absorption of a 60 keV photon in Si resulted

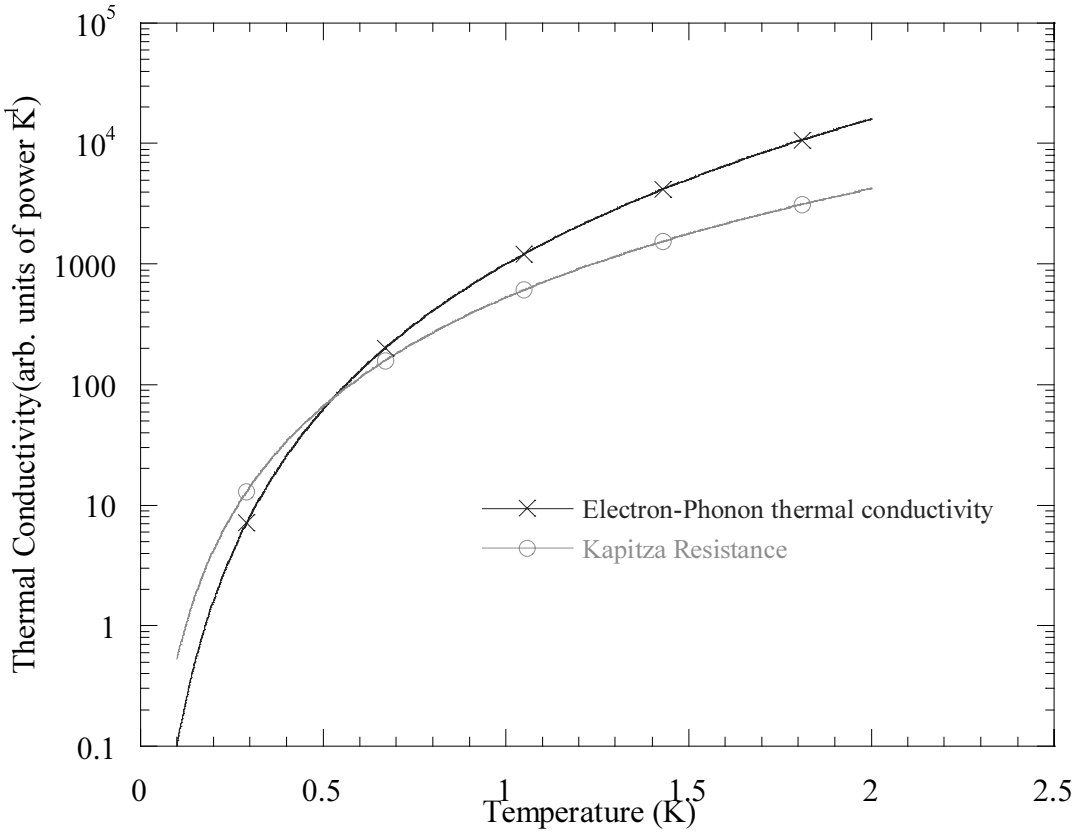

Figure 6.24 Kapitza resistance and electron-phonon power flow

in a response at a Au/Ir phase transition thermometer composed of both an athermal and a thermal phonon component.

Our results with the device on the membrane would suggest that the saturation in the response is associated with heat loss to the substrate when the local electron temperature reaches a limiting value. Heat transfer from the metal electron system to the lattice will be limited both by the thermal conductance between electrons and phonons in the metal (which since thermal conductance is the differential of power flow w.r.t. temperature, by (2.61) scales as T^4) and the Kapitza resistance between metal and substrate phonons (which scales as T^3). Using values for the Kapitza resistance between Au and sapphire from(Probst 1995) and the thermal conductivity constant between the electrons and phonons in Au from(Wellstood 1994), we show these thermal conductivities in figure 6.24. Below a certain temperature (0.5 K in figure 6.24), the thermal resistance is dominated by the electron-phonon coupling, and above it by the Kapitza resistance. Hence as we inject power into the system, at first the electron temperature will rise substantially, until the cross-over temperature is

reached, whereupon the Kapitza resistance dominates and the phonon temperature rises substantially.

Ideally, one would wish to model this accurately by solving the relevant coupled heat flow equations. In practice this is difficult as the input power to the system and the region being heated are not well defined in this experimental configuration.

CHAPTER 7

Superconductor Base SIN Devices

7.1 Introduction

In this chapter, we present the results from our work on studying coupled Superconductor-Insulator-Normal metal tunnel junction in which pairs of junctions share a common superconducting electrode.

In sections 3.3.3 and 3.3.4, we saw that a critical limiting factor in the performance of SIN tunnel junctions in Bolometer readouts was the self-heating of the device due to back-tunnelling quasiparticles and recombination phonon absorption. Both of these processes will be minimised if quasiparticles are removed quickly from the junction region. In chapter 5 we showed that with an epitaxial superconducting layer, in which the mean free path of quasiparticles is relatively long, quasiparticles may diffuse tens of microns before being lost. For the development of bolometers, however, epitaxial base layers are not possible due to constraints on the choice of substrate required to form membranes. Therefore, we need to maximise the quasiparticle lifetime. In balance with this, we also wish to retain a reasonable critical temperature and energy gap to maximise temperature sensitivity at our relatively high operating temperature of 300 mK.

The motivation, therefore, in carrying out this work has been to develop a device structure that will give an optimum quasiparticle lifetime whilst retaining an energy gap and critical temperature sufficient to allow our devices to be measured in the available apparatus.

7.1.1 Quasiparticle Scattering in Proximity Structures

In section 2.5 we presented the equations introduced by Kaplan(Kaplan 1976) to calculate the quasiparticle and phonon lifetimes in a homogeneous superconductor in thermal equilibrium, and the model of the proximity effect developed by Golubov(Golubov 1993). In a further work, Golubov(Golubov 1994) has combined his proximity effect model with calculations of quasiparticle lifetimes to develop a model of quasiparticle lifetimes in inhomogeneous superconductors. Using the same formalism as Kaplan, Golubov gives the quasiparticle lifetimes as:

$$\tau^{-1}_{phonon-emission}(\omega,\mathbf{r}) = \frac{2\pi}{\hbar Z_1(0)\left[1-f(\omega)\right]}\times$$
$$\int_0^{\omega-\Delta(\mathbf{r})} d\Omega\alpha^2(\Omega)F(\Omega)\left(\mathrm{Re}\left\{G(\mathbf{r},\omega-\Omega)\right\}-\frac{\Delta(\mathbf{r})}{\omega}\mathrm{Re}\left\{F(\mathbf{r},\omega-\Omega)\right\}\right)\times \quad (7.1)$$
$$\left[n(\Omega)+1\right]\left[1-f(\omega-\Omega)\right]$$

$$\tau^{-1}_{phonon-absorption}(\omega,\mathbf{r}) = \frac{2\pi}{\hbar Z_1(0)\left[1-f(\omega)\right]}\times$$
$$\int_0^{\infty} d\Omega\alpha^2(\Omega)F(\Omega)\left(\mathrm{Re}\left\{G(\mathbf{r},\omega+\Omega)\right\}-\frac{\Delta(\mathbf{r})}{\omega}\mathrm{Re}\left\{F(\mathbf{r},\omega-\Omega)\right\}\right)\times \quad (7.2)$$
$$n(\Omega)\left[1-f(\omega+\Omega)\right]$$

$$\tau^{-1}_{recomb}(\omega,\mathbf{r}) = \frac{2\pi}{\hbar Z_1(0)\left[1-f(\omega)\right]}\times$$
$$\int_{\omega+\Delta(\mathbf{r})}^{\infty} d\Omega\alpha^2(\Omega)F(\Omega)\left(\mathrm{Re}\left\{G(\mathbf{r},\Omega-\omega)\right\}-\frac{\Delta(\mathbf{r})}{\omega}\mathrm{Re}\left\{F(\mathbf{r},\Omega-\omega)\right\}\right)\times \quad (7.3)$$
$$\left[n(\Omega)+1\right]f(\Omega-\omega)$$

where Re{G(**r**,ω)} and Re{F(**r**,ω)} are the spatially dependent density of states of quasiparticles and pairs. In the homogeneous case, $\Delta(\mathbf{r})\rightarrow\Delta$ and Re{G(**r**,ω)} and Re{F(**r**,ω)} are given by:

$$\mathrm{Re}\left\{G(\mathbf{r},\omega)\right\} = \mathrm{Re}\left\{\frac{\omega}{\sqrt{\omega^2-\Delta^2}}\right\}$$
$$\mathrm{Re}\left\{F(\mathbf{r},\omega)\right\} = \mathrm{Re}\left\{\frac{\Delta}{\sqrt{\omega^2-\Delta^2}}\right\} \quad (7.4)$$

and the equations given by Kaplan(Kaplan 1976), (2.51), (2.52) and (2.54), are obtained. In the proximity model G and F need to be calculated before being inserted into (7.1),(7.2) and (7.3).

Golubov *et al.* were primarily interested in the process of quasiparticle trapping in a proximity structure in order to model the performance of their STJ detectors more accurately. They have concentrated therefore, in addition to the tunnelling time for quasiparticles, on the processes of quasiparticle scattering, both of quasiparticles at an energy of $\Delta(\mathbf{r}\rightarrow\infty)$ emitting a phonon to enter the trap and those already in the trap absorbing phonons to de-trap.

We are more interested in the quasiparticle lifetime against recombination in the proximity structure in order to calculate an effective lifetime for quasiparticles at the gap edge in the proximitised layer. In our particular applications, quasiparticles may be taken to be injected into the structure primarily at the gap edge, since the SIN tunnel junction will generally be biased so that $eV \lesssim \Delta$.

A simpler approach to estimating the quasiparticle lifetimes in a proximity structure was taken by Warburton(Warburton 1993a). He avoided the need to calculate the density of states Re{F(**r**,ω)} and Re{G(**r**,ω)} by using an experimentally determined quasiparticle density of states and replacing the BCS density of states in (7.1)-(7.3) with this empirical density of states. This is strictly incorrect, since the density of quasiparticle states and density of pair states are found from the Green's function of a superconductor and should satisfy:

$$\begin{aligned} &Z^2(\omega)\omega^2 - \varepsilon_p^2 - \varphi^2(\omega) = 0 \qquad ,\varphi(\omega)/Z(\omega) = \Delta(\omega) \\ &\frac{Z^2(\omega)}{\varepsilon_p^2}\omega^2 - \frac{Z^2(\omega)}{\varepsilon_p^2}\Delta^2 = 1 \\ &G^2 - F^2 = 1 \end{aligned} \tag{7.5}$$

However, the advantage is that it does not make any assumptions on the model of proximity effect used. Warburton used SIS'S tunnel junctions in his experiments and so employed a numerical method developed by Blamire(Blamire 1993) to de-convolute the density of quasiparticle states in the S'S electrode. In our devices, we use a SS'IN tunnel junction and by measuring a current-voltage characteristic at sufficiently low temperature, can extract the density of states directly from the differential conductance.

Using current-voltage characteristic data to extract a density of states, however, only gives us one density of states in a situation where we expect there to be a spatial variation. We assume that our measured tunnelling density of states is in fact the density of states throughout the trap region. This would seem logical since one expects tunnelling particles to tunnel to states close to the barrier. Furthermore, in the thin trap limit that we expect to be working in, the dimensions are less than the coherence length and so the superconducting properties are expected to be constant over the trap thickness.

7.1.2 Quasiparticle Transport in Proximity Structures

We have the following model of quasiparticle transport in our devices. Quasiparticles are injected via a tunnel junction at or close to the reduced energy gap due to the presence of a proximitised layer. From the model of Golubov, we expect the gap parameter to vary as shown schematically in figure 2.19. The value of the energy gap in the trap layer is determined by the proximity parameters γ_m and γ_b (see section 2.6.3). For simplicity, we will assume that the interfacial barrier given by γ_b is small. This is expected to be the case in a Nb/Al system deposited under clean conditions, such as we have used.

Quasiparticles are then free to diffuse in the structure, however they are confined close to the barrier layer by the fact that they would need to absorb a phonon in order to escape the trap. At the low temperatures ($\lesssim$500 mK) we expect in our system, the number of phonons with sufficient energy to de-trap a quasiparticle is very low. The quasiparticles therefore diffuse through the layer, being lost by recombination and tunnelling events. Given the disparity between the characteristic quasiparticle lifetimes in our two materials (Nb and Al), we expect any quasiparticles that enter the Nb region to be lost substantially faster than those in the Al region. Phonons produced by recombination events may break pairs to create further quasiparticles. However, this is less likely unless excellent phonon trapping can be achieved as the characteristic phonon lifetime is long in Al and the recombination phonons are sub 2Δ phonons outside the trap. This phonon trapping is actually easy to provide, since a SIN detector should be mounted on a membrane to ensure that all the deposited energy is absorbed and thermalised in the normal metal region, so phonon loss to the substrate is minimal. The only difficulty is that the recombination phonons are likely to couple back to the normal metal region.

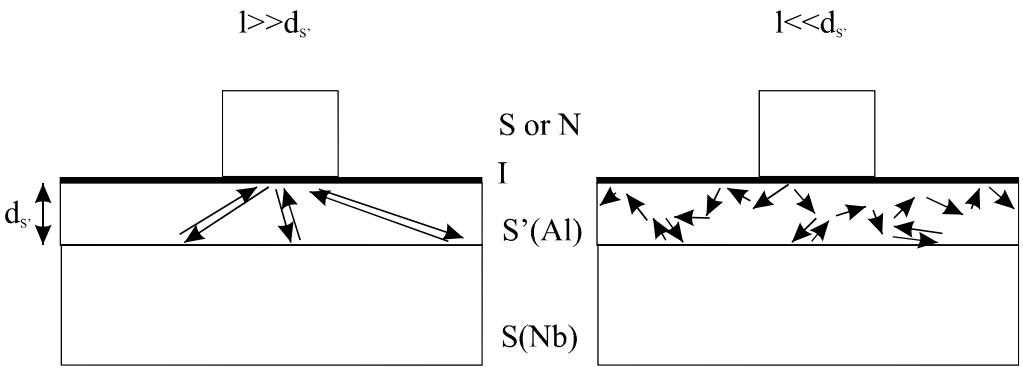

Figure 7.1 Andreev reflection limited quasiparticle diffusion in a superconductor bilayer in the clean and dirty limits.

In some situations, the lateral diffusion of quasiparticles in a proximity structure may be hindered. This occurs in cases where the mean free path of quasiparticles in the trap layer is much longer than the thickness of the trap layer. Under these circumstances, quasiparticles may undergo Andreev reflection at the interface with the trap and bulk superconductor rather than specular reflection. Such quasiparticles will be reflected along a time-reversed track - i.e. back to where they originated from (figure 7.1). Thus, quasiparticles tend to be confined to close to their point of injection to the superconductor. This effect has been demonstrated by Warburton, using epitaxial Ta traps on Nb layers. In our case however, we expect the mean free path of quasiparticles to be of order of 10 nm (which is nearly the same thickness as the trap) as the Al traps are not epitaxial.

The conclusion then, would be that although such a device structure will enhance the quasiparticle lifetimes, the trapping of quasiparticles close to the junction in a thin layer will encourage back-tunnelling and absorption of recombination phonons. This device structure is, however, useful for studying quasiparticle dynamics in a proximity structure where we will use a second SIN tunnel junction to attempt to observe phonons produced from recombination events at some distance from the quasiparticle injection point.

7.2 Device production

7.2.1 Film Deposition

The films deposited to produce the devices reported in this chapter were deposited by the author using the ultra-high vacuum deposition system described in chapter 4.

As for the films used in the devices in the previous chapter, the superconducting layer was polycrystalline. Unlike the devices in the previous chapter the counter-electrode was composed of a thin (2-3 nm) Al layer and a rather thicker tungsten layer. This change in the device structure was made to overcome a problem with the previous structure. An incomplete milling of the Nb capping layer could result in the thin layer of Al in the counter-electrode having a true superconducting character rather than having proximitised T_c lower than the measurement temperature, and the resultant junction therefore having a degree of SIS characteristic to it.

Initial experiments to deposit W directly on the AlO_x barrier were carried out, however it was found that it was not possible to produce high quality junctions. It is not clear whether this was due to damage of the barrier during deposition, or during processing; at the time these experiments were made, a new photoresist had been introduced and the processing parameters had not been fully optimised. The final deposition sequence used was as follows:

- 2 minutes at 60 W Nb, argon pressure 0.5 Pa
- 13 minutes at 60 W Nb, pressure 0.8 Pa
- Variable time at 16.7 W Al, pressure 0.8 Pa
- 1 hour oxidation at 1 kPa pure O_2
- 5 minutes at 10 W Al, pressure 0.74 Pa
- 12 minutes at 30 W W, pressure 1.2 Pa

The substrate material used for these experiments was r-plane sapphire. Although it was intended to move to Si_3N_4 membranes, due to fabrication difficulties

of both devices and membranes, this was not possible. Prior to deposition, the substrates were cleaned as has been described in the previous chapters and then mounted on a sputter deposition flange with a rotating sample stage. The stage was rotated at 1 rpm during all but the base electrode Al deposition stage. The stage was driven by a stepper motor controlled by computer with a software program written by M.G. Blamire and modified slightly by the author. This program allowed the speed of the stage to be varied within one revolution, so that samples placed at different angular positions would be exposed to a sputter target for different lengths of time. By using this technique, it was possible to grow batches of films in which all the conditions were the same bar the thickness of the lower Al layer. At the standard rotation rate of 1 rpm, the deposition rates were 0.1 $nmW^{-1}min^{-1}$ for Nb, 0.06 $nmW^{-1}min^{-1}$ for Al. The rate was not measured for W, but was assumed to be similar to Ta which was known to be approximately twice that of Nb.

The films then had Nb base thickness of 90 nm, lower Al layer thicknesses of 20, 10 and 5 nm, barrier thickness of order 1 nm, upper Al thicknesses of 3 nm and W thicknesses of around 70 nm.

7.2.2 Device Fabrication

We refer to the detailed descriptions of the fabrication stages given in chapter 4. Like the devices described in chapter 5, the devices used for this work were produced using the CAM-13 mask set (figure 5.1) designed by P.A. Warburton, however the fabrication stages were slightly different. It was found during development of the fabrication for these devices that it was not possible to define junctions successfully by selective anodisation of the tungsten counter-electrode layer. It is believed that this was due to the excess compressive strain exerted by the increase in lattice parameter between the oxide and metal. It should be noted that the deposition conditions used already gave a compressive stress in the W film(Moseley 1998). Rather than use the mesa definition mask developed by the author and used in for the devices in chapter 5, a semi-self-aligned technique was employed. For all the devices reported here the spacing between the pairs of junctions on each of the common electrodes was 8 μm. The stages in the processing were as follows.

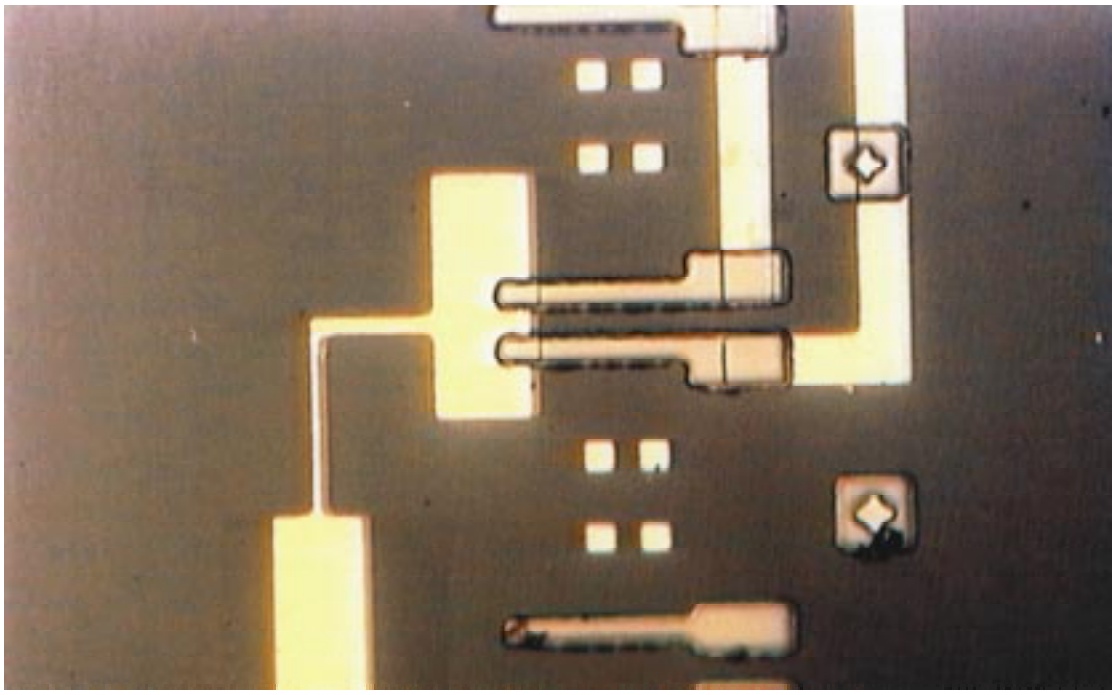

Figure 7.2 Detail of a completed device showing the CAM13 mask offset from base by 2 μm to allow etching and anodisation of one edge.

- Base definition and etch (4.3.2)
- Resist removal
- Reapplication of the base definition mask, but offset by 1-2 μm (see figure 7.2) and a counter-electrode/mesa definition etch (4.3.3) and anodisation of the exposed Al/Nb edge.
- Resist removal
- Wiring layer definition

- Wiring layer deposition (5 minutes Au sputter deposition in the high vacuum deposition system at approximately 12 W, 1.5-2 Pa Ar, then 30 sec. Nb deposition at 150 W, 0.7 Pa Ar).
  - Wiring layer lift off and resist removal
  - Counter-electrode removal

The final stage, counter-electrode removal, was to ensure that the pairs of junctions on each common electrode were only connected though the common base electrode and not through the counter-electrode. Initial trials using a CF_4 plasma

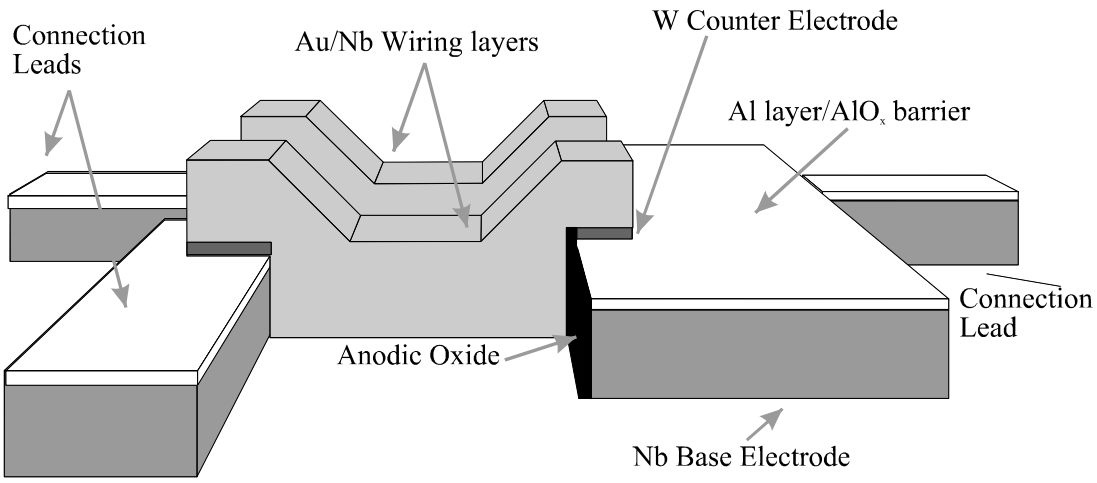

Figure 7.3 Schematic of one common base electrode and pair of junctions on a completed CAM13 SIN device.

etcher were unable to prevent the two junctions from being coupled via the counter-electrode. This was believed to be due to the presence of the 3 nm of Al above the barrier in the counter-electrode (Al is an effective etch-stop for CF_4). Rather than use a more reactive etching gas such as $SiCl_6$ to remove this Al, the counter-electrode was removed by Ar ion milling. It was found that using only a few seconds milling (beam voltage 800 V, beam current density approximately 6 mA cm^{-2}, sample-ion gun distance 10 cm) that the counter-electrode could be entirely removed and yet leave sufficient base layer Al to be optically visible even for the thinnest Al layers.

During this process some of the Nb deposited during the wiring layer deposition was also removed, however this layer was sufficiently thick that enough Nb remained that its critical current density at 4.2 K was larger than the typical maximum current used (of the order of a few mA). The function of this superconducting layer was to reduce the series resistance of the device and to ensure that any joule heating of the device was minimised and localised to the actual junction area.

A schematic of the completed device structure is shown in figure 7.3.

7.3 Characterisation

Following fabrication, the devices were initially characterised at 4.2 K to verify the success of fabrication. It was found that for successful devices the

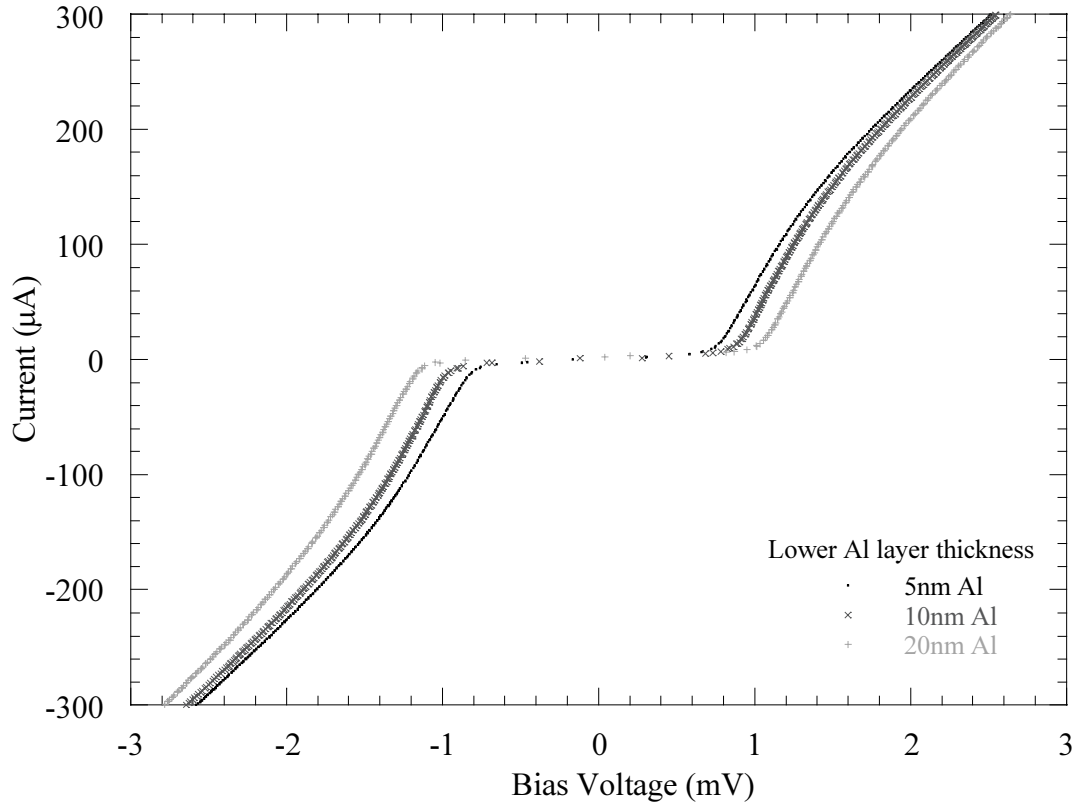

Figure 7.4 Current-voltage characteristics for devices with differing lower Al layer thicknesses.

differential conductance at zero bias to that at high bias (i.e. the normalised differential conductance given by(2.38)) was thermally limited. Following this initial testing, the devices were re-measured using the Heliox™ ^{3}He probe at temperatures between 350 mK and 7 K.

7.3.1 Current-Voltage Characteristics

Typical current-voltage characteristics for devices with the three different thicknesses of lower Al layer and at a temperature of approximately 0.5 K are shown in figure 7.4. Prior to measuring these devices, we had improved the RF filtering in our measurement set-up, and this gave a noticeable increase in the sub-gap resistance that we were able to measure. As one would expect, the increase in proximity effect due to thicker Al layers gave lower measured energy gaps and higher sub-gap currents.

In practice, we found that the sub-gap resistance (i.e. differential resistance measured at zero bias) was limited to approximately 150 times the normal state resistance. Among the factors that can reduce the sub-gap resistance are micro-shorts in the tunnel barrier, flux threading the junction to create Abriskov vortices in the S electrode, an inhomogeneous energy gap or self-heating effects. The latter factor will be discussed later in this chapter; of the first two, micro-shorts have been a problem in fabricating the test devices for this work and may well be responsible for the ultimate limit in sub-gap resistance.

7.3.2 Density of States

The density of states in the superconducting electrode of an SIN tunnel junction device may be found directly from the current-voltage characteristic if the temperature is sufficiently low using (2.36). At finite temperatures, the density of states is smeared by convolution with a gaussian-like function of width $\approx \pm 2k_BT$. At the base temperature of our measurement system this smearing is approximately 0.06 meV. We extracted the density of states for our devices, therefore, from the differential conductance as a function of the bias voltage at base temperature (figure 7.5).

We compared our measured density of states with those for the Golubov model of the proximity effect for both S-S' and S-N structures as published in the literature((Golubov 1988; Le Grand 1994a)) also shown in figure 7.5. The theoretical densities of states that have been plotted are for the superconductor S at the S-N or S-S' layer. In the absence of a potential barrier at the interface, which as we have stated previously is expected to be the case in the Nb/Al system, the normalised density of states in the two layers at the interface are equal. We have further assumed that the measured tunnel current is determined by the density of states in the Al layer (which corresponds to the S' or N layer), thus we can directly compare the experimental data and theoretical densities of states.

As stated above, we observe an effective energy gap that decreases with increasing thickness of Al (1.17 meV for 5 nm Al, 0.99 meV for 10 nm and 0.76 meV for 5 nm). The measured density of states has only one peak, and that at an energy

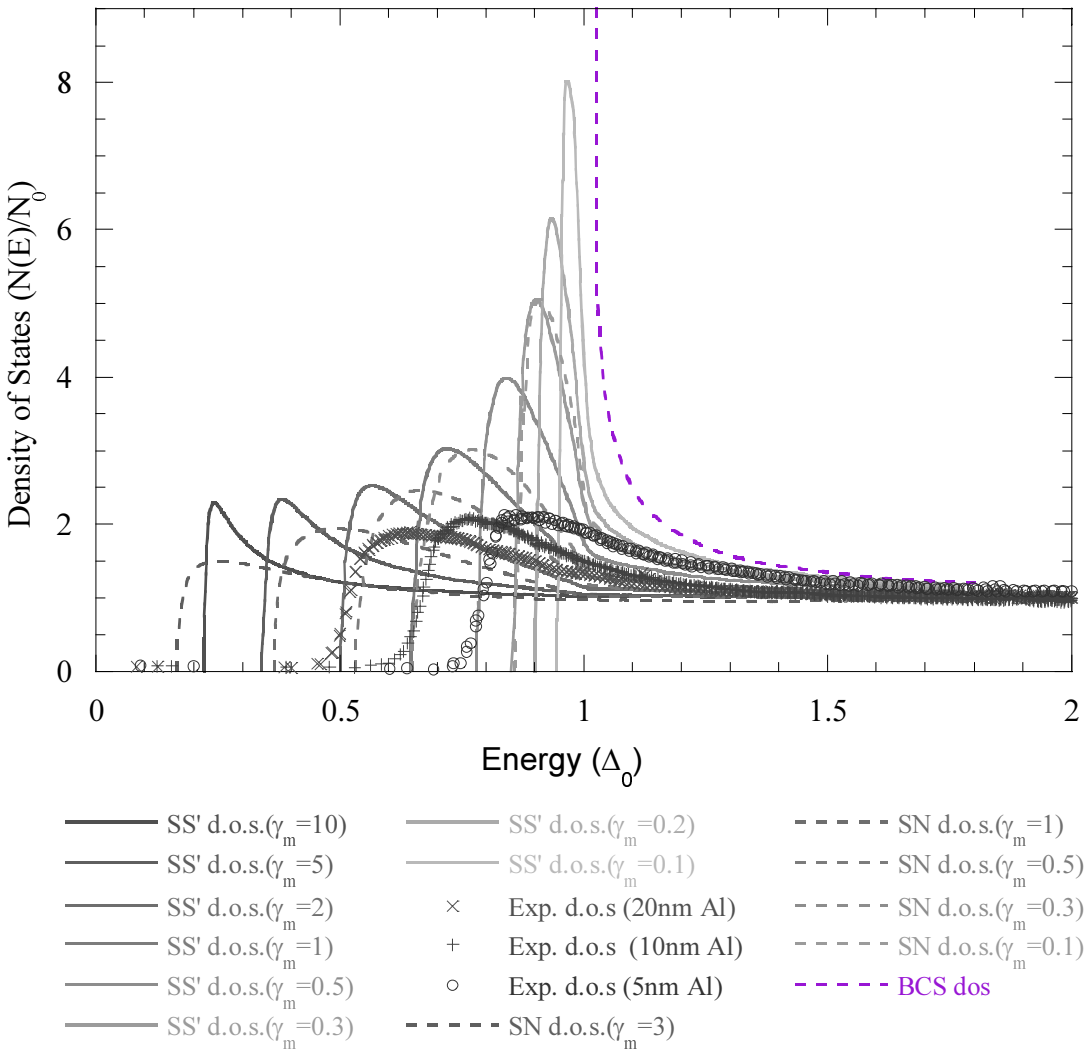

Figure 7.5 Experimental and theoretical density of states

close to the measured energy gap. Under the McMillan model of the proximity effect there are two peaks in the density of states, one at the effective energy gap and one at the non-proximitised energy gap. Since we only observe the one peak, we conclude that the Golubov model is more appropriate, as we would expect given the highly transparent interface between Nb and Al. The experimental data have 'tails' that extend below the steepest drop in the density of states. Whilst this could be due to gap inhomogeneity, the width of the 'tails' are around 0.1 meV which is close to the smearing effect due to the non-zero base temperature at which the data was measured.

Our experimental data shows an increase in the height of the peak in the density of states as the proximity effect is reduced (i.e. for thinner layers of Al). This

increase is not as pronounced, however, as would be expected from the Golubov model for either S-S' or S-N type interfaces. In addition, in our data the shape of the peak in the density of states is more reminiscent of the S-N type curves than the S-S' curves. This is despite the fact that the T_c of Al layers of these thicknesses should be approximately 4 times greater than the experimental temperature. A similar result has been reported by other workers(Zhao 1997) also using SIN tunnel junctions to directly measure the density of states in a Nb/Al proximity structure.

If we assume that the Al layer in our devices is genuinely acting as a normal metal layer, as opposed to the Golubov model for S-S' layers being substantially incorrect, then we can advance two possible reasons for it being in the normal state. Firstly, we might suspect the purity of the film - the inclusion of even a trace magnetic impurity in the Al layers could have sufficient effect to suppress T_c of the Al to below our measurement temperature. In that case, however, one would expect the energy gap in our devices to be significantly reduced, as the Nb would also have a reduced energy gap due to the magnetic impurities. If we assumed that this was not the case, and that our devices were able to be described by the theory of S-N proximity structures with a bulk, pure Nb Δ, then we would find that $\gamma_m/d_{Al} \approx 0.03\ nm^{-1}$, which is remarkably close to the value of $0.032\ nm^{-1}$ reported in the literature for SIS devices(Golubov 1995). Secondly, we might imagine that our device is suffering from sufficiently extreme self-heating that the Al is held above its T_c. This heating could result from back tunnelling of quasiparticles, re-absorption of recombination phonons or from simple Joule heating due to non-ideal junction characteristics. In all these cases, the normal metal electron system is being directly heated, which in turn couples to the phonon system. If self heating is the limiting factor then this should be apparent from the sub-gap resistance (or equally conductance) as a function of temperature.

7.3.3 Differential Conductance

The differential conductance of an SIN tunnel junction when normalised to the normal state resistance can be found for a BCS distribution of states from equation (2.38). For $\Delta >> k_B T$,

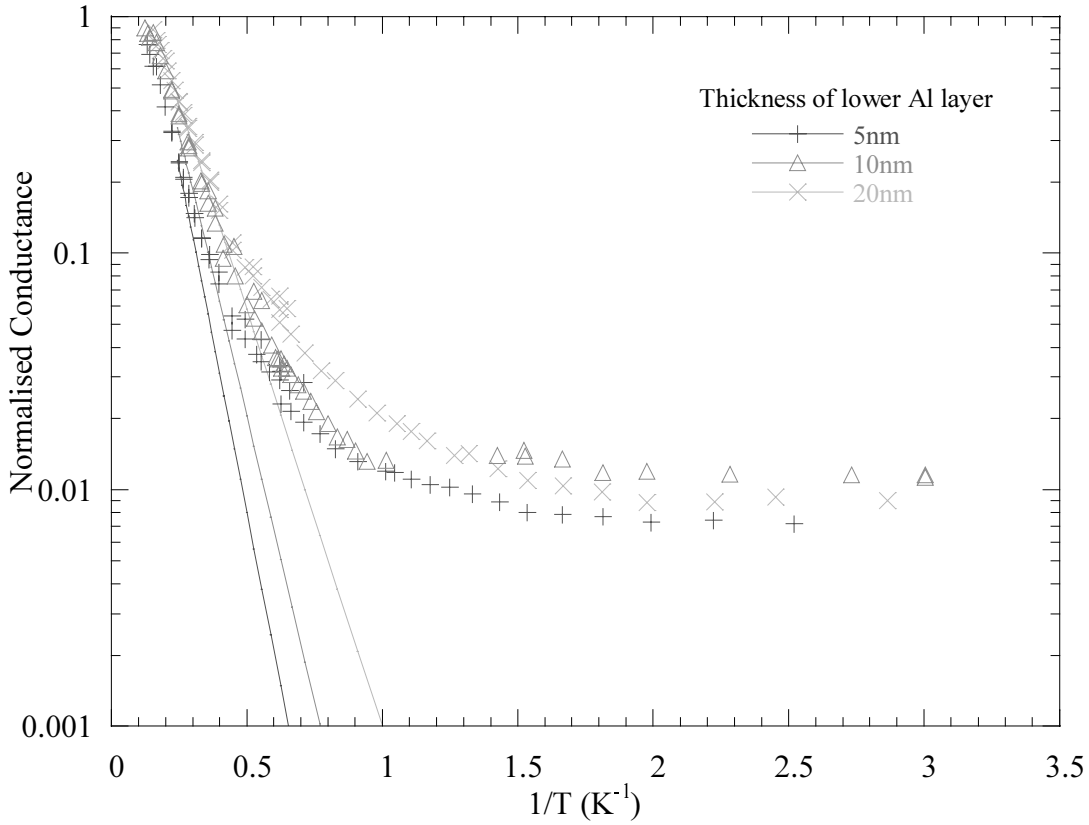

Figure 7.6 Differential conductance versus 1/T, modelled and experimental for the three Al thicknesses.

$$\left.\frac{G_{SIN}(V)}{G_N}\right|_{V\to 0} \propto \exp\left(-\frac{\Delta}{k_B T}\right) \tag{7.6}$$

so that a plot of log(G_{SIN}) versus 1/T will give a straight line. For a device that is limited by a leakage current (e.g. due to an ohmic micro-short) below a certain temperature the conductance is constant. In the case of a device that is being strongly self-heated then again the conductance would be constant. In general, however, we would expect that any self-heating mechanism would be temperature dependent since the thermal conductivity is a function of temperature and that will determine the actual localised electron temperature at the junction.

In figure 7.6 we plot the differential conductance at zero bias (normalised to the normal state conductance) against 1/T for representative devices for the three different thicknesses of Al used. It is immediately obvious from the curvature in the plots (given that the conductance is plotted on a logarithmic scale) that the conductance is not thermally limited for most of the temperature range. The ultimate

limit gives us the maximum sub-gap resistance to normal state resistance ratio of approximately 150. The fact that the limit is nearly the same for all the devices would suggest that it is not due to processing introduced defects in the film, but is a consequence of intrinsic pinholes in the barrier or self-heating or trapped flux. For whatever reason we are ultimately limited, the very fact that we see a monotonic decrease in the sub-gap conductance down to a sample holder temperature of 0.5 K, indicates that the junction area is being cooled until this point. On the other hand the curvature indicates that the measured sample holder temperature and actual junction temperature are not identical, i.e. there is self heating.

To examine this, we used the density of states that we had extracted from current-voltage characteristic measurements to calculate current-voltage characteristics of known normal electrode temperature. This merely involved substituting the experimentally measured density of states for the bcs density of states in (2.34). To facilitate the calculations it was necessary to construct an interpolation table, so that the density of states could be evaluated at arbitrary energies. Furthermore, it was assumed that for quasiparticle energies greater than the range of the experimental data the normalised density of states was exactly one. Despite smoothing the experimental data using a Savitzky-Golay filter, residual noise in the data resulted in an occasional lack of accuracy in the numerical integration, leading to a number of obvious 'glitches' in the calculated current-voltage characteristics. Normalised differential conductance for the calculated current-voltage characteristics were found and have been plotted in figure 7.6. It is apparent that the local electron temperature at the junction is substantially greater than the measured sample temperature.

In figure 7.7 we plot the measured sample holder temperature against the inferred electron temperature from the calculated current-voltage characteristics. The device with a 20 nm Al film clearly has a lower limiting junction temperature relative to the 5 nm Al device (1.37 K v 1.97 K). This alone could just be due to the fact that for a given conductance (e.g. due to leakage) the device with the smaller energy gap will be at the lower temperature. In our data, however, the 20 nm Al device deviates from the line of equal sample and junction temperatures less for all temperatures. In

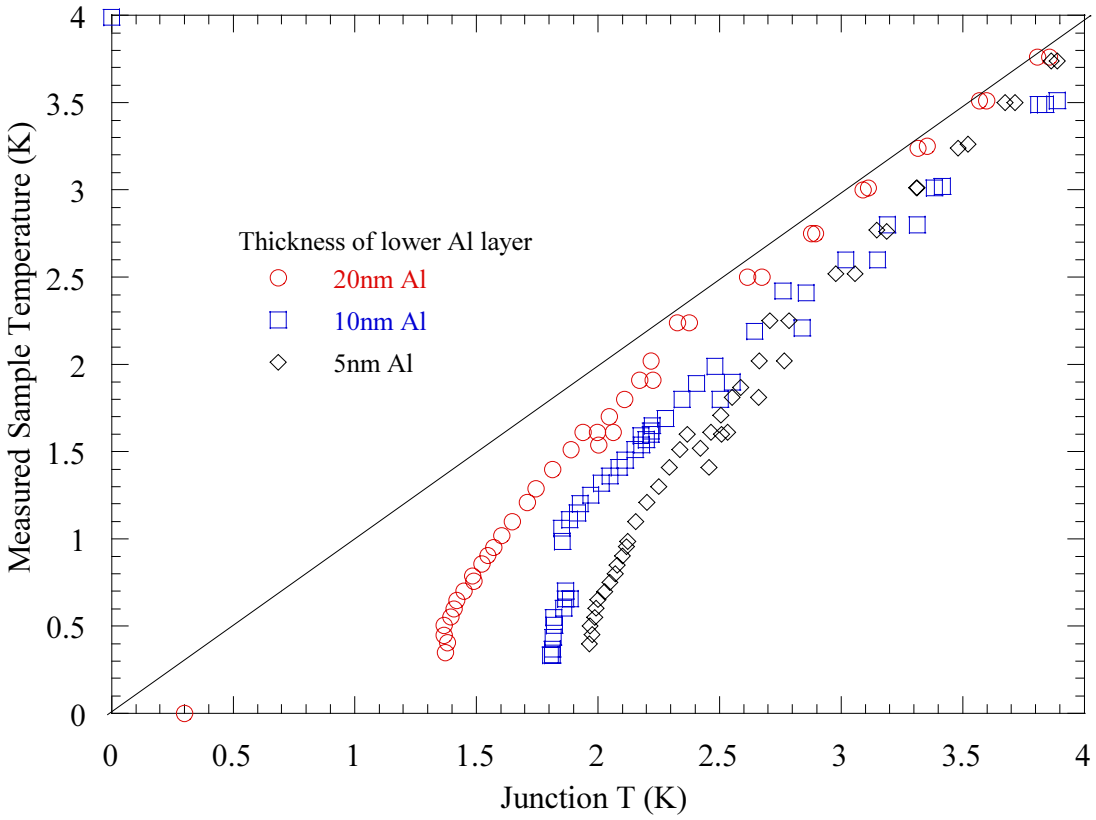

Figure 7.7 Sample temperature versus inferred junction temperature for the three Al layer thicknesses. The line indicates the no-self heating limit where the junction and measured temperature are equal.

other words, the 20 nm Al device seems not to be self-heating to the same extent as the 5 nm Al device. If this is the case then in the devices with thicker Al layers there are fewer quasiparticles back-tunnelling or undergoing recombination events with the recombination phonons being absorbed in the normal metal. This naturally leads us to ask how the quasiparticle lifetimes differ between the devices.

7.3.4 Calculation of Quasiparticle Scattering Rates

As we discussed in section 7.1.1, it is possible to calculate the quasiparticle scattering times for thermal equilibrium populations of quasiparticles by using the theory of Kaplan(Kaplan 1976) but inserting the appropriate spatially varying functions for the normal and anomalous Green's functions for the superconducting electrode. A simpler, albeit not strictly correct, approach is to substitute only the quasiparticle density of states and use Kaplan's equations in their original form (see section 2.5). In this case one is effectively assuming that the real part of the

anomalous Green's function is directly related to the real part of the normal Green's function which describes the quasiparticle density of states. For simplicity, we have used this method to estimate the quasiparticle lifetimes in our devices.

We have calculated the quasiparticle lifetime against phonon emission and absorption and against recombination by direct substitution of our experimental density of states extracted from the current-voltage characteristics of our devices at low temperatures into (2.51), (2.52) and (2.54). These equations also include coherence terms like:

$$\left(1-\frac{\Delta^2}{\omega(\omega-\Omega)}\right) \tag{7.7}$$

for which we replaced the Δ term with the effective energy gap as measured from the density of states. Likewise, the limits for calculating the phonon emission and recombination times include a factor of Δ (reflecting the fact that a quasiparticle can only scatter to the gap edge and can only recombine with another quasiparticle above the energy gap) that we replaced with the effective energy gap. Since we are interested primarily in the lifetimes for quasiparticles within only a few Δ of the energy gap, we limited our investigation to quasiparticles with energies of less than 4 meV.

Figure 7.8 shows the results of the calculations for our devices for temperatures of 0.3 K, to 4.3 K. Our calculated lifetimes are in terms of the characteristic lifetime for quasiparticles τ_0, which is dependent on material parameters. Since we have assumed that the density of states in the Al is the same as the density of states at the Nb/Al interface, we normalise our results against τ_0(Al) for quasiparticles in the Al layer and against τ_0(Nb) for quasiparticles at the Nb/Al interface.

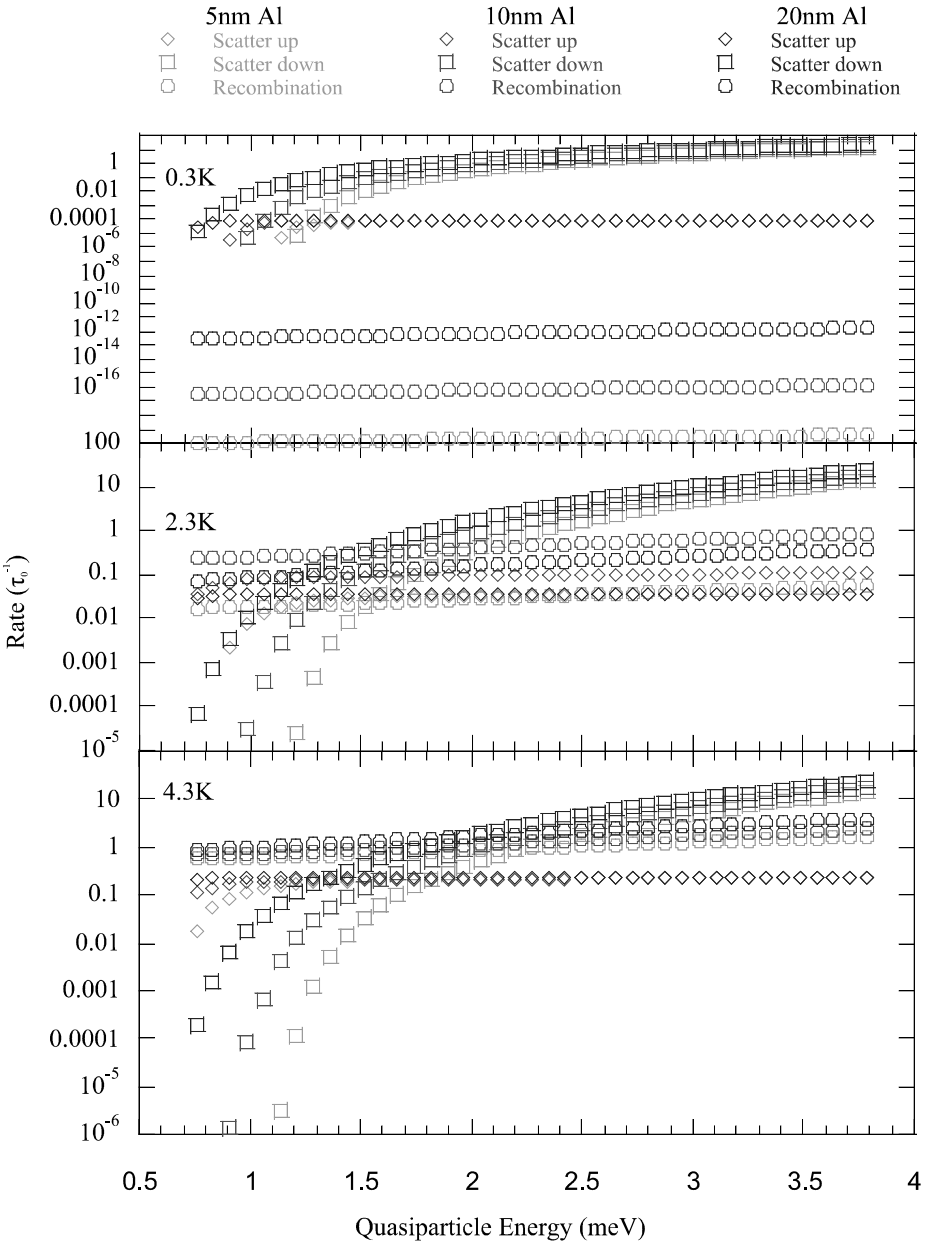

Figure 7.8 Calculated quasiparticle lifetimes for temperatures of 0.3, 2.3 and 4.3 K.

We see that the lifetime against phonon absorption is not strongly affected by either the change in the density of states (beyond the obvious fact that the minimum energy of quasiparticles must increase with increasing energy gap) or the quasiparticle energy. This is readily understood by considering that the limiting factor in the lifetime against absorption is the population of thermal phonons to be absorbed, which is only dependent on the temperature (since the phonon density of states is rolled up into τ_0). In contrast, the lifetime against phonon emission is determined by the density of states into which a quasiparticle can scatter. Thus, the lifetime against

phonon emission increases for quasiparticles nearer the energy gap since there are no states to which the quasiparticles could scatter. The recombination lifetime is dominated by the density of quasiparticles at the gap edge. This is sensitive to the density of states, particularly at low temperatures, since even a small reduction in the minimum energy that a quasiparticle can occupy will dramatically increase the occupation fraction of quasiparticles and thus reduce the recombination time. At 0.3 K, we see that there is a difference of eight orders of magnitude between the 5 nm Al device and the 20 nm Al device in recombination lifetime. As the temperature is increased this difference is reduced as the difference in energy gaps becomes smaller relative to k_BT. At 2.3 K the difference is less than 2 orders of magnitude and at 4.3 K less than one.

Given these results, how do we explain our result that the 20 nm Al device showed less self-heating than the 5 nm Al ? After, all the recombination rates would seem to suggest that recombination phonon re-absorption should be worse for the thicker Al layer devices. Since the characteristic lifetime for quasiparticles in Nb is orders of magnitude faster than for Al, most of the recombination events will occur for quasiparticles that have left the Al region. Therefore, the limiting factor for recombination is likely to be the loss from the Al layer and not the recombination rate within the Al. The loss rate from a layer of thickness d should scale as d^{-1}, therefore the thicker Al layer devices should in fact show less recombination events than the thinner ones, so long as the temperature is sufficiently high that quasiparticle recombination is rapid.

7.4 Injection Detection Experiments

The motivation in carrying out these experiments was to determine if any component of the heating at a junction could be attributed to localised recombination of quasiparticles injected from a second junction close by. In this section, we report the results of these experiments.

7.4.1 Experimental

The injection-detection experiments were carried out in our Oxford Instruments Heliox™ probe at a temperature of 0.35 K. The method of the experiments was similar to that described in previous chapters, the current-voltage characteristic of one junction being monitored whilst a constant current was injected via a second junction. The detector current-voltage characteristics were acquired and recorded using a LabVIEW™ program and analysed off-line.

In addition to these measurements, we sought a method to allow a more rapid acquisition of data to characterise the response of our devices to an injection current. To this end, we also measured the voltage across the detector junction which was biased using a small constant current (such that the detector was biased in the sub-gap region), whilst sweeping a large current through the injector. In the limit that the sub-gap portion of the detector current-voltage characteristic was linear, this voltage measurement was directly proportional to the sub-gap resistance, thus we can readily convert our measurements to ϑ (defined in (6.3)). This method had the advantage that the form of the response could be seen whilst the acquisition was performed in addition to requiring significantly less storage space.

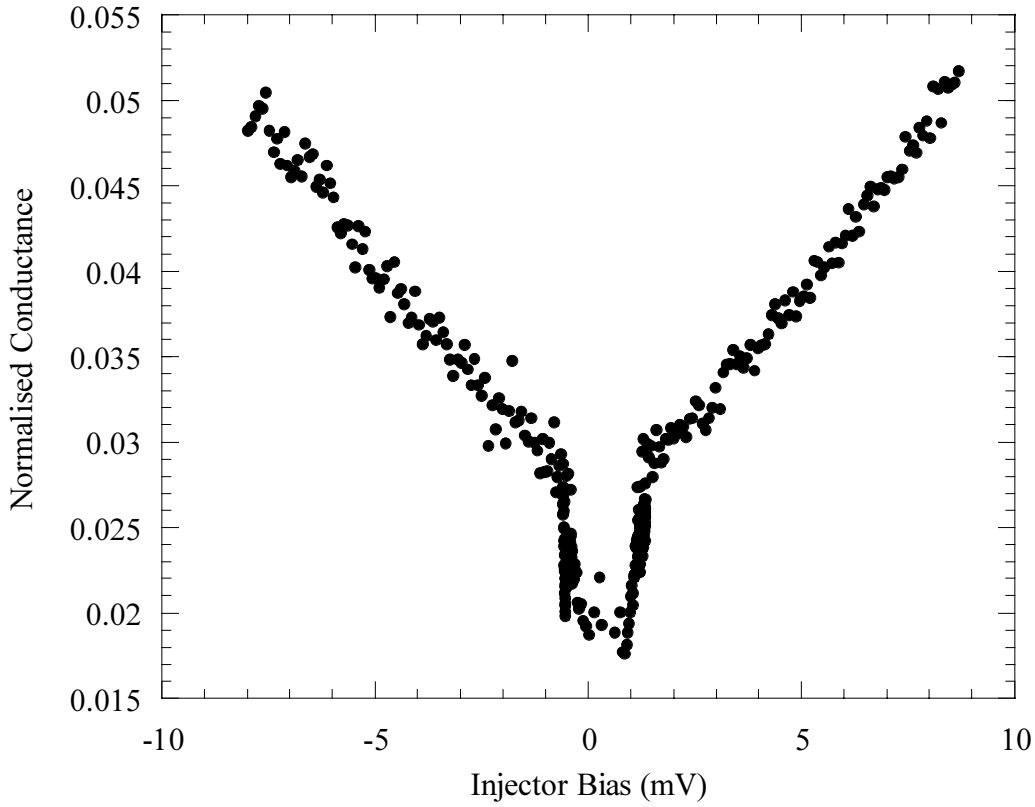

Figure 7.9 Normalised conductance versus injector bias. Lower Al layer thickness was 20 nm.

7.4.2 Results

A typical result of normalised conductance (ϑ) as a function of the injector bias is shown in figure 7.9. Qualitatively similar results were obtained independently of the configuration - i.e. whether the injector was the junction on the same common base as the detector or not, and independently of the Al layer thickness. The most striking element of these results is that unlike the similar results reported in the previous chapter, there is no evidence of saturation in ϑ at high bias. We retain the sharp increase as the injector is biases past the energy gap for the measurement shown in figure 7.9, this was not consistently observed for all configurations measured.

Figure 7.10 shows a plot of the shift in detector bias for a constant biased detector as the injector junction is biased over a range of ±12 mV. As discussed above, we can use this data to obtain an estimate of the normalised conductance changes. The curvature in figure 7.10 suggests that the normalised conductance was scaling with the injector power, so for the remainder of the results we plot against

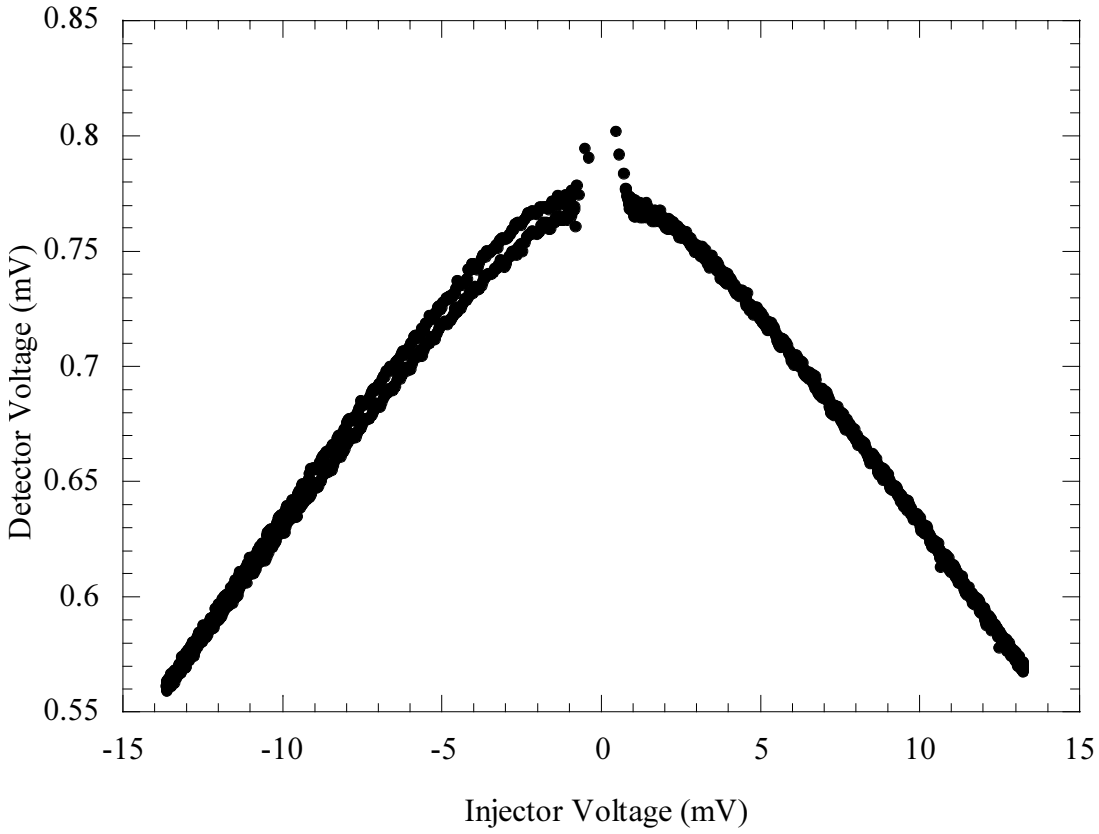

Figure 7.10 Detector voltage (detector current=3 μA) versus injector bias. Lower Al layer thickness for this device was 20 nm.

injector power rather than bias. We stated above that we were unable to distinguish between the injector immediately adjacent to the detector and on a different base electrode area. In figure 7.11 we plot the normalised conductance against injector power a range of the injector and detector distances (i.e. injector on each of the four common base areas on each device). As is readily apparent, none of the devices were sensitive to any effect of local injection of significant numbers of quasiparticles.

Clearly, the devices must have been responding only to substrate mediated phonons since they respond equally to injection in the same common electrode and to injection at some distance. From our work in the previous chapter, we have seen that our SIN tunnel junctions are very sensitive to athermal 2Δ phonons which propagate through the substrate, and we suggest that the devices respond to these rather than to an increase in the sample temperature. This follows as the solution to the three dimensional heat flow equation for a semi-infinite slab for a continuous heating at a point gives a temperature rise that is inversely proportional to distance from the point

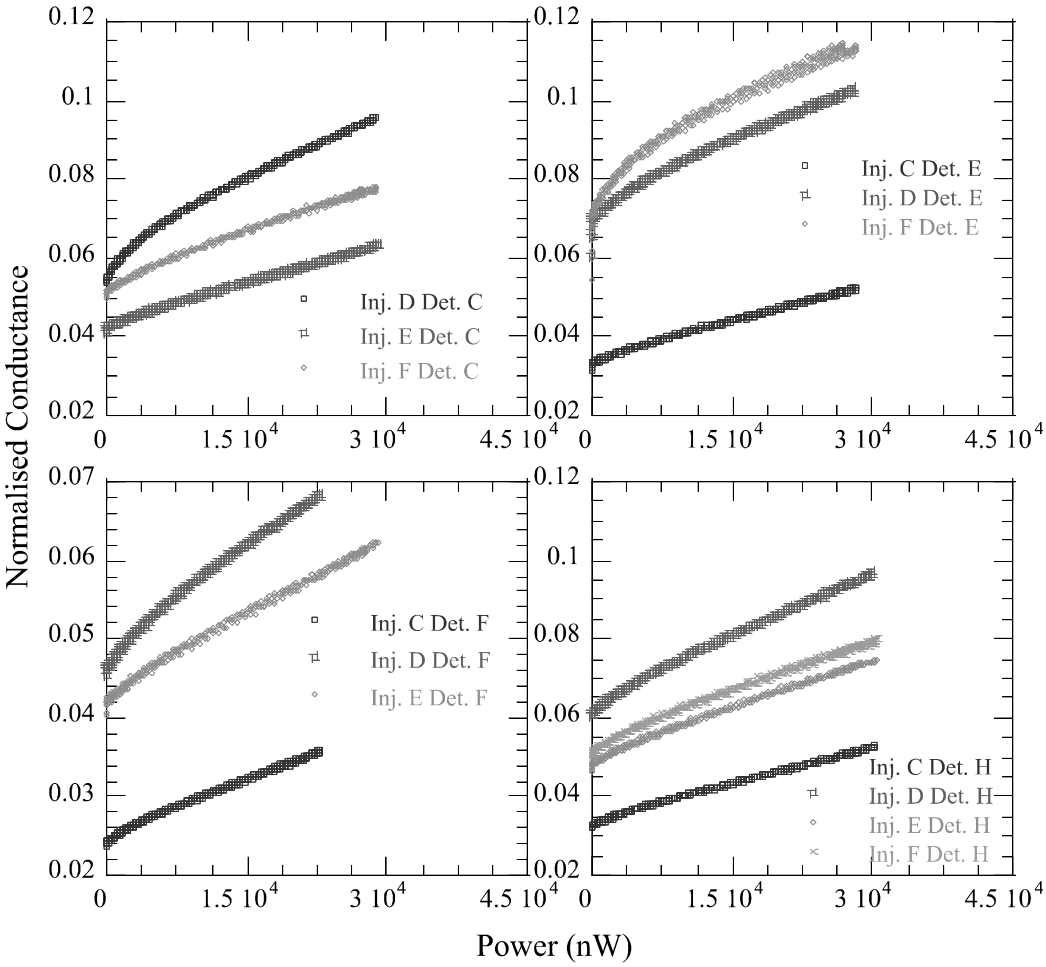

Figure 7.11 Normalised conductance versus injected power for many different measurement configurations.

of heating (6.9). For our devices, any effect of distance is much less than the intrinsic variation between devices - i.e. some detectors consistently gave a stronger signal. The source of this intrinsic variation was not fully understood but was believed to be a device production issue.

7.4.3 Random Walk Model

Having concluded that our devices did not respond to localised recombination near the detector junction, we used the random walk model that we developed in chapter 5 to investigate the numbers of quasiparticles likely to reach the detector junction.

To recapitulate, the model simulates a quasiparticle injected at a random point within the area covered by the injector junction, then allowing it to scatter randomly

for a fixed number of scattering steps of fixed length. At each scatter stage, the location of the quasiparticle is noted and a count of the number of times it had been in that area of the base electrode incremented. The free parameters in the model are the scattering step length (which is equivalent to the mean free path of the quasiparticles), and the total number of steps that are taken by a quasiparticle (which is equivalent to the lifetime of the quasiparticle). The density of quasiparticles can be found from the mean number of times a quasiparticle passes through a region within its lifetime and the number of quasiparticles injected into the electrode.

In order to find the mean free path of quasiparticles in these devices we measured a residual resistance ratio (RRR) of the base electrode of a completed device. The counter-electrode had been removed from the whole of the area of the chip whose resistance we measured, thus the RRR is for the base electrode alone. From this we found that the mean free path was 7 nm - this is comparable with mean free paths for similar polycrystalline Nb devices reported in the literature ((Gijsbertsen 1996b)). Unlike our previous simulations, the mean free path is much smaller than the film thickness. For this reason, we used a true 3D simulation rather than a 2D one as in previous cases. Whilst this would tend to underestimate the number of quasiparticles able to tunnel at the detector; we were interested in the number of recombination events under the detector junction. Assuming the density of quasiparticles to be far from thermal equilibrium populations, the rate of recombination phonon production, as given by the Rothwarf-Taylor Equations ((2.76) and (2.77)) will scale as the density of quasiparticles squared. Since we do not know the lifetimes of quasiparticles in this structure, we can use the figure we found for Nb in chapter 5 (100 ns) as a lower bound estimate. An upper bound to the lifetime is difficult to estimate, however we could assume that the upper limit is represented by the effective lifetime in Al. This itself is not as well characterised as might be desired, however an effective lifetime of order 10 times the quasiparticle lifetime against recombination would not be unreasonable. This would give an upper bound limit of around 1 μs.

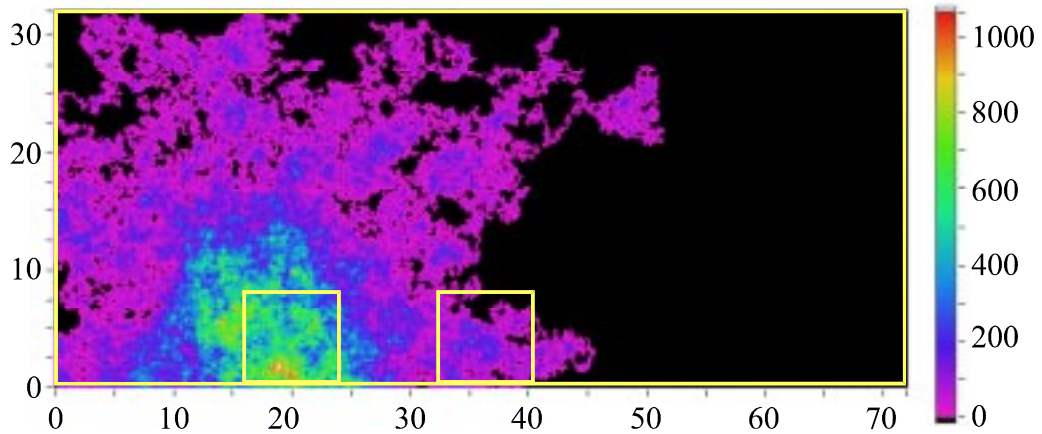

Figure 7.12 Random walk model after 14 million scatters. Step length was 7 nm.

If we assume that the quasiparticle velocity is approximately half the fermi velocity - see 5.4.4.1 for a justification of this, then the elastic lifetime, τ_{els}=6.88 femto-seconds. Thus, our simulation requires between 14 million and 140 million scattering events. However, the mean-free path is very short, so we expect much higher quasiparticle densities, in which case the recombination rate would be expected to be very high, and so the effective lifetime (which is given by (2.78)) will be correspondingly shorter. Therefore, our lower lifetime is rather too long.

As we did in chapter 5, we divided the common base electrode area into 100×100 nm regions to calculate the relative density of quasiparticles. A typical distribution of quasiparticles after 14 million scatters is shown in false colour in figure 7.12. The peak density is around 1000 per injected quasiparticle per 100×100×100 nm volume. By summing the density over the injector and detector junction regions, we were able to find the relative density of quasiparticles as the effective lifetime is increased. From the Rothwarf-Taylor equations, we see that the recombination rate is proportional to the square of the quasiparticle density, thus we can find the relative recombination rates at the injector and detector, which we plot in figure 7.13. For very short lifetimes, of order 20 ns, no quasiparticles get as far as the detector junction, some 8 μm from the injector. Even after 14 million scatters, the rate of quasiparticle recombination at the detector is a factor 6.5 less than the rate at the injector. Therefore, unless we are able to isolate the detector from the phonons produced during recombination at the injector, we are unlikely to be able to observe recombination at the detector. Given that the athermal recombination phonons are

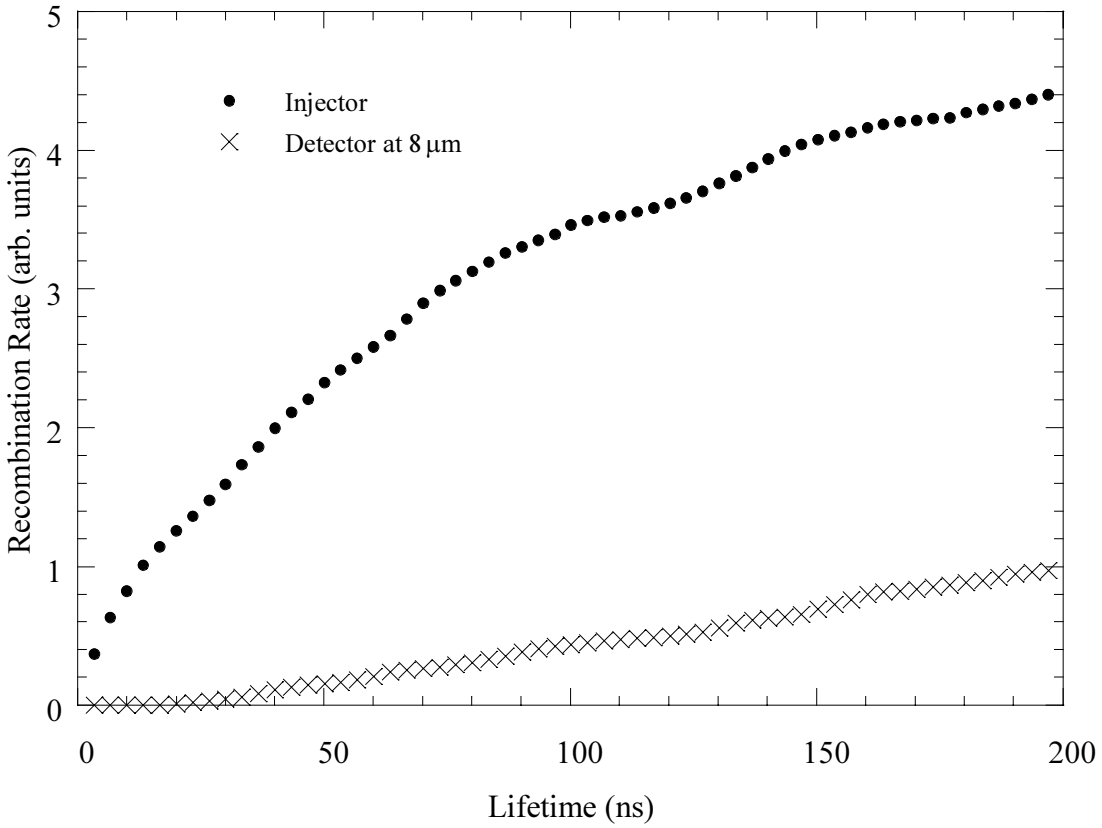

Figure 7.13 Relative recombination rate at injector and detector.

relatively long lived in the sapphire substrate, and assuming that the coupling between the injector and detector when on the same common base is via the substrate; it follows that we are also unlikely to be able to differentiate between injectors on the same common base electrode and on different ones.

7.5 Summary and Conclusions

In this chapter, we have presented measurements on devices with a common superconducting electrode and SIN tunnel junctions, in which the superconductor is composed of a proximitised Nb/Al structure.

We have shown that for our devices the proximitised structure is better described by a model of an S-N layer rather than an S-S' layer, even at a cryostat temperature that is well below the T_c of Al. By measurement of the normalised sub-gap conductance of our devices, we have shown that the devices are not thermally limited below a temperature of around 2 K, dependent slightly upon the device

structure. However, the sub-gap conductance does not saturate until a rather lower cryostat temperature, typically 0.5 K. In between these regimes, the sub-gap resistance continues to decrease, albeit at a lesser extent than a simple calculation based upon the measured density of states would suggest. We attribute this to self-heating of the devices due to reabsorption of recombination phonons and back tunnelling of quasiparticles. By comparing the measured sample temperature with that inferred from the measured sub-gap conductance and calculated current-voltage characteristics, we have shown that the degree of self-heating is less in devices with a thicker proximitised Al layer.

Our attempt to measure a localised recombination rate of quasiparticles by means of an injection-detection experiment has been hampered by the inability to discriminate between recombination events that might be occurring directly under our detector junction and the substrate mediated phonons from distant recombination events. A simple random walk model has demonstrated that our devices are likely to experience a very high rate of self-recombination of quasiparticles close to the injector, which unless isolated from the detector is likely to overwhelm any signal from the detector. It is possible that fabricating such devices on a membrane and thus reducing the likelihood of significant substrate phonon coupling between injector and detector would enable a direct measure of the recombination length in our devices. In addition, such a geometry would closely resemble the intended geometry of a SIN tunnel junction detector or electron refrigerator.

CHAPTER 8

Conclusions

And furthermore, my son, be admonished: of the making of many books there is no end; and much study is a weariness of the flesh.

(Ecclesiastes 12:12)

We have already given some conclusions from the experimental work at the ends of the relevant chapters, so in this chapter we bring together these conclusions into one summary. Where appropriate, indications are given of other avenues of investigation.

8.1 Quasiparticle Lifetimes in Niobium

In chapter 5 we reported our measurements of the lifetime of quasiparticles in niobium. We found an effective lifetime of between 100 ns±20 ns and 80 ns±20 ns. This is in good agreement with measurements made by other workers in the field in similar experiments. This lifetime is much shorter than that which would be predicted by the Rothwarf-Taylor equations for recombination alone. We conclude, therefore, that another quasiparticle loss process dominates. Our measurements do not indicate, however, that the presence of anodic oxides in the device is the primary source of quasiparticle loss. This is contrary to the results of Gijsbertsen(Gijsbertsen 1995), who showed a similar quasiparticle loss time associated with anodic oxide in his devices. We speculate that these contradictory results may be explained by the difference in the microstructure of the Nb films; ours are epitaxial whilst Gijsbertsen's were polycrystalline. We suggest that the loss process is associated with oxide formation in the Nb grain boundaries.

We have found, however, that the niobium oxide suppresses the process of quasiparticle multiplication. We interpret our results as indicating a process of rapid inelastic quasiparticle scattering in or at the Nb/Nb_2O_5 interface, resulting in phonons with energies less than 2Δ. This process may also explain why the distribution of quasiparticles at the detector is well described by a thermal model with an increased temperature (the so-called T* model), whereas previous experimenters have found a non-thermal distribution(Warburton 1993b).

Major resolution limiting factors in STJ detectors, and other classes of detectors that rely on quasiparticle transport to the detector (e.g. the Superconducting Large Area Phonon Sensor of (Nam 1996)), are the much slower than expected diffusion and rapid loss of quasiparticles. It has been suggested that this is a result of

localised energy gap suppression by, amongst other factors, metallic oxides and grain boundaries. Our results would suggest that the presence of anodic oxide alone is not the cause. Further investigation of devices with a range of different grain sizes would help pin down the exact role of grain boundaries in quasiparticle loss. In such an experiment one would hope to see a systematic change in the quasiparticle lifetime when analysed using a model similar to our random walk model. The advantage of this kind of model is that it includes the reduction in mean free path of quasiparticles associated with a reduction in grain size. It would also be desirable to relate the results to a diffusion model, possibly by using pulsed currents to establish a quasiparticle transport time.

8.2 Superconductor-Insulator-Normal Metal Detectors

In chapter 6 we reported our work on developing detectors using a SIN tunnel junction to readout a change in the electronic temperature of a region of normal metal. Our results have highlighted that for detectors based on absorption of incident particles in a normal metal film, the loss of energy to the phonon system of a thick substrate is a major limiting factor. On the other hand, detectors that absorb the incident particle in a thick dielectric crystal, such as our sapphire substrates, and then sense the athermal phonons, will operate in a fashion similar to our devices. Our results are relevant to these types of detector since we show that the design of the athermal phonon collector - i.e. where athermal phonons are absorbed and the energy transferred to an electron system - may severely influence the performance of the detector. In our devices, we found that the absorber effectively 'blocked' athermal phonons generated at a junction on one side from being detected by one on the other side. Furthermore we observed a rapid saturation of response when a relatively low threshold of power was injected into the system.

Our attempts to introduce a controlled barrier to the athermal phonons were inconclusive. It is possible that our barrier structures were too narrow to act as efficient phonon traps in the same way as the actual absorber. Our device fabricated

on the membrane, however, clearly indicates the role of the substrate in determining the response of the device to power injection. Without a substrate to transmit athermal phonons, both the strong and rapidly saturated response of the device to only very small injected currents, and the geometrical dependencies are removed.

Our original intention had been to perfect the fabrication techniques and optimise the device structure for high quality SIN tunnel junctions on bulk substrates, before attempting to manufacture real devices on membranes. In the event, our injection detection experiments on bulk substrates proved sufficiently intriguing that this was pursued further. For the continued development of SIN tunnel junction based detectors these experiments have reached a natural end, since it is clear that substrate originated effects are dominating.

The major problem that is likely to limit the usefulness of SIN tunnel junction detectors is their tendency to self-heat, either due to back tunnelling or due to reabsorption of recombination phonons. We have started to address these issues in chapter 7 by examining the use of a proximitised heterostructure to influence the quasiparticle dynamics. From the density of states in our devices, we conclude that our devices are best described by an S-N proximity model rather than the S-S' that we would expect from the device structure. We have shown that the junctions are not limited by the bath temperature for temperatures less than about 2 K. However, nor are they simply leakage limited at least until temperatures of 0.5 K. By calculating the conductance as a function of temperature based on the measured density of states and comparing with the measured conductance and temperature, we have inferred an effective local electron temperature for different proximity structures. We have shown that indeed the self-heating is less for structures with a thicker S'(N) layer.

Much further work could profitably be accomplished following this, to gain a better understanding of quasiparticle dynamics in proximitised heterostructures. Our attempt to measure directly a local recombination rate was hampered by the conduction of recombination phonons via the substrate. An obvious next stage of the experiments would be to repeat these injection-detection experiments with a device on a membrane.

8.3 State of the Art Cryogenic Detectors

Finally, we should consider the state of the low temperature detector field at the conclusion of this work. In this thesis, we considered the use of niobium as the superconductor in our detectors. One of the attractions in the choice of material was the relatively high T_c of niobium, which allowed operation of a detector (which ideally should be at less than $T_c/10$) in ^{3}He cryostats at 0.3K. During the last 5 years, there has been a shift in the operating temperature to lower temperatures, as low as 50mK. Whether this has been driven by the use of lower T_c superconductors, such as Al, or has been the result of wider availability of space-capable sub 100mK cooling systems is a moot point. The result has been that the current state of the art detector designs utilise Al predominantly. Al offers the benefits of long intrinsic quasiparticle and phonon lifetimes, and its native oxide is insulating, thus overcoming many of the problems with Nb which we have identified in this work. As a detector material it suffers from its low Z number, however this may be overcome by coupling to a Ta absorber.

In recent years, there has been a drift away from the use of STJs, due to inherent difficulties in their production and use as detectors. Despite this, those groups that have continued STJ development have made impressive improvements in resolution particularly at lower energy ranges. SIN tunnel junctions have not been developed to the same extent as STJ detectors and although SIN detectors' speed may lead to their use in specific applications, for our applications they offer little advantage over detectors based on transition edge sensors. It has only been in the last few years that the difficulties due to excessive quasiparticle back-tunneling and recombination have been highlighted within the cryogenic detector community. Thus, our work may not directly contribute to the development of a successful detector, but may indirectly help the design of other detector types through the understanding of energy transport in these devices. Transition edge sensors may offer the necessary resolution, or may, in turn, suffer from as yet undiscovered disadvantages. Meanwhile, the date for the first space mission using one of these competing detector concepts approaches ever closer.

Bibliography

C. J. Adkins (1973). *Phys. Lett.* **43A**(6) 537.

A. F. Andreev (1964). *Sov. Phys. JETP* **19**(5) 1228.

N. W. Ashcroft and N. D. Mermin (1976). "Solid State Physics.", W.B. Saunders Co.

J. Bardeen, L. N. Cooper and J. R. Schrieffer (1957). *Phys. Rev.* **108** 1175.

M. G. Blamire, R. E. Somekh, Z. H. Barber, G. W. Morris and J. E. Evetts (1988). *J. Appl. Phys.* **64**(11) 6396.

M. G. Blamire, J. E. Evetts and D. G. Hasko (1989). *IEEE Trans. Mag.* **25**(2) 1123.

M. G. Blamire, E. C. G. Kirk, J. E. Evetts and T. M. Klapwijk (1991). *Phys. Rev. Lett.* **66**(2) 220.

M. G. Blamire (1993). *Physica C* **211**(3-4) 467.

M. G. Blamire, F. S. Porter, E. C. G. Kirk and D. Van Vechten (1995). *IEEE Trans. Appl. Super.* **5**(3) 3014.

M. G. Blamire and Z. H. Barber (1997). "X-Ray Cryogenic Spectrometer Programme." *Particle Physics and Astronomy Research Council* , grant **PPA/1997/O/G/000232.**

N. N. Bogoliubov (1958). *Nuovo Cimento* **7** 794.

N. N. Bogoliubov (1959). *Sov. Phys.-Uspekhi* **67** 236.

W. E. Booij (1997). PhD Thesis "Josephson junctions and Devices Fabricated by Focussed Electron Beam Irradiation." , Dept. Materials Science, University of Cambridge, Cambridge.

N. E. Booth (1987). *Appl. Phys. Lett.* **50**(5) 293.

N. E. Booth, P. L. Brink, R. J. Gaitskell, D. J. Goldie, A. D. Hahn, G. L. Salmon and A. M. Swift (1993). *J. Low Temp. Phys.* **93**(3-4) 521.

M. P. Bruijn, F. Kiewiet, O. J. Luiten, F. A. Michels and P. A. J. de Korte (1996). *Nucl. Inst. Meth.* **370**(1) 101.

M. P. Bruijn, F. B. Kiewiet, M. L. van den Berg, O. J. Luiten, P. A. J. de Korte, C. G. S. Brons, A. W. Hamster and J. Flokstra (1997). *IEEE Trans. Appl. Super.* **7**(2 Pt3) 3387.

G. Burnell, P. A. Warburton and M. G. Blamire (1994). *J. Appl. Phys.* **76**(2) 1105.

H. S. Carslaw and J. C. Jaeger (1959). "Conduction of Heat in Solids.", OUP, Oxford.

J. J. Chang and D. J. Scalapino (1977). *Phys. Rev. B* **15**(5) 2651.

C. C. Chi and J. Clarke (1979). *Phys. Rev. B* **19** 4495.

A. Chrestin, T. Matsuyama and U. Merkt (1997). *Phys. Rev. B* **55**(13) 8457.

L. N. Cooper (1956). *Phys. Rev.* **104**(4) 1189.

S. Cooper and H. Kraus (1997). "X-Ray Cryogenic Spectrometer Programme." *Particle Physics and Astronomy Research Council* , grant **PPA/1997/O/G/000248.**

R. Cristiano, L. Frunzio, S. Pagano, V. G. Palmieri and M. P. Lisitskii (1997). *J. Appl. Phys.* **82**(10) 5024.

P. D. Desai, T. K. Chu, H. M. James and C. Y. Ho (1984). *Journal Of Physical and Chemical Reference Data* **13**(4) 1069.

G. B. Donaldson (1967), PhD Thesis " Electron tunnelling studies of the superconducting state", Dept. Physics, University of Cambridge, Cambridge, UK.

O. B. Drury, J. P. Castle, S. R. Golwala, J. Jochum, B. Neuhauser, C. A. Mears, W. C. Fellers, F. P. Lipschultz and B. Sadoulet (1997). in the proceedings of *Low Temperature Detectors 7*, Munich, Germany, 56.

W. Eisenmenger (1976). "Superconductive Tunneling Junctions as Phonon Generators and Detectors." in *Physical Acoustics, Principles and Methods*, **12,** 79.

G. M. Eliashberg (1960). *Sov. Phys. JETP* **11** 696.

P. A. Fisher, J. N. Ullom and M. Nahum (1995). *J. Low Temp. Phys.* **101**(3-4) 561.

P. A. Fisher, J. N. Ullom and M. Nahum (1997). in the proceedings of *ISEC '97*, Berlin.

S. Friedrich, K. Segall, M. C. Gaidis, D. S. Toledano, D. E. Prober, A. E. Szymkowiak and S. H. Moseley (1996). *Nucl. Inst. Meth.* **370**(1) 44.

S. Friedrich, K. Segall, M. C. Gaidis, C. M. Wilson, D. E. Prober, A. E. Szymkowiak and S. H. Moseley (1997). *Appl. Phys. Lett.* **71**(26) 3901.

M. C. Gaidis, S. Friedrich, D. E. Prober, A. E. Szymkowiak and S. H. Moseley (1993). *J. Low Temp. Phys.* **93**(3/4) 605.

V. F. Gantmakher (1974). *Rep. Prog. Phys.* **37** 317.

P. G. de Gennes and D. Saint-James (1963). *Phys. Lett.* **4** 151.

R. Giacconi, H. Gursky, F. R. Paolini and B. B. Rossi (1962). *Phys. Rev. Lett.* **9** 439.

J. G. Gijsbertsen, E. P. Houwman, J. Flokstra and H. Rogalla (1994). *Physica B* **194**(Pt2) 1705.

J.G. Gijsbertsen (1995). PhD Thesis "Superconducting Tunnel Junctions for X-Ray Detection." , Dept. Applied Physics, University of Twente, Enschede, Netherlands.

J. G. Gijsbertsen and J. Flokstra (1996a). *J. Appl. Phys.* **80**(7) 3923.

J. G. Gijsbertsen, J. Flokstra and H. Rogalla (1996b). *Nucl. Inst. Meth.* **370**(1) 75.

A. Gilabert, C. Van Hasendonck, L. Ven den Dries and Y. Bruynserade (1979). *Solid State Comm.* **31** 109.

V. L. Ginzburg and L. D. Landau (1950). *Zh. Exsp. Teor. Fiz.* **20** 1064.

D. J. Goldie, N. E. Booth, C. Patel and G. L. Salmon (1990). *Phys. Rev. Lett.* **64** 954.

D. J. Goldie, N. E. Booth, C. Patel and G. L. Salmon (1991). *Physica B* **169**(1-4) 443.

D. J. Goldie, P. L. Brink, C. Patel, N. E. Booth and G. L. Salmon (1994). *Appl. Phys. Lett.* **64**(23) 3169.

A. A. Golubov and M. Y. Kupriyanov (1988). *J. Low Temp. Phys.* **70**(1-2) 83.

A. A. Golubov and E. P. Houwman (1993). *Physica C* **205**(1-2) 147.

A. A. Golubov, E. P. Houwman, J. G. Gijsbertsen, J. Flokstra, H. Rogalla, J. B. Le Grand and P. A. J. de Korte (1994). *Phys. Rev. B* **49**(18) 12953.

A. A. Golubov, E. P. Houwman, J. G. Gijsbertsen, V. M. Krasnov, J. Flokstra, H. Rogalla and M. Y. Kupriyanov (1995). *Phys. Rev. B* **51**(2) 1073.

A. A. Golubov, T. Klocke, J. Kaufmann, T. Schapers, J. Appenzeller, D. Uhlisch, A. V. Ustinov, M. Hollfelder, H. Luth and A. I. Braginski (1996). *Phys. Rev. B* **54**(23) 17018.

L. P. Gor'kov (1960). *Sov. Phys. JETP* **10** 998.

K. E. Gray (1971). *J. Phys.* **F1** 290.

X.-R. A. P. W. Group (1994). "A 15 Year Plan For X-Ray Astronomy.", High Energy Astrophysics Branch, Astrophysics Division, Office of Space Science, NASA.

M. Gutsche, P. Hettl, J. Jochum, B. Kemmather and H. Kraus (1996). *Nucl. Inst. Meth.* **370**(1) 91.

J. Halbritter (1987). *Appl. Phys. A* **43**(1) 1.

A. W. Hamster, E. Ferraro, D. J. Adelerhof, G. C. S. Brons, J. Flokstra, H. Rogalla, M. P. Bruijn, F. Kiewiet, I. J. E. Schoofs, O. J. Luiten and P. A. J. de Korte (1996). *Nucl. Inst. Meth.* **370**(1) 124.

R. d. Hartog, A. Peacock, F. Jansen, J. Verveer, A. v. Dordecht, J. Salmi and R. Venn (1997). in the proceedings of *SPIE International Symposium on Optical Science, Engineering and Instrumentation*.

S. G. d. Hartog, B. J. van Wees, Y. V. Nazarov, T. M. Klapwijk and G. Borghs (1998). *Physica B* **251** 467.

G. C. Hilton, J. M. Martinis, D. A. Wollman, K. D. Irwin, L. L. Dulcie, D. Gerber, P. M. Gillevet and D. Twerenbold (1998). *Nature* **391**(6668) 672.

K. H. Huang (1991). PhD Thesis , Dept. Materials Science and Metallurgy, University of Cambridge, Cambridge.

K. D. Irwin (1995). *Appl. Phys. Lett.* **66**(15) 1998.

K. D. Irwin, G. C. Hilton, D. A. Wollman and J. M. Martinis (1996). *Appl. Phys. Lett.* **69**(13) 1945.

S. P. Isaac (1998). PhD Thesis "Grain Boundary Devices in Perovskite Materials." , Dept. Materials Science and Metallurgy, University of Cambridge, Cambridge, UK.

J. Jochum, C. Mears, S. Golwala, B. Sadoulet, J. P. Castle, M. F. Cunningham, O. B. Drury, M. Frank, S. E. Labov, F. P. Lipschultz, H. Netel and B. Neuhauser (1998). *J. Appl. Phys.* **83**(6) 3217.

B. D. Josephson (1962). *Phys. Lett.* **1** 251.

B. Jug and Z. Trontelj (1997). in the proceedings of *ISEC '97*, Berlin.

P. L. Kapitza (1941). *Sov. J. Phys.* **4** 181.

S. B. Kaplan, C. C. Chi and D. N. Langenberg (1976). *Phys. Rev. B* **14**(11) 4854.

S. B. Kaplan (1979). *J. Low Temp. Phys.* **37**(3/4) 343.

T. M. Klapwijk and J. E. Mooij (1976). *Physica B* **81** 132.

P. G. Klemens (1967). *J. Appl. Phys.* **38** 4573.

T. Kommers and J. Clarke (1977). *Phys. Rev. Lett.* **38** 1091.

P. A. J. de Korte (1992). in the proceedings of *ESA Symposium on Photon Detectors for Space Instrumentation (ESA SP-356)*, ESA/ESTEC Noordwijk, The Netherlands, 41.

H. Kraus, F. Vonfeilitzsch, J. Jochum, R. L. Mossbauer, T. Peterreins and F. Probst (1989). *Phys. Lett. B* **231**(1-2) 195.

N. M. Krishna, L. S. Lingam and K. N. Shrivastava (1997). *Mod. Phys. Lett. B* **11**(19) 849.

H. Kroger, L. N. Smith and D. W. Jillie (1981). *Appl. Phys. Lett.* **39**(3) 280.

M. Kurakado (1982). *Nucl. Inst. Meth.* **196** 275.

M. Kurakado, T. Takahashi and A. Matsumura (1993). *J. Low Temp. Phys.* **93**(3/4) 567.

J. B. Le Grand (1994a). PhD Thesis "X-ray Response of Superconductive Tunnel Junctions with Trapping Layers." , Space Research Organisation, Netherlands.

J. B. Le Grand, M. P. Bruijn, C. Patel, P. Valko, P. A. J. de Korte, E. P. Houwman, J. G. Gijsbertsen and J. Flokstra (1994b). in the proceedings of *International Workshop on Superconductivity and Particle Detection*, Toledo, Spain.

J. B. Le Grand and a. others (1995). Unpublished personal communication at Low Temperature Detectors 6 at Beatenberg, Switzerland .

J. B. Le Grand, J. Martin, R. Gross, R. P. Huebener, A. W. Hamster, G. C. S. Brons, D. J. Adelerhof, J. Flokstra and P. A. J. de Korte (1996). *Nucl. Inst. Meth.* **370**(1) 131.

M. M. Leivo, J. P. Pekola and D. V. Averin (1996). *Appl. Phys. Lett.* **68**(14) 1996.

S. Lemke, F. Hebrank, R. Gross, R. P. Huebener, T. Weimann, R. Popel, J. Niemeyer, U. Schnakenberg and W. Benecke (1993). *J. Appl. Phys.* **73**(6) 2659.

F. London and H. London (1935). *Proc. Roy. Soc. (London)* **A149** 71.

A. J. Manninen, M. M. Leivo and J. P. Pekola (1997). *Appl. Phys. Lett.* **70**(14) 1885.

J. Martin, S. Lemke, R. Gross, R. P. Huebener, P. Videler, N. Rando, T. Peacock, P. Verhoeve and F. A. Jansen (1996). *Nucl. Inst. Meth.* **370**(1) 88.

A. Matsumura, T. Takahashi and M. Kurakado (1993). *Nucl. Inst. Meth.* **329**(1-2) 227.

G. Meagher, J. Pond, A. Kotlicki, B. G. Turrell and A. K. Drukier (1996). *Nucl. Inst. Meth.* **370**(1) 8.

C. A. Mears, S. E. Labov and A. T. Barfknecht (1993). *J. Low Temp. Phys.* **93**(3/4) 561.

C. A. Mears, S. E. Labov, M. Frank, M. A. Lindeman, L. J. Hiller, H. Netel and A. T. Barfknecht (1996). *Nucl. Inst. Meth.* **370**(1) 53.

W. Meissner and R. Ochsenfeld (1933). *Naturwissenschaften* **21** 787.

R. W. Moseley (1998). Unpublished personal communication at Dept.. Materials Science, Cambridge University .

B. Mühlschlegel (1959). *Z. Phys.* **155** 313.

NAG (1995). FORTRAN Subroutine "d03eafe" Mk 17 on Sun Microsystems Ultra Sparc, Numerical Algorithms Group

M. Nahum, J. M. Martinis and S. Castles (1993). *J. Low Temp. Phys.* **93**(3-4) 733.

M. Nahum, T. M. Eiles and J. M. Martinis (1994). *Appl. Phys. Lett.* **65**(24) 3123.

M. Nahum and J. M. Martinis (1995). *Appl. Phys. Lett.* **66**(23) 3203.

S. W. Nam, B. Cabrera, B. Chugg, R. M. Clarke, C. Fertig, K. D. Irwin and B. A. Young (1996). *Nucl. Inst. Meth.* **370**(1) 187.

H. Netel, J. Jochum, S. E. Labov, C. A. Mears, M. Frank, D. Chow, M. A. Lindeman and L. J. Hiller (1997). *IEEE Trans. Appl. Super.* **7**(2 Pt3) 3379.

T. Nussbaumer, F. Finkbeiner, P. Lerch, A. Zehnder and H. R. Ott (1996). *Nucl. Inst. Meth.* **370**(1) 115.

M. Ohkubo, J. Martin, K. Drachsler, R. Gross, R. P. Huebener, I. Sakamoto and N. Hayashi (1996). *Phys. Rev. B* **54**(13) 9484.

H. K. Onnes (1911). *Leiden Communications* **120b, 122b, 124c**.

R. Orbach and L. A. Vredevoe (1964). *Physics* **1** 91.

C. Patel, P. L. Brink, D. J. Goldie, N. E. Booth, G. L. Salmon, F. Gatti and S. Vitale (1996). *Nucl. Inst. Meth.* **370**(1) 112.

A. Peacock, P. Verhoeve, N. Rando, A. van Dordrecht, B. G. Taylor, C. Erd, M. A. C. Perryman, R. Venn, J. Howlett, D. J. Goldie, J. Lumley and M. Wallis (1997). *J. Appl. Phys.* **81**(11) 7641.

T. Peacock, P. Verhoeve, N. Rando, C. Erd, M. Bavdaz, B. G. Taylor and D. Perez (1998). *Astronomy & Astrophysics Supplement Series* **127**(3) 497.

A. B. Pippard (1953). *Proc. Roy. Soc. (London)* **A216** 547.

F. S. Porter, D. Van Vechten, M. G. Blamire and E. C. G. Kirk (1994). *Submitted to ASC 1994*.

F. S. Porter, D. van Vechten, M. G. Blamire and G. Burnell (1996). *Nucl. Inst. Meth.* **370**(1) 50.

K. Pretzl (1996). *Nucl. Inst. Meth.* **370**(1) R 9.

F. Probst, M. Frank, S. Cooper, P. Colling, D. Dummer, P. Ferger, G. Forster, A. Nucciotti, W. Seidel and L. Stodolsky (1995). *J. Low Temp. Phys.* **100**(1-2) 69.

N. Rando, A. Peacock, A. van Dordrecht, C. Foden, R. Engelhardt, B. G. Taylor and P. Gare (1992). *Nucl. Inst. Meth.* **A313** 173.

N. Rando, P. Verhoeve, A. Poelaert, A. Peacock and D. J. Goldie (1998). *J. Appl. Phys.* **83**(10) 5536.

J. P. Romagnon, A. Gilabert, J. C. Noiray and E. Guyon (1974). *Solid State Comm.* **14** 83.

A. Rothwarf and B. N. Taylor (1967). *Phys. Rev. Lett.* **30** 167.

B. Sadoulet (1996). *Nucl. Inst. Meth.* **370**(1) 1.

D. Saint-James (1964). *J. de Phys.* **25** 899.

A. Savitzky and M. J. E. Golay (1964). *Anal. Chem.* **36**(8) 1627.

S. Schafroth, R. Fuchslin and P. F. Meier (1996). *Nucl. Inst. Meth.* **370**(1) 69.

J. Schnagl, M. Buhler, P. Hettl, J. Hohne, E. Kellner, M. L. Sarsa and F. van Feilitzsch (1997). in the proceedings of *Low Temperature Detectors 7*, Munich, Germany, 151.

M. Sisti, C. Bucci, M. Buhler, S. Cooper, F. van Feilitzsch, J. Hohne, V. Jorgens, M. Loidl, O. Meier, U. Nagel, F. Probst, F. Rulofs, M. L. Sarsa, J. Schnagl, W. Seidel, L. Stodolsky, A. Stolovits and L. Zerle (1997). in the proceedings of *Low Temperature Detectors 7*, Munich, Germany.

G. Siuzdak (1994). *Proc. Nat. Acad. Sci. USA* **91**(24) 11290.

C. M. Soukoulis and D. A. Papaconstantopoulos (1982). *Phys. Rev. B* **26**(7) 3673.

A. H. Steinbach, J. M. Martinis and M. H. Devoret (1996). *Phys. Rev. Lett.* **76**(20) 3806.

D. A. Stricker, D. D. Bing, R. W. Bland, S. C. Dickson, T. D. Dignan, R. T. Johnson, J. M. Lockhart, K. Laws, M. W. Simon and R. Watson (1991). *IEEE Trans. Mag.* **27**(2) 2669.

E. J. Tarte (1992). PhD Thesis "The Electrical Properties of Interfaces Between Nobel Metals and $YBa_2Cu_3O_{7-\delta}$." , Dept. Physics, University of Cambridge, Cambridge, UK.

M. Tinkham and J. Clarke (1972). *Phys. Rev. Lett.* **28** 1366.

M. Tinkham (1996). "Introduction to Superconductivity.", McGraw-Hill Book Co., Singapore.

B. G. Turrell (1997). in the proceedings of *Low Temperature Detectors 7*, Munich, Germany, 188.

D. Twerenbold (1986). *Phys. Rev.* **B34** 7748.

D. Twerenbold (1996). *Nucl. Inst. Meth.* **370**(1) 253.

J. N. Ullom, P. A. Fisher and M. Nahum (1997). in the proceedings of *Low Temperature Detectors 7*, Munich, Germany, 142.

K. Usadel (1970). *Phys. Rev. Lett.* **25** 560.

J. G. Valatin (1958). *Nuovo Cimento* **7** 843.

B. van den Brandt, G. Czapek, U. Diggelmann, T. Ebert, D. Huber, S. Janos, K. U. Kainer, K.-M. Knoop, J. A. Konter, S. Mango, U. Moser, V. G. Palmieri and K. Pretzl (1997). in the proceedings of *Low Temperature Detectors 7*, Munich, Germany, 193.

T. van Duzer and C. W. Turner (1981). "Principles of Superconductive Devices and Circuits.", Elsevier, New York.

D. Van Vechten, K. S. Wood, M. N. Lovellette and G. Arnold (1992). in the proceedings of *Low Temperature Detectors for Neutrinos and Dark Matter 4*, Oxford, England, 347, Editions Frontieres.

P. Verhoeve, N. Rando, A. Peacock, A. van Dordrecht, D. Lumb, D. J. Goldie and R. Venn (1996). *Nucl. Inst. Meth.* **370**(1) 136.

P. Verhoeve, N. Rando, T. Peacock, A. van Dordrecht, M. Bavdaz, J. Verveer, D. J. Goldie, M. Richter and G. Ulm (1997). in the proceedings of *Low Temperature Detectors 7*, Munich, Germany, 97.

P. A. Warburton (1993a). PhD Thesis "Quasiparticle Trapping in Superconducting Heterostructures." , University of Cambridge.

P. A. Warburton and M. G. Blamire (1993b). *J. Low Temp. Phys.* **93**(3-4) 593.

P. A. Warburton and M. G. Blamire (1994). *Physica B* **194**(Pt2) 1769.

P. A. Warburton and M. G. Blamire (1995). *Nucl. Inst. Meth.* **357**(2-3) 477.

F. C. Wellstood, C. Urbina and J. Clarke (1994). *Phys. Rev. B* **49**(9) 5942.

G. K. White (1987). "Experimental Techniques in Low Temperature Physics.", OUP, Oxford.

D. A. Wollman, K. D. Irwin, G. C. Hilton, L. L. Dulcie, D. E. Newbury and J. M. Martinis (1997). *J. Microscopy* **188**(Pt3) 196.

G. H. Wood and B. L. White (1969). *Appl. Phys. Lett.* **15** 237.

P. M. Zavracky, T. Earles, N. L. Pokrovskiy, J. A. Green and B. E. Burns (1994). *J. Electrochem. Soc.* **141**(11) 3182.

A. Zehnder (1995). *Phys. Rev. B* **52**(17) 12858.

S. P. Zhao, H. Du, R. F. Wang, G. H. Chen, F. Z. Xu and Q. S. Yang (1997). *Physica C* **282**(Pt4) 2445.

Appendix A

Electronic Cooling in $Nb/AlO_x/Al/AlO_x/Nb$ Double Tunnel Junctions

Lucia Capogna,
Dipartimento di Fisica, Università di Salerno, Italy*
Gavin Burnell and Mark G. Blamire
Department of Materials Science, University of Cambridge, CB2 3QZ, UK

***Abstract*—Several recent papers have predicted the feasibility of superconducting tunnel junction-based electronic cryocooler devices operating in the temperature range 0.1 - 4K. We have extended previous work in stacked Nb/AlO_x devices to investigate the nonequilibrium effects in them and to examine the influence of barrier conductance and layer thickness on the electronic cooling achievable by this technique. We have also analysed the maximum cooling possible with junctions of our present conductance.**

I. Introduction

Under certain conditions, significant electronic cooling can be achieved in the operation of superconducting tunnel junction based devices [1]. Such an effect has been observed both indirectly via gap-enhancement in double junction SINIS [2][3] and directly in single junction SINS [4] configurations. In order to utilise such cryocoolers for practical applications, it is necessary to optimise the design for maximum cooling efficacy. To do this a detailed understanding of the physics of such structures when driven in to extreme nonequilibrium conditions is required.

We have investigated $Nb\text{-}Al\text{-}AlO_x\text{-}Al\text{-}AlO_x\text{-}Al\text{-}Nb$ (SIS'IS) devices in which the Al layer between the two junctions is cooled by extraction of quasiparticles through both junctions. The high transparency of the barriers and small thickness of the middle electrode promote very fast extraction, while the low inelastic relaxation time in Al maintains the nonequilibrium state. Such a system has previously been analysed by Heslinga *et al.* using a simple SINIS model [5] which predicted that a gap enhancement in the Al layer occurs in the bias range between $2(\Delta_1-\Delta_2)/e$ and $2(\Delta_1+\Delta_2)/e$ where Δ_1 and Δ_2 are the energy gaps in the Nb and the enhanced gap in the middle Al layer respectively. They also calculated the I-V curves showing that a sub-gap cusp is predicted to occur at the voltage $2(\Delta_1-\Delta_2)/e$ and a sharp current rise at a gap sum of $2(\Delta_1+\Delta_2)/e$ as expected in a conventional double junction device with different electrodes. In this paper we report new experimental results on the position of the gap sum feature, showing that, unlike the theoretical prediction, this kind of nonequilibrium structure exhibits the current rise at a voltage equal to $2(\Delta_1)/e$. We also demonstrate that no gap enhancement is possible at $2(\Delta_1+\Delta_2)/e$.

Manuscript received August 26, 1996.
This work was supported partly by the US Naval Research Laboratory, Washington D.C.
*Present Address: Department of Physics and Space Research, University of Birmingham, U.K.

To investigate the refrigeration power of our devices we have followed the analysis of Edwards *et al.* [6] in calculating the cooling power, and the temperature to which the electrons in the middle Al layer can be cooled. We show that the cooling power in our devices is not limited by the junction conductance, but rather by the mean free path in the middle Al layer.

II. Device Fabrication

The devices studied here were fabricated in a whole wafer multilayer sputter deposition process, performed in sequence without breaking the vacuum in a turbo-pumped ultra-high vacuum (UHV) system, fitted with dual dc magnetron targets. Samples were fabricated in single deposition runs with different barrier conductances and middle Al layer (Al^{mid}) thickness, and all other layers identical. The substrate was R-plane sapphire and the deposition was carried out at ambient temperature. The tunnel barriers were formed by admitting pure O_2 into the deposition system at pressures between 100Pa and 10Pa for 6 minutes. The structures were processed using a standard Selective-Niobium-Etch Process (SNEP), giving a vertical stack structure with junction sizes of 60 μm^2. The device design was such that contacts could only be made to the top and bottom Nb electrodes in the stack structure so that both junctions are measured in series. The measurements were performed in an Oxford Instruments Helix™ He^3 system in the temperature range 0.3-10K.

III Theory

A.. SINIS Model

The SINIS model [5] is illustrated in Fig. 1. The applied voltage is assumed to drop across the tunnel barriers and if the barriers are identical, the voltage is distributed equally over the two interfaces. The voltage drop across the middle electrode is therefore neglected. This assumption distinguishes a SINIS structure from a SNS junction in which the voltage is distributed over the N region.

The schematic diagram in Fig. 1 illustrates under what conditions of bias the quasiparticle extraction is sufficiently effective to sustain a gap enhancement in the middle Al layer.

For voltages below $2(\Delta_1-\Delta_2)/e$, quasiparticles can not be removed from the central film because they are blocked by the gap of the right S electrode. When $2(\Delta_1-\Delta_2)<eV<2(\Delta_1+\Delta_2)$, the extraction is effective enough and those quasiparticles remaining in the range $0 \rightarrow \Delta_1 - eV/2$ will be extracted, if $2\Delta_1 <eV<2(\Delta_1+\Delta_2)$ then quasiparticle injection from the external electrodes will be possible unless

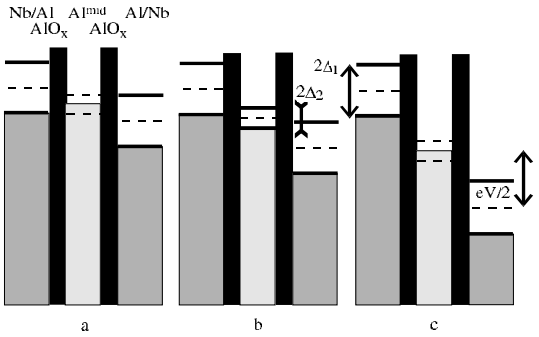

Fig. 1: The nonequilibrium gap in the Al middle electrode is most likely to exist in a limited voltage range. a) $eV<2(\Delta_1-\Delta_2)$ extraction is not effective; b) $2(\Delta_1-\Delta_2)<eV<2(\Delta_1+\Delta_2)$ a gap can be sustained; c) $eV>2(\Delta_1+\Delta_2)$ extraction is not effective

the Al has developed a gap $\Delta_2(0)$. If $eV>2(\Delta_1+\Delta_2)$, direct quasiparticle injection will occur and the gap is quenched. In all cases, at finite T a few particles are injected above the energy gap of the left electrode at $E>eV/2+\Delta_2$, but these states are far from the Fermi level and thus do not have much weight in the BCS integral.

B. Maximum Cooling Power

The potential cooling power for a SIS'IS based device has been analysed by Edwards *et al.* [6] by considering an equilibrium between the maximum cooling power for an SIN junction limited by tunneling and scattering rates and the heating of the electrons from phonons in the Al^{mid} layer. Since the structure is vertical stack on a large (1/2" x 1/8" x 0.5mm) substrate, we assume that there is no thermal isolation from the substrate and consequently that the phonon temperature in the Al^{mid} layer is equal to the measured sample temperature.

For a SIN junction limited by the tunneling rate the maximum cooling power is given by [4];

$$P=\left(\frac{G}{e^2}\right)(k_BT_0)^2 \qquad (1)$$

Where G is the conductance of the junction, k_B is the Boltzmann constant and T_0 the electron temperature. The tunneling rate as limited by both the intrinsic clean limit scattering rate and a correction term for disorder is given by [6]:

$$\tau_{ee}^{-1}=(k_BT_0)VN_F(\tau_{disorder}^{-1}+\tau_{clean}^{-1}) \qquad (2)$$

where N_F is the density of states at the Fermi level, V is the volume of the Al^{mid} layer and [6][7]

$$\tau_{clean}^{-1}=\frac{(k_BT_0)^2}{hE_F} \qquad (3)$$

$$\tau_{disorder}^{-1}=\left(hN_F\frac{\hbar v_F l}{k_BT_0}t\right)^{-1} \qquad (4)$$

with E_F and v_F the aluminium Fermi energy and velocity respectively. T_0 is the effective electron temperature, t the thickness of the Al^{mid} layer and l the mean free path in it (which we take to be approximately 1nm for our devices). The heat flow from a scattering limited junction is thus given by:

$$P_{scat}=k_BT_0\tau_{ee}^{-1} \qquad (5)$$

The heat flow from the phonon bath to the electrons in the Al^{mid} layer is given by[4]:

$$P_{ph}=\Sigma V\left(T_{ph}^5-T_0^5\right) \qquad (6)$$

with T_{ph} the lattice temperature and Σ is a material dependent parameter which we take as 0.2 $GWm^{-3}K^{-5}$ [8].

The electron temperature at which the cooling becomes dominated by the electron scattering rate rather than the tunneling rate, T_0^*, can be found by setting $P=P_{scat}$, and solving for T_0. Below this temperature the cooling power of our device is given by $2P_{scat}$ and above it by 2P. In a steady state the cooling power must be balanced by the heat flow from the lattice to the electrons:

$$P_{ph}=\begin{cases}2P & T_0>T_0^*\\ 2P_{scat} & T_0<T_0^*\end{cases} \qquad (7)$$

This then gives an expression for T_0 in terms of the ambient temperature T, which in turn allows the cooling power to be calculated.

This model, however, is lacking in that it ignores the superconductivity (both equilibrium and nonequilibrium) of the Al layer, however it is illuminating to apply the calculations to obtain a qualitative estimate of the possible cooling effect in a normal metal.

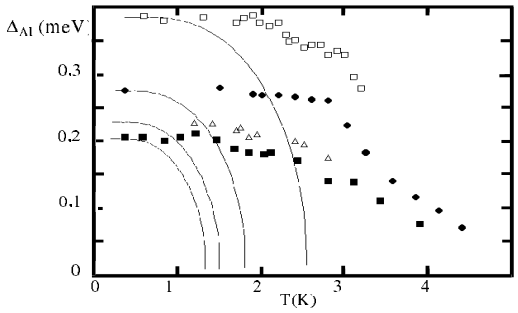

Fig. 2: Measured Al energy gap as a function of temperature. Full squares, empty triangles, full circles and empty squares refer to devices with t=1, 1.5, 2, 2,8 nm respectively. The solid lines show the BCS temperature dependence of the equilibrium gaps with the experimental equilibrium T_c of the Al^{mid} layer.

IV. Experimental Results

At higher temperatures the structure behaves like a simple double SIN structure, showing a very high sub-gap current and a faint gap sum feature. At lower temperatures, but still higher than the intrinsic temperature reported in bulk Al (T_c=1.175) [9], the devices show features that are typical of a SIS'IS double junction device, i.e. very low sub-gap current, a steep current rise at a gap sum-like feature and a very pronounced step at a voltage equal to $2(\Delta_1-\Delta_2)$. Finally, when the temperature is further lowered, a critical current appears at zero voltage. Devices with thin (2-5nm) middle Al layer exhibit a SIS'IS behaviour at higher temperatures. In all cases the position of the peak edge at $2(\Delta_1-\Delta_2)$ is temperature and thickness dependent: it shifts to higher voltage as the temperature is lowered and/or the Al_{mid} thickness is reduced. It is this sub-gap step structure which persists to higher temperatures above T_{ceq} that provides the evidence for a tunneling-induced superconducting state. The small temperature dependence of this sub-gap step suggests that the superconducting state in the Al layer is very strongly enhanced by quasiparticle tunneling up to a value close to $\Delta_2(0)$.

In Fig. 2 the temperature dependence of the Al gap is shown in devices with different Al thickness and is compared with the BCS prediction.

The gap in the Al was measured from the position of the sub-gap step edge (at V_1 on Fig. 4) and the current rise at the gap sum (at V_2 on Fig. 4). These features were assumed to be located by the peaks in the conductance. In this measurement the sub-gap step is assumed to occur at a voltage equal to $2(\Delta_1-\Delta_2)/e$. Under these bias conditions the gap reaches its largest value because this value corresponds to the highest rate of extraction from the Al to the Nb film.

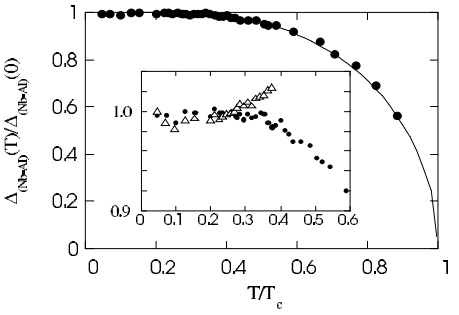

Fig. 3 Temperature dependence (Full circles) of the external electrode gap (Δ_1) derived from the gap step voltage on the assumption that this corresponds to $V_2=2\Delta_1$ and no middle Al contribution is present at this bias. The line shows the BCS prediction for comparison. The temperature is normalised to the value Tc=8.5 K for the critical temperature in the external electrode. In the inset we compare the data reported in the main figure (Full circles) with the electrode gap derived on the assumption that the gap step occurs at $V'_2=2(\Delta_1+\Delta_2)$, that is $\Delta_1=(V'_2+V_1)/4$ (Empty triangles).

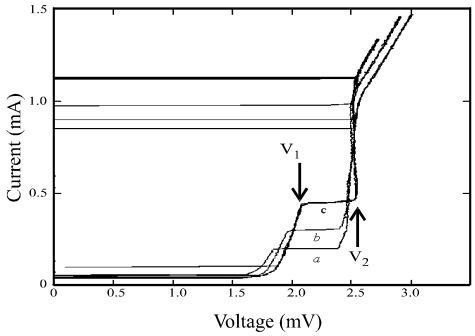

Fig. 4: I-V curves of devices with different Al thickness and same barrier transparency at 0.36K. a), b), c) refer to d_{Al}^{mid}=1.5, 2, 2.8 nm respectively

If the device was an equilibrium SIS'IS structure below the equilibrium T_c of the Al, then the gap sum feature would occur at $2(\Delta_1+\Delta_2)/e$ where the gaps would have their equilibrium values. In the nonequilibrium case there has been much uncertainty whether under these bias conditions there is sufficient extraction of quasiparticles to maintain the gap in the Al layer above $2\Delta_1/e$. Our new experimental evidence strongly suggests that the higher voltage step corresponds to the gap in the external electrodes only, i.e. that at this voltage the middle Al layer is not contributing to the gap sum feature. Fig. 3 shows the temperature dependence of Δ_1 derived in two different ways: from the voltages at which the nonequilibrium step edge, and the gap sum step occur. The nonequilibrium step is assumed to appear at $V_1=2(\Delta_1-\Delta_2)/e$. If one assumes that the feature at the gap sum occurs at $V_1=2(\Delta_1+\Delta_2)/e$ the derived temperature dependence of $\Delta_1=(V_1+V\Delta_2)/4$ does not follow the BCS temperature dependence (Fig. 3 inset). On the contrary, if one supposes that the Al^{mid} does not contribute its gap to the voltage at the gap sum step, i. e. $V_2=2\Delta_1$, the temperature dependence of $\Delta_1=V/2$ fits very well to the BCS theoretical prediction. The absence of an Al film contribution to the voltage at which the gap sum feature appears implies that no enhancement is possible under these bias conditions and would rather suggest that the gap in Al is quenched.

Further evidence for the lack of a gap in the Al at the gap sum feature is provided by the dependence of the position of the features on the degree of nonequilibrium. In Fig. 4 we compare the I-V curves of three devices with different Al thickness taken at very low temperature (0.36K). It is evident that while, the position of the subgap step edge depends upon the thickness, the inflection point at the gap sum feature occurs at the same voltage independently of the degree of nonequilibrium. That implies that under these bias conditions no gap enhancement is achievable by modulating the degree of nonequilibrium.

In Fig. 5 we show IV curves of 3 devices with different barrier transparencies and equal Al^{mid} layer thickness (20nm).

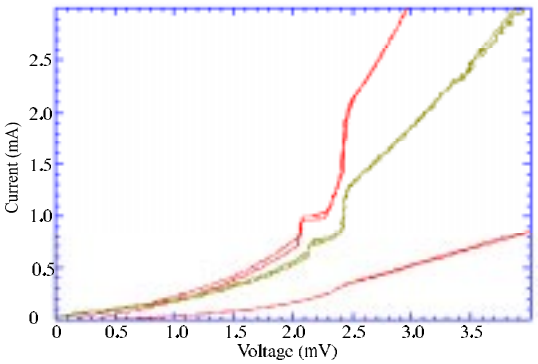

Fig. 5: I-V curves of devices with different barrier transparency and same Al thickness) at 4.2K.

The normal state conductances of the individual junctions are 3.75 Ω^{-1}, 2.31Ω^{-1} and 0.67Ω^{-1}, which from (1) and (2) and assuming a mean free path of 1 nm in the Al^{mid} film gives electron temperatures at which scattering dominates the cooling power, T_0^*, of 23K, 14K and 4.4K. Given that the sample temperature was 4.2K, it is clear that the higher conductance junctions were operating in the scattering limited regime. The lowest conductance junction is marginal; assuming scattering limited cooling, and equating this with the heat transfer from the phonon system, the phonon bath temperature that corresponds to the transition between tunneling and scattering limited cooling is 4.76K; however, these temperatures vary linearly to a first approximation with the mean free path in these conditions.

Returning to Fig. 4 we can calculate the electron temperature in the Al^{mid} layer by repeating the analysis outlined above, noting that the junction conductance of ½ Ω^{-1} gives a tunneling limited - scattering limited transition electron temperature of approximately 13K. Given a phonon temperature of 0.36K, a mean free path of 1nm, we find an electron temperature of 36mK, 40mK, and 45mK for device a, b and c respectively. By substituting back into (5) we calculate cooling powers of 0.1pW (1.67 mW m^{-2}), 0.15pW (2.5mW m^{-2}) and 0.2pW (3.33 mW m^{-2}).

It is interesting to consider what the electron temperature and cooling power would be for a device of similar conductance, with a 100nm Al layer and extremely small mean free path. In this case we take the mean free path l to be $a/\sqrt{2}$ where a is the lattice parameter of Al (0.405 nm). In this case we calculate an electron temperature of 97mK and a cooling power of 7.2pW (100 mW m^{-2}).

As our devices lack any form of independent contact to the Al^{mid} layer, we are unable to measure directly the electronic temperature. In principle we could do so by measuring Δ_2, however as Fig. 2 indicates the variation in Δ_2 in the mK region is very slight, the effects of adjusting the Al^{mid} layer thickness on the T_c swamp any variation due to changes in electron temperature. However the measured data are not inconsistent with estimated cooling effect.

V. Conclusions

In this paper we have presented clear experimental evidence on the bias dependence of the enhanced energy gap in the middle Al film of Nb-Al-AlO_x-Al-AlO_x-Al-Nb nonequilibrium structures. We have demonstrated that no gap enhancement is possible at the gap sum feature voltage, while the maximum enhancement is achieved at a voltage equal to $2(\Delta_1-\Delta_2)/e$. We also have showed that the current rise at the gap sum occurs at a voltage equal to $2\Delta_1/e$, suggesting that under this bias conditions the Al gap is quenched.

These results disagree with the theoretical predictions derived by Heslinga and Klapwijck within the SINIS model and which locate the gap sum feature at $2(\Delta_1+\Delta_2)/e$. This discrepancy would suggest that modifications need to be brought to the model for it to account for the observed behaviour.

We have made qualitative estimates of the electronic cooling obtainable with our device parameters, demonstrating that the cooling is not limited by our junction conductances, rather that the limiting factors are the mean free path and dimensions of the Al^{mid} layer. In order for the calculations to be quantitative we require a new model that allows for the superconductivity of the Al^{mid} layer and our device structure needs to be modified to allow independent measurement of the Al^{mid} layer electron temperature. Further improvements in the performance of the devices should be possible with reasonable thermal isolation of the cooled layer from the environment, thus allowing a reduction in the phonon temperature in the cooled layer for complete cryocooler operation.

References

[1] R.H. Parmenter, *Phys. Rev. B.*, vol. 11, pp. 274, October,1961.
[2] M.G. Blamire, E.C.G. Kirk, J.E. Evetts and T.M. Klapwijk, "Extreme Critical-Temperature Enhancement of Al by Tunneling In Nb/AlOx/Al/AlOx/Nb Tunnel-Junctions," *Phys. Rev. Lett.*, vol. 66, pp. 220-223, January, 1991.
[3] M.M. Leivo, J.P. Pekola and D.V. Averin, "Efficient Peltier Refrigeration by a Pair Of Normal Metal/Insulator/Superconductor Junctions," *Appl. Phys. Lett.*, vol. 68, pp. 1996-1998, April,1996.
[4] M. Nahum, T.M. Eiles and J.M. Martinis, "Electronic Microrefrigerator Based On a Normal-Insulator- Superconductor Tunnel Junction," *Appl. Phys. Lett.*, vol. 65, pp. 3123-3125, December,1994.
[5] D.R. Heslinga and T.M. Klapwijk, "Enhancement of Superconductivity Far Above the Critical-Temperature in Double-Barrier Tunnel-Junctions," *Phys. Rev. B*, vol. 47, pp. 5157-5164, March, 1993.
[6] H.L. Edwards, Q. Niu, G.A. Georgakis and A.L. Delozanne, "Cryogenic Cooling Using Tunneling Structures With Sharp Energy Features," *Phys. Rev. B*, vol. 52, pp. 5714-5736, August, 1995.
[7] N.W. Ashcroft and N.D. Mermin, *Solid State Physics*. College Edition ed. 1976, Saunders College Publishing.
[8] F.C. Wellstood, C. Urbina and J. Clarke, "Hot-Electron Effects In Metals," *Phys. Rev. B*, vol. 49, pp. 5942-5955, March, 1994.
[9] R.C. Weast, *Handbook of Chemistry and Physics*. 57th Edition ed. 1976, Cleveland, Ohio: CRC Press.

Appendix B

Phonon Coupling Between SIN Tunnel Junctions

G. Burnell[1], I. Kanno[1,a], M. G. Blamire[1]
[1] *Dept. Materials Science, University of Cambridge, Cambridge CB2 3QZ UK.*
[a] *Permanent address: Dept. Nucl. Engineering, Kyoto University, Japan*

Abstract

As part of our work developing Superconductor-Insulator-Normal Metal (SIN) tunnel-junction based bolometers, we have fabricated devices with multiple distributed junctions and have investigated the coupling between junctions and devices using injection-detection experiments. The observed non-linearity in the coupling between junctions is discussed in terms of the non-equilibrium phonon distribution and propagation in our devices.

1 Introduction

Bolometers with SIN tunnel junction readouts are promising candidates for high energy resolution X-ray and phonon detectors due to the strong dependence of the thermal tunnel current on the electron temperature in the normal metal[1][2].

In order to assess and optimize our device structures and deposition parameters for producing SIN tunnel junction bolometers we have produced devices with multiple distributed junctions with common absorbers. We have studied these devices with injection-detection experiments to assess the magnitude, reproducibility and uniformity of the response of the detector sub-gap current to the increased electron temperature in the absorber.

Here we report results showing that although the coupling between two junctions is mediated via substrate phonons, the presence of a normal metal absorber between the junctions will effectively suppress the coupling. We attribute these results to localized heating by athermal 2Δ phonons and thermalisation of the signal in the absorber with subsequent thermal leakage to the substrate.

2 Experimental

For the results presented here, the devices fabricated were $Nb/Al/AlO_x/Al/Pd/Au$ multilayers produced in a combination of whole wafer multilayer processing and lift-off techniques, on R-plane sapphire substrates. For most devices a final 50nm Nb layer was sputtered when depositing the absorber. One device was fabricated on a $1\mu m$ thick Si_3N_4 membrane of approximately $1mm^2$ area, created by wet etching a Si_3N_4 coated Si wafer.

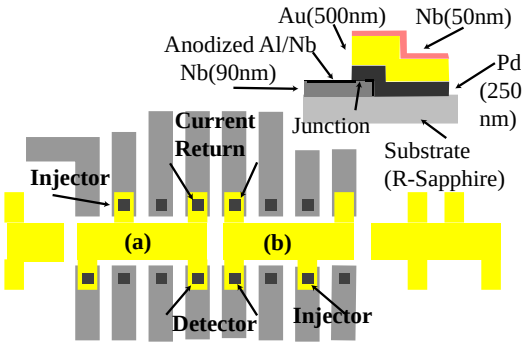

Figure 1: Device structure and plan view, showing two measurement configurations (a) and (b).

Fig. 1 shows a schematic of the final device structure with a plan view of a device with two absorbers, one with 3 junctions and an SN contact, the other with 4 junctions. Two different measurement configurations are also shown; (a) injector and current return adjacent, detector junction opposite, and (b) detector junction adjacent to injector junction, current return junction opposite .

The devices were measured in a He^3 insert at a temperature of 0.350K. Injection-detection experiments were performed by measuring the change in I-V characteristic of one junction with an injected current from a second junction. Data were taken for injector currents corresponding to junction bias in the range $0-4\Delta/e$ (0–5mV). Since the common electrode in this configuration is a normal metal, the measured bias across the detector junction exhibits an offset proportional to the injector current which related to the relative geometry of the injector, detector and other current voltage contacts to the absorber. To eliminate this extra factor, a thin Nb layer was deposited on top of the normal metal. This effectively equalized the potential across the absorber and removed the geometrical factors, although the interactions between the injected ('hot') electrons and this SN interface do have to be considered.

3 Results

Depending on the measurement configuration, two types of response were observed for sapphire substrate devices; essentially no response (Fig. 2a) – measurement configuration as in Fig. 1a, and a step in the

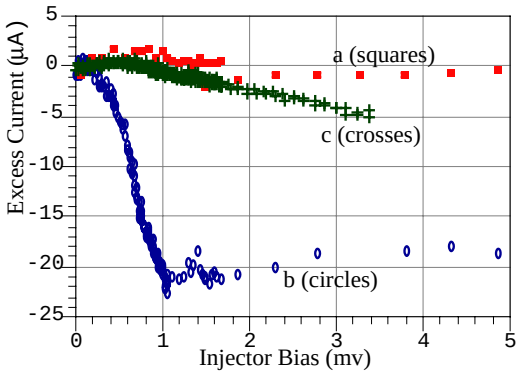

Figure 2: Additional detected current (at a detector bias of -0.5mV) as a function of injected current for (a) configuration in fig. 1a, (b) configuration in fig. 1b, and (c) device on membrane.

response at a bias in the injector of approximately Δ/e (Fig. 2b) – configuration as in Fig. 1b. Increasing the distance between the detector junction and second junction did not result in a significant difference in the response. Measurements between the two electrically isolated absorbers demonstrated coupling between the two devices, thus implying coupling via substrate phonons. For the device on a membrane the response was independent of configuration and qualitatively different (Fig. 2c)

4 Discussion

There are two particular points to be explained in these results, firstly the form of the response with a sharp step at an injector bias of Δ/e and secondly the geometrical effect where coupling is not observed across the absorber.

A simple scaling with injected current or power would not explain the essentially constant response for injector biases in the range $\Delta/e - 4\Delta/e$. Since coupling between electrically isolated devices implies phonon mediation, an alternative explanation involving the phonon emission processes is required.

When the injector junction is biased at the energy gap, the current flow introduces a large population of quasi-particles into the superconductor, well in excess of the thermal population[3]. This will result in a large local concentration of recombination phonons. For biases between Δ and 4Δ, quasiparticles will scatter inelastically before recombination to produce 2Δ and sub 2Δ energy phonons[4].

Phonons which enter the normal metal will rapidly inelastically scatter to create a hot electron since in this temperature regime the majority of the heat capacity of the metal is electronic[5]. Although the hot electron will have a relatively long lifetime against inelastic scattering, the distance between inelastic scattering events is short as the elastic mean free path is of order nm[6]. Thus a phonon's energy is deposited within a relatively small region of the normal metal, within a length scale of order 10μm. It could be expected that the electron temperature would relax to the phonon temperature over a length-scale similar to the device dimensions[7], however the effect of Andreev reflection combined with good thermal conductance to the substrate will reduce this effect.

If there is little normal metal between the detector and phonon source then 2Δ phonons will be absorbed in the normal metal adjacent to the junction, creating a local hot spot, which will give rise to the observed increase in detector current. Otherwise the athermal phonons will be absorbed and thermalised away from the detector, resulting in no signal. For this reason we observe the geometrical effects in the sapphire substrate devices.

If the device is on a membrane, the energy deposited at the injector is almost entirely coupled to the normal metal electron system. Since the energy loss via thermal phonons to the substrate is much reduced, the electron temperature is increased significantly throughout the normal metal; thus we observe no geometrical dependence and a linear increase in detected excess current for injector biases in excess of Δ/e.

5 Conclusions

We have fabricated devices with multiple distributed SIN tunnel junctions with a common normal metal electrode. We have explained the observed geometrical dependence of the coupling between junctions in our injection-detection experiments by localized heating in the absorber from athermal phonons produced as a result of recombination of the non-equilibrium population of quasi-particles close to the injecting junction.

Further information can be found at: http://www-dmg.msm.cam.ac.uk/dmg/people/gb119/

References

[1] H. Kraus, Supercond. Sci. Technol. 9 (1996) 827

[2] J.M. Martinis, Nucl. Instr. Meth. A 370 (1996) 171

[3] J.J. Chang, D.J. Scalapino, Phys. Rev. B 15 (1977) 2651

[4] G. Burnell, P.A. Warburton, M.G. Blamire, J. Appl. Phys. 76 (1994) 1105

[5] M. Nahum, J.M. Martinis, S. Castles, J. Low Temp. Phys. 93 (1994) 733

[6] F.C. Wellstood, C. Urbina, J. Clarke, Phys. Rev. B. 49 (1994) 5942

[7] A.H. Steinbach, J.M. Martinis, M.H. Devoret, Phys. Rev. Lett. 76 (1996) 3806